STUDY OF CRYOGENIC PROPERTIES OF TIN ALLOYS FOR THE DEVELOPMENT OF A SUPERCONDUCTING BOLOMETER

By

MAZUMDAR APARAJITA SOUMITRA

PHYS01201504024

BHABHA ATOMIC RESEARCH CENTRE, MUMBAI

A thesis submitted to the
Board of Studies in Physical Sciences

In partial fulfillment of requirements
For the Degree of

DOCTOR OF PHILOSOPHY
of
HOMI BHABHA NATIONAL INSTITUTE

July, 2021

Homi Bhabha National Institute

Recommendations of the Viva Voce Committee

As members of the Viva Voce Committee, we certify that we have read the dissertation prepared by **Mazumdar Aparajita Soumitra** entitled **"Study of cryogenic properties of tin alloys for the development of a superconducting bolometer"** and recommend that it may be accepted as fulfilling the thesis requirement for the award of Degree of Doctor of Philosophy.

Chairman - Dr. Bency John   Date: 15/12/'21

Guide / Convener - Dr. Aradhana Shrivastava   Date: 15.12.21

Co-Guide - Prof. Vandana Nanal   Date: 15/12/21

Examiner - Prof. Deepshikha Jaiswal-Nagar   Date: 15/12/2021

Member 1 - Prof. R. G. Pillay   Date: 15/12/2021

Member 2 - Prof. S. Ramakrishnan   Date: 20/12/2021

Member 3 - Prof. Satyajit Saha   Date: 15/12/2021

Final approval and acceptance of this thesis is contingent upon the candidate's submission of the final copies of the thesis to HBNI.

We hereby certify that we have read this thesis prepared under our direction and recommend that it may be accepted as fulfilling the thesis requirement.

Date: 15-12-21

Place: Mumbai

Prof. Vandana Nanal   Dr. Aradhana Shrivastava
(Co-Guide)   (Guide)

i

Statement by the Author

This dissertation has been submitted in partial fulfillment of requirements for an advanced degree at Homi Bhabha National Institute (HBNI) and is deposited in the library to be made available to borrowers under rules of the HBNI.

Brief quotations from this dissertation are allowable without special permission, provided that accurate acknowledgement of source is made. Requests for permission for extended quotation from or reproduction of this manuscript in whole or in part may be granted by the Competent Authority of HBNI when in his or her judgement the proposed use of the material is in the interests of scholarship. In all other instances, however, permission must be obtained from the author.

July 2021, Mumbai

Mazumdar Aparajita Soumitra

DECLARATION

I hereby declare that the investigation presented in the thesis has been carried out by me. The work is original and has not been submitted earlier as a whole or in part for a degree/diploma at this or any other Institution/University.

July 2021, Mumbai

Mazumdar Aparajita Soumitra

List of Publications arising from the thesis

Refereed journals

1. Studies on $\beta \rightleftharpoons \alpha$ transition in Sn and Sn-rich alloys for a cryogenic tin bolometer, **A. Mazumdar**, A. Garai, H. Krishnamoorthy, G. Gupta, A. Reza, A. Thamizhavel, V. Nanal, R.G. Pillay, A. Shrivastava, Materials Research Express, **6**, 076521 (2019).

2. Synchrotron x-ray diffraction studies of the $\alpha \rightleftharpoons \beta$ structural phase transition in Sn and Sn-Cu, **A. Mazumdar**, A. Thamizhavel, V. Nanal, R.G. Pillay, A. Upadhyay, V. Vatsa, A. Reza, A. Shrivastava, Bhagyashree Chalke S. Mallikarjunachary, Scripta Materialia, **199**, 113858 (2021).

Conference proceedings

1. Study of long-lived activities from fast neutron-induced reactions in tin-bismuth alloys, **A. Mazumdar**, Rebecca Pachuau, V. Vatsa, H. Krishnamoorthy, A. Garai, A. Reza, V. Nanal, R.G. Pillay, A. Shrivastava, A. Thamizhavel, Proc. DAE-BRNS Symp. on Nucl. Phys. **64**, 264 (2019).

2. Radiopurity studies of tin-lead and tin-bismuth alloys for the development of a cryogenic bolometer, **A. Mazumdar**, G. Gupta , A. Garai, H. Krishnamoorthy, A. Reza, V. Nanal, R. G. Pillay, A. Shrivastava, A. Thamizhavel, Proc. DAE-BRNS International Symp. on Nucl. Phys. **63**, 1152 (2018).

3. Radiopurity studies of indium-doped tin alloys for *TIN.TIN*, **A. Mazumdar**, G. Gupta, J. Raval, A. Garai, H. Krishnamoorthy, V. Nanal, R.G. Pillay, A. Shrivastava, A. Thamizhavel, R. Mondal, Proc. DAE-BRNS Symp. on Nucl. Phys. **62** (2017), 1118.

Conferences presentations

1. Presented a poster on 'Estimation of the internal radiation background of Sn-Bi bolometers for *TIN.TIN*' at the Invisibles21 Workshop, Virtual (ITN HIDDeN, Madrid), May-June 2021.

2. Presented a poster on 'Radiation background studies for superconducting Sn-Bi bolometers' at the International workshop on Weak Interactions and Neutrinos 2021, Virtual (University of Minnesota), June 2021.

3. Presented a poster on 'Testing of a cryo-vibration free isolation platform for a cryogen-free dilution refrigerator at TIFR' at Pressing for Progress, University of Hyderabad, Hyderabad, September 2019.

4. Presented a poster on 'Radiopurity studies of tin-lead and tin-bismuth alloys for the development of a cryogenic bolometer' at the DAE International Symposium on Nuclear Physics, Bhabha Atomic Research Centre, Mumbai, December 2018.

5. Presented a poster 'Radiopurity studies of indium-doped tin alloys for *TIN.TIN*' at the DAE-BRNS Symposium on Nuclear Physics, Thapar University , Patiala, December 2017.

Others

Refereed journals

1. Systematic Studies of a Sapphire Bolometer with Phonon Pulses in the Temperature Range of 10-100 mK, A. Garai, **A. Mazumdar**, A. Reza, H. Krishnamoorthy, G.Gupta, V. Nanal, R. G. Pillay, S. Ramakrishnan, J Low Temp Phys **199**, 95 (2020).

2. A Cryogenic Front-End Preamplifier Operating at 120 K for Bolometric Detector, A. Reza, V. Vatsa, M. S. Pose, **A. Mazumdar**, A. Garai, H. Krishnamoorthy, G. Gupta, V. Nanal, R. G. Pillay, A. Shrivastava, J Low Temp Phys **199**, 200 (2020).

3. Thermal neutron-induced γ-ray background in ^{124}Sn, G. Gupta, H. Krishnamoorthy, A. Garai, **A. Mazumdar**, V. Nanal, A. Shrivastava, R. G. Pillay, Applied Radiation and Isotopes **158**, 108923 (2020).

4. Study of the effect of external noise pickups on the performance of a cryogenic bolometer, A. Garai, A. Reza, **A. Mazumdar**, H. Krishnamoorthy, G. Gupta, M. S. Pose, S. Mallikarjunachary, V. Nanal, R. G. Pillay, S. Ramakrishnan, Rev. Sci. Instrum. **90**, 096104 (2019).

5. Study of γ-ray background from cosmic muon induced neutrons, H. Krishnamoorthy, G. Gupta, A. Garai, **A. Mazumdar**, A. Reza, S. Pal, S. Pethuraj, V. Nanal, A. Shrivastava, and R.G. Pillay, Eur. Phys. J. A **55**, 1 (2019).

Conference proceedings

1. Study of neutron production from stopping muons, H. Krishnamoorthy, G. Gupta, A. Garai, **A. Mazumdar**, A. Reza, V. Vatsa, R. Pachuau, S. Pal, V. Nanal, R.G. Pillay, A. Shrivastava, Proc. DAE-BRNS Symp. on Nucl. Phys. **64**, 872 (2019).

2. A low noise high gain differential amplifier for bolometric detector, A. Reza, V. Vatsa, M.S. Pose, **A. Mazumdar**, A. Garai, H. Krishnamoorthy, G. Gupta, R. Pachuau, V. Nanal, R.G. Pillay, Proc. DAE-BRNS Symp. on Nucl. Phys. **64**, 938 (2019).

3. Estimation of carrier concentration of a NTD Ge from the resistivity measurement at 4K, V. Vatsa, A. Reza, S. Saraf, **A. Mazumdar**, A. Garai, H. Krishnamoorthy, V. Nanal, R.G. Pillay, A. Shrivastava, Proc. DAE-BRNS Symp. on Nucl. Phys. **64**, 980 (2019).

4. Bolometer pulse analysis using optimal filter, A. Garai, V. Vatsa, **A. Mazumdar**, A. Reza, H. Krishnamoorthy, G. Gupta, V. Nanal, R.G. Pillay, Proc. DAE-BRNS Symp. on Nucl. Phys. **64**, 982 (2019).

5. A pulse height analysis technique for cryogenic bolometers, A. Garai, **A. Mazumdar**, A. Reza, H. Krishnamoorthy, G. Gupta, V. Nanal, R.G. Pillay, Proc. DAE-BRNS International Symp. on Nucl. Phys. **63**, 1140 (2018).

6. Design and development of a front-end preamplifier for bolometric detector, A. Reza, A. Garai, **A. Mazumdar**, V. Vatsa, H. Krishnamoorthy, G. Gupta, M.S. Pose, S. Mallikarjunachary, V. Nanal, R.G. Pillay, Proc. DAE-BRNS International Symp. on Nucl. Phys. **63**, 1124 (2018).

7. The neutron induced γ-ray background in ^{124}Sn, G. Gupta, H. Krishnamoorthy, A. Garai, **A. Mazumdar**, V. Nanal, A. Shrivastava, R.G. Pillay, Proc. DAE-BRNS International Symp. on Nucl. Phys. **63**, 232 (2018).

8. Modeling of an electrically cooled HPGe detector, G. Gupta, H. Krishnamoorthy, A. Garai, **A. Mazumdar**, A. Reza, V. Nanal, R.G. Pillay, Proc. DAE-BRNS International Symp. on Nucl. Phys. **63**, 1142 (2018).

9. Muon Induced Neutron measurement setup at TIFR (MINT), H. Krishnamoorthy, G. Gupta, A. Garai, **A. Mazumdar**, A. Reza, S. Pal, V. Nanal, R.G. Pillay, A. Shrivastava, Proc. DAE-BRNS International Symp. on Nucl. Phys. **63**, 1146 (2018).

10. Assessment of borated rubber for neutron shield, H. Krishnamoorthy, G. Gupta, A. Garai, **A. Mazumdar**, S. Pal, V. Nanal, R.G. Pillay, A. Shrivastava, Proc. DAE-BRNS International Symp. on Nucl. Phys. **63**, 1148 (2018).

11. Radiopurity Study of CsI and CsI(Tl) detectors for the mini-DINO, G. Gupta, H. Krishnamoorthy, A. Garai, **A. Mazumdar**, V. Nanal, R.G. Pillay, S. Saha, S. Ghosh, S.G. Singh, Shashwati Sen, S.C. Gadkari, Proc. DAE-BRNS Symp. on Nucl. Phys. **62**, 998 (2017).

Conference presentations

- Presented a poster on 'Systematic Studies of a Sapphire Bolometer with Phonon Pulses in the Temperature Range of 10-100 mK' at the 18th International Workshop on Low Temperature Detectors, Milan, Italy, July 2019.

July 2021, Mumbai

Mazumdar Aparajita Soumitra

Dedicated to

My late grandfather, Bimal Chandra Mazumdar

For introducing me to the fascinating world of physics

ACKNOWLEDGEMENTS

very close to my heart, and I am very glad that I was able to complete it during my Ph.D.

I am grateful to the members of the NDBD lab at TIFR for their invaluable help through the course of my work, as well as general camaraderie. Sincere thanks to Abhijit, Ashif, Rebecca, Vishal, Harisree, Ghnashyam, Mahesh, Mallikarjunachary and Kiran. I thank lab alumni Dr. Vivek Singh, Dr. Neha Dokania and Dr. S. Mathimalar, for their helpful advice.

Thanks to the scientific officers of DCMP & MS for helping me in the material characterization experiments and sharing their considerable expertise with me – Ruta, Smita, Ganesh, Bhagyashree, Rudheer, Jayesh, Nilesh, Vilas, Anil and Ulhas. I am grateful to the students and postdocs of DCMP & MS for their help and useful discussions – Rajib da, Biplob da, Soham da, Souvik and Gaurav. I sincerely thank Prof. R. Mallik and Prof. S. Mazumdar and their students for help in incubating the alloy samples. Special thanks to Taher and Jagjeet. I have really benefited from the collaborative nature, knowledge and expertise of the several researchers at TIFR, which made this thesis work possible. I would also like to acknowledge the technical support extended by the TIFR central workshop and glass blowing sections.

Thanks to all the past and present members of the India-based Neutrino Observatory (INO) Collaboration, for supporting me as an INO graduate student. A special thanks to my instructors during the coursework of the INO graduate school: Prof. Vivek Datar, Prof. Kajari Mazumdar, Prof. Gobinda Majumder, Ms. Mandakini Patil, Prof. Vandana Nanal, Prof. S. Uma Sankar and Prof. Sudeshna Banerjee.

I am really grateful to all of my family and friends for always believing in me, and wishing for my success. I express my heartfelt thanks to my closest confidante and partner, Sayantan, for staying by my side through the good and bad times. The company of my friends Sayantan, Gunjan, Bhandari, Poonam and Ravi made life at TIFR truly enjoyable. Some interactions transcend spatial proximity: Suchetana, Sarvesh, Nandani, Manik, Soham, Garima, Shubho (and Mainak) - thanks for being there for me. Most importantly, I would never have made it to this point in my life without the unfailing love and support of my dear father, Soumitra Mazumdar and brother, Rishab.

Contents

Synopsis

The experimental observation of neutrino oscillations [1, 2] has established that neutrinos have a finite mass, making neutrino physics a prime candidate in the search for physics beyond the Standard Model. Since the neutrino (ν) is a chargeless fermion with finite mass, a fundamental question exists regarding its distinctness from its antiparticle, which remains unsolved. Fermionic particles which are indistinguishable from their antiparticle are known as Majorana fermions, as opposed to Dirac fermions which are distinct from their antiparticles. The observation of a lepton number violating process, known as neutrinoless double beta decay ($0\nu\beta\beta$ or NDBD), would definitively establish the Majorana nature of the neutrino. The $0\nu\beta\beta$ process is a second order weak decay in which a parent nucleus $X(A, Z)$ decays to a daughter nucleus $Y(A, Z + 2)$, without producing antineutrinos ($\bar{\nu}$) in the final state. The main experimental signature is a peak at the end point ($Q_{\beta\beta}$) in the sum energy spectrum of the emitted β particles. There are about 35 $\beta\beta$ candidate nuclei where single β decay is energy or spin forbidden. Currently, several experimental collaborations across the world [3] are searching for $0\nu\beta\beta$ decay. Although the Standard Model process $2\nu\beta\beta$ has been observed in about a dozen nuclei, $0\nu\beta\beta$ is yet to be observed.

The **In**dia-based **tin** detector (*TIN.TIN*)[4] proposes to explore $0\nu\beta\beta$ in the isotope ^{124}Sn using an array of cryogenic tin-based bolometers. Cryogenic bolometers are calorimetric detectors which are expected to have an excellent energy resolution, and are typically operated at ~mK temperatures [5]. The bolometer consists of an absorber which is strongly coupled

to a sensitive thermometer and is weakly coupled to a heat bath. The choice of the absorber is crucial to the performance and stability of the bolometer. For the search of $0\nu\beta\beta$, the absorber is usually made out of the $0\nu\beta\beta$ isotope or its compound. A central challenge in the fabrication of Sn-based cryogenic bolometers is the phenomenon of tin pest, a metal (β) to semiconductor (α) phase transition in Sn, which occurs in near-ambient conditions. Due to the sudden lattice expansion associated with the phase transition, this process leads to the deformation and cracking of the Sn sample. Given that $0\nu\beta\beta$ is a rare decay process with typical half-life limits $T_{1/2} > 10^{26}$ y [3], *TIN.TIN* is expected to utilize a large mass of Sn (100 - 1000 kg) and acquire data for several years. During this period, the detector array would be susceptible to this damaging transition during the thermal cycling from room temperature to mK temperatures [6]. Therefore, tin pest poses a complex challenge for the longevity and performance of Sn-based bolometers. It is known that alloying Sn with an appropriate element can pin the dislocations in the crystal, thereby suppressing the lattice expansion associated with tin pest formation [7]. The $\beta \rightarrow \alpha$ transition becomes kinematically unfavourable when the lattice expansion associated with the change of crystal structure is suppressed.

This thesis involves a multi-disciplinary approach towards qualifying a Sn-rich alloy as a candidate for the fabrication of superconducting bolometers for *TIN.TIN*, on the basis of resistance to tin pest, superconductivity and radiopurity of the alloys. The first section briefly describes various maintenance and instrumentation involving dilution refrigerators, which are a central technology for experiments involving cryogenic bolometers. The next section describes the preparation and testing of several alloy candidates for resistance to tin pest. The Sn-Bi alloy showed the most resistance to tin pest and was subsequently investigated thoroughly on other parameters. The superconductivity measurements of the Sn-Bi alloys were performed, in order to check that critical temperature T_c did not vary significantly from that of pure tin. The subsequent section describes the detailed studies of the allotropic $\alpha \leftrightharpoons \beta$ transition which affects Sn and Sn-rich alloys, using modern techniques such as synchrotron x-ray diffraction at RRCAT Indore [8], differential scanning calorimetry and temperature-resolved scanning electron microscopy. Based on these studies, a protocol to reduce the risk of tin pest has been discussed which would be useful to *TIN.TIN*. It should be mentioned that this protocol would also be useful for critical electronic systems using lead-free solders and

operating at low temperatures. Finally, the background and radiopurity estimations for Sn-Bi bolometers have been discussed.

Millikelvin measurement setup

Cryogen-free dilution refrigerators are the preferred technology for maintaining ~mK temperatures of bolometric experiments at underground laboratories, as continuous access to liquid Helium is challenging. A custom-built cryogen-free dilution refrigerator (CFDR-1200) is installed at TIFR for research related to the development of bolometers for *TIN.TIN* [9]. The system has a high cooling power (1.4 mW at 120 mK) and is capable of supporting ~100 kg on its mixing chamber plate. Following a major blockage in the dilution lines, the *still* was upgraded to a unit designed with pressure dependent primary impedances, making the system resistant to future blockages [10]. Maintenance and instrumentation for the CFDR-1200 was an important part of this thesis. Calibration checks of the secondary diagnostic Carbon Speer thermistors mounted on the mixing chamber were performed using a Fixed Point Device and/or Cerium Magnesium Nitrate thermometers. A motorized probe station was installed and tested in the CFDR-1200. Leak testing of the probe lift was performed to qualify the system. Additionally, a commercial cryo-vibration isolation plate was installed to mitigate vibration induced noise in the system as this can affect the performance of the bolometer. A significant reduction in the noise spectrum of shielded thermistors was observed at high frequencies (>5 kHz).

Growth and characterization of Sn-rich alloys

Addition of elements such as Bi and Pb to Sn is known to inhibit tin pest, although there are inconsistencies among studies by various groups [11, 12] regarding the efficacy of different alloying elements and the concentrations that are beneficial. For the present study, Sn-rich alloys (Sn-X, X= Cd, In, Sb, Bi, Pb) of a wide range of concentrations were independently grown and tested for resistance to tin pest. Pure Sn and Sn-Cu crystals were grown as control samples. High purity Sn (99.99999%) and alloying elements (99.999% or more) were used for the sample fabrication. Initially, the vertical Bridgman technique was used to grow Sn and

Sn-In single crystals. Laue back-diffraction images were recorded and the crystals were found to be single crystals of good quality. However, this methodology was soon replaced with polycrystalline sample growth in a box furnace, which allowed multiple samples to be grown simultaneously thus improving the turnover time tremendously. Polycrystalline samples are expected to show better thermalization at low temperatures compared to single crystals, due to smaller mean free paths associated with the phonons.

Cooling tests of alloys to check inhibition of tin pest

The $\beta \rightarrow \alpha$ Sn transition (tin pest) is a two-step process comprising of nucleation and growth. It is difficult to study the exact conditions necessary for spontaneous nucleation in nature, as this could take anywhere between a few hours to a few years. Thus, nucleation is the rate determining step of the transition. The process can be accelerated by introducing an isomorphic seeding agent such as α-Sn, Cd-Te, In-Sb, etc. [13]. For the present study, the alloy samples were seeded with a small mass of α-Sn powder and maintained at temperatures of 248 to 253 K (i.e., -25 to -20°C) for long durations of time. These samples were regularly checked for signs of transformation such as volume increase, micro-fractures, cracks, development of warts and change in the colour of the sample. The Sn-Cu and Sn-Cd samples were found to be susceptible to tin pest. The Sn-Pb alloys performed better in comparison, but developed tin pest over long durations of time. The Sn-In, Sn-Bi and Sn-Sb samples showed promising results with respect to the inhibition of tin pest. However, the Sn-Sb and Sn-In samples were regarded as unsuitable due to the anticipated background from neutron activation channels in the region of interest (ROI). The Sn-Bi alloy was found to be the most suitable candidate and we focussed our efforts on growing and characterizing Sn-Bi crystals with progressively lower concentrations. The best performance was found in 0.22% Sn-Bi which showed no development of tin pest for ∼1 year.

Superconductivity measurements of Sn-Bi alloys

The energy resolution of bolometers ΔE is given by $\Delta E = \sqrt{k_B T^2 C}$, depending only on the temperature of the heat bath (T) and the heat capacity of the absorber (C). Superconductors are good candidates for fabricating bolometers since they have low heat capacity at temperatures

below the critical temperature T_c. The electronic heat capacity of a superconductor falls off exponentially below the T_c and it behaves as a Debye solid with phononic heat capacity $\propto T^3$. It is important that the T_c of Sn-Bi samples should not vary greatly from that of pure Sn. Magnetic susceptibility measurements for the Sn-Bi alloys (0.08% -1.69%) were performed using a DC SQUID magnetometer. The alloys were found to be superconducting at a critical temperature within 2% of that of pure Sn. The transition width of pure tin was found to be ~0.1 K and that of the alloy samples varied between ~0.1 - 0.2 K. The superconductivity for a few samples was also tested using heat capacity measurements and SQUID vibrating sample magnetometry. The robustness of the observed superconducting transition implies that Sn-Bi alloys are suitable for use in superconducting bolometers.

Investigations of the structural phase transition in tin

Differential scanning calorimetry measurements

The reported differential scanning calorimetry (DSC) measurements of the $\alpha \rightarrow \beta$ transition temperature in Sn [14, 15, 16, 17] were inconsistent. This work resolved this inconsistency by independently studying the $\alpha \rightarrow \beta$ transition in Sn using DSC. The present observations in Sn were found to be consistent with the observations by Ojima *et. al.* [14]. The $\alpha \rightarrow \beta$ transition temperature in Sn is measured to be 34.4°C (onset). Additionally, the transition temperature for the $\alpha \rightarrow \beta$ process in Sn-Cu (alloyed 0.5% by weight) is measured for the first time and found to be 36.3°C (onset).

Synchrotron x-ray diffraction measurements at RRCAT

While no direct phase information can be revealed from DSC measurements, the unique phase signatures from the α and β Sn phases can be studied using x-ray diffraction. Temperature resolved synchrotron x-ray diffraction measurements were performed at BL-12 of the Indus-2 synchrotron at the national facility RRCAT Indore [8]. These measurements were performed for Sn, Sn-Cu, Sn-Cd and Sn-Pb using x-rays tuned to a wavelength of $\lambda = 0.83$ Å. The data obtained for the Sn and Sn-Cu samples were of high quality and the results were found to be consistent with the DSC study. The measurements for Sn were further verified on a

conventional Rigaku diffractometer at TIFR Mumbai. Fig. A.4 shows the XRD data for the Sn sample. Based on these measurements, it is suggested that the *TIN.TIN* bolometer array
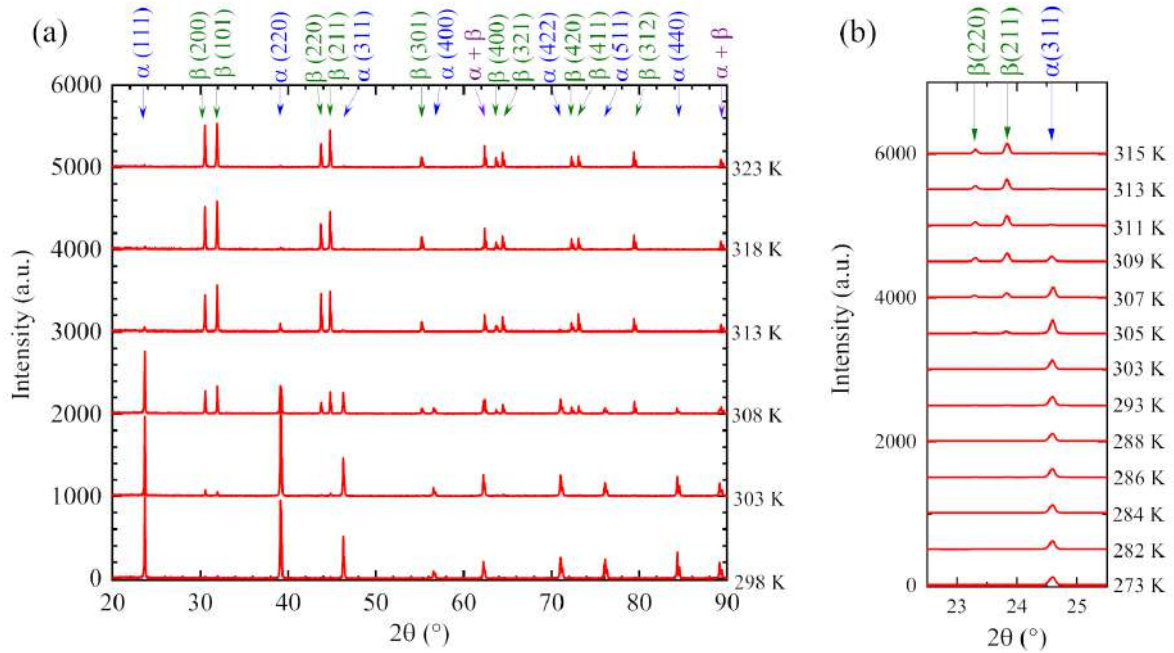
Figure 0.1: (a) Conventional XRD data for Sn acquired on Rigaku diffractometer using Cu-K_α x-ray (b) Synchrotron XRD data for Sn acquired with $\lambda = 0.83$ Å at RRCAT Indore.

should be baked at 50°C for a few min (20 - 30 min) between thermal cycling to further reduce the risk of tin pest. This protocol would also be useful in low temperature systems utilizing lead-free solders such as Sn-Cu.

Temperature-resolved scanning electron microscopy

In the literature, the $\alpha \rightarrow \beta$ transition temperature is quoted as 13.2°C [12]. However, repeated measurements of the transition temperature performed for this thesis using different techniques consistently placed the transition temperature to be closer to the temperature region around ~35°C, rather than ~13°C. The measurement for 13.2°C comes from dilatometric type experiments [18], which tracks the volume expansion of the sample. For the present study, an analogous experiment was performed to track the volume change associated with the transformation using temperature-resolved scanning electron microscopy. Images of the $\beta \rightarrow \alpha$ transition in Sn were recorded over a period of ~27 h. In the case of the $\alpha \rightarrow \beta$ transition a real-time video was recorded. This measurement, like the others described above, was consistent with an $\alpha \rightarrow \beta$ Sn transition temperature in the temperature region close to

~35°C. Since α-Sn is a material with novel topological properties and may have applications for developing qubits [19], it is important to note that the material is more stable at room temperature than previously believed.

Radiation background studies for Sn-Bi bolometers

Estimations of radioimpurities in Sn-Bi crystals

In the absence of a clearly observed signal, a lower limit on the half-life of $0\nu\beta\beta$ ($T_{1/2}^{0\nu}$) can be set using data acquired for a counting period t using a detector of mass M with an isotopic abundance i of the $\beta\beta$ candidate using $T_{1/2}^{0\nu} > \frac{ln2 N_A i\epsilon}{A f_{CL}} \sqrt{\frac{Mt}{B\Delta E}}$, where N_A is Avogadro's number, ϵ is the efficiency of the detector, A is the molar mass of the absorber material, f_{CL} is the no. of standard deviations corresponding to a confidence level, B is the background index in the ROI and ΔE is the energy resolution of the detector. Since, the sensitivity of a $0\nu\beta\beta$ decay experiment can be improved by reducing the background index, these experiments have stringent background requirements. Detector materials are screened for radio-purity since the internal background of the detectors comprise an irreducible background, especially in bolometric experiments like *TIN.TIN*, where particle discrimination is practically impossible. The radiopurity of a Sn-Bi sample (alloyed ~9% Bi by weight) was checked by counting it for ~ 5 days in the low background HPGe detector set-up TiLES [20]. This was done to check for any radioimpurities that may have been introduced during the crystal growth process. A Sn crystal was also counted for comparison. No new γ lines or enhancements were observed in the spectrum of the Sn-Bi sample in comparison to the background or the Sn crystal, at the sensitivity level of TiLES.

Neutron activation studies of Sn-Bi at the Pelletron Linac Facility

Neutron-induced backgrounds in the detector material can often be a limiting background for rare decay experiments such as $0\nu\beta\beta$. The neutron activation technique was used to investigate the neutron-induced background in Sn-Bi alloys. The samples were irradiated with fast neutrons at the 6m target setup of the Pelletron Linac Facility, TIFR Mumbai [21]. Fast neutrons were generated through the $^9Be(p,n)^9B$ reaction (Q_{th}= 2.057 MeV) by using

proton beams with energy E_p = 15 - 21 MeV on a ^9Be target, upto a maximum flux of $\phi_n \sim 10^6$ ncm^{-2}s^{-1}. The materials studied were 0.09% and 4.53% Sn-Bi (Bi weight%), 99.99999% pure Sn and 99.999% pure Bi. Short (30 min - 1 hour) and long irradiation (~11 h) times were used to probe short and long-lived activities. The samples were counted offline in HPGe detectors. No activity above the background level could be found in the Bi sample. Additionally, no measurable activity arising from any impurity was found in the Sn-Bi crystals and all the activity could be attributed to reaction products arising from the neutron activation channels of Sn - ^{111}Sn, ^{111}In, ^{113}Sn, ^{115m}In, ^{116m}In, ^{117}In, ^{117m}Sn, ^{117m}In, ^{117m}Cd, ^{123m}Sn, ^{123}Sn, ^{125m}Sn and ^{125}Sn. Half-life tracking was done wherever possible. These activation channels were compared to the channels observed in an earlier neutron activation experiment in Sn by Dokania *et. al*. [22], and additional channels leading to the production of ^{111}Sn, ^{113}Sn, ^{115}Cd, ^{117}Cd, ^{117m}Cd, ^{117}In and ^{117m}In were observed.

Estimation of internal background in the Sn-Bi bolometer

In 2003, ^{209}Bi was found to undergo a very rare α decay with a half-life of 2.0×10^{19} y [23] which is comparable to the half-lives of some $2\nu\beta\beta$ emitters. In the case of Sn-Bi bolometers, it is important to note that only the surface events contributing to the partial energy deposition from the ~3.1 MeV α particles from this decay channel would contribute to the ROI around $Q_{\beta\beta}$. This background was estimated for various detector sizes (27, 64 and 125 cc) and Bi alloying concentrations (0.25%, 0.5%, 0.75% and 1.0%). As expected, due to their smaller surface to volume ratio, the 125 cc bolometers are expected to have lower background contributions from ^{209}Bi α decay.

The background contribution that could be expected from the primordial ^{238}U/^{232}Th impurities if we assume a CUORE-like radiopurity level of 0.2 ppt [24] was also estimated. The background arising from the ^{238}U decay chain was found to be the dominant background source. The activity from ^{209}Bi and the ^{232}Th chain is α dominated while the activity from the ^{238}U chain is dominated by the β decay of ^{214}Bi. Thus, only surface events would contribute in the prior cases while there is no such restriction in the latter cases. It is interesting to note that there is no improvement in the background level between 25 - 125 cc bolometers in the case of background arising from the ^{238}U chain, as this is dominated by β decays.

The total background from these sources are listed in Table 0.1 and are found to be within the background limit of 10^{-2} counts/(keV.kg.y), which is typical for the first generation bolometric experiment without particle discrimination. A $0\nu\beta\beta$ event generator was written

Table 0.1: Internal background estimation for Sn-Bi bolometers using GEANT4 simulations.

Source	Impurity level	Background (counts/(keV.kg.y))		
		27 cc	64 cc	125 cc
^{209}Bi α decay	0.25 wt.%	2.6×10^{-5}	2.0×10^{-5}	1.6×10^{-5}
Th chain	0.2 ppt	5.7×10^{-5}	3.9×10^{-5}	3.1×10^{-5}
U chain	0.2 ppt	5.6×10^{-3}	5.7×10^{-3}	5.8×10^{-3}

in GEANT4 [25] using the single electron energy spectra described in [26]. The $0\nu\beta\beta$ events were generated isotropically neglecting angular correlations, to estimate the signal strength expected. The code was benchmarked by computing the $0\nu\beta\beta$ efficiency for the TeO_2 crystals, which was found to be within 2% of the efficiency reported by CUORE [27]. The efficiency of Sn-Bi bolometers for $0\nu\beta\beta$ signal was found to be 86.6% (27 cc), 89.0% (64 cc) and 90.7% (125 cc). The sensitivity of the experiment for $0\nu\beta\beta$ was calculated for a range of enrichment percentages (natural - 99%) and detector sizes using these simulated efficiencies.

Summary

To summarize, the properties of tin-rich alloys central to cryogenic bolometer development were explored. Various instrumentation and low temperature tests relating to the dry dilution refrigerator were performed as part of this thesis. Several alloy candidates were fabricated and tested for resistance to tin pest. A promising alloy candidate Sn-Bi (0.08 % - 1.69 %) was checked for superconductivity. The $\alpha \leftrightharpoons \beta$ transition was studied in Sn and Sn-Cu using differential scanning calorimetry, synchrotron x-ray diffraction studies and temperature resolved scanning electron microscopy. Based on these measurements, a protocol to further reduce the risk of tin pest has been suggested. Radiation background studies were performed for Sn-Bi bolometers. This thesis provides important inputs towards the various aspects

needed to qualify a suitable alloy for a cryogenic bolometer, and Sn-Bi alloy with 0.22% Bi by weight is suggested as a suitable candidate. In the future, fabrication and comparison of the performance of prototype Sn and Sn-Bi bolometers can be explored.

List of Figures

List of Tables

List of Abbreviations

$0\nu\beta\beta$ **or NDBD** Neutrinoless double beta decay

α-**Sn**   Semiconducting phase of tin

α Alpha

$\bar{\nu}$ Anti - neutrino

β-**Sn**   Metallic phase of tin

β Beta

$\beta\beta$ Double beta decay

γ Gamma

μ^- Muon

ν Neutrino

ν_μ Muon - type neutrino

ν_τ Tau - type neutrino

ν_e Electron - type neutrino

ϕ Flux

τ^-	Tauon
e^-	Electron
$T_{1/2}$	Half-life of the decay
T_c	Superconducting critical temperature
7N purity	Purity at the level of 99.99999% (i.e., seven nines)
TIN.TIN	The India-based tin detector
ADXRD	Angle Dispersive X-ray Diffraction
AMoRE	Advanced Molybdenum-based Rare Process Experiment
BGO	Bismuth Germanate
BSM	Beyond standard model
CDMS	Cryogenic Dark Matter Search
CFDR	Cryogen-Free Dilution Refrigerator
CKM	Cabbibo-Kobayashi-Maskawa
CMN	Cerium Magnesium Nitrate
CMOS	Complementary Metal Oxide Semiconductor
CP violation	Charge Parity violation
CRESST	Cryogenic Rare Event Search with Superconducting Thermometers
CUORE	Cryogenic Underground Observatory for Rare Events
CUPID	CUORE Upgrade with Particle Identification
CVIP	Cryo-vibration isolation platform
DARWIN	Dark matter WIMP search with noble liquids

DI water	Deionized water
DM	Dark Matter
DSC	Differential scanning calorimetry
EBSD	Electron Backscatter Diffraction
EcHo	Electron capture ^{163}Ho experiment
EC	Electron capture
EMI	Electromagnetic interference
ETP Cu	Electrolytic Tough Pitch Copper
EXO	Enriched Xenon Observatory
FC	Field Cooled
FPD1000	Superconducting Fixed Point Device
GALLEX	Gallium Experiment
GEANT4	GEometry ANd Tracking
GERDA	Germanium Detector Array
GHS	Gas Handling System
HPGe	High Purity Germanium
INO	India-based Neutrino Observatory
IO (IH)	Inverted ordering (hierarchy)
Kamiokande	Kamioka Nucleon Decay Experiment
KATRIN	Karlsruhe Tritium Neutrino Experiment
LAMPS	Linux Advanced MultiParameter System

LEGEND	Large Enriched Germanium Experiment for Neutrinoless $\beta\beta$ Decay
LSM	The Modane Underground Laboratory
LZ	Lux-Zeplin
m.w.e	metre water equivalent
MC	Mixing chamber of the dilution refrigerator
MJD	MAJORANA DEMONSTRATOR
MKID	Microwave Kinetic Inductance Device
MMC	Metallic Magnetic Calorimeter
MPMS	Magnetic Property Measurement System
MSW	Mikheyev-Smirnov-Wolfenstein effect
NAA	Neutron Activation Analysis
NEMO	Neutrino Ettore Majorana Observatory
nEXO	Next EXO
NEXT	Neutrino Experiment with Xenon TPC
NNDC	National Nuclear Data Center
NO (NH)	Normal ordering (hierarchy)
NoνA	NuMI Off-axis ν_e appearance
NTC	Negative Temperature Coefficient
NTD Ge	Neutron Transmutation Doped Ge
NTME	Nuclear Transition Matrix element
OFHC Cu	Oxygen Free High Conductivity copper

PandaX	Particle and Astrophysical Xenon Detector
PID controller	Proportional Integral Derivative controller
PLF	Pelletron Linac Facility
PMNS	Pontecarvo-Maki-Nakagawa-Sakata
PPMS	Physical Property Measurement System
PT	Pulsed Tube
QD	Quasi degenerate
R & D	Research and Development
RoHS	Restriction of Hazardous Substances
ROI	Region of Interest
ROI	Region of interest
RRCAT	Raja Ramanna Centre for Advanced Technology
RTD	Resistance Temperature Detector
SEM	Scanning electron microscope
SM	Standard model of particle physics
Sn-Bi	tin-bismuth
Sn-Cd	tin-cadmium
Sn-Cu	tin-copper
Sn-In	tin-indium
Sn-Pb	tin-lead
Sn-Sb	tin-antimony

SNO	Sudbury Neutrino Observatory
SQUID	Superconducting Quantum Interference Device
STJ	Superconducting Tunnel Junction
T2K	Tokai to Kamioka
TES	Transition Edge Sensor
TIFR	Tata Institute of Fundamental Research
TIFR	Time Projection Chamber
TiLES	TIFR low background experimental setup
TPC	Time Projection Chamber
XRD	X-ray diffraction
Y2L	YangYang Underground Laboratory
ZFC	Zero Field Cooled
Z	Atomic Number

Chapter 1

Introduction

This chapter provides a brief overview of central topics in this thesis. It is broadly divided into two parts. The first part is an introduction to neutrino physics with a special emphasis on neutrinoless double beta decay. The second part focusses on a broad overview of the bolometer technology and briefly introduces the phenomenon of tin pest, which poses a complex challenge for pure tin bolometers.

1.1 Neutrinos

The study of radioactivity has led to several insights ever since its discovery in 1896 by Henri Becquerel. In particular, the study of β decays culminated in the discovery of the neutrino (ν). The continuous nature of the β energy spectrum was initially considered to be an anomaly as it was believed to be in direct conflict with the discrete nature of nuclear energy levels [28]. The consensus in 1929 was that the β energy spectrum should have been monoenergetic like the spectra of α and γ emitters. Experimentalists and theorists heatedly debated the reason for this 'anomaly', with Niels Bohr even suggesting that perhaps energy was not conserved in β decays. In 1930, Wolfgang Pauli recognized that the continuous energy spectrum of

β emitters was consistent with a three-body decay rather than a two-body decay [29]. The spectrum could be understood if a particle (having negligible interaction with matter) escaped detection, carrying the 'missing' energy with it. Pauli proposed that a chargeless, spin 1/2 particle accompanied the β particle in weak decays, and it was later named the neutrino. The existence of the neutrino ensured the conservation of energy and angular momentum in β decays. By 1934, Enrico Fermi had developed a quantum mechanical theory of β decays by considering the existence of a massless and chargeless spin 1/2 neutrino [30].

It was generally believed that it would be impossible to verify the existence of the neutrino in any feasible experiment due to its negligible interaction cross section with matter [31]. Clyde Cowan and Frederick Reines defied these expectations by detecting the (anti) neutrino in 1956 [32]. They succeeded in observing the elusive particle by employing a huge $\overline{\nu}_e$ flux from the Savannah River nuclear reactor and exploiting the delayed coincidence between the annihilation and neutron capture signals from the inverse beta decay channel. This discovery was later awarded the Nobel prize. In 1957, independent experiments by C.S. Wu and collaborators [33], and Garwin, Lederman and Weinrich [34] provided strong experimental evidence of the parity violation of weak decays. In the following year, Goldhaber *et. al.* measured the helicity of the ν ($\overline{\nu}$) to be -1 (+1) [35]. Several Nobel prize winning experiments have since been performed in neutrino physics and while many interesting properties have been understood, many fundamental questions remain unanswered.

1.2 Neutrino oscillations

According to the standard model of particle physics (SM), all matter is constituted from the fundamental particles (namely, leptons and quarks) and all interactions can be understood as the exchange of bosons. Three 'flavours' of neutrinos exist in SM, namely the ν_e, ν_μ and ν_τ. These comprise the neutral leptons, and together with their left-handed charged leptonic counterparts they form weak isospin doublets

$$\begin{pmatrix} \nu_e \\ e^- \end{pmatrix}_L \quad \begin{pmatrix} \nu_\mu \\ \mu^- \end{pmatrix}_L \quad \begin{pmatrix} \nu_\tau \\ \tau^- \end{pmatrix}_L \tag{1.1}$$

While there are hints of the existence of 'sterile' neutrinos [1] in the eV [36, 37] and keV energy scales [38], nothing can definitively be concluded as yet. For the following overview, it is implicitly assumed that 'sterile' neutrinos do not exist.

The 'solar neutrino problem' refers to a discrepancy observed by several experiments (Homestake [39], GALLEX [40], Super-Kamiokande [41], etc.) which measured only 30 - 50% of the predicted solar neutrino flux [42]. This was later understood to be the physical signature of neutrino oscillations [2]. At a time when only one type of neutrino was known, Bruno Pontecarvo pioneered the formalism for neutrino oscillations, in a version where neutrinos could oscillate into antineutrinos and vice versa ($\nu \leftrightarrow \overline{\nu}$) [43]. This idea was later refined by Ziro Maki, Masami Nakagawa and Shoichi Sakata to describe a phenomenon by which neutrinos spontaneously oscillate among flavours as they propagate [44]. Neutrino oscillations are a direct consequence of the existence of a mass basis which is distinct from the flavour basis of the neutrinos. Spontaneous flavour oscillations in solar neutrinos were subsequently confirmed by SNO, an experiment which was sensitive to the flux from all three neutrino flavours [45]. It resolved the solar neutrino problem by showing that the total flux ($\phi_{\nu_e} + \phi_{\nu_\mu} + \phi_{\nu_\mu}$) measured was consistent with the predicted value. Neutrino oscillations have now been well established in solar [2, 40, 45, 46], atmospheric [1, 41], reactor [47, 48, 49, 50] and accelerator [51, 52, 53] experiments. The observation of neutrino oscillations directly implies that lepton flavour is not a conserved quantity. More profoundly, experimental measurements of neutrino oscillations established that neutrinos have non-zero mass. In SM, mass is typically generated due to the Yukawa coupling of the scalar Higgs field between the left-handed and right-handed components of the fermion.

$$-\mathcal{L}_{Yuk} = Y_{ij}^l \, \overline{\psi}_{Li} \, \varphi \, \psi_{Rj} + h.c. \tag{1.2}$$

where Y_{ij}^l is the Yukawa coupling and φ is the Higgs field and $h.c.$ stands for hermitian conjugate. Spontaneous symmetry breaking leads to the generation of mass

$$m_{ij}^l = Y_{ij}^l \frac{\upsilon}{\sqrt{2}} \tag{1.3}$$

---

[1]neutrinos which do not couple to the $W^\pm$ and Z^o bosons and do not participate in weak interactions.

[2]To be precise, the solar neutrino problem is actually explained by neutrino oscillations enhanced by matter, i.e., the Mikheyev-Smirnov-Wolfenstein (MSW) effect.

where v is the vacuum expectation of the Higgs field. At the Lagrangian level, neutrinos are massless in the standard model as the (neutral mode) Yukawa interaction does not exist, owing to the absence of right-handed neutrino in SM. Thus, the observation of neutrino oscillations extends physics beyond the standard model (BSM).

The neutrino wavefunction can be expressed either in terms of its mass eigenstates ($|v_i\rangle$, $i = 1, 2, 3$) or its flavour eigenstates ($|v_l\rangle$, $l = e, \mu, \tau$), both of which individually form an orthonormal basis. The flavour eigenstates can be expressed as a linear combination of the mass eigenstates as follows

$$|v_l\rangle = \sum_i U_{li} |v_i\rangle \tag{1.4}$$

where U_{li} terms are the Pontecarvo-Maki-Nakagawa-Sakata (PMNS) mixing matrix terms. The PMNS mixing matrix is the leptonic analogue of the Cabbibo-Kobayashi-Maskawa (CKM) mixing matrix of the quark sector. The PMNS matrix can be expressed as

$$U = \begin{pmatrix} U_{e1} & U_{e2} & U_{e3} \\ U_{\mu 1} & U_{\mu 2} & U_{\mu 3} \\ U_{\tau 1} & U_{\tau 2} & U_{\tau 3} \end{pmatrix} \tag{1.5}$$

The mixing matrix has 1 Dirac and 2 additional Majorana CP violating phases. If the neutrinos are Dirac particles, the Majorana CP violating phases will be zero [3]. The standard parametrization of the PMNS matrix is

$$U = VP \tag{1.6}$$

$$U = \begin{pmatrix} c_{12}c_{13} & s_{12}c_{13} & s_{13}e^{-i\delta} \\ -s_{12}c_{23} - c_{12}s_{23}s_{13}e^{i\delta} & c_{12}c_{23} - s_{12}s_{23}s_{13}e^{i\delta} & s_{23}c_{13} \\ s_{12}s_{23} - c_{12}c_{23}s_{13}e^{i\delta} & -c_{12}s_{23} - s_{12}c_{23}s_{13}e^{i\delta} & c_{23}c_{13} \end{pmatrix} \begin{pmatrix} 1 & 0 & 0 \\ 0 & e^{i\frac{\alpha_{21}}{2}} & 0 \\ 0 & 0 & e^{i\frac{\alpha_{31}}{2}} \end{pmatrix} \tag{1.7}$$

where θ_{ij} are the mixing angles, c_{ij} and s_{ij} are $cos(\theta_{ij})$ and $sin(\theta_{ij})$, δ is the Dirac phase and α_{ij} are the Majorana phases. Neutrino oscillations are neither sensitive to the Majorana phases nor to the absolute mass scale of neutrinos. Instead they are sensitive to the mass squared differences $\Delta m_{ij} = m_i^2 - m_j^2$. The probability of observing a v_β in a beam which

---

[3] By contrast, if neutrinos are Majorana particles, the PMNS matrix will retain the Dirac phase as well as the Majorana phase.

originally (at t = 0) comprised exclusively of ν_α is

$$P_{\alpha\beta} = \delta_{\alpha\beta} - 4 \sum_{i>j} Re(U^*_{\alpha i} U_{\alpha j} U_{\beta i} U^*_{\beta j}) sin^2(\frac{\Delta m_{ij} L}{4E}) + 2 \sum_{i>j} Im(U^*_{\alpha i} U_{\alpha j} U_{\beta i} U^*_{\beta j}) sin^2(\frac{\Delta m_{ij} L}{2E})$$

(1.8)

where $\delta_{\alpha\beta}$ is the Kronecker delta function, L is the distance between the detector and the source, and E is the energy of the neutrino beam. The best fit oscillation parameters from the 2020 global analysis of neutrino oscillation data [54] are listed in Table 1.1. While neutrino oscillation studies have truly entered an era of precision measurements, certain lacunae remain in the understanding of neutrinos. The next section will outline the open problems that are of prime importance in neutrino physics presently.

Table 1.1: Table of bfp (best fit parameter) from a global analysis of neutrino oscillation datasets available as of 2020 (adapted from [54]). IO stands for inverted ordering and NO stands for normal ordering type of mass hierarchy.

Parameter	$bfp \pm 1\sigma$	2σ range	3σ range
Δm^2_{21} [$10^{-5} eV^2$]	$7.50^{+0.22}_{-0.20}$	7.12 - 7.93	6.94 - 8.14
$|\Delta m^2_{31}|$ [$10^{-3} eV^2$] (NO)	$2.55^{+0.02}_{-0.03}$	2.49 - 2.60	2.47 - 2.63
$|\Delta m^2_{31}|$ [$10^{-3} eV^2$] (IO)	$2.55^{+0.02}_{-0.03}$	2.49 - 2.60	2.47 - 2.63
$sin^2\theta_{12}/10^{-1}$	3.18 ± 0.16	2.86 - 3.52	2.71 - 3.69
$sin^2\theta_{23}/10^{-1}$ (NO)	5.74 ± 0.14	5.41 - 5.99	4.34 - 6.10
$sin^2\theta_{23}/10^{-1}$ (IO)	$5.78^{+0.10}_{-0.17}$	5.41 - 5.98	4.33 - 6.08
$sin^2\theta_{13}/10^{-2}$ (NO)	$2.200^{+0.069}_{-0.062}$	2.069 - 2.337	2.000 - 2.405
$sin^2\theta_{13}/10^{-2}$ (IO)	$2.225^{+0.064}_{-0.070}$	2.086 - 2.356	2.018 - 2.424
δ/π (NO)	$1.08^{+0.13}_{-0.12}$	0.84 - 1.42	0.71 - 1.99
δ/π (IO)	$1.58^{+0.15}_{-0.16}$	1.26 - 1.85	1.11 - 1.96

1.3 Open problems in neutrino physics

Although neutrinos have been studied for more than 90 years, several fundamental questions regarding them remain open.

- **Hierarchy of neutrino mass ordering**

  Neutrino oscillation experiments have revealed that the neutrinos have mass eigenstates,

but the ordering of these mass eigenstates is yet unresolved. While solar neutrino data reveals that $m_2^2 > m_1^2$, the sign of Δm_{32}^2 is undetermined. There are two possible scenarios for the mass ordering of neutrinos, namely, the normal ordering (NO) and the inverted ordering (IO). The normal ordering corresponds to the case where $m_1 < m_2 < m_3$ while the inverted ordering corresponds to the case where $m_3 < m_1 < m_2$. Both these scenarios are illustrated in Fig. 1.1. The current global data analysis suggests that the normal ordering is preferred at a 2.5σ level [54].
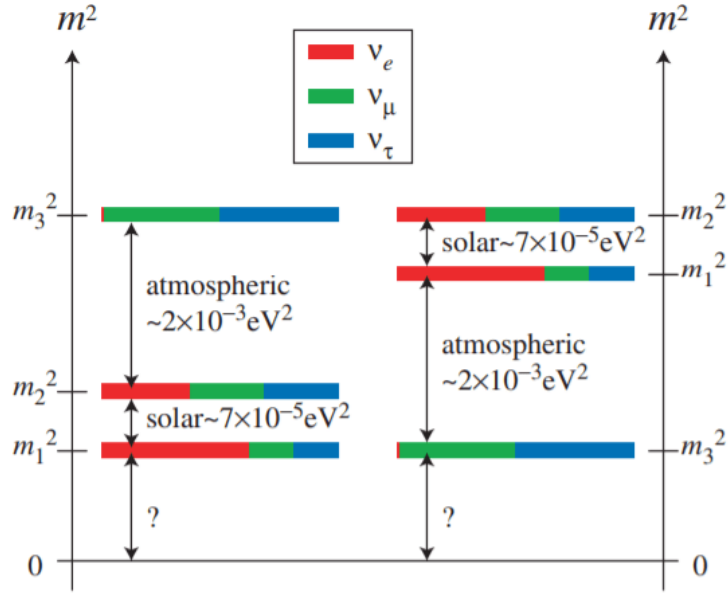
Figure 1.1: Schematic diagrams showing the normal (left scheme) and inverted (right scheme) neutrino mass orderings, taken from [55]. The probability that the neutrino mass state contains a particular flavour state is depicted by the colours as given in the key. The mass of the lightest neutrino is unknown and this is depicted by the question mark in each scheme.

- **Absolute neutrino mass scale**

  The absolute mass of the lightest neutrino is not known. Depending on its magnitude, there are three possible arrangements for the neutrino masses: normal ($m_1 \approx m_2 <<$ m_3), inverted ($m_3 << m_1 \approx m_2$) and quasi-degenerate ($m_1 \approx m_2 \approx m_3$). As mentioned earlier, neutrino oscillations are not sensitive to the absolute mass of the neutrino. Therefore, it is important to pursue experiments which are sensitive to it. An upper limit on the sum of all the neutrino masses can be set using observational cosmological data. The most stringent upper bound is $\sum_i m_{\nu_i} < 120$ meV (95% C.L.) [56]. Direct

detection of the neutrino mass is possible if sensitive measurements can quantify deviations at the end point energy of single β decay or electron capture spectra. Precise spectral measurements of the β decay of tritium (KATRIN [57] and Project 8 [58]) and electron capture of ^{163}Ho (ECHo [59] and HOLMES [60]) are ongoing. Neutrinoless double beta decay can also probe the absolute scale of the neutrino mass since its half-life depends on the effective mass. However, it should be mentioned that this calculation also depends on the Nuclear Transition Matrix Elements (NTMEs) for the decay, which are model dependent and presently have large uncertainties.

- **CP violation in the neutrino sector**

  CP violating effects, arising from a non-zero Dirac CP violating phase δ, would lead to differences in the oscillation probabilities for neutrinos ($\nu_\alpha \rightarrow \nu_\beta$) and antineutrinos ($\overline{\nu}_\alpha \rightarrow \overline{\nu}_\beta$). The value of δ can be probed using the data from long baseline experiments (T2K and NOνA). However, there is a clear tension in the data from T2K and NOνA for the normal mass ordering analysis, with NOνA favouring a best fit value of $\delta \approx 0.8\pi$ and disfavouring the region around $\delta \approx 1.5\pi$, which is the best fit value for T2K [54].

- **Nature of the neutrino - Majorana or Dirac?**

  Since the neutrino (ν) is a chargeless fermion with finite mass, there is a fundamental question regarding its distinctness from its antiparticle, i.e., whether it is a Majorana or Dirac fermion. Fermionic particles which are indistinguishable from their antiparticle are known as Majorana fermions, as opposed to Dirac fermions which are distinct from their antiparticles. If the neutrino is a Majorana particle, it would shed light on the mechanism by which neutrinos gain mass and also provide insight into why the mass is small. Understanding the nature of the neutrino is of utmost importance for fundamental particle physics. The observation of neutrinoless double beta decay is the only known experimental signature which would provide conclusive evidence for the Majorana nature of the neutrino.

1.4 $\beta\beta$ decays in the Standard Model and beyond

Double beta decay or $\beta\beta$ decay[4] is a second order weak decay in which a parent nucleus $X(A, Z)$ decays to a daughter nucleus $Y(A, Z + 2)$ by undergoing two simultaneous β decays. In 1935, a year after Fermi formulated the theory of β decays, Maria Geoppert-Mayer first suggested this possibility [61]. The process suggested by her (often termed as $2\nu\beta\beta$) involves a nucleus decaying by the emission of two β particles and two $\bar{\nu}_e$. It can be represented by the following equation

$$X(A, Z) \rightarrow Y(A, Z + 2) + 2e^- + 2\bar{\nu}_e \tag{1.9}$$

This is a standard model process, and the total lepton number is conserved. In 1937, Majorana showed that Fermi's β decay theory would remain unchanged even if the neutrino was its own antiparticle [62]. Considering a scenario in which the neutrino and the antineutrino were equivalent, Racah put forth a $\beta\beta$ decay sequence by which this hypothesis could be tested. The sequence involved the decay of a nucleus X(A,Z) to a virtual state Y'(A,Z+1) with the emission of a β particle and an antineutrino. This antineutrino would then be reabsorbed as a neutrino by Y'(A, Z+1), inducing its decay to Y(A,Z+2) with the emission of another β particle. The Racah sequence is as follows

$$X(A, Z) \rightarrow Y'(A, Z + 1) + \bar{\nu}_e + e^- \tag{1.10}$$

$$\nu_e + Y'(A, Z + 1) \rightarrow Y(A, Z + 2) + e^- \tag{1.11}$$

Furry suggested the possibility of a $\beta\beta$ decay in which a parent nucleus X(A, Z) decays to a daughter nucleus $Y(A, Z + 2)$ in a single step, without producing antineutrinos ($\bar{\nu}$) in the final state [63]. This was equivalent to the Racah sequence mediated by the exchange of virtual Majorana neutrinos. This decay is known as neutrinoless double beta decay (NDBD or $0\nu\beta\beta$) and can be represented by the following equation

$$X(A, Z) \rightarrow Y(A, Z + 2) + 2e^- \tag{1.12}$$

If $0\nu\beta\beta$ decay is observed, it would be conclusive evidence for the non-conservation of the total lepton number ($|\Delta L| = 2$) and the Majorana nature of the neutrino. This would have

---

[4]In this overview, $\beta\beta$ implicitly refers to $\beta^-\beta^-$ decays.

significant implications for cosmological models of the early universe, reveal the absolute mass scale of neutrinos and help understand the mechanism by which neutrinos obtain (small) masses. The Feynman diagrams for both the $\beta\beta$ decays modes can be seen in Fig. 1.2.

In addition to the $0\nu\beta\beta$ and $2\nu\beta\beta$ decays, $\beta\beta$ decays that are mediated by Goldstone bosons known as Majorans (J) have also been proposed. In the case of $0\nu\beta\beta$, the end point energy $Q_{\beta\beta}$ is shared between the two electrons. Thus, the unique experimental signature of $0\nu\beta\beta$ is a peak at $Q_{\beta\beta}$ in the sum energy spectrum of the electrons. Fig. 1.3a is a schematic which depicts the experimental signatures from the various $\beta\beta$ decay modes.

(a) $0\nu\beta\beta$ decay   (b) $2\nu\beta\beta$ decay
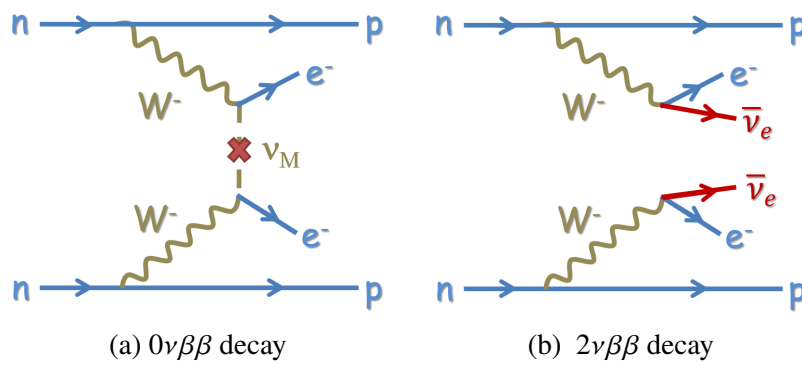
Figure 1.2: Feynman diagrams of the $\beta\beta$ decays modes.
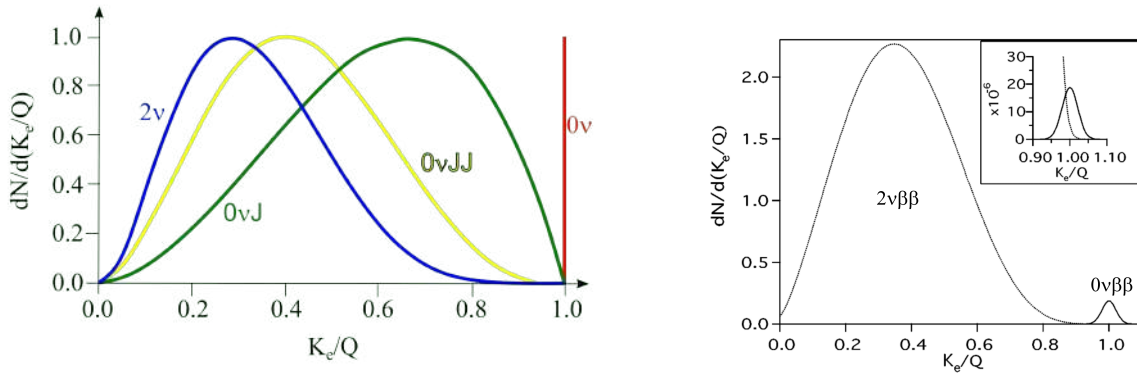
(a) Signals of different $\beta\beta$ decay modes. The modes are colour coded as follows: $0\nu\beta\beta$ (red), $2\nu\beta\beta$ (blue), $0\nu J\beta\beta$ (green), $0\nu JJ\beta\beta$ (yellow).

(b) The effect of energy resolution on the region of interest (inset). The figure is adapted from [64].

Figure 1.3: (a) Schematic representation of the electron sum energy spectra corresponding to different $\beta\beta$ decay modes. The normalization of this plot is arbitrary. (b) The $2\nu\beta\beta$ and $0\nu\beta\beta$ spectra are both convolved with an energy resolution of 5%. The inset shows the region of interest around $Q_{\beta\beta}$. The $0\nu\beta\beta$ peak has been amplified for visibility purposes.

$\beta\beta$ decays (see Fig. 1.4) can be potentially observed in 35 even-even naturally occurring nuclei for which single β decay is energy or spin forbidden. The ground states (g.s.) of

even-even nuclei have a spin of 0 and a positive parity. Thus, the g.s. to g.s. $\beta\beta$ decays are characterized by $0^+ \rightarrow 0^+$ transitions (see Fig. 1.5). Transitions to the excited 2^+ and 0^+ states are also possible, but are less probable.

Some prominent $\beta\beta$ decay candidates are listed in Table 1.2. A graphical depiction of the same can be found in Fig. 1.6. It should be noted that other second order weak decays such as $\beta^+\beta^+$, $ECEC$ or β^+EC are also possible. However, these modes are generally disfavoured for experimental searches due to their smaller phase space and fewer candidate nuclei.
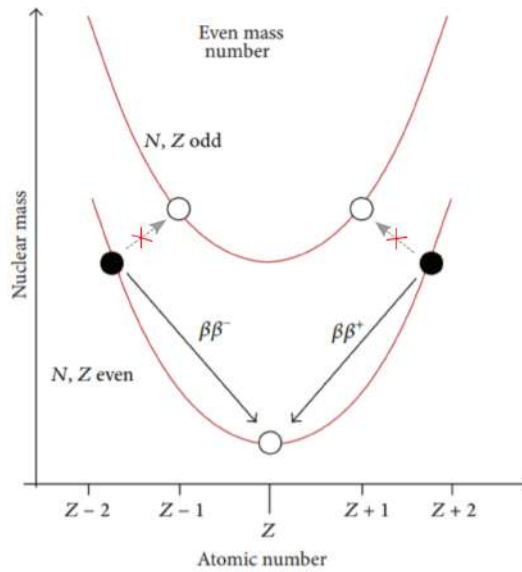
Figure 1.4: Mass parabolas for even A nuclei, having $\beta\beta$ decay candidates. The parabola corresponding to the odd-odd nuclei is shifted with respect to that of the even-even nuclei due to the nuclear pairing term. The figure is adapted from [65].
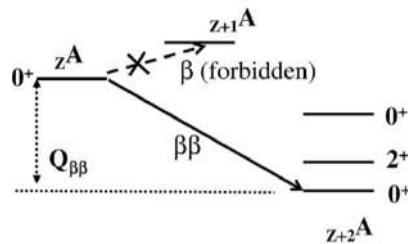
Figure 1.5: Representative level diagram for $\beta\beta$ decay, taken from [66].

The SM process $2\nu\beta\beta$ has been observed in 12 nuclei, with the first direct experimental observation dating back to 1987 [67]. The measured half-lives range from 10^{18} to 10^{24} y. No undisputed observation of $0\nu\beta\beta$ has been made till date, with the typical half-life limits set by various experiments exceeding $T_{1/2}^{0\nu} > 10^{25}y$ [3]. Neutrinoless double beta decay can also

Table 1.2: Table of end point energy $Q_{\beta\beta}$ and isotopic abundance i of naturally occurring candidates having $Q_{\beta\beta} > 2\ MeV$ [68].

$\beta\beta$ decay $^{A}X \rightarrow^{A} Y$	$Q_{\beta\beta}$ keV	i %
$^{48}Ca \rightarrow^{48} Ti$	4268.08 ± 0.08	0.2
$^{76}Ge \rightarrow^{76} Se$	2039.06 ± 0.01	7.7
$^{82}Se \rightarrow^{82} Kr$	2997.9 ± 0.5	8.7
$^{96}Zr \rightarrow^{96} Mo$	3356.03 ± 0.07	2.8
$^{100}Mo \rightarrow^{100} Ru$	3034.36 ± 0.17	9.8
$^{110}Pd \rightarrow^{110} Cd$	2017.1 ± 0.5	11.7
$^{116}Cd \rightarrow^{116} Sn$	2813.49 ± 0.13	7.5
$^{124}Sn \rightarrow^{124} Te$	2291.1 ± 1.5	5.8
$^{130}Te \rightarrow^{130} Xe$	2527.51 ± 0.01	34.1
$^{136}Xe \rightarrow^{136} Ba$	2457.8 ± 0.3	8.9
$^{150}Nd \rightarrow^{150} Sn$	3371.38 ± 0.20	5.6

probe the absolute mass scale of neutrinos since the half-life of the decay depends on the the effective neutrino mass $\langle m_{\beta\beta}\rangle$. The definition of $\langle m_{\beta\beta}\rangle$ is

$$\langle m_{\beta\beta}\rangle = \left| \sum_i U_{ei}^2 m_i \right| \tag{1.13}$$

It is commonly assumed that the dominant mechanism of $0\nu\beta\beta$ decay is via the exchange of light Majorana neutrinos. Under this assumption, the half-life of $0\nu\beta\beta$ decay is related to $\langle m_{\beta\beta}\rangle$ by

$$(T_{1/2}^{0\nu})^{-1} = G^{0\nu}|M^{0\nu}|^2 (\frac{\langle m_{\beta\beta}\rangle}{m_e})^2 \tag{1.14}$$

where $G^{0\nu}$ is the phase factor available to the $0\nu\beta\beta$ decay, $M^{0\nu}$ is the Nuclear Transition Matrix Element (NTME) of the transition and m_e is the mass of the electron. The NTME can vary greatly depending on the model used for calculation, and this term dominates the experimental uncertainty. If $0\nu\beta\beta$ decay is observed, then utilizing the standard radioactive decay law and considering that $t \ll T_{1/2}^{0\nu}$, the half-life can be calculated using

$$T_{1/2}^{0\nu} = \frac{ln2N_A\varepsilon iMt}{AN_{obs}} \tag{1.15}$$

11

where N_A is Avogadro's number, ε is the detector efficiency for the signal. i is the isotopic fraction of the $\beta\beta$ candidate, M is the mass of the detector, t is the experimental runtime, A is the molar mass and N_{obs} is the number of observed $0\nu\beta\beta$ events. The quantity Mt is collectively termed as the detector exposure. In the absence of a clearly observed signal, a lower limit on the half-life can be set using

$$T_{1/2}^{0\nu} > \frac{ln2 N_A i\varepsilon}{A f_{CL}} \sqrt{\frac{Mt}{B\Delta E}} \tag{1.16}$$

where f_{CL} is the number of standard deviations corresponding to a confidence level, B is the background index in the region of interest (in terms of counts/(keV.kg.y)) and ΔE is the energy resolution of the detector.

1.4.1 Experimental design aspects for $0\nu\beta\beta$ searches

As is evident from the formulae for the half-life $T_{1/2}^{0\nu}$, the 'ideal' characteristics of a $0\nu\beta\beta$ experiment are as follows:

- **High $Q_{\beta\beta}$**

  Candidates with a high $Q_{\beta\beta}$ are preferred as the decay rate $\Gamma_{0\nu} \propto Q_{\beta\beta}^5$. Moreover, if the $Q_{\beta\beta} > 2615$ keV, the experiment would enjoy a region of interest which would be above the common γ background lines arising from the activity of ^{40}K, ^{137}Cs and from the decay chains of primordial uranium and thorium.

- **High isotopic abundance**

  The sensitivity of the experiment is directly proportional to the isotopic abundance of the $\beta\beta$ candidate. If the natural isotopic abundance is high, costly and time-consuming enrichment operations can be avoided.

- **Large detector exposure**

  The sensitivity of the experiment can be improved by employing large detectors and acquiring data for long periods. $0\nu\beta\beta$ experiments typically comprise of 100 - 1000 kg of detector mass and run for several years.
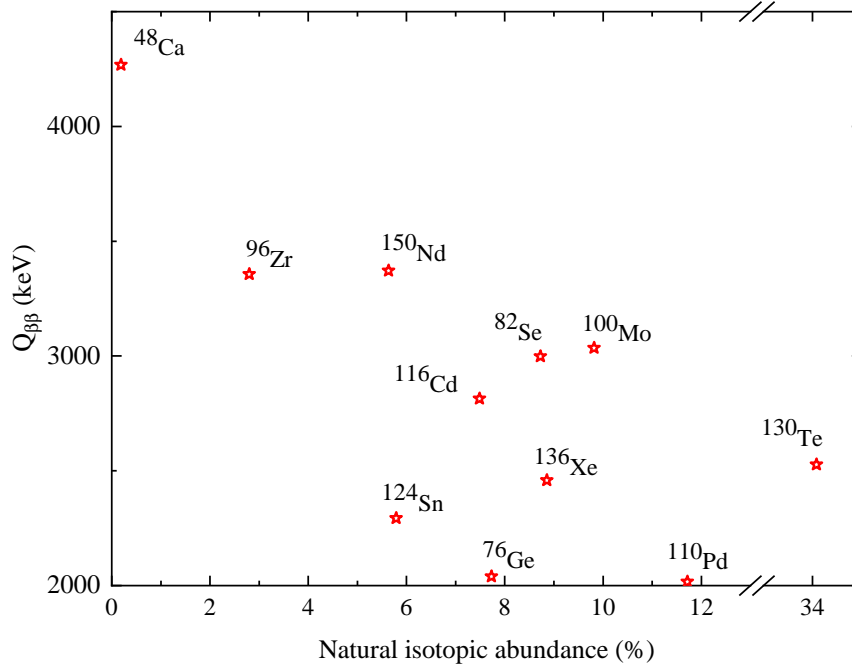
Figure 1.6: Naturally occurring $\beta\beta$ candidates with $Q_{\beta\beta} > 2\,MeV$. There is a break in the x-axis for visibility purposes.

- **Good energy resolution**

  The tail events of the $2\nu\beta\beta$ decay can act as a source of background in the $0\nu\beta\beta$ region of interest, especially if the energy resolution of the detector is poor (see Fig. 1.3b). Detectors with good energy resolution can discriminate against the background more effectively.

- **High detector efficiency for the $0\nu\beta\beta$ signal**

  Since the energy $Q_{\beta\beta}$ is shared between the two electrons which are emitted, it is important that the detector should have high detection efficiency for the electrons.

- **Low background**

  High background levels can dramatically limit the sensitivity of the experiment. Thus, it is unsurprising that a lot of effort is directed towards understanding and mitigating sources of background for the experiment.

- **Smaller uncertainties in the Nuclear Transition Matrix Element**

  Even in the case that no signal is observed, a limit on the absolute neutrino mass can be calculated from the measured lower bound of the half-life. However, this calculation

13

is dominated by the model dependent uncertainty in the Nuclear Transition Matrix Element.

Due to the large uncertainties in the Nuclear Transition Matrix Elements, it is important to measure the half-life corresponding to $0\nu\beta\beta$ decay for multiple nuclei. Currently, several experimental collaborations across the world [3] are searching for $0\nu\beta\beta$ decay.

1.5 The landscape of major $0\nu\beta\beta$ experiments
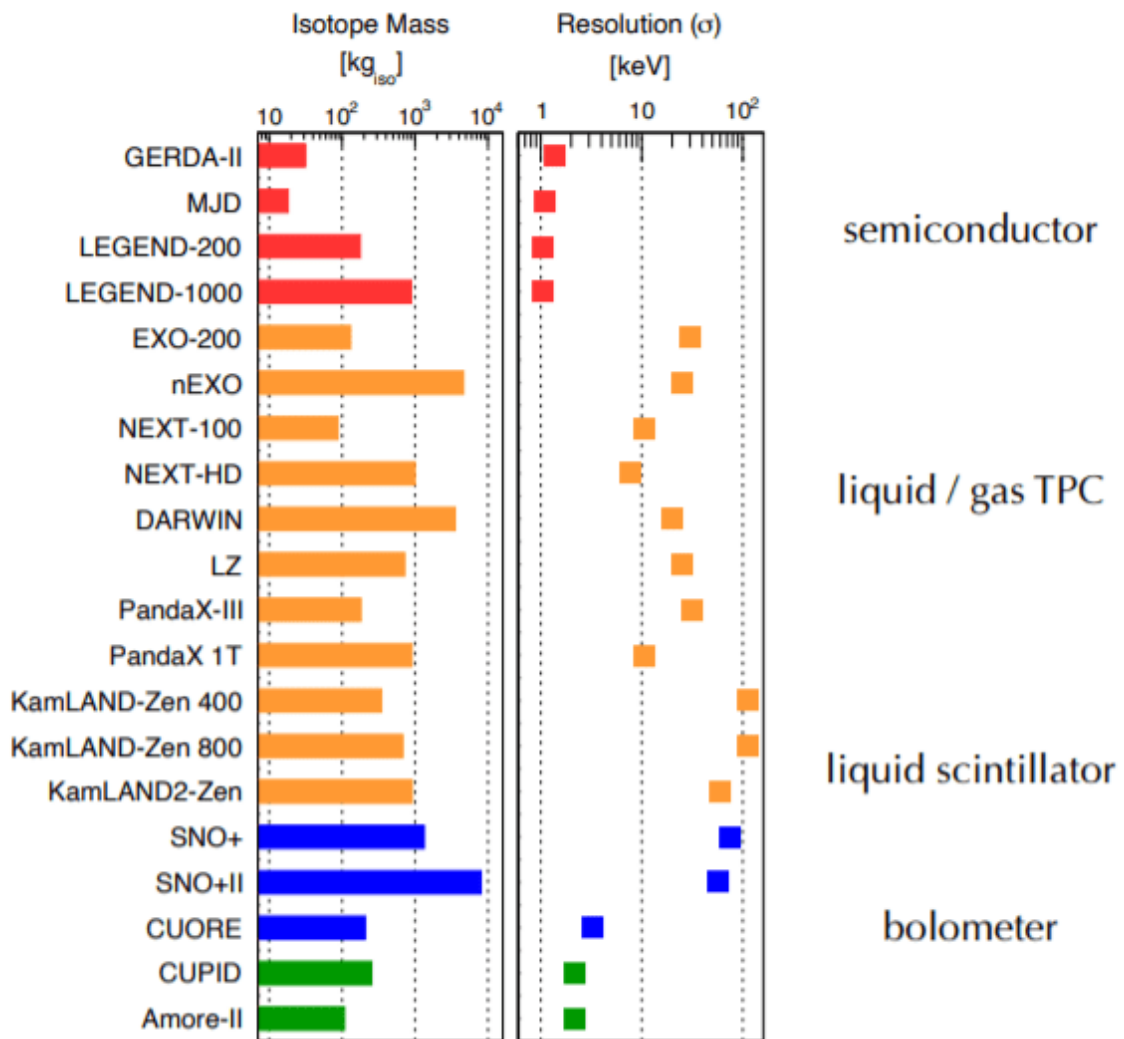
Figure 1.7: Schematic comparison of the isotope mass and energy resolution of major $0\nu\beta\beta$ experiments. The bars are colour-coded to depict experiments exploring $0\nu\beta\beta$ in ^{76}Ge (red), ^{136}Xe (yellow), ^{130}Te (blue) and ^{100}Mo (green). The acronyms MJD and LZ stand for the MAJORANA DEMONSTRATOR and Lux-Zeplin, respectively. This figure has been adapted from [69].

The sensitivity of $0\nu\beta\beta$ decay experiments have increased by around five orders of magnitude, since they began in the 1960s. This is largely due to breakthroughs in detector technology and careful background reduction strategies. Several collaborations are searching for the elusive $0\nu\beta\beta$ by employing complementary detector technologies and studying different $\beta\beta$ candidates. Fig 1.7 shows a schematic comparison among the major $0\nu\beta\beta$ experiments.

The following is a brief overview of the general detection strategies employed by $0\nu\beta\beta$ experiments:

- **Semiconductor detectors**:

  The typical band gap of a semiconductor is of the order of $\sim$ eV. Thus, a large number of charge carriers are generated for a signal of the order of $\sim$MeV. The generation of charge carriers is a probabilistic process and the number generated follows the Poisson distribution. Hence, the relative energy resolution is $\sim \frac{\sqrt{N}}{N}$. This implies that semiconductor detectors having much better resolutions (0.12% at $Q_{\beta\beta}$) in comparison to gaseous detectors or scintillators. The use of bare HPGe detectors which are enriched in ^{76}Ge have been actively pursued by GERDA [70] and MAJORANA DEMONSTRA-TOR [71]. These experiments can discriminate against the background on the basis of single-site versus multi-site topologies. The LEGEND collaboration [72] plans to combine the expertise from both these experiments and pursue a tonne scale experiment which will attempt to have a final sensitivity of $\sim 10^{28} y$. A novel but nascent idea of using CMOS pixel arrays for $0\nu\beta\beta$ decays is also being explored, which shows that this detector technology is still evolving [73].

- **Bolometers**:

  Bolometers are cryogenic calorimeters, which can measure the energy deposited by a particle by measuring the increase in its temperature. They have excellent energy resolution when operated at ultra-low temperatures (typically 10 mK). The typical energy resolution is $\sim$0.3% at $Q_{\beta\beta}$. Unlike semiconductor detectors, the energy resolution is independent of the energy deposited. The use of bolometers offers several advantages including a large choice of absorber crystals and mK thermometers available to experimentalists. These experiments are modular, with the possibility of upscaling the mass

15

in future iterations. Future experiments are also trying to incorporate particle identification by combing simultaneous readouts of light and heat signals. Major experiments using cryogenic bolometers are CUORE [74] and AMoRE [75]. CUPID [76] is a future tonne scale scintillating bolometer experiment which aims to have a final sensitivity of at least $10^{27}y$.

- **Time Projection Chamber (TPC)**

  A TPC utilizes a detection medium which produces ionization electrons as well as scintillation light. A combined analysis of these signals allows for the reconstruction of the event topology, position and energy. Thus, background discrimination is inherent to the detector. The biggest advantage of the TPC is its the mass scalability. Xe can be enriched in the $\beta\beta$ candidate ^{136}Xe, and used as the source as well as the detection medium in the search for $0\nu\beta\beta$. Xe can be used to fabricate gaseous, liquid or dual phase TPCs. NEXT [77] and PandaX [78] use a gaseous TPC which is maintained at a pressure of 15 bar and 10 bar, respectively. EXO [79] uses 200 kg of ultra-pure liquid TPC, with plans to upscale to 5 tonnes in its next phase nEXO. The planned dark matter experiments LUX-ZEPLIN [80], XENON-nT and DARWIN [81], which will use dual phase TPCs, will also have a good sensitivity for $0\nu\beta\beta$ of ^{136}Xe.

- **Organic scintillators**

  Although organic scintillators are inferior in energy resolution compared to other detector technologies, these detectors allow for a large mass scalability. Another advantage is that they can be purified in real time, removing impurities that can contribute to the background. The same property can be exploited to allow for systematic checks by removing the $\beta\beta$ decay isotope, if needed. Both KamLAND-Zen [82] and SNO+ [83] employ loaded liquid scintillator detectors to search for $0\nu\beta\beta$ in ^{136}Xe and ^{130}Te, respectively.

- **Tracking calorimeters**

  Most experiments are insensitive to the distribution of the opening angle between the emitted electrons in $0\nu\beta\beta$ decay. However, precise measurements of the angular distribution can reveal the underlying mechanism of the decay. Tracking calorimeters

can acquire precise topological information, due to their 'sandwich' design. The $\beta\beta$ source foil is immediately surrounded by a low pressure gaseous tracking layer and then subsequently by a calorimetric layer to measure the energy of the event. However, a drawback to utilizing a source which is distinct from the detection medium is that extremely thin source foils need to be used in order to avoid self-absorption. Thus, the total mass that can be used is extremely limited, traded off for excellent background rejection. On the other hand, a benefit of using this approach is that several candidates can be studied under identical experimental systematics. Using this detector technology, NEMO-3 [84] set limits for seven $\beta\beta$ candidates. Plans are underway for the next generation experiment SuperNEMO, with a demonstration module being constructed at LSM, France.

Fig. 1.8 shows the discovery sensitivity (measured and projected) for major $0\nu\beta\beta$ experiments.
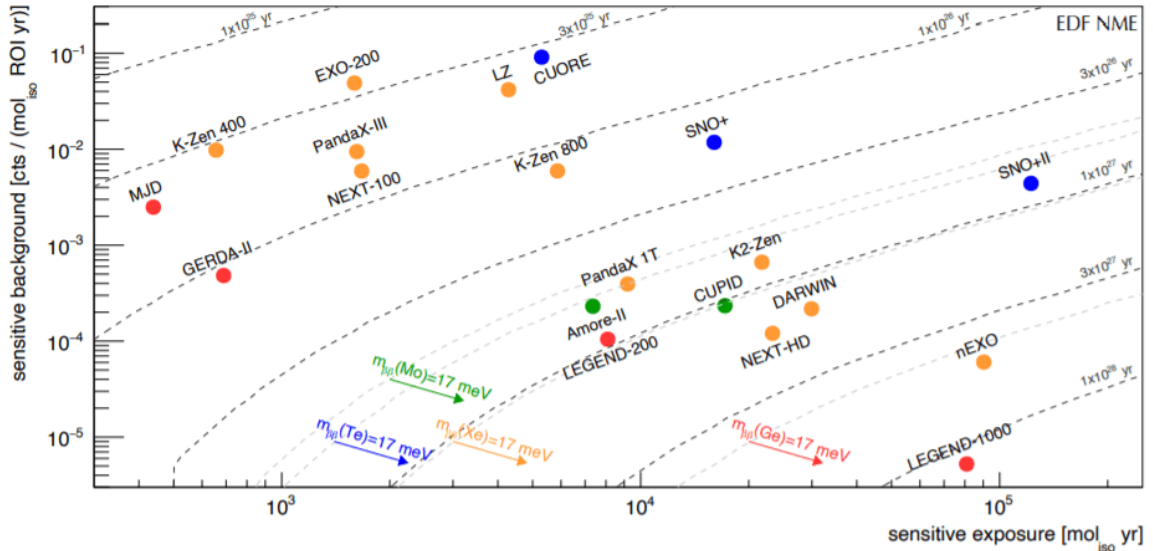
Figure 1.8: The major $0\nu\beta\beta$ experiments have been graphed as a function of their background and exposure, normalized with respect to their active mass. Isochronic contours of half-life sensitivity have been represented by dashed lines. The colour scheme is the same as in Fig. 1.7. This figure has been adapted from [69].

The best half-life and neutrino mass sensitivity limits which have been measured for $0\nu\beta\beta$ are listed in Table 1.3.

If the mass of the lightest neutrino is found to be < 40 meV, the effective neutrino mass $\langle m_{\beta\beta}\rangle$ can reveal whether the mass ordering is normal or inverted. The sensitivity of $\langle m_{\beta\beta}\rangle$ to the mass ordering has been shown in 1.9. There are several experiments which will aim for

Table 1.3: The best half-life and neutrino mass sensitivity limits for $0\nu\beta\beta$ (at at 90% C.L.).

$\beta\beta$ isotope	Experiment	$|\langle m_{\beta\beta}\rangle|$	$T_{1/2}^{0\nu}$	Reference
^{76}Ge	GERDA	(0.08 - 0.182) eV	$> 1.8 \times 10^{26}$y	[70]
^{130}Te	CUORE	(0.075 - 0.350) eV	$> 3.2 \times 10^{25}$y	[27]
^{136}Xe	KamLAND-Zen	(0.061 - 0.165) eV	$> 1.07 \times 10^{26}$y	[82]

a sensitivity in the region $|\langle m_{\beta\beta}\rangle| \sim (0.01 - 0.05)$ eV, spanning the entire inverted ordering region.
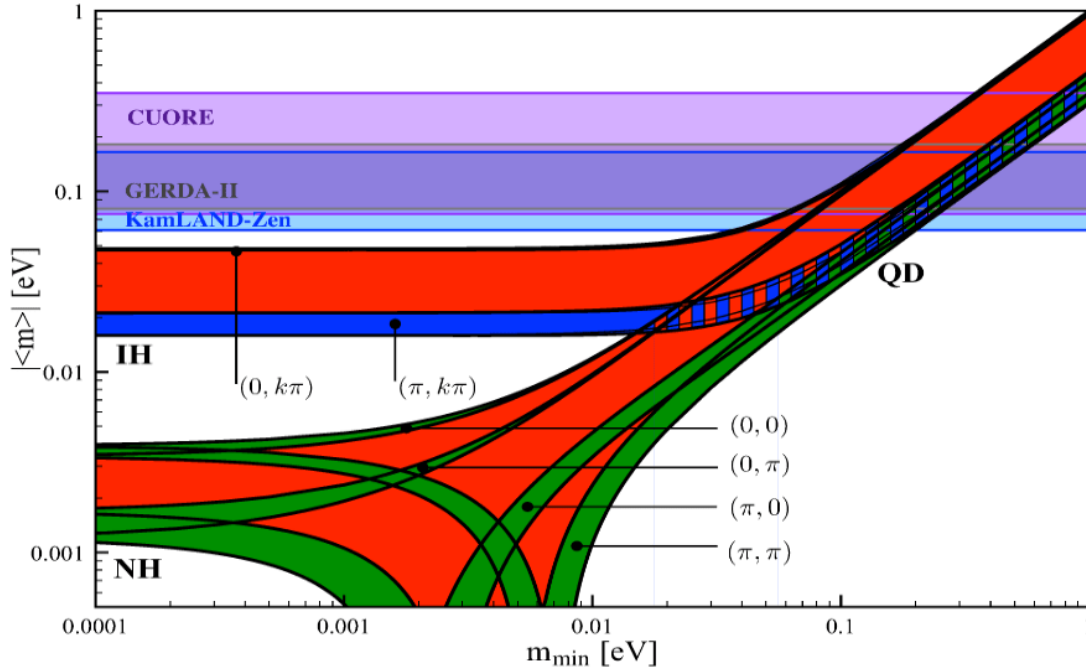
Figure 1.9: The sensitivity of $\langle m_{\beta\beta}\rangle$ to the mass ordering. NH is the normal hierarchy (ordering), IH is the inverted hierarchy (ordering) and QD is the quasi-degenerate region. The regions excluded by current $0\nu\beta\beta$ experiments have been marked. This figure is updated from [85], taken from [86].

1.6 *TIN.TIN* experiment

TIN.TIN (**T**he **In**dia-based **tin** detector) will employ a tin-based superconducting bolometer array operating at about ~ 10 mK to search for $0\nu\beta\beta$ in ^{124}Sn [4]. *TIN.TIN* will be situated at the upcoming India-based Neutrino Observatory (INO) [87], which aims to build a facility having a rock overburden of ~ 1.2 km. This rock overburden will serve to reduce the cosmic

muon flux by around six orders of magnitude compared to the value at sea level.

^{124}Sn has a moderately high $Q_{\beta\beta}$ of 2291.1 ± 1.5 keV [68] and a moderate natural isotopic abundance of 5.8%. Natural tin consists of ten isotopes in total, with mass number *A* lying in the range 112 to 124. It should be mentioned that 7 isotopes are stable while 3 are candidates for rare decays (see Table 1.4). There is a possibility of enrichment of ^{124}Sn upto ~99% [88]. Since tin is superconducting below ~ 3.7 K, only the phononic component of heat capacity contributes at 10 mK. Therefore, it is expected that superconducting bolometers fabricated from tin should perform with good energy resolution. Development of the cryogenic bolometer has been initiated [4]. Neutron Transmutation Doped Germanium (NTD Ge) sensors have been indigenously fabricated for mK thermometry [89, 90].

Table 1.4: Sn isotopes which undergo rare weak decays.

Isotope	Natural isotopic abundance	Decay mode	Q value
^{112}Sn	0.97%	ECEC	1919.80 ± 0.16 keV
		β^+EC	897.8 ± 0.2 keV
^{122}Sn	4.63%	$0\nu\beta\beta$ / $2\nu\beta\beta$	373 ± 3 keV
^{124}Sn	5.79%	$0\nu\beta\beta$ / $2\nu\beta\beta$	2291.1± 1.5 keV

Currently, the best limit on the half-life for $0\nu\beta\beta$ of ^{124}Sn is 2.0×10^{19}y with 90% C.L. [91]. This was measured at the YangYang Underground Laboratory (Y2L) [92], which is a 700 m deep underground facility in South Korea, using a tin loaded liquid scintillator. Interestingly, the rate of $2\nu\beta\beta$ decay of ^{124}Sn has not yet been experimentally measured. Shell model calculations predict the half life of the $2\nu\beta\beta$ (g.s. to g.s.) transition to be $1.6 \times 10^{21}y$ [93]. Experimental efforts to measure the $2\nu\beta\beta$ decay rate using tin loaded liquid scintillator detectors have been initiated by another group [94, 95]. The bolometer array which will be used by *TIN.TIN* will have an advantage in terms of energy resolution as compared to tin loaded liquid scintillator experiments.

1.7 Cryogenic bolometers

Bolometers have been briefly discussed in Section 1.5, while discussing various detector technologies. However, since it forms the core of the *TIN.TIN* experiment, it warrants a more detailed description. Since the invention of room temperature bolometers in 1878 [96], bolometer performance has improved significantly, receiving a technological impetus after the development of dilution refrigerators and low temperature sensors. Cryogenic bolometers consist of the following components:

- an insulating / superconducting absorber crystal

- a temperature sensor which is in strong thermal contact with the absorber

- weak links which thermally couple the system to a heat bath maintained typically at 10 mK.

A schematic of the bolometer can be seen in Fig. 1.10.
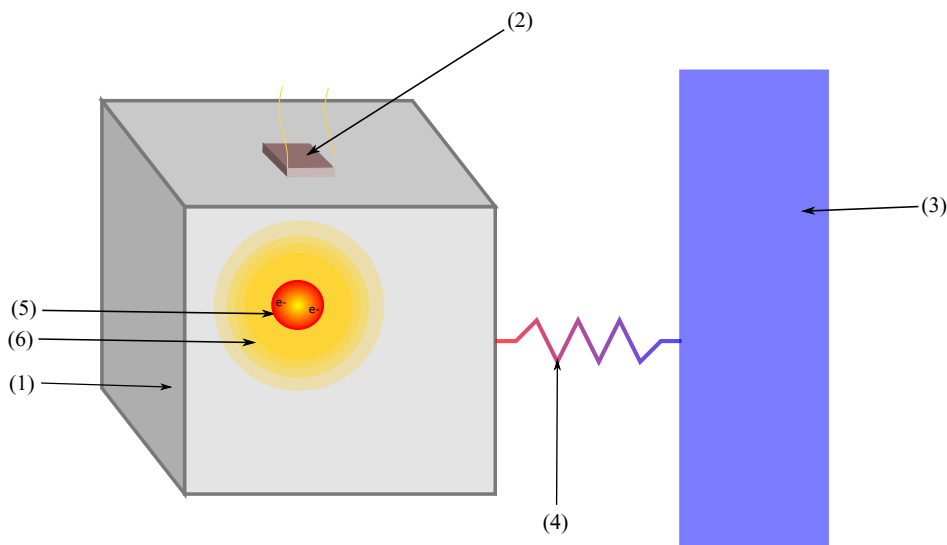
Figure 1.10: The labelled schematic of a bolometer is shown. The labels correspond to (1) the absorber (2) thermometer (3) heat bath (mixing chamber of dilution refrigerator) (4) the thermally weak link (5) the radiation stopping zone for the bulk $0\nu\beta\beta$ event and (6) representation of the thermalization of the crystal.

When a particle interacts with the bolometer, it can lose its energy via several interactions, depending on whether the particle is electrically charged or neutral. These processes could also lead to the generation of secondary particles or athermal phonons. Eventually, the

energy is converted to thermal phonons via electron-phonon and phonon-phonon coupling. In superconductors, the energy conversion can also lead to the generation of quasi-particles. The time required for thermalization can vary from a few μs to a few ms, depending on the mass of the bolometer as well as the material used. The amplitude of the thermal signal (ΔT) is given by

$$\Delta T = E/C \tag{1.17}$$

where E is the energy deposited by the particle and C is the heat capacity. The thermal pulse decays exponentially, returning to the base temperature T with a time constant τ_d

$$\tau_d = C/K \tag{1.18}$$

where K is the conductance of the weak link coupling the bolometer to the heat sink. Theoretically, the energy resolution of a bolometer is limited by the statistical fluctuation of the number of thermal phonons generated. Hence, it is given by the equation

$$\Delta E = \sqrt{k_B T^2 C} \tag{1.19}$$

when an energy E is deposited in the bolometer having total heat capacity C at temperature T. From the equations 1.17 and 1.19, it is clear that reducing the heat capacity of the bolometer would improve its performance. A small caveat is that the decay constant τ_d of the pulse depends on the ratio of the heat capacity C and the conductance K (equation 1.18). This ratio needs to be sensibly optimized for the experiment. If τ_d is too small then high data sampling rates will be needed to record the data. Given the long runtimes of these experiments, this will lead to data storage issues. On the other hand, if τ_d is too large, signal pileup can occur. Thus, the counting rate of bolometers is limited to ~Hz by the decay time of the pulse.

The major advantages of bolometers are as follows:

- Bolometers have excellent energy resolution and low threshold when operated at mK temperatures.

- The energy resolution is independent of the energy deposited. This is advantageous at higher energies.

- There is a large flexibility in the choice of the absorber material, the mK thermometer and electronic readout used. In the case of $0\nu\beta\beta$ experiments, the absorber crystal is usually made out of the $0\nu\beta\beta$ isotope or its compound. There are a variety of extremely sensitive temperature sensors that have been developed by the low temperature detectors (LTD) community, which measure either resistance, magnetization or kinetic inductance as a function of temperature. These include Neutron Transmutation Doped Ge (NTD Ge), superconducting Transition Edge Sensor (TES), Metallic Magnetic Calorimeter (MMC), Superconducting Tunnel Junctions (STJ) and Microwave Kinetic Inductance Device (MKID). Superconducting Quantum Interference Devices (SQUIDs) are used to readout most of these sensors, except NTD Ge which has a simpler electronic readout. The recently published book by Klaus Pretzl [97] has detailed information about the state of the art in mK thermometry.

- Since the source is the detection medium, bolometers have high detection efficiency for the $\beta\beta$ signal.

- The crystal growth process allows for a high degree of radiopurity of the absorber.

- Bolometer detectors are modular and have a provision for mass scalability.

However, a drawback of bolometers in general is that they are insensitive to the identity of the particle depositing energy. There has been considerable effort towards the development of bolometers with particle discrimination capabilities, with recent success [75, 76, 98, 99, 100]. For this, it is necessary to simultaneously readout an auxiliary signal (ionization, Cherenkov or scintillation light) in addition to the thermal signal. By combining the information from these signals, α versus β/γ particle discrimination is possible (see Fig. 1.11).
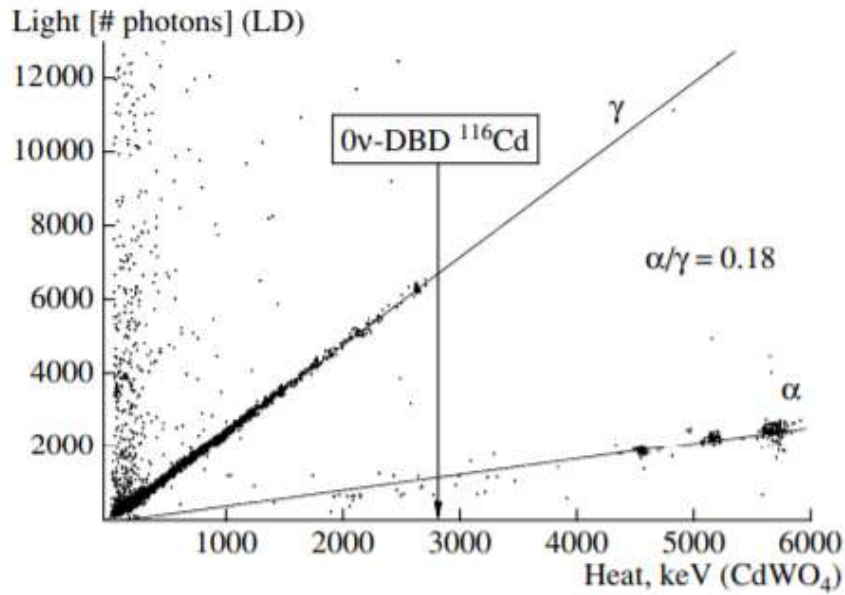
Figure 1.11: Particle discrimination in scintillating bolometers, taken from [101].

The bolometer detector is the preferred technology for several sophisticated rare event experiments. The major experiments that utilize bolometers to search for $0\nu\beta\beta$ have already been mentioned in Section 1.5. The following are major experiments in which bolometers were (or are) used to search for other rare processes:

- **Rare α decays**

  Scintillating bolometers were used to measure the rare α decays of ^{209}Bi [23] and ^{151}Eu [102]. Bismuth germanate (BGO) crystals were used for the former while europium doped CaF_2 crystals were used for the latter. The half-lives of the decays were found to be $\sim 2 \times 10^{19}$ y and $\sim 4.6 \times 10^{18}$ y, respectively.

- **Dark matter (DM) search**

  Bolometers are also suitable for dark matter searches, since they have low energy thresholds which are necessary to detect potential DM events. Edelweiss [99] and SuperCDMS [100] use undoped germanium absorbers, which become depleted of charge carriers when cooled to cryogenic temperatures. When energy is deposited in the germanium crystal, an ionization signal is generated in addition to the thermal signal. CRESST [98] has taken a slightly different approach by adopting scintillating $CaWO_4$ bolometers.

1.8 Tin pest challenge

Tin pest presents a complex challenge to the fabrication of pure tin bolometers. It is well known that tin occasionally shows an allotropic $\beta \rightarrow \alpha$ phase transition, commonly termed as tin pest, when cooled below its reported thermodynamic transition temperature, 13.2°C [5] [12]. While β-Sn is metallic, α-Sn is a semiconductor like the other members of Group 14 (C, Si and Ge). The unit cell volume of α-Sn is ~27 % greater than that of β-Sn. Thus, tin pest can lead to the deformation and cracking of the tin sample due to sudden volume expansion and is a major concern in most applications involving tin at low temperatures. Fig. 1.12 shows a schematic representation of the allotropic phase transition in tin.
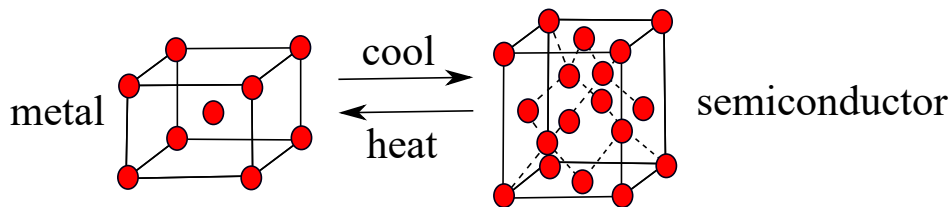
Figure 1.12: The allotropic phase transition between the metallic (β) and semiconducting (α) phases of tin.

Given that $0\nu\beta\beta$ is a rare decay process with typical half-life limits $T_{1/2} > 10^{25}$ y [3], *TIN.TIN* is expected to utilize a large mass of Sn (100 - 1000 kg) and acquire data for several years. During this period, the detector array would be susceptible to this damaging transition during the thermal cycling from room temperature to mK temperatures [6]. Therefore, it is imperative to inhibit or at least greatly suppress this transition for the longevity and performance of the bolometer array.

1.8.1 The search for a suitable alloy for *TIN.TIN*

It is known that alloying Sn with an appropriate element can pin the dislocations in the crystal, thereby suppressing the lattice expansion associated with tin pest formation [7]. The $\beta \rightarrow \alpha$ transition becomes kinematically unfavourable when the lattice expansion associated with the change of crystal structure is suppressed.

---

[5]The $\alpha \rightleftharpoons \beta$ transition temperature commonly reported in the literature is inconsistent with recent calorimetric experiments [14, 15, 16, 17]. The transition temperature is studied in detail in Chapter 4 of this thesis.

Although there are other groups searching for suitable tin alloys which will inhibit tin pest, from the perspective of using them as lead-free solders, there are additional constraints on the requirements for a suitable alloy for *TIN.TIN*. The following characteristics are preferable for a candidate for *TIN.TIN*:

- It should effectively inhibit tin pest (or at least suppress it greatly, so as to minimize the probability of tin pest formation during thermal cycling).

- It is preferable that the alloying element should have a high solubility in tin. It would be ideal if the alloying element could form a substitutional solid-solution with tin. The ideal conditions under which solid solutions are formed, as per the Hume-Rothery rules, are as follows:

  - If the crystal structure of the pure elements are similar.

  - If the differences between the atomic radii of the solute and solvent are within 15%.

  - If the elements share similar electronegativity.

  - If the solvent and solute share the same valency.

  In case these conditions are not fulfilled, it does not imply that an alloy cannot be formed. However, it should be noted that solid solutions conforming to the Hume-Rothery rules tend to form more homogeneously in comparison to those that do not.

- The alloy should be made as tin-rich as possible, as this would maximize the active mass in the detector array. The exact upper limit on the acceptable concentration of the alloying element would depend on the expected background, but it would be preferable if it did not exceed ~1% by weight.

- The resulting alloy should be superconducting. Moreover, in order for the alloy to have a comparable performance at low temperature, it is important the the alloy should not have a superconducting critical temperature T_C which is lower than that of pure tin (~ 3.7 K). A T_C which is similar to or greater than that of pure tin is preferable.

- The additional background arising from introducing the alloying element into the tin matrix needs to be carefully evaluated. This background should be minimized as far as possible.

- It is likely that polycrystalline samples would be be more suitable in comparison to single crystals since they are expected to have better thermalization at mK temperatures, owing to smaller mean free paths for the phonons.

The main focus of this thesis was to qualify a tin-rich binary alloy which would be a suitable absorber crystal for the *TIN.TIN* experiment. The phenomenon of tin pest is an interesting phase transition, and although the transition has been known for more than a century, there were several inconsistencies in the literature. Improved measurements of the transition temperature using various experimental techniques (differential scanning calorimetry, temperature resolved x-ray diffraction and scanning electron microscopy) were performed as a part of this dissertation. Based on these measurements, a protocol is suggested to minimize the risk of the formation of tin pest in *TIN.TIN* and other critical tin-based low temperature systems. Chapter 2 presents the maintenance, installation and testing performed in the cryofree dilution refrigerator at TIFR, which is an crucial technology for the development of cryogenic bolometers. Chapter 3 describes the growth of various candidate crystals and cooling tests to check their inhibition against tin pest. The superconductivity measurements of Sn-Bi alloys is also described in this chapter. Chapter 4 describes studies relating to the phase transition in tin. Chapter 5 describes radiation background studies for Sn-Bi bolometers. Chapter 6 summarizes this thesis and provides an outlook for future work.

Chapter 2

Millikelvin measurement setup at TIFR

Dilution refrigerators are used ubiquitously in science and technology, most notably in bolometric searches for rare processes and in quantum computers composed of superconducting qubits. They provide a stable and continuous refrigeration, and are capable of delivering large cooling powers. In the case of rare decay searches using cryogenic bolometers, large masses consisting of the bolometer array, cryostat components and lead shielding are maintained at ~10 mK for several years in a dilution refrigerator.

In this chapter, the history and working principle of dilution refrigerators will be briefly described (Section 2.1), followed by a description of the cryogen-free dilution refrigerator (CFDR-1200) which is used for bolometer R & D by the *TIN.TIN* group (Section 2.2). The maintenance, diagnostics, modifications and testing performed in the CFDR-1200 as a part of this thesis will be the emphasis of this chapter. This includes

- the temperature calibration of the diagnostic thermistors at the mK stage (Section 2.3)

- the installation and testing of the motorized probe (Section 2.4)

- the installation and testing of the cryo vibration isolation platform (Section 2.5).

A summary is provided in Section 2.6.

2.1 Reaching millikelvin temperatures

Although evaporative cooling using pumped cryogen baths is a relatively straightforward technique for attaining low temperatures, it cannot be used to achieve temperatures below $\sim$300 mK. This is because the cooling power of this technique is limited by the partial vapour pressure of the cryogen, which falls rapidly with the decreasing temperature in accordance with the Clausius-Clapeyron equation. Fig. 2.1 shows the partial vapour pressures of the two isotopes of helium as a function of temperature. Evaporative cooling is only feasible for cooling down to $\sim$ 1 K and $\sim$300 mK using ^4He and ^3He, respectively.
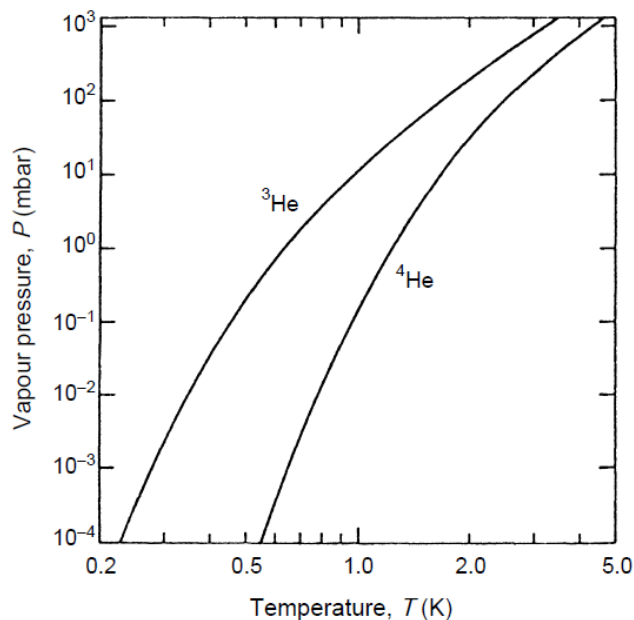
Figure 2.1: The partial vapour pressures of ^3He and ^4He, taken from [103].

There are two techniques which are widely used to achieve temperatures down to $\sim$10 mK: (1) the adiabatic demagnetization of the electronic spins of a paramagnetic salt and (2) dilution refrigeration. However, it should be noted that adiabatic demagnetization is a one-shot technique, and therefore, it is unsuitable for temperature stabilization. Thus, dilution refrigeration is more suited to bolometric experiments which require continuous and stable refrigeration.

2.1.1 The working principle of a dilution refrigerator

In 1951, H. London proposed that millikelvin temperatures could be achieved if the heat of mixing of the two helium isotopes was exploited instead of their latent heat of vaporisation [104]. In 1964, this idea was implemented and the first dilution refrigerator was built at Leiden university, which registered a lowest temperature of 220 mK [105]. In the present times, dilution refrigerators routinely achieve 10 mK and the world record for the lowest temperature achieved by a dilution refrigerator is ~2 mK [106]. The phase diagram of $^3He - ^4He$ mixtures (see Fig. 2.2) has unique properties which make dilution refrigeration possible. The salient features which should be noted from the phase diagram are as follows:

- The isotope ^4He is a boson, and it shows a transition from normal to superfluid state when it is cooled. In the phase diagram, the λ-line separates the normal and superfluid phases. The transition occurs at 2.177 K for pure ^4He, but the transition temperature is depressed when the fermionic isotope ^3He is mixed with it. Superfluidity is lost when the ^3He concentration in the mixture exceeds 67.5%.

- In the superfluid state, ^4He offers zero viscosity and, thus, behaves as an inert solvent for ^3He, which acts as a 'Fermi gas'.

- The λ-line meets the phase separation line at a temperature of 867 mK and a ^3He concentration of 67.5%. The region below the phase separation line is unphysical and is termed the forbidden region. Thus, the $^3He - ^4He$ mixture, which is completely miscible at higher temperatures, splits into a ^3He rich phase and a ^3He dilute phase once it reaches the phase separation line. The concentrations of these phases change as the mixtures are cooled. To illustrate this, consider the following example involving the red and blue lines marked in Fig. 2.2. The red line shows the concentrations of the ^3He rich and dilute phases at the temperature T_1, namely, $x_r(T_1)$ and $x_d(T_1)$. As the mixtures cool, the solubility of ^3He in the dilute phase reduces while the ^3He rich phase becomes more concentrated (illustrated by the blue line showing the concentrations at temperature T_2). The phases behave differently as the temperature asymptotically approaches absolute zero. It can be seen that the ^3He rich phase attains a purity of

100% ^3He as $T \rightarrow 0$, but the dilute phase always has a minimum solubility of 6.6% ^3He. The reason for the finite solubility of ^3He in ^4He is because the ^3He atoms are more strongly bound to ^4He atoms in comparison to other ^3He atoms.

Since the process of dilution of ^3He into ^4He is an endoenthalpic process, it has a cooling effect. The cooling power of dilution refrigerators $\dot{Q}$ is given by

$$\dot{Q} = \dot{n}_3 \Delta H \tag{2.1}$$

where $\dot{n}_3$ is the number of ^3He moles that cross the phase interface per unit time and mix into the dilute phase, ΔH is the change in enthalpy. For an ideal heat exchanger, ΔH (in J/mole) can be calculated using

$$\Delta H = (\gamma_D - \gamma_C)T^2 \tag{2.2}$$

where γ_D and γ_C are the coefficients of the heat capacity of ^3He in the dilute and concentrated phases, $\gamma_D - \gamma_C = 84$ J/(mole.K^2) and T is the base temperature (in K).
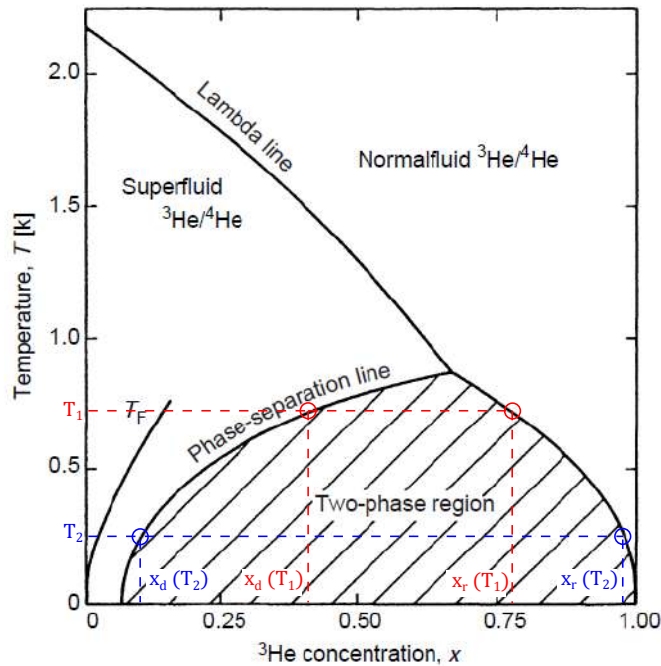
Figure 2.2: The phase diagram of $^3He -^4 He$ mixtures as a function of ^3He concentration and temperature, adapted from [103]. Detailed description of the figure and annotations can be found in the text.

The general schematic of a dilution refrigerator is shown in Fig. 2.3. The dilution process occurs inside the mixing chamber, and the samples are thermally coupled to this stage in

30

order to be cooled down to mK temperatures. As evidenced from the phase diagram, there is a minimum concentration of ^3He in the dilute phase. Thus, if ^3He is removed from the dilute phase, ^3He from the rich phase crosses the interface to replace the displaced atoms, in order to maintain the equilibrium concentrations. In this manner, a continuous closed cycle can be established. A portion of the liquid from the dilute phase is taken by means of a capillary into the *still*, which is maintained at a temperature T >700 mK. The liquid in the *still* is then pumped, which causes the ^3He to preferentially vaporize due its greater partial vapour pressure at the given temperature (see Fig. 2.1). The helium vapour pumped out of the *still* contains at least 90% ^3He. This results in a change in the concentration of the dilute phase, which immediately causes ^3He atoms to cross the phase interface to maintain the equilibrium concentration. The ^3He vapour in circulation is liquefied using a Joule-Thompson stage, cooled and then recirculated to the the ^3He rich phase. Heat exchangers allow for efficient heat transfer from the incoming ^3He which needs to be cooled and the outgoing dilution mixture which needs to be heated during its transportation to the *still*.
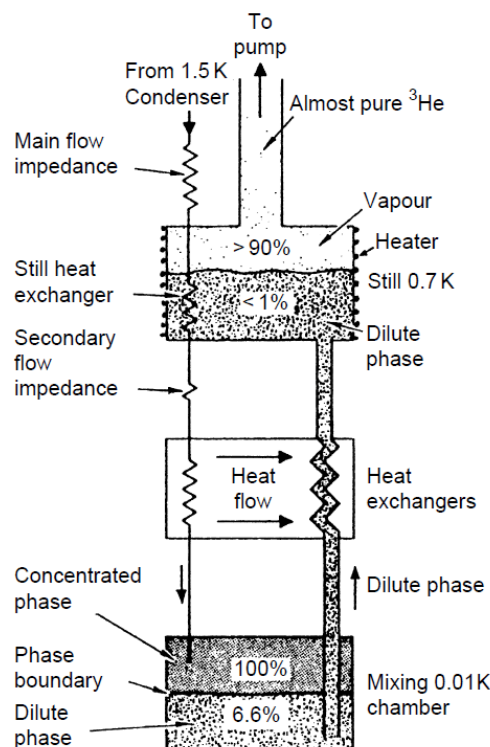
Figure 2.3: The general schematic of a dilution refrigerator is shown in the figure. The figure is taken from [103].

2.2 The cryogen-free dilution refrigerator CFDR-1200

Dry dilution refrigerators are preferred to wet dilution refrigerators for operation in underground laboratories, since they do not require any external supply of liquid Helium. For the purpose of bolometer R & D, a cryogen free dilution refrigerator (CFDR-1200) was custom built by M/s Leiden cryogenics and installed at the Tata Institute of Fundamental Research [9]. The CFDR-1200 has a high cooling power of 1.36 mW at 120 mK when using a *still* heater of 35 mA, which is sufficient for cooling a mass of ∼ 100 kg.

Figure 2.4: The Cryogen Free Dilution Refrigerator (CFDR-1200) at TIFR Mumbai: (a) The gas handling system (GHS) and the cryostat (b) The thermal stages of the cryostat, which are visible after removing the thermal and vacuum shields.

The CFDR-1200 uses ∼ 45 l of ^3He and 142.5 l of ^4He. The gases are stored in their respective gas dumps, located in the hollow frame of the gas handling system (GHS), when the dilution refrigerator is not in operation. The GHS also houses the vacuum systems and the control for the valves (piezoelectric and solenoid) in the gas circuit. The salient design features of the CFDR-1200 are listed below. These design features minimize the heat load from room temperature to the millikelvin stage, without compromising mechanical strength or the ability to make meaningful electrical measurements.

- **Thermal shielding:** The cryostat comprises of the following thermal stages : 300 K, 40 K, 3 K, *still*, 50 mK, mixing chamber (MC). The 40 K and 3 K stages are cooled by a two-stage pulsed tube cryocooler (Cryomech PT-415) which has a nominal cooling

power of 1.5 W at 4.2 K. The thermal stages below the 3 K plate are cooled by the dilution system. The thermal stages have been fabricated from copper which are gold plated to reduce the emissivity of the surface. A thermal shield is mounted on each thermal stage (except the MC). The thermal shields for 40 K and 3 K are made from aluminium and wrapped in multiple layers of superinsulation and the rest of the stages are made from gold plated copper. The implementation of multiple thermal stages with shielding minimizes the radiative heat load on the MC.

- **Vacuum in the cryostat:** The cryostat is divided into two separate vacuum chambers - the outer vacuum chamber (OVC) and the inner vacuum chamber (IVC). The vacuum vessel for the IVC also functions as a thermal shield for the 3 K stage, while the OVC vacuum vessel is mounted at room temperature. A special kapton o-ring is used for the IVC, which is occasionally lubricated with low temperature N-grease. Maintaining a good vacuum ($\sim 10^{-4}$ mbar) is necessary for reducing the convective heat loads due to the residual gas.

- **Low thermal conductivity of the interconnects:** The thermal stages are massive, and therefore, the connections between the stages are required to be mechanically strong while offering a low thermal conductance. Fibre reinforced plastic (FRP) structures are used as interconnects which support the cryostat, while maintaining the required temperature offsets between the stages.

- **Low thermal conductivity of the electrical readout:** Shielded twisted pair electrical connections have been provided in the CFDR-1200, which allows for readout of upto 75 sensors in four probe configuration. Special wiring with good electrical conductance but poor thermal conductance has been implemented in order to ensure that electric connections do not act as a conductive heat load from room temperature to the mixing chamber plate. The wiring from room temperature down to the 3 K plate is fabricated from phosphor bronze and the wiring below the 3 K plate is made from NbTi, which is superconducting below 9.7 K.

- **Reduction of sources of vibrational noise at the design and operation level:**

  – The cryostat is isolated from the ground and its vibrations by suspending it on a tripod, which rests on individual shock absorbing rubber pads.

  – The compressor unit of the pulsed tube cryocooler generates a tremendous amount of noise. It is kept in a separate room and connected to the cold head by means of a ~20 m long hose which is suitably anchored, in order to minimize transmission of vibrational noise to the cryostat.

  – There is a provision to change the motor control of the pulsed tube cryocooler valve from normal to linear drive (LNX-G from Precision Motor Control). This results in less vibration at T < 100 mK since the motor current is ramped linearly with microsteps instead of coarse steps.

  – The cold head of the motor is mounted on a vibration dampner, separated from the cryostat using 65 cm long flexible bellow. There is also a provision to isolate and separately suspend the cold head. However, this has limited benefits since the gas pipes are in strong mechanical contact with the 40 K and 3 K plates inside the cryostat. The large mass of the cryostat serves to dampen these vibrations but this is found to be inadequate. In order to further mitigate the vibrations at the mixing chamber, tests with a cryovibration isolation platform has been carried out as a part of this thesis work (Section 2.5).

- **Mitigation of electrical noise:**

  – The vacuum systems are electrically isolated from the cryostat by the means of insulating o-rings and clamps.

  – The CFDR-1200 is shielded from electromagnetic interference (EMI) using a Faraday cage enclosure, fabricated from copper and galvanized iron. Special care is taken to avoid running power lines through the Faraday cage.

  – The readout in the CFDR-1200 is further shielded against EMI, in particular, the high frequency harmonics, by means of a RF-EMI absorber (Eccosorb).

  – All the power lines to the DAQ systems are connected via EMI filters.

– Ground loops have been systematically eliminated from the grounding circuit, with the NI chassis providing the master clean earthing.

The CFDR-1200 allows for a large cooling power with a relatively small volume of ^3He (45 l), due to its improved heat exchanger design consisting of a tube in tube heat exchanger followed by sintered silver heat exchangers. For comparison, a typical wet dilution refrigerator DRS-1000 uses ~175 l of ^3He for a similar cooling power. In order to monitor the temperatures of the various thermal stages, the CFDR-1200 is equipped with several diagnostic thermistors. The temperature of the mixing chamber plate is stabilized within 0.1% fluctuations with a Proportional-Integral-Derivative (PID) controller.

2.3 Calibration of the diagnostic resistance thermometers

The accurate measurement of millikelvin temperatures is as important as the techniques by which the temperature is attained. A thermometer can be defined as an object which has a physical property which is strongly dependent on the temperature, and by precise measurement of the property one can infer the temperature. Thus, thermometers can be broadly grouped into two categories - primary and secondary thermometers. Primary thermometers do not require calibration, since the temperature can be calculated from the measured property using a fundamental law of physics. Primary thermometers include gas thermometers, noise thermometers, superconducting fixed point devices, etc. Secondary thermometers need to be calibrated against a primary thermometer periodically, since the calibration tends to drift. However, they are preferred due to their ease of use and greater sensitivity compared to primary thermometers. Resistance thermometers are most commonly used due to their simple readout using cryogenic bridges.

The CFDR-1200 uses negative temperature coefficient (NTC) thermistors to monitor the temperatures below 1 K [1], and positive temperature coefficient (PTC) thermistors to monitor the temperatures above 10 K. The mixing chamber plate has two Carbon Speer thermistors (S1109, S1102) to monitor its temperatures in the mK temperature range and a PT1000

---

[1]The ruthenium oxide sensors mounted on the 3 K, still and 50 mK stage are also sensitive around ~3 K, but the Carbon Speer sensors are not.

sensor, to monitor its temperature during the warmup and cooldown of the cryostat. It should be noted that the PID temperature control of the CFDR-1200 is performed using the temperature readout of the Carbon Speer thermistor S1109. There is a provision to mount a superconducting Fixed Point Device (FPD1000) and / or a Cerium Magnesium Nitrate (CMN) thermometer for calibration purposes. A typical mounting can be seen in Fig. 2.5.
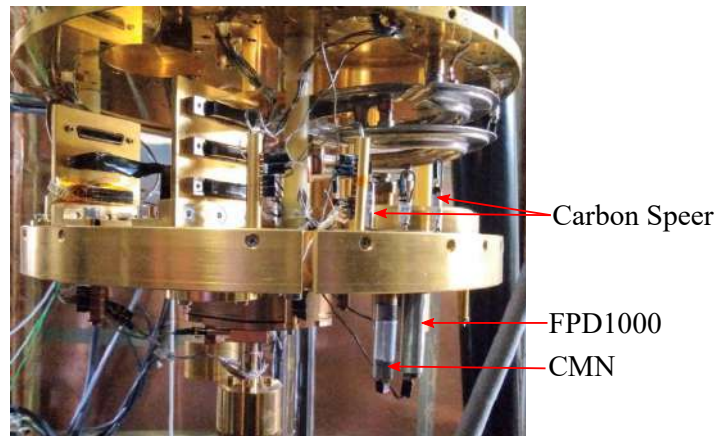
Figure 2.5: A typical mounting arrangement for a calibration run with the CMN and the FPD1000.

The FPD1000 (M/s Small Coil, Overlook Drive, USA) contains multiple superconducting samples, which are placed in a primary coil. When the samples transition to the superconducting state on cooling, they expel their internal magnetic flux lines due to the Meissner effect. This is detected as a decrease in the mutual inductance, which can be measured by the voltage induced in the secondary pick up coil. The critical temperature (T_c) for the samples are well known and highly reproducible. In a magnetic field of 1μT, the shifts and reproducibility of the critical temperatures are within 0.1 mK typically. The outer layers of the FPD1000 consists of a magnetic shielding fabricated from niobium (T_c = 9.3 K) and cryoperm. The cryoperm has a high magnetic permeability which traps magnetic flux lines in the material itself. The superconducting niobium shield expels magnetic flux lines, shielding the interior. Thus, the cryoperm and the niobium effectively shield the samples against external magnetic fields, which would otherwise affect their critical temperature. The FPD1000 uses eight superconducting standards spanning the temperature range of 15 - 3300 mK. The materials and their respective critical temperatures are listed in the Table 2.1.

Table 2.1: Superconducting standards used in the FPD1000 and their corresponding critical temperatures.

Standard material	Critical temperature (mK)
In	3300
Al	1175
Zn	840
Cd	520
$AuIn_2$	208
$AuAl_2$	161
Ir	97
W	15
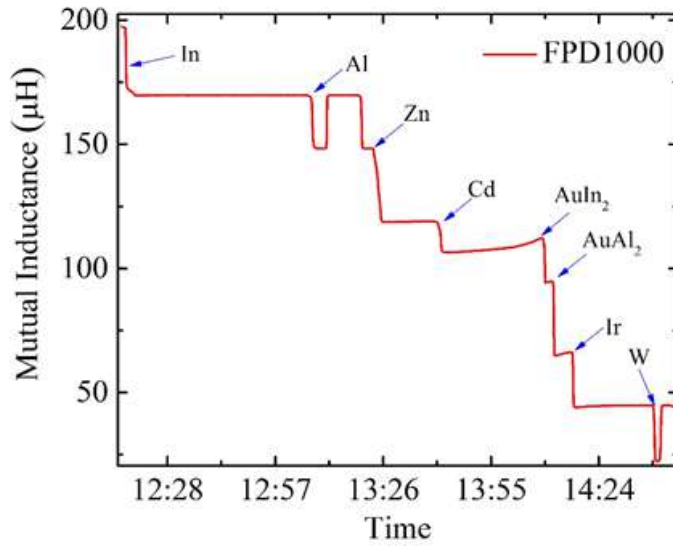
Figure 2.6: The mutual inductance characteristics of the FPD1000 shows a transition whenever a sample becomes superconducting.

The CMN thermometer derives its name from the strongly paramagnetic salt it is fabricated from - Cerium Magnesium Nitrate. The susceptibility of a paramagnetic substance χ is related to its temperature by the Curie-Weiss law, given by

$$\chi = \frac{\lambda}{T - \Delta} \tag{2.3}$$

where λ is the material dependent Curie constant, T is the temperature and Δ is the Weiss constant, which depends on the geometry of the sample, crystal symmetry and the interaction

of magnetic moments. The mutual inductance M is related to the temperature by

$$M = M_0 + \frac{C}{T} \tag{2.4}$$

and the constants M_0 and C can be determined by a linear fit against a minimum of three superconducting standard samples. Once the CMN thermometer is calibrated against the FPD1000, it can be used to calibrate other sensors. The CMN thermometer is useful since it can be used in the temperature stabilization mode, thus offering more calibration points for the resistance thermometers.

The FPD1000 and CMN thermometers were read out using a digital mutual inductance bridge (MubridgeUSB Type A), which has an inbuilt multifunctional NI-6211 unit. A small sinusoidal AC current is supplied alternately to the primary coil of the thermometer and then through a 10 Ω reference resistor. A suitable AC frequency is chosen [2], so that the measurement is not affected by the harmonics and sub-harmonics of the mains frequency 50 Hz. The output voltage across the secondary coil is amplified, filtered and then finally digitized for data processing, from which the mutual inductance is calculated and displayed using a LabVIEW program.
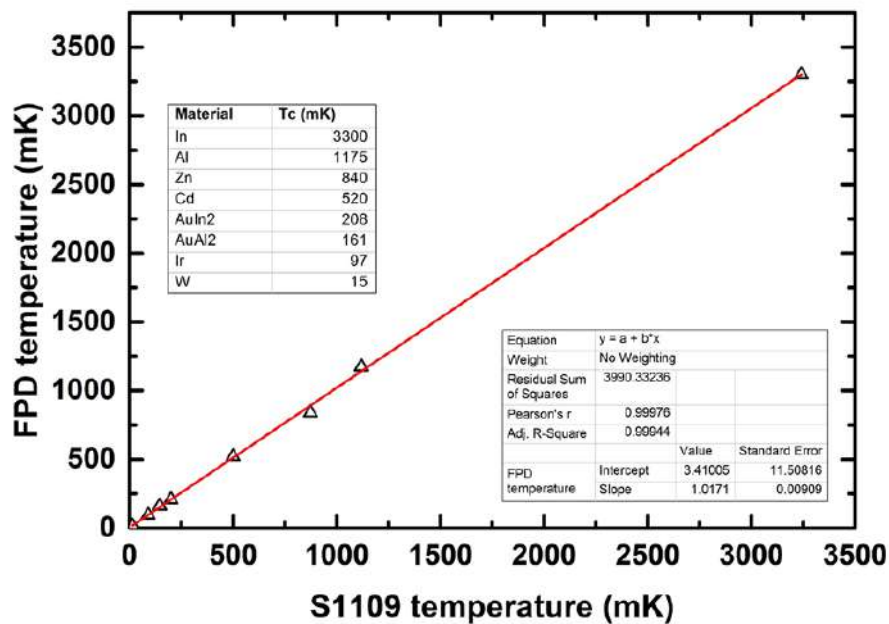
Figure 2.7: Verification of the calibration of the Carbon Speer S1109 against an FPD1000, after the installation of the new *still* unit.

---

[2]DEV1 319 Hz, DEV2 937 Hz; In this case, FPD1000 was DEV1 while CMN was DEV2.

Following a major blockage in the dilution lines, the *still* was upgraded to a unit designed with pressure dependent primary impedances [10]. Soon after, the calibration of the Carbon Speer thermistor S1109 was checked against the FPD1000 before any experimental runs were resumed. No significant calibration drift was observed (see Fig. 2.7).

In a calibration run performed in 2019, the FPD1000 and CMN were mounted on the mixing chamber along with the Carbon Speer sensors (S1109 and S1102). Calibration drifts were significant at the lowest temperature, so the sensors were recalibrated against the CMN, after it was calibrated against the FPD1000. The recalibration fit of the CMN against the FPD1000 is shown in Fig 2.8.
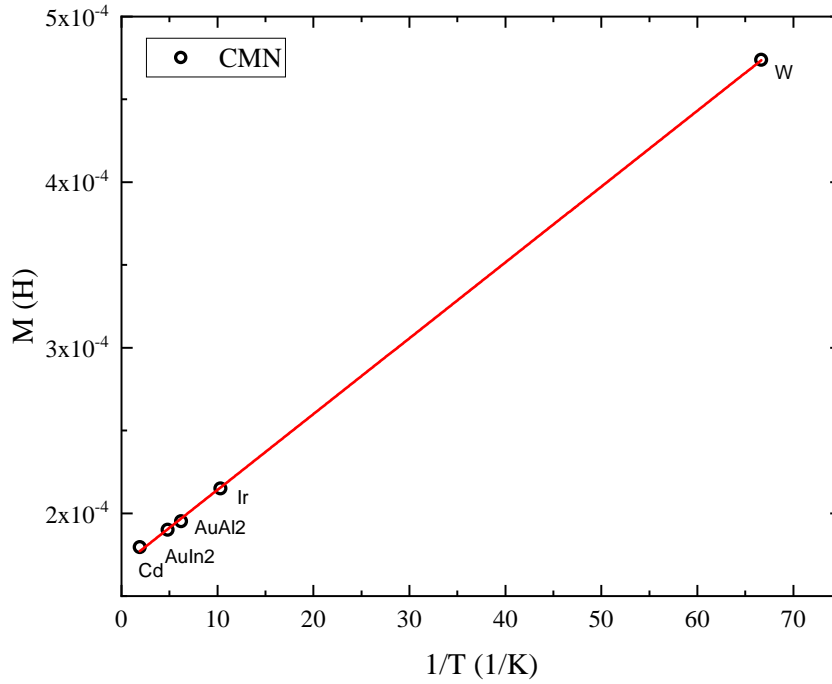
Figure 2.8: Recalibration of the CMN against the FPD1000.

The calibration function used for the mK diagnostic thermistors is

$$log(T) = \sum_{n=0}^{n_{max}} a_n (log(R))^n \tag{2.5}$$

where n_{max} can take values upto at most 9. The calibration curve of S1109 is shown in Fig. 2.9. The calibration of the ruthenium oxide sensors which were mounted in the same run (TT1808 and TT1614) was also checked, and no significant drift was found.
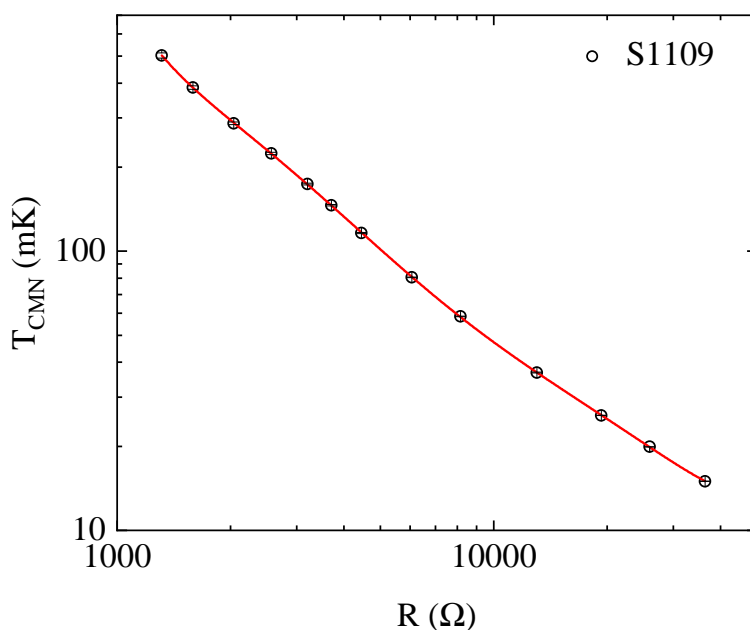
Figure 2.9: Recalibration of the Carbon Speer thermistor S1109. The red line shows the 6th order polynomial fit.

2.4 Installation and testing of new motorized probe

The CFDR-1200 incorporates an option of mounting samples on a probe insert, as opposed to mounting it on the mixing chamber. This allows for a quick change of samples, while the cryostat is in the cold state. However, since the procedure of inserting the probe involves engaging several moving parts, the components of the probe are susceptible to damage and degradation over time. Specifically, the thermal contact between the clamping guide and the probe clamp can degrade, and few electrical channels can become unusable to the electrical contacts breaking or developing poor isolation to the electrical ground. Due to these reasons, the old probe was upgraded to a new model (see Fig 2.10), which has an additional feature whereby the motion of the probe is automated by means of an electrical motor. Similar to the old probe, the new probe insert is equipped with Fischer and coaxial Lemo connections and diagnostic thermistors are provided to readback the temperatures of the thermal stages.
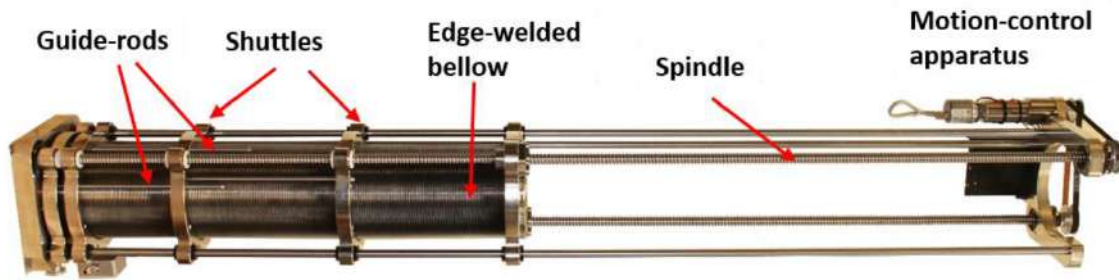
Figure 2.10: The motorized probe, which replaced the manual probe.

The motorized probe comprises of a probe lift which houses the edge welded vacuum bellow in which either the radiation shield or the probe insert can be fitted on the top flange which contains an o-ring seal. The motion control apparatus is mounted at the top of the probe lift and contains the electrical motor, the driving electronics, the rubber conveyor belt and gear system. It controls the up / down motion of the probe in a precise manner via a rotating spindle. A 24 V DC power supply is used to drive the motor control. During the movement of the probe, the vacuum bellow and probe are supported by the guide rods and shuttles. The base of the probe lift houses the electrical connections for the power supply and the USB interface for communication. It also has the vacuum pumping port which is connected to a Pirani gauge and manual valve. This is generally connected to a rotary pump, but can be connected to a turbomolecular pump for better vacuum. The Fig. 2.11 shows the vacuum and the electrical connections at the base of the probe lift and the motion control apparatus located at the top of the probe lift. As the probe is moving inside the edge welded bellow under vacuum, the new probe design eliminates the need for a Wilson seal, which was essential in the manual probe. The original sliding seals design in the manual probe was a potential source of leak. This is eliminated in the motorized probe design by using the edge welded bellow as a load lock.
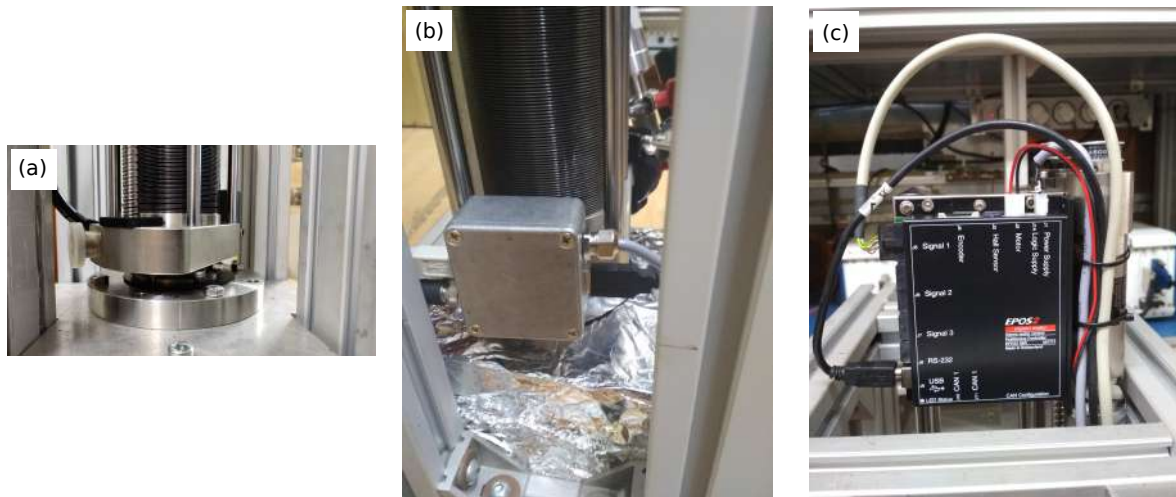
Figure 2.11: The figure shows the (a) vacuum pumping port (b) the electrical connections at the base of the probe lift and (c) the motion control apparatus located at the top of the probe lift.

Another change in the design from the old probe design is the mechanism controlling the clamping of the probe contacts to the thermal stages of the CFDR. While the old probe used a manual turnscrew to engage the spring-loaded contacts, the new probe uses pneumatic actuators. The Fig. 2.12 shows this mechanism.
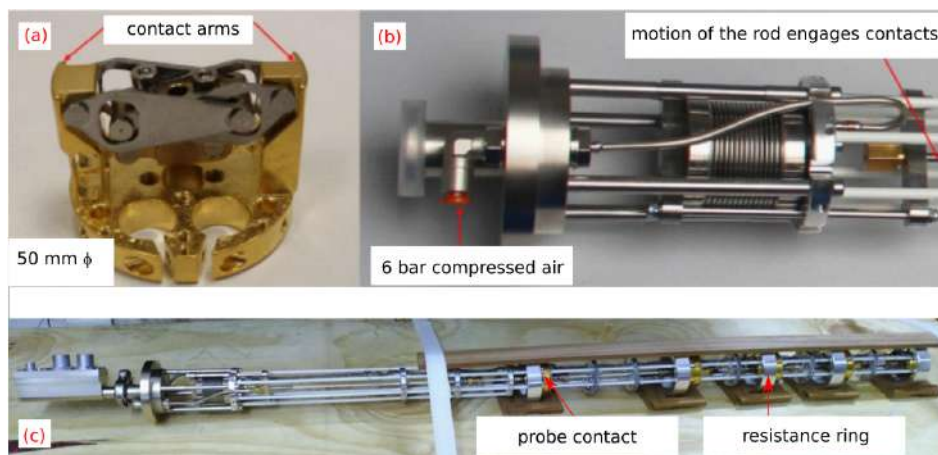
Figure 2.12: (a) The probe contact (b) compressed air clamping mechanism in the new probe (c) testing jig to test the clamping mechanism of the new probe outside the cryostat.

Compressed air flows into the inlet and fills the bellow, which in turn pulls up a central rod. When the central rod is fully pulled up, the clamps engage the probe contacts to the inner surface of the clamping guides, maintained at the temperature of their respective thermal stages. In order to disengage the probe contacts, the overpressure needs to be released. This is done by the means of a one-way valve attached at the inlet. The compressed air pressure

is maintained at ~ 6 bar, which is the rated pressure for operating the clamping mechanism. It is suggested by Leiden Cryogenics that the operating pressure should not exceed 7 bar, and that in no circumstance should it exceed 8 bar (which poses a risk of permanent damage).

Figure 2.13: Initial vacuum test of the probe lift.

As the clamping mechanism is driven by high pressure gas, it is possible to damage the probe contacts if the probe is clamped at a position which offers no resistance to the probe contact. The clamping mechanism was first tested outside the cryostat using dedicated testing jig, which was made using the resistance rings supplied by the manufacturer (see 2.12).
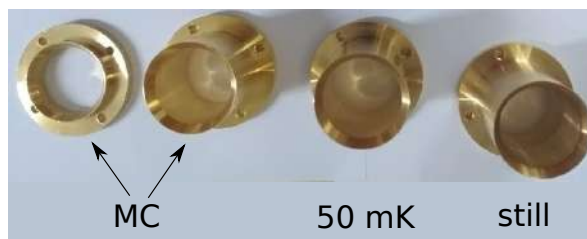
Figure 2.14: The gold-plated clamping guides for the motorized probe.

The motor of the new probe is powerful, and can damage the cryostat components if the probe gets stuck or misaligned during the insertion process. Therefore, the old clamping guides mounted for thermal contact to the CFDR were replaced by new guides (see Figs. 2.14

and 2.15), which were significantly longer. The guides received from the manufacturer did not have enough tolerance to fit, and the outer cylindrical surface of each guide was machined on a lathe to reduce the thickness by 0.3 mm to allow for the required tolerance. The guides were cleaned and then gold-plated after machining. They were then were installed in the CFDR-1200 after gold plating, and the alignment was checked manually with a special teflon jig (ϕ = 50 mm).
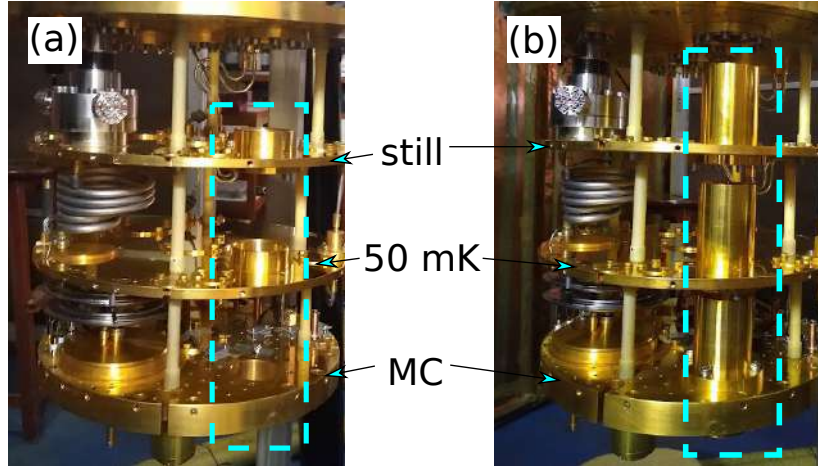
Figure 2.15: The CFDR-1200 with (a) the old clamping guides (b) the new clamping guides, which are significantly longer.

After replacing the clamping guides, the cooling power of the old probe and radiation shield was measured at 120 mK using 20 mA still heater current and this was compared with the original cooling power. By using the old probe and radiation shield, the change in the cooling power of CFDR-1200 resulting from the replacement of the clamping guides could be directly assessed. The measured values are tabulated in Table 2.2. A decrease of 1.6%

Table 2.2: The comparison of the cooling powers measured at 120 mK using 20 mA *still* heater current, before and after changing the clamping guides.

Insert	Cooling Power (μW)	
	with old guides	with new guides
Old probe	973	868
Old radiation shield	732	720

and 10.8% was observed in the cooling power when using the radiation shield and probe, respectively, which can be attributed to the increased heat load due to the longer guiding

clamps. However, the change in cooling power was within an acceptable tolerance of 11%, for all the configurations.

Before attempting a cold test, a room temperature test was performed using the motorized probe in the open cryostat, to confirm the alignment of the clamping guides and ascertain the clamping positions. Generally, the cryostat is supported by the extended tripod legs when in the open state, but the probe cannot be mounted in this state due to height limitations. In order to perform tests at room temperature in the open cryostat, a special stand was fabricated from aluminium (see Fig. 2.16).
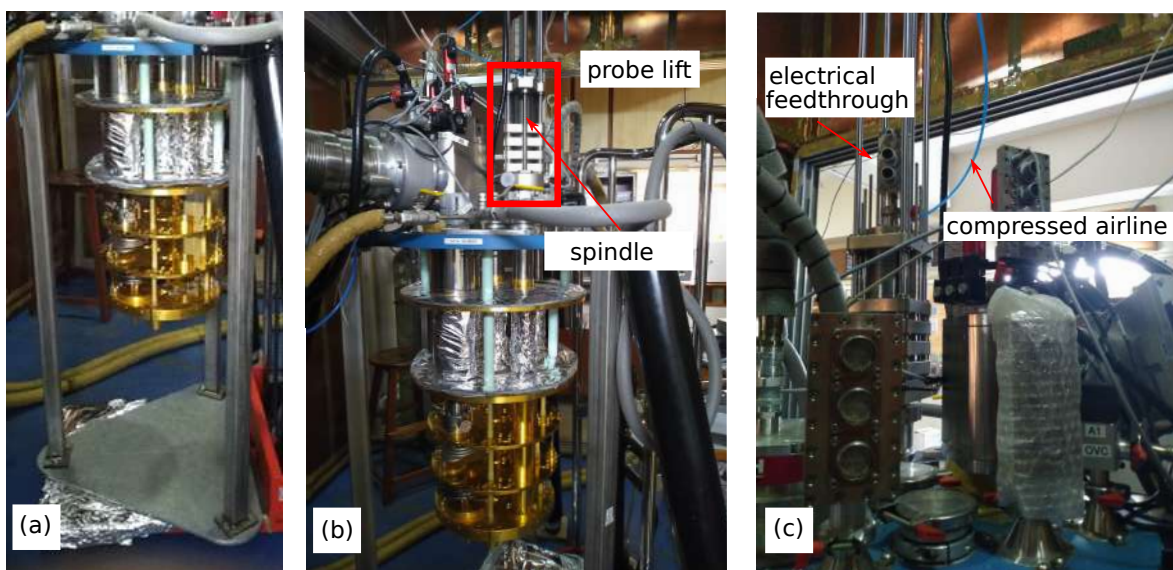
Figure 2.16: (a) Dedicated aluminium stand for room temperature motorized probe tests (b) Room temperature testing of the motorized probe in the open cryostat (c) The electrical feedthrough for the probe insert and the compressed airline for the pneumatic actuators.

The probe motion is controlled through a LabView based software interface. As an additional safety feature, the distances on the spindle when the mK stage crossed the various thermal stages of the CFDR have been physically measured and recorded in addition to the encoder distances on the LabVIEW GUI. This distance is unaffected by any potential software glitches and should be verified before clamping the probe in the cold state, in order to ensure that the clamps are in proper thermal contact with their respective stages. The comparison of the clamping positions of the old and the new probe can be seen in Fig. 2.17.
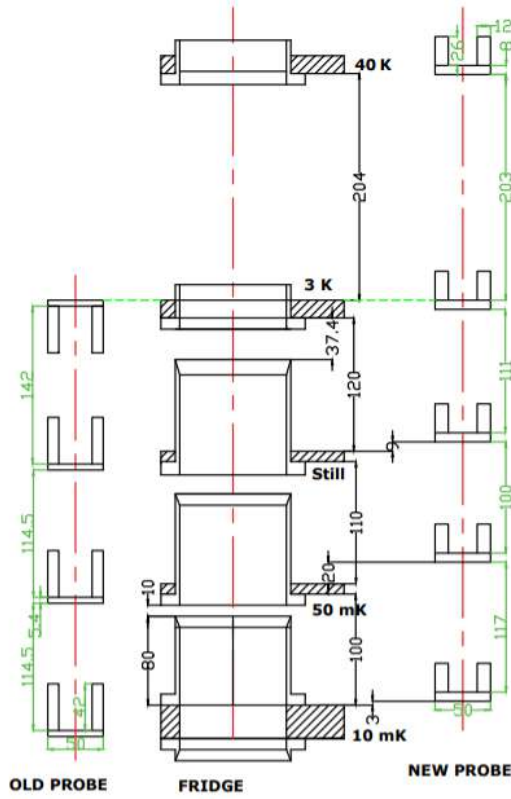
Figure 2.17: A schematic diagram showing the clearances between the thermal stages after the installation of the new clamping guides. The clamping positions of the old and the new probes are also marked in the schematic. Note that the widths of the probe contacts and the guiding clamps are not to scale in the figure.

After the room temperature tests, a cold test was performed to check the performance of the motorized probe. The cooling power of 703μW was measured at 120 mK using 20 mA *still* heater current with the new probe, which is similar to the cooling power achieved using the old radiation shield. The lowest temperature recorded was ~11 mK and ~14 mK, using a *still* heater current of 15 mA and 5 mA, respectively.

2.5 Installation of the cryo-vibration isolation platform

While bolometers have excellent energy resolution, their performance can degrade in the presence of external sources of noise such as EMI pickup, the presence of ground loops, vibrations from vacuum and compressor systems, etc. The effective resolution is give by

$$\Delta E^2 \approx \Delta E_{TFN}^2 + \Delta E_{el}^2 + \Delta E_{vib}^2 \tag{2.6}$$

In practice, the energy resolution is dominated by the electrical and vibration induced noise terms rather than the theoretical limit given by the thermal fluctuation noise (TFN). Hence, there is scope to further improve the detector performance if the electrical and vibration induced noise can be suitably mitigated. Dry dilution refrigerators are susceptible to the vibration noise generated from the operation of the pulsed tube cooler. This vibration noise can couple with cryogenic systems mainly in two ways:

- It can induce relative motion between the various components of the detector. This effectively increases the temperature of the system, leading to fluctuations at the mK stage.

- The microphonics of the wires used for electrical readout induce electrical noise via triboelectric effects [107].

Both these effects lead to the degradation of the bolometer baseline and energy resolution. The bolometer based $0\nu\beta\beta$ experiment AMoRE has invested significant effort in implementing a dual stage vibration isolation in its cryostat [108].
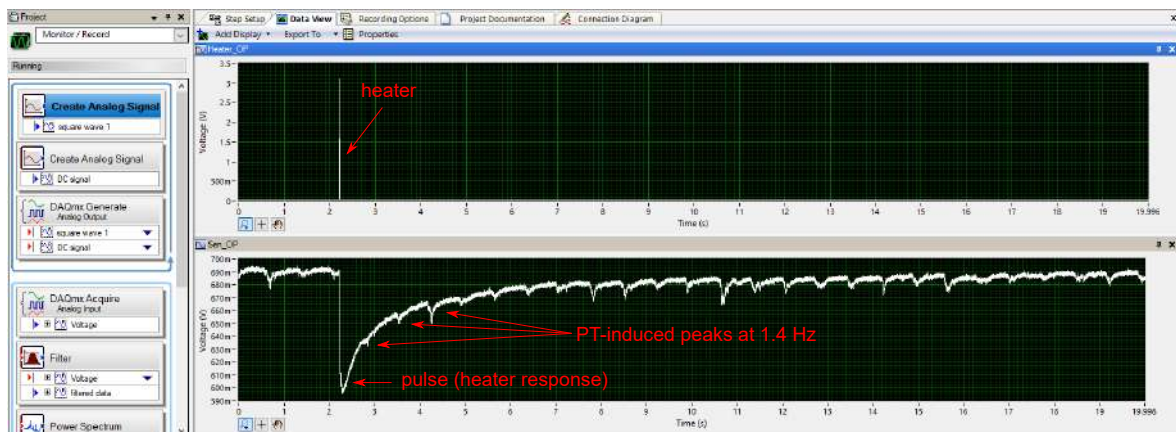
Figure 2.18: An example of a bolometer pulse (bottom panel) in which the vibration induced noise can be distinctly observed. The envelope of the signal in the bottom panel is the response to the heater input (shown in the top panel). There are several pulses riding on this envelope, which are induced by the vibrational noise of the pulsed tube cryocooler. The frequency of the vibration induced noise matches the operating frequency of the pulsed tube cooler, i.e., 1.4 Hz.

Fig. 2.18 shows the example of a pulse which is affected by vibrational noise. In the figure, several vibration induced peaks can be distinctly observed, which distort the baseline and shape of the heater response pulse. These pulses occur at a frequency of 1.4 Hz, which

corresponds to the operating frequency of the pulsed tube cooler. The presence of vibration induced noise can often be confirmed by momentarily switching off the pulsed tube cooler for 1-2 min.

There is a strong motivation to implement vibration isolation in the CFDR-1200, since the pulsed tube is rigidly coupled to the 40 K and the 3 K stages via the gas lines. The CFDR-1200 relies on its large mass to dampen the vibrations. This is a different strategy compared to that of dilution refrigerators fabricated by other companies such as Oxford Instruments or Bluefors, which use copper braids to thermally connect the pulsed tube stages to the cryostat plates, while mechanically isolating them.

A commercial cryo-vibration isolation platform (CVIP) was purchased from M/s Janssen Precision Engineering [109]. The design is based on passive isolation techniques. Due to its propriety nature, the manufacturer has not shared the exact nature of the design. However, it can be surmised that the vibration isolation has been achieved by using springs with a high stiffness coefficient and good thermal conductivity. Copper beryllium springs are preferred for these applications, as they achieve the necessary vibration isolation without introducing any significant temperature offset across the device. The CVIP mitigates vibrations along three degrees of freedom - z, R_x and R_y. It is imperative that the maximum permissible load of the CVIP must not be exceeded, else there would be a risk of permanent damage to the vibration damping component. The CVIP allows for a large number of setups to be mounted on the system, and can support upto 6 kg of maximum payload. The specifications of the CVIP have been summarized in Table 2.3. Since the hole patterns for the CVIP and the

Table 2.3: Summary of the specifications of CVIP-3. Note that the cut-off frequency given corresponds to the condition where the maximum payload has been deployed.

Parameter	Specifications
Isolated axes	z, R_x and R_y
CVIP mass	1.3 kg
Moving mass (excluding payload)	0.69 kg
Max payload	6 kg
z, R_x and R_y cut-off frequencies	42 Hz, 30 Hz and 30 Hz

mixing chamber are different, an interface plate was fabricated from ETP copper to mount the cryo-vibration isolation platform to the mixing chamber plate of the CFDR-1200. Fig. 2.19 shows the manner in which the CVIP is mounted in CFDR-1200.
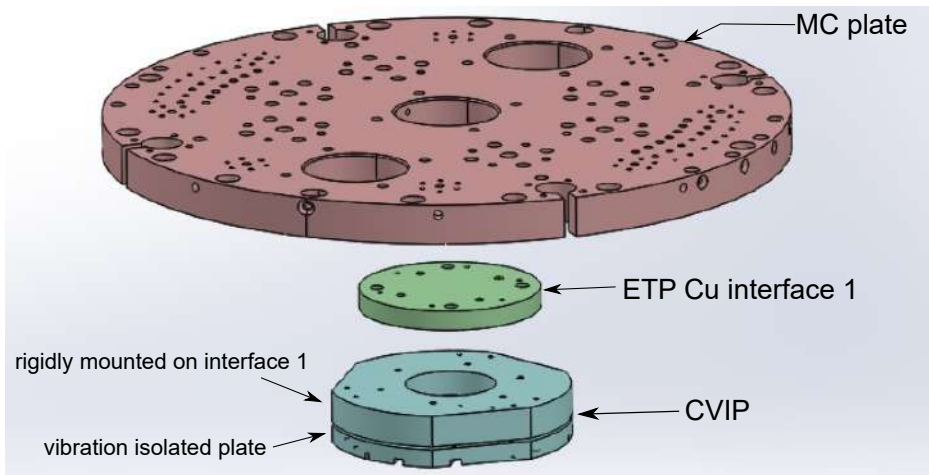
Figure 2.19: Exploded view of the assembly of the cryo-vibration isolation platform in CFDR-1200.

The CVIP has been fabricated from phosphor bronze, which is a non-magnetic material. However, due to the relatively poor thermal conductivity of phosphor bronze at low temperatures, additional copper braids are necessary for the thermalization of the CVIP. As per the manufacturer the CVIP is insensitive to the addition of copper braids and wiring. The copper shield of a RG8 cable was found to be the most suitable for use as a copper braid, due to its high flexibility. The copper was etched in citric acid followed by a deionized water wash. The copper braids were then vacuum annealed at 600°C for 16 h. This was done to minimize the trapped hydrogen content in the copper braids, since the ortho - para phase transition of hydrogen acts as a heat leak below 20 K. Three copper braids were added from the MC to the CVIP for uniform thermalization. Care was taken to ensure to maintain sufficient slack while anchoring copper braids and electrical wire, since these connect the MC directly to the CVIP, bypassing the vibration isolation element. If there is tension in the wires or braids, these can transmit vibrations directly from the MC to CVIP.

In order to test the performance of the CVIP, calibrated ruthenium oxide sensors TT1808 and TT1613 were chosen since they have similar and reproducible resistance-temperature characteristics. Their intrinsically similar response makes it possible to compare the noise spectra of the sensor mounted on the CVIP and the MC in the same run. Moreover, since the

sensors are shielded, they are less susceptible to EMI pickup in comparison to bare sensors. Thus, the noise primarily originates from vibration induced sources. A heater Q100 was mounted on the CVIP for the cooling power measurement. The sample mounting is shown in Fig. 2.20.
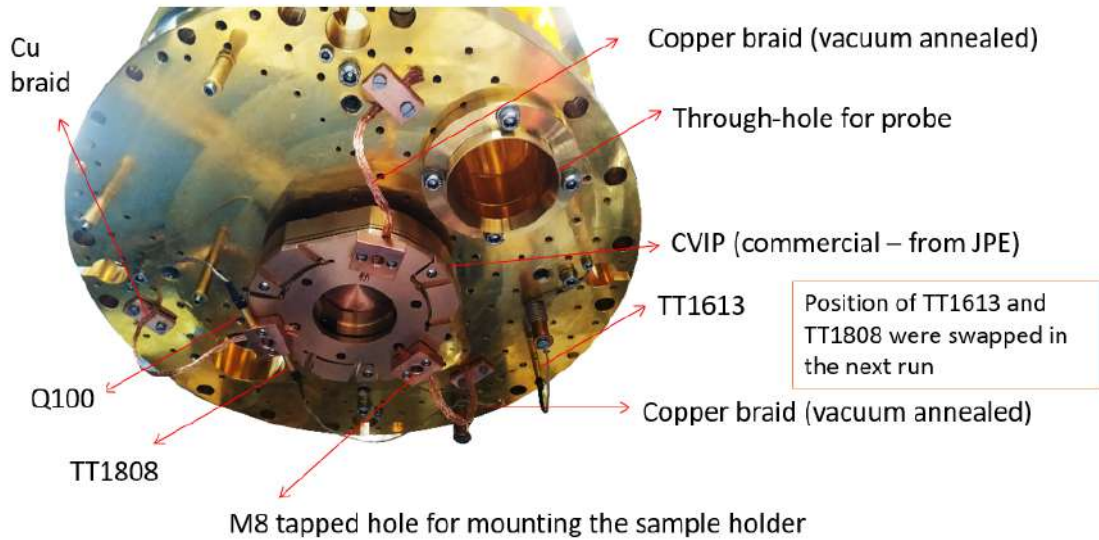
Figure 2.20: The CVIP testing configuration. The annealed copper braids were added for thermalization purposes.
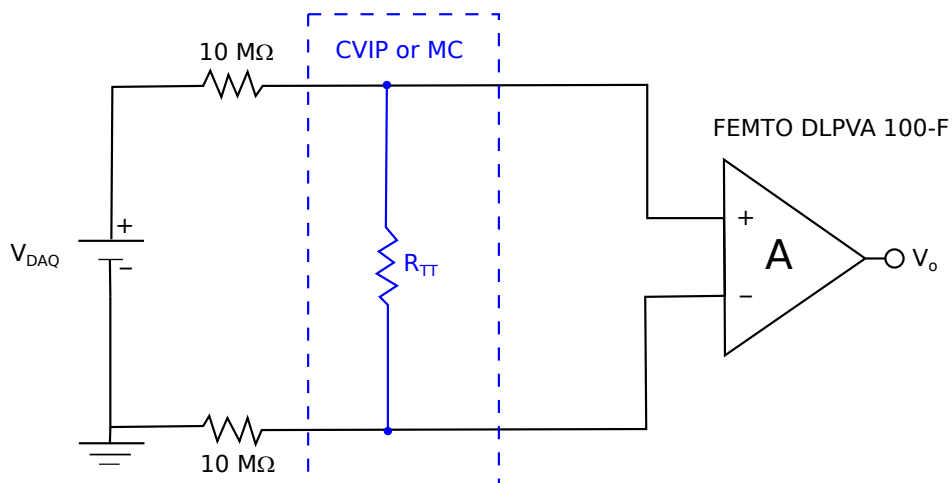
Figure 2.21: The readout circuit for the ruthenium oxide sensors.

The Fig. 2.21 shows the readout circuit used for the noise measurements of the ruthenium oxide sensors. The data acquisition system is based on the I/O module NI PXI-6281, which is used to supply 16 bit single ended DAC output and readback 18 bit differential ADC. The NI PXI-6281 is operated in the PXIe-1082 chassis, which in turn interfaces with the data acquisition PC through an optical fibre connection. The ruthenium oxide sensors were

connected in series to 20 MΩ resistance. The output voltage across the sensor was amplified by a factor of 1000 using a low noise differential amplifier FEMTO DLPVA 100-F and the amplified signal was readback to an ADC channel. The resistance was acquired using the commercial AC bridge AVS47-B by applying an excitation voltage of 30μV.

In comparison to a previous iteration without any copper braids mounted in which the CVIP did not cool down below 38 mK, there were no such thermalization issues after the connection of the three copper braids. The system was stabilized at 20 mK using the PID controller, and the resistance and noise data were acquired. It should be noted that two runs were performed - M2003M01 and M2004M01. In the former, TT1613 was mounted on the MC and TT1808 was mounted on the CVIP while in the latter the positions were flipped. The second run was taken in order to check for possible systematics due to sensor-specific noise sources. It also served to confirm the effect observed in the first run. In both the runs, the sensors had similar resistances at 20 mK. In the run M2003M01, TT1808 and TT1613 had resistances of 27 kΩ and 38 kΩ at 20 mK, respectively. The noise spectra of the ruthenium oxide sensors in the range from DC - 25 kHz is shown in Fig. 2.22. It can be clearly seen that for both runs, the sensor mounted on the CVIP has no significant noise peaks above the thermal baseline of the amplifier. In contrast, vibration induced noise peaks can clearly be seen in the sensor mounted on the MC plate in both the runs. Thus, it can be clearly inferred from the data that the CVIP significantly reduces the vibration induced noise at high frequencies (>5 kHz). The effect is especially visible on the prominent peaks at 16.1 kHz and the bundle of peaks around 21 - 24 kHz. While it is expected that the CVIP will effectively cut off the vibrational noise for frequencies > 0.042 kHz [109], it was not possible to draw any inferences on the effect of the CVIP on the low frequency region (< 5 kHz), which is significant for bolometer performance, from the present tests as the noise pickup was below the baseline noise levels.

The cooling power was measured on the mixing chamber and the CVIP at 120 mK using a *still* heater current of 20 mA. For this measurement, the heater Q100 was biased using a voltage DAC output from NI PXI-6281, and the current flowing in the circuit was measured using an ammeter (least count of 0.01 mA). The pseudo-constant current circuit could not be used in this case since the maximum current available would be limited (50 μA if a 200 kΩ

51

load resistor is used). In this case, a larger current of ~0.62 mA was required so the heater was biased directly. The cooling power on the CVIP is 39 μW, which is significantly lower than the cooling power at the mixing chamber (681 μW). Thus, cooling power is traded off in return for mitigating the vibration induced noise.
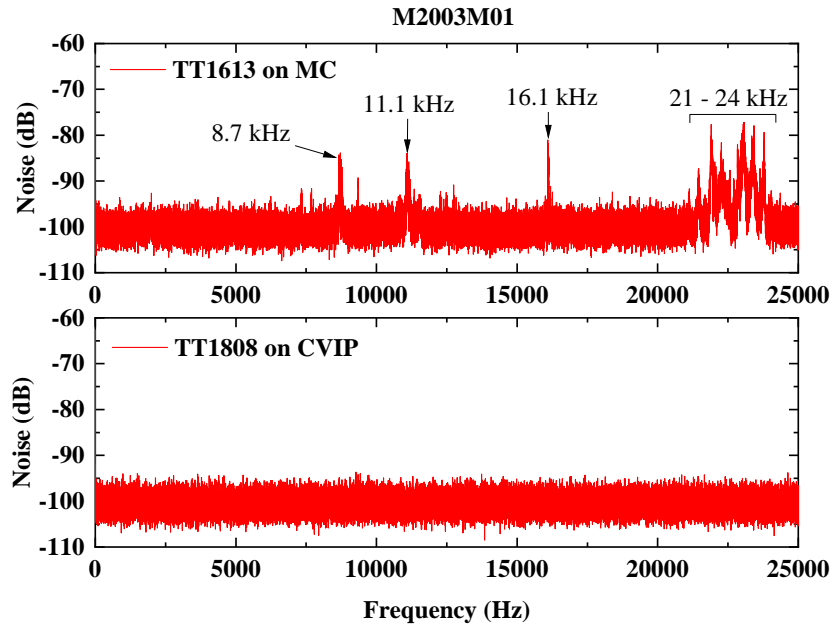
(a) TT1613 on CVIP, TT1808 on MC.
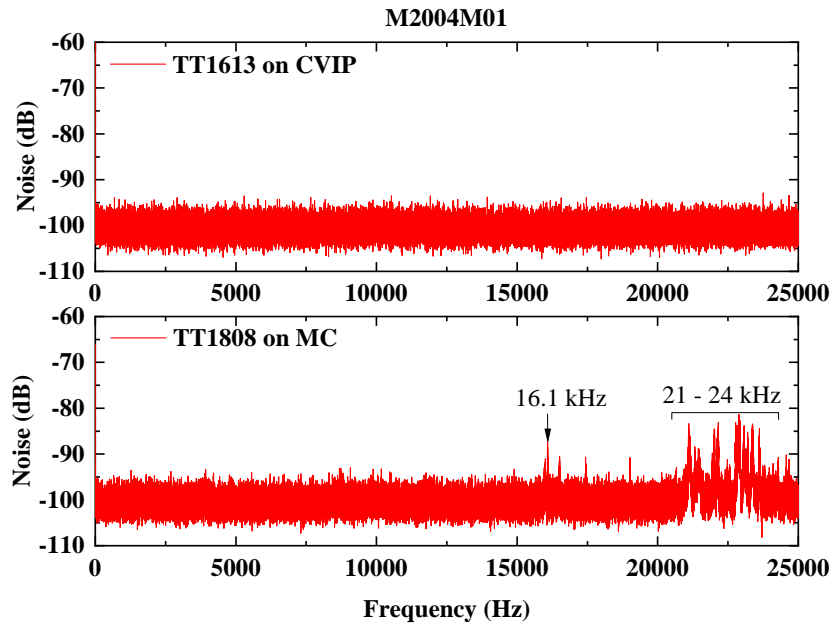
(b) TT1613 on MC, TT1808 on CVIP.

Figure 2.22: Noise spectra of the shielded ruthenium oxide thermistors (a) Run M2003M01 (b) Run M2004M01. The prominent peaks which are above the level of -90 dB have been marked.

2.6 Summary

Low temperature measurements cannot be performed without the use of accurate millikelvin thermometers. It is important to check for calibration drifts in secondary thermometers regularly and recalibrate if necessary. Important calibration checks and recalibrations were performed for the diagnostic thermistors on the MC stage. The CFDR-1200 has a provision for sample mounting on the probe, for sample changes in the cold state. Due to the repeated insertion and removal of the probe, the associated components are susceptible to wear and tear. The manual probe was upgraded to a motorized probe. Several stands and testing jigs were fabricated for the room temperature testing of the motorized probe, after which the performance was checked with cold tests. The cooling power was measured to monitor the performance of the fridge, since the clamping guides in the dilution had been replaced. Although a decrease in the cooling power was observed, which may be attributed to the increased heat load due to the use of longer guides, the change was within an acceptable tolerance of 11%. The cooling power of 703μW was measured at 120 mK using 20 mA *still* heater current with the new probe, which is similar to the cooling power achieved using the old radiation shield. The lowest temperature recorded was ~11 mK, using a *still* heater current of 15 mA. A commercial cryo-vibration isolation platform was installed below the mixing chamber plate to mitigate the vibrations arising from the pulsed tube cryocooler. The performance was tested by comparing the noise spectra of shielded ruthenium oxide sensors. A significant improvement was observed in the high frequency regime of the noise spectra (> 5 kHz).

It would be interesting to see if mounting a bolometer on the the CVIP leads to an improvement in its energy resolution. This exercise was attempted with a sapphire bolometer during the tests, but could not be performed due to saturation of the resistance of the NTD Ge thermistor ~50 MΩ. Subsequently, diagnostic checks performed using an FPD1000 coupled to a sapphire bolometer using GE varnish which confirmed that the saturation in resistance was genuinely caused by a thermal decoupling between the sapphire platform and the mixing chamber plate. Currently, studies to optimize a stronger heat link are underway in the *TIN.TIN* group.

Chapter 3

Tin pest: a challenge for tin bolometers

As mentioned in Chapter 1, tin pest is a concern for applications involving tin at low temperatures, as it affects the stability of the system. Given the rare nature of neutrinoless double beta decay events, it is envisaged that the detector will be of a large size (100 - 1000 kg) and is expected to run for a period of several years. During the cool-down and warm-up of the cryostat from mK to room temperature, the detectors are susceptible to tin pest since the setup will remain at intermediate temperatures for several hours to several days depending on the mass of the cryostat. These conditions are highly suitable for the formation of tin pest. Therefore, for the longevity and performance of the detector array, it is crucial that the risk of tin pest formation must be inhibited or greatly suppressed. It is known that alloying tin with a suitable alloying element can inhibit tin pest.

This chapter describes the crystal growth and testing of tin rich alloys in order to find a suitable candidate for the superconducting *TIN.TIN* bolometer. Section 3.1 introduces the phenomenon of tin pest, Section 3.2 describes the synthesis of the tin alloys and Section 3.3 details the cooling tests performed to qualify the alloys. The superconductivity measurements are described in Section 3.4. Finally, Section 3.5 summarizes the chapter.

3.1 Tin pest

While tin is commonly regarded as the first metal of Group 14 of the periodic table, a semiconducting allotrope of tin (α-Sn) also exists. α-Sn has generated a lot of interest recently due to its tunable topological properties and is the only known elemental member of a class of 3-D topological materials called Topological Dirac Semimetals [19, 110, 111]. Table 3.1 lists the crystal structures of both the allotropic forms of tin. The structural

Table 3.1: Crystal structures of the major allotropes of tin.

Allotrope	Crystal structure	Space group
α (semi-conductor)	Diamond cubic	*Fd-3m*
β (metal)	Tetragonal	*I4$_1$/amd*

phase transformation from the metallic β-Sn to the semiconducting α-Sn is known as tin pest [12] and this transformation occurs very close to room temperature when the sample is cooled under ambient conditions. During this transformation, the crystal structure of tin changes from body-centred tetragonal to diamond cubic, which leads to a 27% increase in the volume of the unit cell. The increase in the interatomic distance results in a decreased overlap between atomic orbitals, which changes the electronic band structure of tin and creates a band-gap of ~80 meV. Thus, α-Sn is semiconducting as evidenced by its NTC type resistance. Semiconducting α-Sn is brittle like most semiconductors, and is unable to withstand the internal stress generated due to this sudden volume expansion of the sample. This leads to its mechanical failure, and the sample develops warts, microfractures, cracks and can even disintegrate completely into powder. Thus, tin pest affects the structural integrity of tin and is a concern in tin-based systems that operate at low temperatures for a long time [6, 7, 12].

The phenomenon of tin pest has found references even in popular culture, and there is a historical debate regarding whether Napoleon's army faced an issue with the bursting of the tin buttons on their uniform while passing through the bitter cold of Russia in 1812. The first published record of tin pest dates back to 1851, where Erdmann reported the failure of tin-based church organ pipes in a German village [112]. Interestingly, tin pest is also

called the 'museum disease', since several historical tin artefacts have been damaged because of the phenomenon [113]. More recently, the enforcement of the Restriction of Hazardous Substances (RoHS) directive [1] in 2006 [7] has invigorated several new studies on tin pest in lead-free solders which have replaced conventional solders [11, 114, 115, 116]. There are several studies on the kinetics of the transformation [15, 117, 118] and techniques to monitor the growth of the α phase [119, 120, 121]. However, the mechanism of the allotropic $\beta \to \alpha$ phase transition is still not well understood in spite of earlier studies [117, 122].

According to the study by Nogita *et. al.* [118], the transformation from $\beta \to \alpha$ Sn requires undercooling and the transformation rate is sluggish at temperatures $\sim +13°$C. The transformation rate increases with decreasing temperature, reaching a maximum between -35°C and -50°C. The rate then starts decreasing with decreasing temperatures and is negligible below $\sim$ -100°C. This behaviour arises due to the interplay between the driving force [2] of the transition and the thermal energy available to tin. As the temperature is reduced, the driving force increases thereby facilitating the transition. However, the thermal energy available to the tin atoms also reduces with decreasing temperature. This reduces the probability of tin atoms crossing the α/β phase interface, which suppresses the growth of the α-Sn phase. The collective behaviour of the system explains the observed transformation rate.
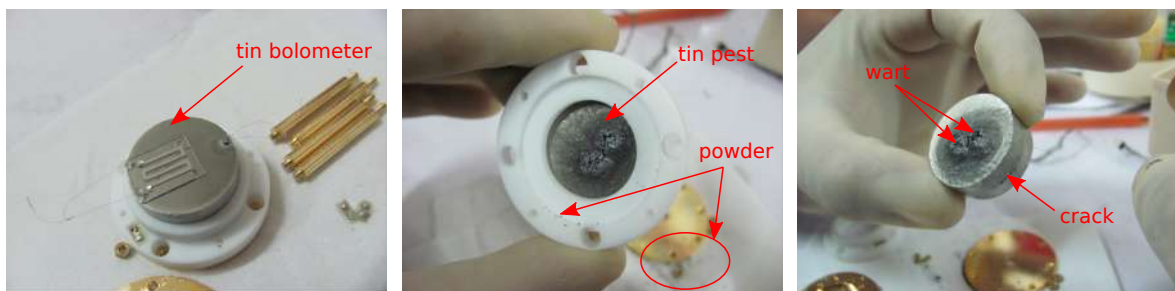
Figure 3.1: The figure shows the development of tin pest in a pure tin bolometer (99.999%) fabricated by the *TIN.TIN* collaboration during testing in the CFDR-1200. The warts and cracks in the tin sample can be clearly seen. The transformed regions have a grey colour.

Tin pest is of concern for the longevity and performance of the *TIN.TIN* detector array. Fig. 3.1 shows a pure tin bolometer which inadvertently developed tin pest after thermally cycling it from room temperature to mK and back in the CFDR-1200. The transformed

---

[1]A directive by the European Union which banned the use of Pb (and 9 other materials) in electrical and electronic products due to its hazardous effects on the environment and human health.

[2]This is equivalent to the difference in the Gibb's free energies of the phases $\Delta G = G_\beta - G_\alpha$.

regions appear greyish rather than a metallic white colour. Large sections of the sample showed signs of damage due to tin pest formation. This motivated the present studies to suppress the $\beta \rightarrow \alpha$ transition in Sn, which are presented in this thesis.

3.2   Crystal growth of tin alloys

It has been shown that alloying Sn with elements like Pb and Bi, which have good solid solubility in Sn, hinders the formation of tin pest [11]. It is generally believed that these elements hinder the transformation by pinning the dislocations in the Sn matrix, which makes the expansion of the lattice energetically unfavourable [7]. Consequently, this arrests the growth of the α-Sn phase. Conversely, elements with limited solubility in Sn (such as Zn, Al, Mg and Mn) accelerate the transformation. However, it should be mentioned that there are inconsistencies among studies by various groups [11, 12] regarding the efficacy of different alloying elements and the concentrations that are beneficial. For the present study, various Sn-rich alloys of a wide range of concentrations were independently grown and tested for resistance to tin pest. The details of the stock materials used for the crystal growth are described in Table 3.2.

Table 3.2: Details of the starting materials used for the synthesis of the Sn alloys.

Material	Source / Vendor	Purity	Form
Sn	Alfa Aesar	7N	Tear drops
Bi	Alfa Aesar	5N	Shots
Cd	Alfa Aesar	5N	Shots
Cu	Leico	5N	Shots
In	Alfa Aesar	6N	Shots
Pb	Alfa Aesar	5N	Shots
Sb	ACL	5N	Chunks

For the crystal growth process, the starting material was sealed in an evacuated quartz tube, which is suitable for crystal growth at temperatures upto ~1200°C. The typical process flow for the synthesis is described below:

1. **Cleaning and baking the quartz tube:** High quality quartz tubes with wall thickness 1 mm and outer diameter 12 mm were used [3] as the crucibles for the melt. Before use, the quartz tubes were cleaned in dil. HF solution, followed by deionized (DI) water and acetone washes. They were then dried and transferred to a dedicated high temperature vacuum furnace for baking. The temperature was ramped from room temperature to 900°C at 50°C/h, stabilized at that temperature for 5 - 6 h and then cooled down to room temperature at 50°C/h. The heating of the quartz at such high temperatures leads to desorption of the absorbed moisture and chemical impurities, which are then pumped away by the vacuum system. Once the quartz tubes are baked, they can be stored in a large vacuum desiccator prior to the sealing. The materials must be vacuum sealed within 24 h of baking the quartz tubes.

2. **Cleaning the starting materials:** Oxide and/or sulphide layers were removed before using the material by using appropriate reagents. The tin was cleaned in 2% dil.HCl followed by a DI water wash. The lead was cleaned using 2% dil. HNO_3 followed by a DI water wash. The copper was cleaned using citric acid and DI water. The other alloying elements were cleaned in acetone and DI water only if needed.

3. **Vacuum sealing the starting materials:** The materials were weighed in the appropriate ratios and transferred to the baked quartz tube. A narrow sealing point (few mm diameter) was made by heating a section of the quartz tube above its softening temperature and reducing the diameter. The sealing point was positioned at least 2 - 3 cm above the starting material, to prevent the starting material from melting due to excessive heat transfer via the conduction through the quartz tube. As an additional measure, wet asbestos wool was wrapped around the section which contained the starting material. Markers such as quartz dots were added for sample identification purposes. After the sealing point was made, the quartz tubes were fitted on a dedicated vacuum setup using a double o-ring seal. The vacuum system is comprised of a turbomolecular pump backed by a rotary pump. There is an added provision for flushing the system with

---

[3]Quartz tubes with outer diameter 19 or 20 mm were also used sometimes for large crystals ($\gtrsim$ 15 g).

dry nitrogen. Multiple samples can be evacuated simultaneously on the setup. The samples are sealed at a typical base vacuum of 5×10^{-5} mbar.

4. **Crystal growth:** The tin alloy crystals were grown by a slow and controlled recrystallization from the melt. The temperature of the furnace is controlled using sensitive PID systems which are coupled to high wattage heaters. In the case of the vertical Bridgman furnace, the temperature of the melt is also controlled by translating it slowly through the hot zone at a rate of 1mm/h. The temperature profile of the vertical Bridgman furnace is hottest at the centre and falls off towards the edges. The sharp tip of the quartz tube acts as the initial nucleation point. These factors allow for a controlled directional crystallization from the melt. It should be noted that the quartz tube should be free from scratches and impurities, as these can act as additional nucleation sites. The quality of the quartz tube and the rate of recrystallization determine the quality of the crystal grown. It was seen that the crystals grown using the vertical Bridgman furnace were single crystals, while the crystals grown in the box furnace tended to be more polycrystalline in nature. The pictures of a few samples that were grown have been shown in Fig. 3.2.

Figure 3.2: Selected pictures of samples that were synthesized. Left: 7N pure Sn single crystal grown using vertical Bridgman technique; Right: A set of Sn-rich alloy samples grown in a box furnace under identical conditions.

Initially, the vertical Bridgman technique was used to grow single crystals of Sn, 0.1% and 16% Sn-In (In by mass %). In order to check the quality of the crystal, Laue back-diffraction images were recorded. The sample was mounted on a triple axis goniometer and mounted in

front of a collimated x-ray source. A tungsten source was used to generate a polychromatic x-ray beam from 0.5 - 3 Å and the diffraction pattern was recorded on a photographic film. The triple axis goniometer and the Laue diffractometer can be seen in Fig. 3.3.

The Laue pattern for the Sn single crystal is shown in Fig. 3.4. Spherical spots, each corresponding to unique (hkl) diffracting planes, form a distinct four-fold symmetry with the perpendicular bisectors deviating slightly from 45°. These observations are consistent with the symmetry expected from a tetragonal crystal system. On comparison with the simulated pattern using ORIENT express, it was inferred that the crystal is aligned along the (110) plane.

Figure 3.3: Left: Triple axis goniometer; Right: Laue diffractometer.
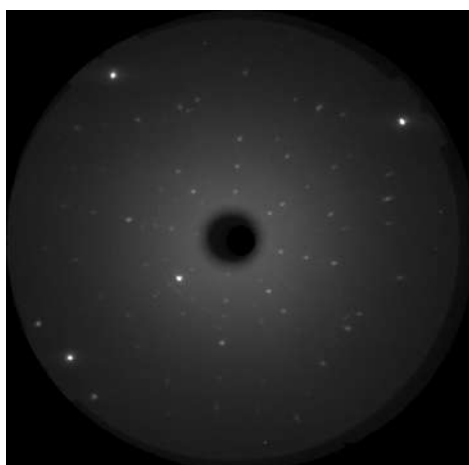
Figure 3.4: Laue back-diffraction pattern for the synthesized Sn single crystal. The pattern corresponds to the (110) plane.

The subsequent samples were grown in a box furnace (make: Carbolite), which allowed multiple samples to be grown simultaneously, thus, improving the turnover time tremendously. Although this method yielded crystals which were polycrystalline, for the purpose of the

cooling tests this was irrelevant. In fact, polycrystalline samples are also expected to show better thermalization at low temperatures compared to single crystals, due to smaller mean free paths associated with the phonons. This could be an advantage for cryogenic bolometers. Using the box furnace, the Sn-X alloys (X = Bi, Cu, Cd, Pb) were synthesized by melting the materials in a vacuum-sealed quartz tube at 1000°C and cooling it slowly over a period of 6 days. The Fig 3.5 shows the temperature profile of the box furnace. The temperature was chosen so as to attempt to form Sn-Si and Sn-Ge samples in the same set. However, the Sn-Ge and Sn-Si alloys did not form due to the poor solubility of the alloying elements in Sn.
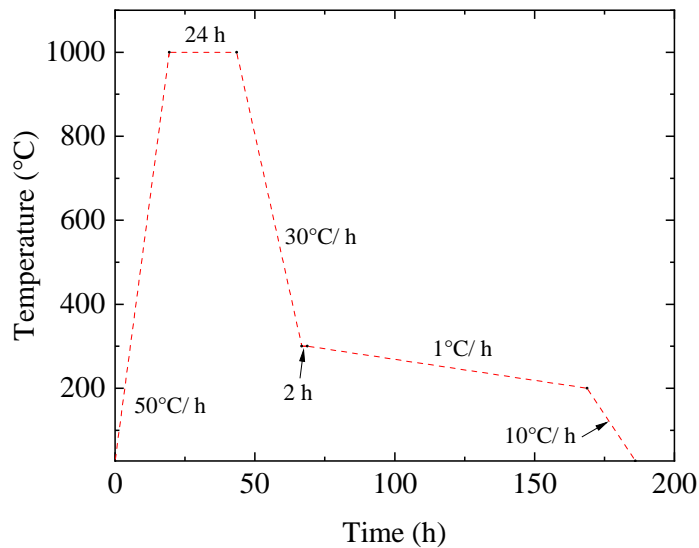
Figure 3.5: Temperature profile of the box furnace for the growth of the Sn alloy samples.

During the preparation of the Sn-Sb alloy, the materials were only heated up to 700°C, as Sb has a much higher vapour pressure at 1000°C which is not conducive to the formation of the Sn-Sb alloy sample. The Sn-Cu alloy was studied as a control sample since it is susceptible to the transformation [116] while the other alloys (with Bi, Cd, In, Pb and Sb) were chosen to check their resistance to the formation of tin-pest. Crystals of Sn-Bi, Sn-Cu, Sn-Cd, Sn-In, Sn-Pb and Sn-Sb were grown in the range of stoichiometric compositions [4] 0.08% - 9.2%, 0.5%, 1.1% - 1.2%, 0.1% - 16%, 1.2% - 9.1% and 0.5%-1.2%, respectively. A greater number of resources were dedicated towards the growth of samples which showed

_____

[4]In this thesis, all the alloy compositions are described in terms of mass % of the alloying element. For better readability, the phrase 'alloying element by mass %' will not be repeated henceforth.

promising results during the cooling tests.

3.3 Cooling tests of the tin alloys

The $\beta \rightarrow \alpha$ transition in Sn consists of nucleation and growth processes [117]. Spontaneous nucleation is rare and may even take years but it is well known that the transformation can be accelerated by bringing a seed in contact with the surface of the Sn sample [13]. This reduces the timescale necessary for the experiment, making it possible to observe effects of the transformation in a span of a few days. The seed should have a crystal structure and lattice parameters similar to that of α-Sn. Hence, InSb, CdTe and α-Sn are commonly used as seeds. It has been reported that seeding is effective even in cases where the seed is not in direct molecular contact with the tin sample, and it is hypothesized that the formation of metastable ice between the seed and the sample induces the transformation in these cases [122]. Table 3.3 lists the crystallographic data for β-Sn, α-Sn and other common seeds which are isomorphic to α-Sn. In the present study, α-Sn has been chosen for the seeded cooling tests, as it is the most effective.

Table 3.3: Crytallographic data for β-Sn, α-Sn and other common seeds [12].

Material	Crystal system	Lattice Parameter (Å)	Coordination number	Interatomic distance (Å)
β-Sn	Tetragonal	a = 5.83, c = 3.18	6	3.03 , 3.18
α-Sn	Cubic	a = 6.489	4	2.79
InSb	Cubic	a = 6.478	4	2.78
CdTe	Cubic	a = 6.41	4	3.277
Metastable ice	Cubic	a = 6.36	4	2.76

The α-Sn seed was obtained from an unseeded Sn sample that underwent multiple $\beta \rightleftharpoons \alpha$ transitions over a period of three years in the dilution refrigerator setup at Tata Institute of Fundamental Research [9]. The Sn sample had disintegrated to a fine powder ($\sim$ 40 g). It was verified using powder x-ray diffraction (PXRD) that the seed powder does not reconvert into the β phase completely even after storage at room temperature for over half a year.

Nevertheless, for the purpose of this study, in order to maximize the α-Sn phase, the powder was stored at -20°C. The residual α-Sn behaves as a seed, converting the remaining β-Sn in the powder to α-Sn.

The allotropes of Sn have visibly different colours – α-Sn is dull grey whereas β-Sn is white with a metallic lustre. Due to this difference in colour, the increase in the concentration of the α-Sn phase in the seed, after storage at -20°C, was qualitatively determined from the change in its colour to a dark grey hue and was verified using PXRD. The PXRD measurements were performed on a Malvern PANalytical diffractometer using the characteristic Cu-K$_\alpha$ x-ray ($\lambda = 1.5406$Å). A Ni-filter was used to cut off the intensity of the accompanying Cu-K$_\beta$ line. The X'Pert HighScore Plus software was used to analyze the acquired spectra and the PDF-4 database was used for the search match and phase quantification analysis. Fig. 3.6 shows the powder x-ray diffraction patterns of the samples before and after storage at -20°C for 20 h. It was observed that the lines from the β-Sn phase almost completely disappeared after incubation while the lines from the α-Sn phase increased in intensity. From the diffraction patterns, the α-Sn phase was quantified to be ~67% and ~96% before and after incubating it at -20°C, respectively.
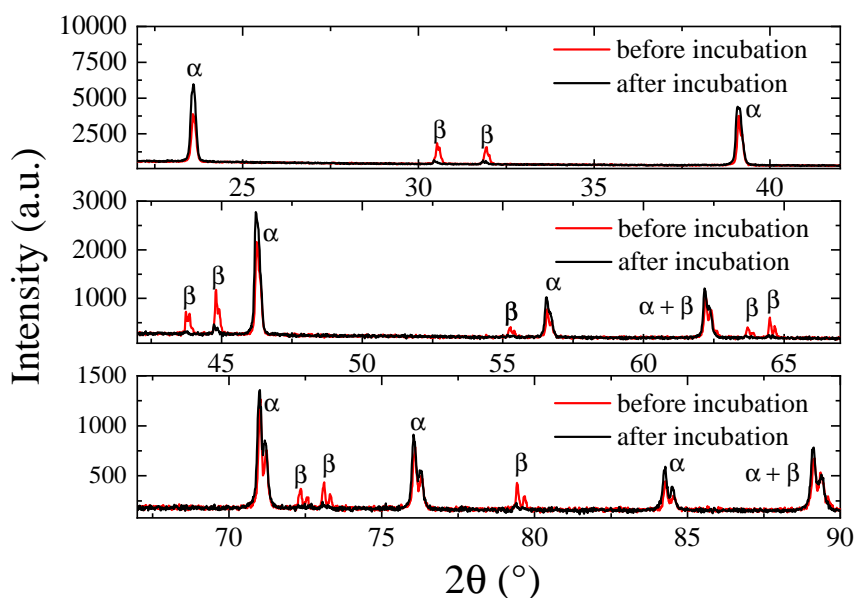
Figure 3.6: Powder x-ray diffraction patterns of the seed before and after incubating it at -20°C for 20 h.

The Sn-X alloys, described earlier in this section, were seeded and maintained at temper-

atures between -20°C to -25°C in order to induce the $\beta \rightarrow \alpha$ transition. As the transformation is characterized by a sudden volume expansion which leads to the fracturing of the sample, Scanning Electron Microscope (SEM) images were taken after the incubation period in order to observe the micro-fractures. The SEM images presented were acquired on the Zeiss Ultra plus scanning electron microscope. Alloy samples that showed signs of the transformation were considered unsuitable for *TIN.TIN*.

The details of the seeded cooling tests performed can be found in Table 3.4. The samples which showed resistance to tin pest were considered as candidates for cryogenic bolometers for *TIN.TIN* while those which were susceptible to tin pest were used to study the $\alpha \rightarrow \beta$ transition (measurements and results are described in Chapter 4). Sample sets also included pure Sn and/or Sn-Cu samples to ensure that the conditions were suitable for tin pest.

Set-1 refers to the first iteration of the cooling tests, in which rectangular pieces of the alloy samples were immersed in seed for a 5 day incubation period at -20°C. After this period, the samples were examined for micro-fractures and signs of its transformation to the α phase. It may be noted that, unlike the seed powder used for the subsequent sets, the seed powder used for Set-1 was not regenerated at -20°C and initially contained ~55 % α phase, as estimated from a powder x-ray diffraction pattern recorded just prior to the cooling tests performed on Set-1. However, as the concentration of the α-Sn phase in the seed also increases during the incubation period, the seed was automatically regenerated during the cooling test. The extent of the transformation can be observed. Figs. 3.7a-3.7d show the SEM images of the samples from the SEM images of the incubated samples. The Sn-Cu sample was heavily fragmented. Based on the degree of fragmentation, it was inferred that the Sn-Cd sample had transformed at a slower rate as compared to the Sn-Cu sample. However, both the alloy samples of Sn-Cu and Sn-Cd failed to inhibit the transformation and are unsuitable for *TIN.TIN*. In comparison, the Sn-Bi and Sn-Pb samples did not show any signs of micro-fractures even at higher magnification. The Sn-Pb and Sn-Bi samples were incubated for an additional 10 days during which it was observed that they continued to resist the formation of tin pest.

Table 3.4: Details of the cooling tests performed on the Sn-X samples. An approximate time limit for which the sample was observed to resist the formation of tin pest is listed (T_{max}) as per the last observation on 4th March 2021.

Alloy	Tag	%X (mass %)	Sample mass (mg)	% seeding	T_{max}
		SET 1 -	**Immersed in seed**		
Sn-Bi	S11	2.7	9.8	66.9	> 15 d
Sn-Cu	S12	0.5	10.9	65.1	< 5 d
Sn-Cd	S13	0.8	10.9	67.5	< 5 d
Sn-Pb	S14	5.0	9.2	68.2	> 15 d
		SET 2 -	**Rolled sample**		
Sn	S21	N/A	10.9	1.8	< 2 d
		SET 3 -	**~ 1 % seeding**		
Sn-Bi	S31	0.9	863.1	1.0	> 940 d
Sn-Cu	S32	0.5	506.3	1.0	< 1 d
Sn-Cd	S33	1.0	377.0	1.0	~ 11 d
Sn-Pb	S34	5.0	746.6	1.1	~ 70 d
Sn	S35	N/A	1115.0	0.9	< 1 d
		SET 4 -	**~ 4 - 5 % seeding**		
Sn-Bi	S41	0.5	73.1	4.4	> 911 d
Sn-Bi	S42	0.8	76.6	4.4	> 911 d
Sn-Pb	S43	1.2	157.9	4.6	~ 46 d
Sn-Pb	S44	0.6	206.8	4.4	> 46 d
Sn-Sb	S45	1.1	102.9	4.9	> 911 d
Sn	S46	N/A	71.8	5.2	< 4 d
		SET 5 -	**Lower concentration Sn-Bi**		
Sn-Bi	S51	0.22	716.2	1.0 [a]	> 370 d
Sn-Bi	S52	0.08	1043.5	1.0	~ 66 d

[a]increased to 4.4% after 143 d

From Set-2 onwards, the seed powder had been stored at -20°C for at least 10 days before using it for seeding in order to ensure ~100% α-Sn phase composition. Further, the amount

of seed used in the cooling tests was reduced so that, in the event of the transformation of the sample, the transformed sample would be useful for the subsequent differential scanning calorimetry (DSC) and synchrotron XRD studies [5], unlike the transformed samples of Set-1 in which the seed overwhelmed the sample.
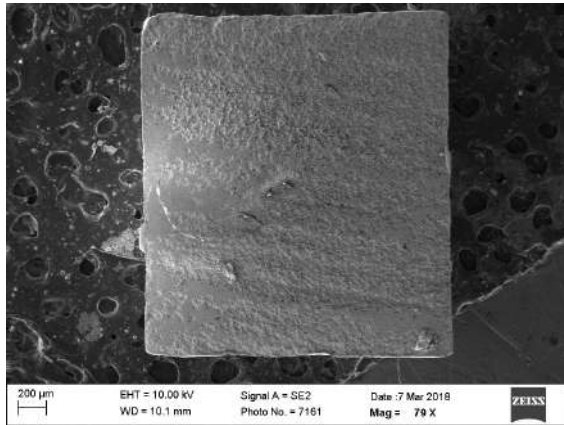
(a) Sn-Bi sample (S11)
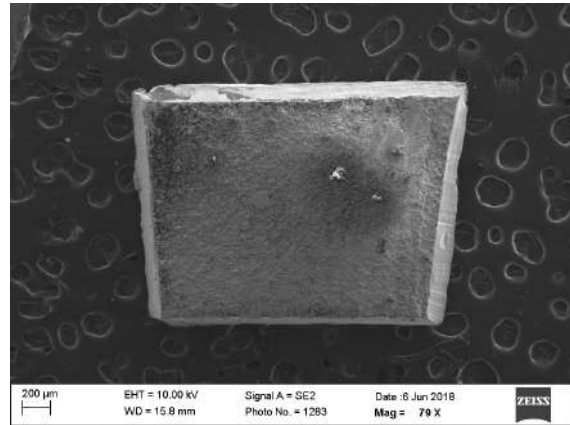
(b) Sn-Pb sample (S14)
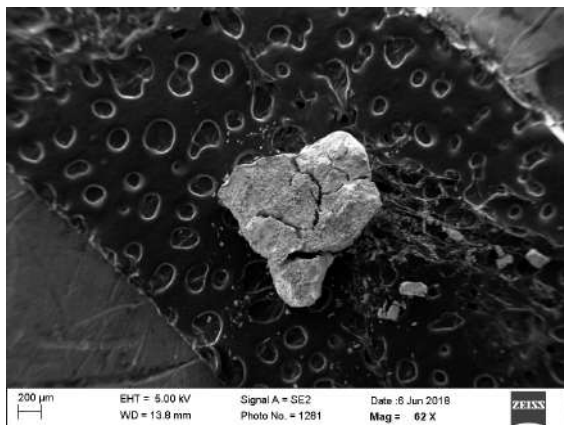
(c) Sn-Cd sample (S13)
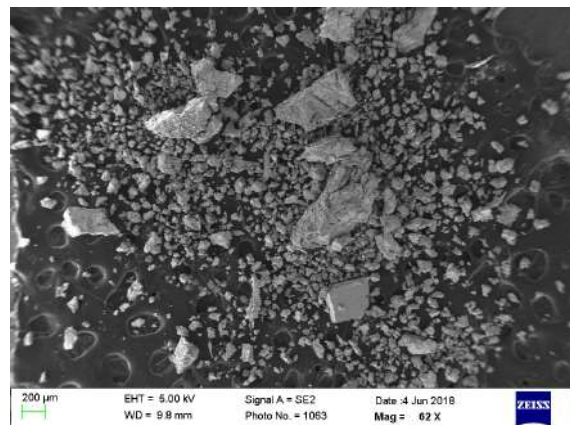
(d) Sn-Cu sample (S12)

Figure 3.7: SEM images of the samples from Set-1 after incubating with the seed at -20°C for a period of 5 days. The Sn-Cd sample clearly showed micro-fractures (a sign of the transformation) and the Sn-Cu sample was heavily fragmented. The Sn-Bi and Sn-Pb samples did not show signs of transformation even at a higher magnification.

Set-2 consisted of a Sn sample (S21) prepared for the purpose of the DSC study. The sample was rolled into a thin foil which was punctured at various locations and these holes were filled with seed. The Sn sample was completely fragmented by the second day.

Set-3 consisted of larger pieces of samples of similar concentrations to those used in Set-1. Redundancy between Sets 1 and 3 was useful to check reproducibility. Set-3 was kept at -20°C for a period of 31 days during which the Sn-Bi and Sn-Pb alloys showed resistance

---

[5]These measurements will be described in detail in Chapter 4.

against tin pest while the Sn-Cu and Sn-Cd alloys underwent the allotropic transformation, as seen in Set-1. The control Sn sample was susceptible to tin pest, as expected. It was observed that nucleation and growth of the α phase was much slower in the case of the Sn-Cd sample, which first started showing signs of transformation (bumps and warts) only on the 11th day, during its incubation. After 31 days, the samples were shifted to a commercial freezer due to a paucity of space in the deep freezer, to make room for lower concentration samples. The Sn-Pb sample (S34) started showing signs of the transformation 39 days after being shifted to the commercial freezer while the Sn-Bi sample (S31) remained unaffected. The samples were then shifted back to a deep freezer maintained at -25°C after a period of 510 days in the commercial freezer. The Sn-Bi sample (S31) showed no signs of tin pest even after an additional period of 399 days in the deep freezer maintained at -25°C. The cumulative time for which the sample has resisted tin pest is 940 days.

Set-4 consisted of samples of Sn-Pb and Sn-Bi with lower concentrations of the alloying element. From radiopurity considerations, it is relevant that the concentrations of Pb and Bi in these alloys be minimized, without affecting its ability to hinder the formation of tin pest. Additionally, the possibility of using Sn-Sb as an alloying candidate was also explored. All the samples (except the control sample Sn) showed resistance against tin pest up to a period of 27 days of incubation at -20°C. After ~150 days, it was observed that both the Sn-Pb samples (S43 and S44) were affected by tin pest while the Sn-Bi (S41 and S42) and Sn-Sb (S45) samples continued to show resistance against the formation of tin pest. Refer to Figs. 3.8a and 3.8b for optical microscope images of the microfractures and other signs of transformation observed on the Sn-Bi samples. The Sn-Bi (S41 and S42) and Sn-Sb (S45) samples have not shown signs of tin pest formation even after a prolonged exposure of 911 days. It was inferred that the Sn-Pb alloy may be susceptible to tin pest formation when maintained at low temperatures over extremely long periods of time.

Set-5 consisted of Sn-Bi samples with concentrations which are even lower than those in Set-4. The sample S52 (0.08% Sn-Bi) showed signs of tin pest after ~66 d. However, it should be noted that the growth of the α phase is extremely slow in this sample even after showing initial signs of tin pest. The sample S51 (0.22% Sn-Bi) is yet to show any signs of tin pest (as of March 2021). In fact, the seeding was increased from 1.0% to 4.4% after

143 d, to allow for more nucleation sites for the transformation. The sample has resisted tin pest formation for 370 days. The present studies show that the Sn-Bi alloy can be considered as a candidate for the *TIN.TIN* experiment since it showed resistance against tin pest even at an alloying concentration of 0.22% by weight. The observed trend in the present study is consistent with the study reported in [116].
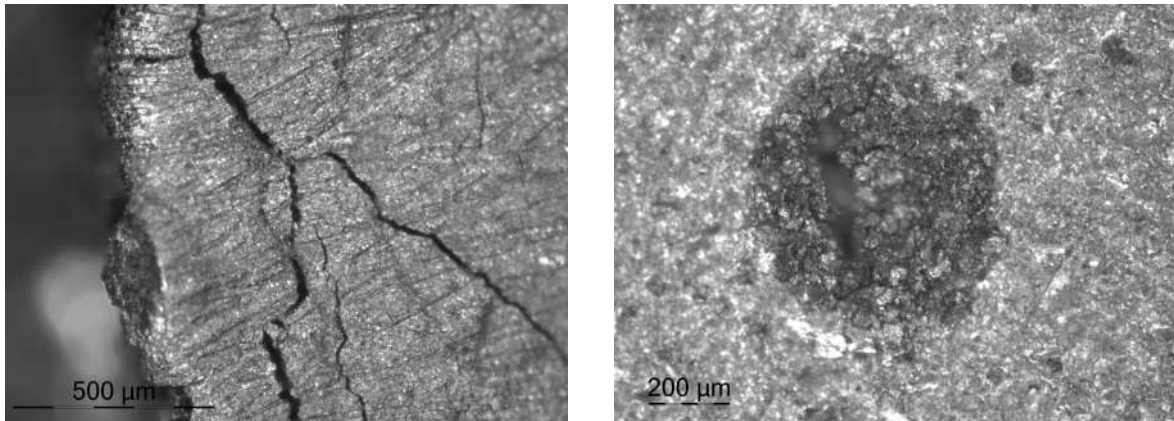
| (a) Microfracture on the Sn-Pb sample (S34) | (b) Tin pest wart on the Sn-Pb sample (S43) |

Figure 3.8: Optical images of the Sn-Pb samples showing signs of transformation.

Note that the cooling tests for Sn-In and Sn-Sb were not pursued as rigorously as the tests for Sn-Pb and Sb-Bi, although the crystal growth of these samples was initially motivated by good solid solubility of In and Sb in Sn. Due to the high thermal neutron cross-sections of In and Sb, Sn-In and Sn-Sb were found to be unsuitable for *TIN.TIN* early in the study, on the basis of the anticipated neutron induced backgrounds (refer to the Appendix Section A.2). Therefore, the growth and testing of these alloys were given a lesser priority. Nevertheless, the broad observations made from the cooling tests performed for these alloys are summarized below:

- Cooling tests of 0.6 % Sn-In and 0.5% Sn-Sb have shown that these alloys are also resistant to tin pest. In seeded cooling tests at -25°C, these samples have resisted tin pest formation for 374 days.

- During initial cooling tests performed in the CFDR-1200 (see Appendix Section A.1), 0.1% Sn-In was tested. The sample showed signs of tin pest after 3 cooling and warming cycles (which is roughly equivalent to 3 - 4 days of exposure time in conditions suitable for the growth of tin pest). Therefore, it can be inferred that 0.1% Sn-In (In by mass %)

suppresses tin pest in comparison to pure tin, but does not inhibit it. However, when comparing the performance of 0.08% Sn-Bi (see sample S52 in Table 3.4) and 0.1% Sn-In, it is clear that the Sn-Bi performs better than Sn-In in terms of suppressing tin pest.

3.4 Superconductivity measurements

As described in Chapter 1, it is necessary that the total heat capacity of the bolometer is minimized for good performance of the detector. This imposes certain restrictions on the material used as the absorber crystal of the bolometer. Generally, insulators or superconductors are preferred due to their low specific heat capacity at mK temperatures.

The specific heat capacity of a non-magnetic solid is given by

$$C(T) = C_e(T) + C_l(T) \tag{3.1}$$

where C_e is the electronic specific heat and C_l is the lattice specific heat. The lattice specific heat is given by

$$\begin{aligned} C_l(T) &= \beta T^3 \\ &= \frac{12\pi^4}{5} N_A k_B \left(\frac{T}{\theta_D}\right)^3 \end{aligned} \tag{3.2}$$

where T is the temperature and θ_D is the Debye temperature. The electronic specific heat of a metal in the normal state is given by

$$C_e(T) = \gamma T \tag{3.3}$$

where the Sommerfeld constant $\gamma = \frac{\pi^2}{2} N_A k_B \frac{T}{T_F}$. In normal metals, the electronic specific heat dominates at lower temperatures ($T << \theta_D$). Therefore, insulators or superconductors are preferred as candidates for bolometer absorbers since free electrons are absent in these materials at low temperatures. When superconductors are cooled below their superconducting critical temperature T_c, pairs of electrons form bound systems known as Cooper pairs which contribute to electrical conductivity but do not contribute to thermal conductivity. The electronic specific heat of a superconductor at $T << T_c$ is given by

$$C_e(T) = 9.17\gamma T_c e^{\frac{-1.5 T_c}{T}} \tag{3.4}$$

Thus, the electronic specific heat falls of exponentially and the solid behaves like a Debye solid ($C \propto T^3$). The parameter T_c is important since the exponent depends on it. In the case of *TIN.TIN*, it is important that for the candidate alloy, the T_c should not be significantly depressed compared to pure tin, i.e., $T_c \gtrsim 3.7\ K$. As Sn-Bi was found to be the most suitable candidate for *TIN.TIN*, the superconductivity of the Sn-Bi samples (0.08% - 1.69% Bi by mass %) was studied using DC magnetization measurements.

3.4.1 Working principle of a SQUID magnetometer

SQUID [6] magnetometers are capable of detecting extremely small magnetic moments (typically down to 10^{-7} emu). The magnetometer consists of a second order gradiometer pick up coil system which is coupled to a DC SQUID. The second order gradiometer configuration consist of the central loops winding counterclockwise and the outer loops winding clockwise. This configuration cancels out the noise which would otherwise arise due to small fluctuations of the externally applied magnetic field. The sample can be moved along the axis of the magnet using a stepper motor. During the measurements, it is scanned through a section of the pick up coil (generally 2 - 6 cm), inducing a current in the pickup coil. The total flux in the pickup coils is quantized since they are superconducting. The impedance of the SQUID (which consists of two Josephson junctions) is a periodic function of the flux passing through it, and it behaves as a sensitive current to voltage transducer. Therefore, the variations of the induced current which are proportional to the magnetic moment of the sample are measured. The response of the detector is recorded at each point of the scan length and a regression fit is performed. The analysis software assumes a point-like magnetic dipole behaviour for the sample to extract the magnetic moment of the sample from fit. For this assumption to be valid, certain constraints must be imposed on the size of the sample. A good practice is to not exceed ~4 mm in the direction of the magnetic field.

---

[6]Superconducting quantum interference device

71

3.4.2 DC Magnetization measurements of the Sn-Bi samples

The DC magnetization measurements of the samples were performed using a commercial Quantum Design MPMS [7]. This system can cool down to 1.8 K and is capable of sustaining large magnetic fields upto 7 T. The remnant field of the system was characterized from the M-H data of a strong paramagnetic standard (Pd), and was found to be 15 gauss. The applied magnetic fields are corrected for this remnant field.
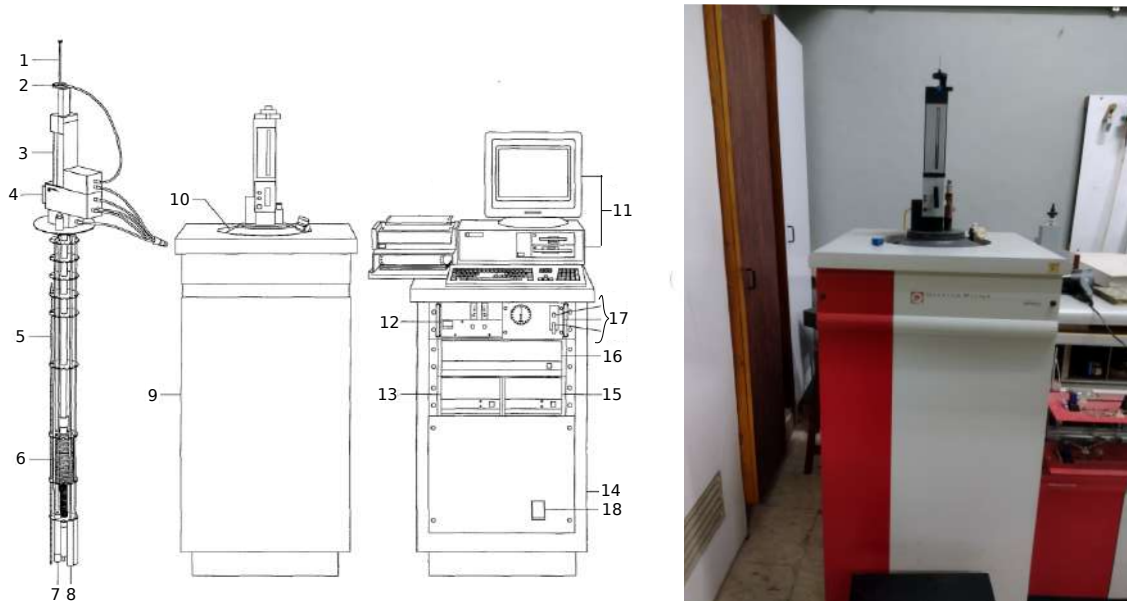
Figure 3.9: (left) The labelled schematic of the Quantum Design MPMS, taken from the manual (right) Quantum Design MPMS at TIFR. The labels in the schematic correspond to the following: (1) Sample rod (2) Sample rotator (3) Sample Transport (4) Probe (5) He level sensor (6) Superconducting solenoid (7) Flow impedance (8) SQUID Capsule (9) Dewar Cabinet (10) Dewar (11) DAQ PC (12) Magnet Power Supply (13) Digital Bridge (14) Console Cabinet (15) Power Distribution Unit (16) MPMS Controller (17) Gas/Magnet Control Unit (18) Vacuum Pump.

Superconductivity measurements were performed for Sn and Sn-Bi samples (0.08% - 1.69% Bi by mass %). The samples were cut using an electric discharge machine wire cutter, and all the dimensions were less than 4 mm. The typical mass of the samples used ranged from 10 - 50 mg. For a reliable measurement, it is important that no magnetic impurities are introduced at any stage. The samples were cleaned in acetone before use. Since the critical field $B_c(0)$ of pure tin is ~300 gauss, the applied magnetic field needs to be << 300 gauss. In order to decide the applied magnetic field which would be used, the magnetic moment of

---

[7]Magnetic Property Measurement System

pure tin was measured as a function of temperature at the applied magnetic fields of 10 and 50 gauss. The signal was clean at both magnetic fields, and the transition to the diamagnetic Meissner state was clearly observed even at the data acquired for 10 gauss. However, the T_C of pure tin was depressed to 3.56 K from 3.71 K when 50 gauss was applied. Therefore, an external magnetic field of 10 gauss was chosen for the subsequent measurements.
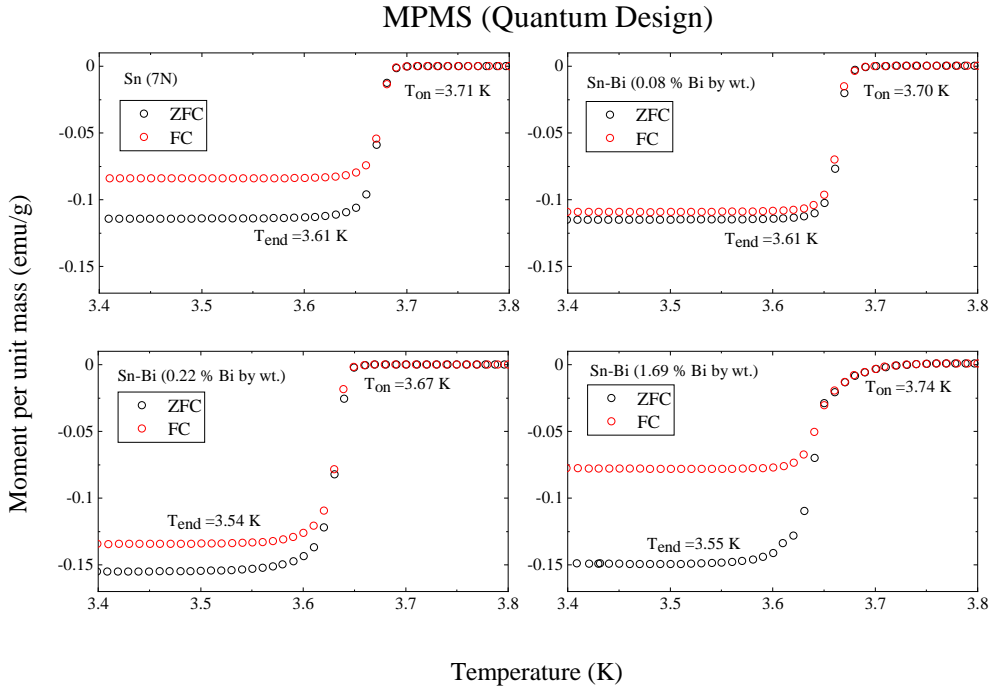
Figure 3.10: DC magnetization data of the samples under Zero Field Cooled (ZFC) and Field Cooled (FC) conditions.

The samples were mounted tightly in plastic drinking straws, which are then coupled at the end of the sample rod. The magnetic moment of drinking straws is negligible, and therefore they are preferred for sample mounting since they do not contribute to the background during measurements. The sample rod was pumped and purged with He gas before insertion into the vacuum space. The sample was cooled down to 2 K and centred in the pickup coil (scan length was 4 cm). The Zero Field Cooled (ZFC) and Field Cooled (FC) data were both acquired after ensuring that the sample is appropriately centred. The warming data from 3.4 to 3.8 K was acquired in steps of 0.01 K, and the temperature was stabilized at each point using a PID controller.

Fig. 3.10 shows the magnetic moment of the samples as a function of the temperature and Table 3.5 lists the extracted superconducting critical temperatures.

Table 3.5: The extracted superconducting critical temperatures T_c for the Sn-Bi samples.

Bi % (mass %)	T_c (K)
0	3.71 ± 0.01
0.08	3.70 ± 0.01
0.22	3.67 ± 0.01
1.69	3.74 ± 0.01

The alloys were found to be superconducting at a critical temperature within 2% of that of pure Sn. The transition width of pure tin was found to be ~0.1 K and that of the alloy samples varied between ~0.1 - 0.2 K. The superconductivity for a few samples was also tested using heat capacity measurements and SQUID vibrating sample magnetometry. The robustness of the observed superconducting transition implies that Sn-Bi alloys are suitable for use in superconducting bolometers.

3.5 Summary

The stability of various Sn-X alloys (X=Bi, Cd, Cu, In, Pb and Sb) against the formation of tin pest was studied by means of seeded cooling tests. From the observations, the alloys (X=Bi, Cd, Cu, Pb) can be arranged as follows in the increasing order of ability to retard the $\beta \rightarrow \alpha$ transition: Sn-Cu (worst), Sn-Cd, Sn-Pb and Sn-Bi. At the level of ~0.5 - 0.6% alloying by mass, Sn-Bi, Sn-In and Sn-Sb seem to effectively inhibit tin pest. However, Sn-In and Sn-Sb are not suitable as candidates for the *TIN.TIN* bolometer due to the anticipated neutron induced reaction channels which would contribute to the background. Moreover, 0.1% Sn-In is susceptible to tin pest, only weakly retarding it in comparison to pure Sn. The 0.08% Sn-Bi sample performed better than 0.1% Sn-In. For these reasons, Sn-Bi is the most suitable candidate for fabricating the *TIN.TIN* bolometer. The lowest concentration of Sn-Bi which was effective in inhibiting tin pest was found to be 0.22% Sn-Bi. The Sn-Bi alloy sample has resisted the formation of tin pest for 370 days in seeded cooling tests performed at -25°C .

DC magnetization measurements were performed on a SQUID magnetometer to check

the superconductivity of the Sn-Bi alloys (0.08% -1.69%). The shift in the T_c of the alloys in comparison to that of pure Sn was found to be < 2%. The superconductivity for a few samples was also tested using heat capacity measurements and SQUID vibrating sample magnetometry. The robustness of the observed superconducting transition implies that Sn-Bi alloys are suitable for use in superconducting bolometers.

Chapter 4

Improved measurements of the transition temperature of the structural phase transition in tin

4.1 Introduction

Despite scientific studies dating back over a hundred years, the transformation between the metallic (β) and semi-conducting (α) allotropes of tin is still not well understood. In this regard, it should be noted that the phase transition temperature stated in the literature, +13.2°C (i.e., 286.2 K), seems to be inconsistent with recent calorimetric measurements. While there are inconsistencies among the differential scanning calorimetry (DSC) measurements, all of them indicate a higher $\alpha \rightleftharpoons \beta$ Sn phase transition temperature as compared to +13.2°C. The peak temperatures of the $\alpha \rightarrow \beta$ Sn phase transition reported by various DSC measurements are summarized in Table 4.1. Note that this table excludes the DSC measurement presented later in this chapter.

A higher transition temperature would also be consistent with the empirical observations

Table 4.1: The peak temperatures of the $\alpha \rightarrow \beta$ Sn transition measured by various differential scanning calorimetry (DSC) experiments.

Reference	Peak temperature
Zuo *et. al.* [16]	+28°C
Ojima *et. al.* [14]	~ +35 to +40°C
Zeng *et. al.* [17]	+42 to +47°C
Gialanella *et. al.* [15]	+65°C

made at TIFR regarding the stability of the α-Sn at 'room temperature', which is maintained ~ 23°C due to the central air conditioning. This can be inferred from Fig. 4.1, which shows the powder x-ray diffraction data of the seed powder maintained at room temperature over a period of 18 days. As can be observed from the XRD data, the peaks belonging to the α-Sn phase do not disappear over the observation period, implying that the α-Sn phase is stable, despite an ambient temperature well above +13.2°C. It may be noted that the sample was stored in the XRD lab between measurements to minimize the handling time. Care was also taken to avoid proximity of the temperature sensitive sample to sources of radiative heat (compressors, CPUs, etc.) during the storage. The measurements were performed on a Malvern PANalytical x-ray diffractometer using Cu K_α x-ray (a Ni filter was installed).
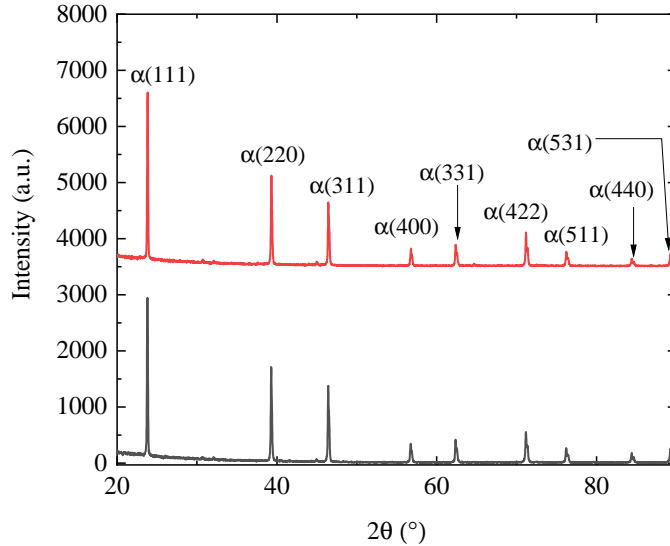
Figure 4.1: Powder x-ray diffraction data of the seed powder. The red and black lines correspond to day 2 and day 18 of storage of the sample at room temperature. The peaks corresponding to the α-Sn phase have been labelled.

The reported value of the thermodynamic transition temperature in the literature is based

on very old dilatometric measurements [18]. In this chapter, measurements of the transition temperature of the structural phase transition in Sn using modern materials characterization techniques (differential scanning calorimetry and temperature resolved synchrotron x-ray diffraction) are described. The $\alpha \rightarrow \beta$ transition was also studied in the Sn-Cu alloy in order to explore the effect of the alloying element (Cu) for the first time. The Sn-Cu sample was chosen as it showed signs of transformation over a relatively short period of time. The choice of Sn-Cu also has a technological significance as it is commonly used as a lead-free solder. Additionally, the $\alpha \rightleftharpoons \beta$ Sn transition was recorded using in-situ heating/cooling experiments in a scanning electron microscope. Based on these measurements, a protocol has been suggested to reduce the formation of α-Sn in potentially susceptible systems. This will be useful in experiments like *TIN.TIN*, and in critical systems using lead-free electronics that often operate for prolonged periods in extreme conditions (such as satellite, military systems, etc.).

Since the static lattice energy difference between α-Sn and β-Sn is estimated to be only $\sim$ 10 - 40 meV/atom, density functional theory (DFT) calculations for this transition are challenging. This calculation has been rigorously pursued and several works exist in the literature [123, 124, 125]. It is very interesting to note that the reported thermodynamic transition temperature of +13.2°C does not arise naturally from the DFT calculations. In fact, in studies such as [126] the temperature +13.2°C is often taken as an input to the calculations to impose a matching of the free energies at that temperature by design. In the studies where the transition temperature is not a fixed parameter and is instead calculated, the typical values obtained are neither consistent with the dilatometric experiments nor the calorimetric measurements. A notable exception is the calculated transition temperature of $\sim$ +38°C by Pavone *et. al.* [125], which is similar to the DSC measurements by Ojima *et. al.* [14], Mazumdar *et. al.* [6] (results presented in this chapter) and Zeng *et. al.* [17]. It has been recently pointed out that this phase transition provides a sensitive test of the accuracy of density functionals and computational methods [119]. Therefore, a precision measurement of $\alpha \rightleftharpoons \beta$ transition in tin is highly important.

The chapter is organized as follows: Section 4.2 presents the DSC measurements, Section 4.3 describes the temperature resolved in-situ SEM studies and Section 4.4 presents the

synchrotron studies. Finally, the chapter is summarized in Section 4.5. Note that for the purposes of consistency, the centigrade scale will be used though the text. Wherever possible, the equivalent absolute scale temperature is provided within parenthesis for quick reference. The labelling of a few images remain in the absolute scale, as was provided for the publication [6].

4.2 Differential scanning calorimetry

Differential scanning calorimetry (DSC) [127] is an established technique to study thermal transitions in materials. There are two types of differential scanning calorimeters: (1) power compensated DSC and (2) heat flux DSC. In a power compensated DSC, the sample and reference crucibles are placed in individual furnaces and the differential power supplied to maintain them at the same temperature is recorded. On the other hand, in a heat flux DSC a common furnace is used to heat the sample and the reference crucible and the differential temperature is recorded. The recorded temperature difference is then further processed to calculate the DSC signal, which is the differential heat flow. As the pressure is constant during the measurement, for both types of DSC, the signal is directly related to the change in enthalpy.

As seen in Table 4.1, the transition temperature for the $\alpha \rightarrow \beta$ transition in Sn as reported in the studies by Zuo *et. al.* [16], Ojima *et. al.* [14], Zeng *et. al.* [17] and Gialanella *et. al.* [15] using DSC are inconsistent. The $\alpha \rightarrow \beta$ transition in Sn was independently studied using DSC to resolve this inconsistency. Further, to see the effect of an alloying element on the transition temperature, the $\alpha \rightarrow \beta$ transition in Sn-Cu was studied using DSC for the first time.

The results presented in this thesis were measured on a heat flux type differential scanning calorimeter (STA 449 F1 Jupiter, NETZSCH). The schematic of the heat flux type DSC cell can be seen in Fig 4.2.
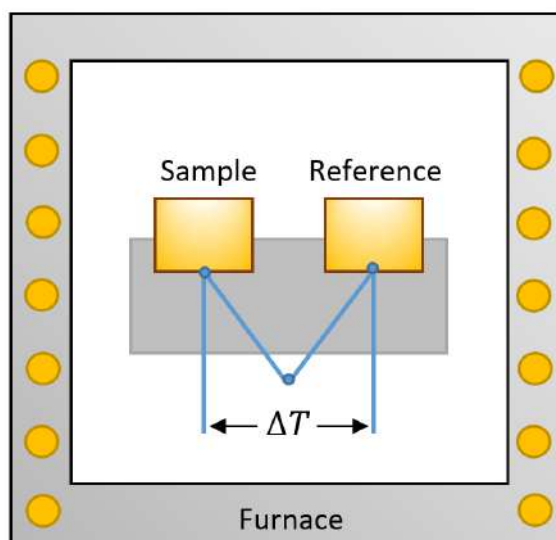
Figure 4.2: The schematic of a heat flux type DSC cell.

The cutaway schematic of the STA 449 F1 Jupiter and an enlarged schematic of its sample carrier can be seen in Fig. 4.3.
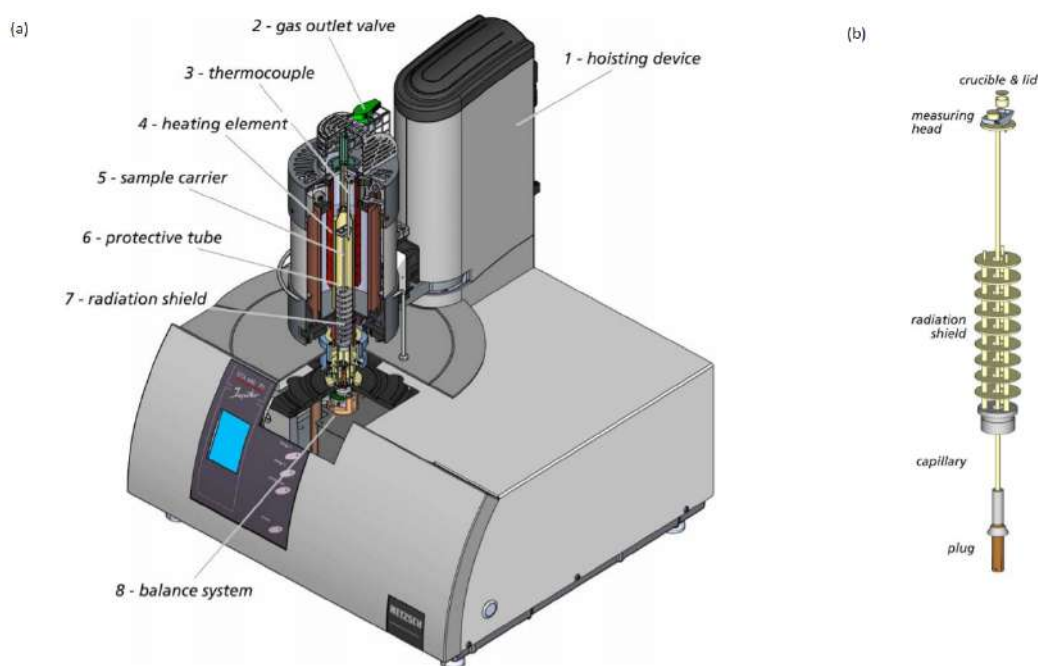
Figure 4.3: (a) Cutaway schematic of the STA 449 F1 Jupiter and (b) Sample carrier. The pictures have been taken from the manual.

Melting transitions of high purity metals were selected to calibrate the system over its entire working range, as these transitions are known to be sharp and accurate [128]. Table 4.2 lists the transitions used for the temperature and energy calibration. As alumina crucibles

do not react with mercury and gallium, it was possible to use these standards, which were relevant in the region of interest.

Table 4.2: Temperature and energy calibration points used for the DSC.

Standard	T_c (°C)	Transition Energy (J/g)
Mercury	-38.8	-11.4
Gallium	+29.8	-80.0
Indium	+156.6	-28.6
Tin	+231.9	-60.5
Bismuth	+271.4	-53.1
Zinc	+419.5	-107.5

The temperature ramping rate was kept at an optimal value of 2°C/min since it is known that the $\beta \rightarrow \alpha$ transition is slow. Further, the temperature ramping rate was kept constant throughout the calibration and sample runs. Helium was used as the inert purge gas since the system was operated in the low temperature DSC mode. The flow rate of the helium purge gas was set at a moderate value of 40 mL/min. Helium was also flowed as a protective purge gas at a lower value of 20 mL/min. Each calibration run consisted of three heating and two cooling cycles of the calibration sample used. The average values of the enthalpy and the onset temperature were considered for the purpose of the calibration. It should be noted that the energy and temperature calibrations are independent procedures, which do not affect each other.

In order to measure the $\alpha \rightarrow \beta$ transition temperatures in Sn and Sn-Cu, small pieces of the samples S21 (Sn) and S32 (Sn-Cu) synthesized in the α phase during the cooling tests were used for the DSC study. After the initial signs of tin pest were observed during incubation of the samples, these were further incubated for an additional period of 88 and 30 days, respectively, to ensure the maximal transformation to the α phase.

Prior to the measurement with the sample, the background signal was recorded for empty alumina crucibles and was used for background correction. An endothermic peak in the heating cycle corresponding to the $\alpha \rightarrow \beta$ transition was observed in both the samples.

Figs. 4.4a - 4.4b shows (smoothened) data of the endothermic peak observed in the heating cycles of the samples.

(a) Sn sample

(b) Sn-Cu sample
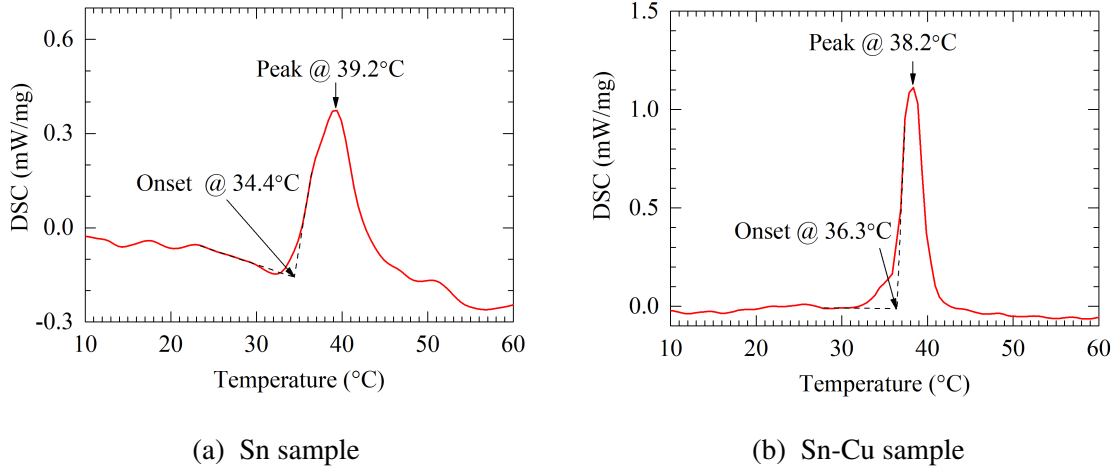
Figure 4.4: Endothermic peak in the heating cycle corresponding to the $\alpha \rightarrow \beta$ process in the samples (background corrected and smoothened data).

It should be noted that the cooling cycle did not show an exothermic peak corresponding to the reverse $\beta \rightarrow \alpha$ process. The absence of a signal in the cooling cycle despite the presence of a signal in the warming cycle is due to the fact that the mechanisms of the $\alpha \rightarrow \beta$ and $\beta \rightarrow \alpha$ processes are different and these processes are not reversible within the conditions of the present experiment. It has been shown (in Sn) that while the former is a 'military'-type diffusionless transformation the latter is a nucleation and growth process [118]. This nucleation can occur spontaneously or can be induced with an isomorphic external seeding agent such as α-Sn, InSb or CdTe. The time taken for spontaneous nucleation varies immensely and could take anywhere from a few hours to a few years. The rates for the two processes differ due to their different mechanisms, $\alpha \rightarrow \beta$ being easier to observe in the DSC measurement as it is faster. Moreover, if a suitable nucleant is absent, tin may remain in the metastable β-phase even after cooling past the transition temperature.

The cooling cycle was subsequently followed by a second heating cycle to confirm the absence of the formation of α-Sn during the cooling cycle. For both the samples, the absence of an endothermic peak in the second heating cycle is consistent with the absence of an exothermic $\beta \rightarrow \alpha$ process in the cooling cycle. Table 4.3 summarizes the characteristic temperatures of the $\alpha \rightarrow \beta$ transition extracted for the samples using the Proteus software

provided by Netzsch.

Table 4.3: Characteristic temperatures of the $\alpha \rightarrow \beta$ transition extracted from the endothermic peak observed in the first heating cycle of the samples.

Sample	Mass (mg)	Onset (°C)	Peak (°C)
Sn (S21)	10.9	+34.4	+39.2
Sn-Cu (S32)	12.7	+36.3	+38.2

The onset temperature is more robust as compared to the peak temperature and has been used to characterize the transition temperature. The peak temperature is also listed for the purpose of comparison with earlier measurements on Sn in literature.

As shown in Table 4.3, the transition temperature for the $\alpha \rightarrow \beta$ process in Sn was measured to be +34.4°C (onset temperature). As per the manufacturer's specifications, the thermocouple used (type E) is accurate to within 1.7°C. On comparing the peak temperatures available in the literature, the value measured in the present study is consistent with the observations by Ojima et. al. [14] but not with those by Zuo et. al. [16] and Gialanella et. al. [15]. With regard to Zeng et. al. [17], the observed temperatures are close, barely outside the allowed error bounds. The transition temperature measured for the $\alpha \rightarrow \beta$ process in Sn-Cu (0.5% Cu alloyed by weight) was +36.3°C. No prior measurement of the $\alpha \rightarrow \beta$ transition temperature in Sn-Cu was found in the literature. Within errors (i.e.±1.7°C), the transition temperatures of Sn and Sn-Cu are found to be similar. It may be noted that the transition width is much narrower in the case of Sn-Cu ($\sim$ 4.0°C) as compared to that of the Sn sample ($\sim$ 6.4°C), which may be indicative of a faster $\alpha \rightarrow \beta$ rate in Sn-Cu as compared to Sn.

4.3   Temperature resolved in-situ SEM studies

Imaging techniques such as in-situ SEM and in-situ electron backscatter diffraction (EBSD) have traditionally been powerful tools to study the microstructure and phase transformations in various systems [129, 130, 131, 132]. Since the volume change associated with the phase transition in tin is significant (27%), the transition can be studied by measuring the volume

change as the signal. Moreover, the observed signal is very clean and cannot be mimicked by a thermal artefact since the thermal behaviour is atypical, i.e., while matter is expected to expand on heating, the Sn sample would be expected to contract during the $\alpha \rightarrow \beta$ transition. It should be noted that the quoted value in the literature (i.e., +13.2 °C) is based on dilatometry experiments [18], in which the tin samples were placed in a fluid medium and the expansion/contraction of the sample was recorded by measuring the change in the height of the liquid meniscus. Since the volume change of the sample can be observed in in-situ temperature-resolved SEM images, this measurement is analogous to the dilatometric experiments. The main difference between the dilatometric experiments and in-situ SEM is that dilatometric experiments require the presence of an external fluid while the in-situ SEM is performed in vacuum.

The present in-situ temperature resolved SEM studies were performed on an EVO LS10 Zeiss scanning electron microscope, using a commercial DEBEN heating/cooling stage. The temperature fluctuations (after stabilization) were maintained within 0.5 °C through a built-in PID controller. The thermocouple, which was mounted on the sample stage, is expected to have been in good thermal contact with the sample due to the conducting nature of the intermediate components (sample stage, carbon tape and the sample itself).

The temperature resolved in-situ SEM images during the heating cycle can be found in Fig. 4.5(a). A close inspection reveals slight changes in the size of the sample at temperature T~ +35°C (308 K). Dramatic shrinkage in the volume of the sample, which is associated with the $\alpha \rightarrow \beta$ transition, was observed at a temperature T~ +40°C (313 K). This can be compared to the observations made during the DSC measurements, where it was observed that the transition shows an onset at +34.4°C and a peak temperature at +39.2°C. A real-time video recording from a different run can be found in the supplementary material of the publication [6]. It should be mentioned that this video is a mere visual indication and the transition temperature is extracted from the still images in the manuscript, which were recorded with proper temperature stabilization.

The $\beta \rightarrow \alpha$ transition could not be recorded in real time due to its slow transformation rate. Still images were recorded to monitor the changes in a tin sample maintained at -25°C over a period of ~ 27 h (see Fig 4.5(b)). The SEM images show an increase in volume, cracks

and micro-fractures, all of which are clear indicators of the $\beta \to \alpha$ transition.
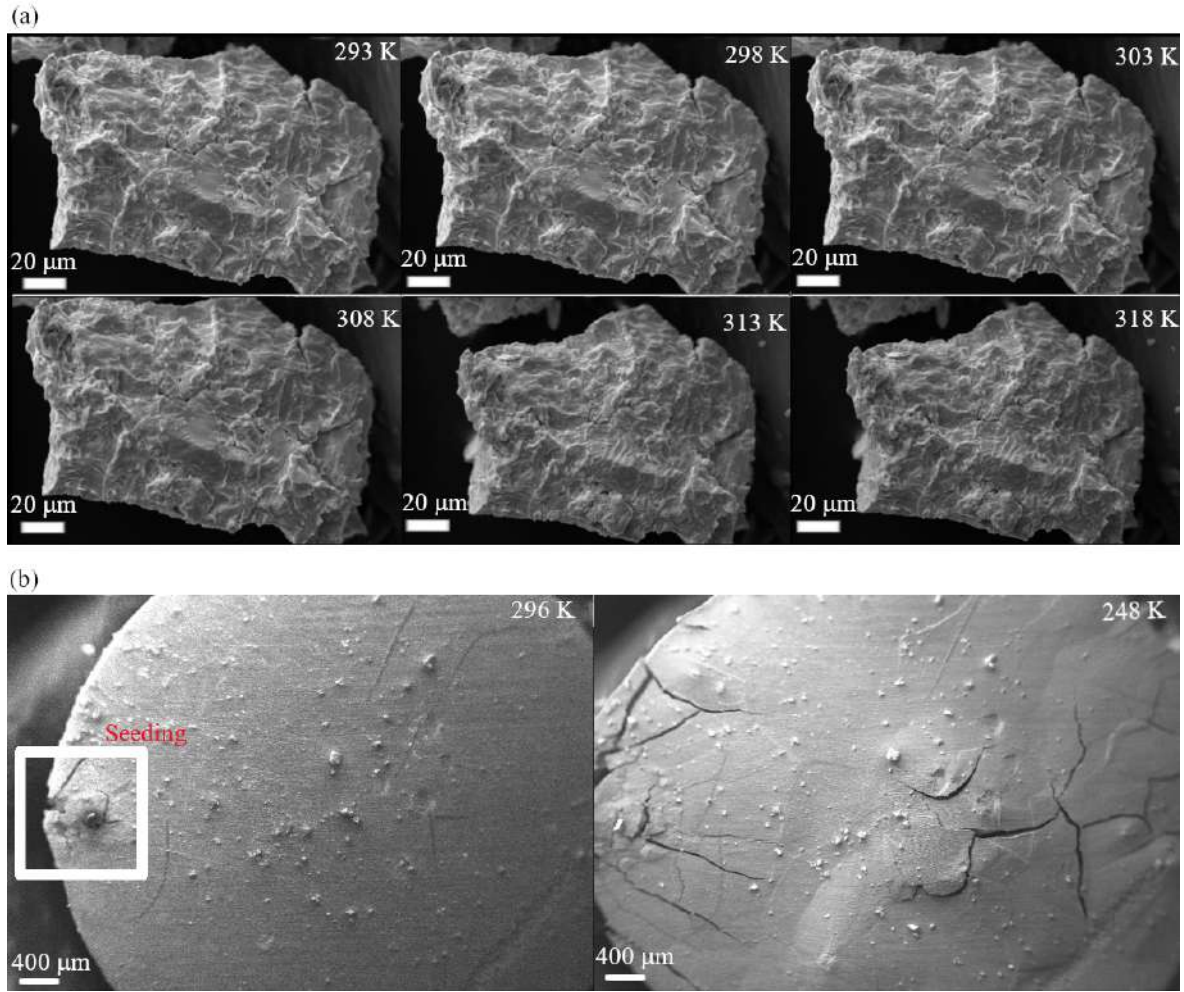
Figure 4.5: SEM images showing (a) tin sample undergoing the $\alpha \to \beta$ transition (b) seeded tin sample maintained at -25°C (248 K) for ~ 27 h undergoing $\beta \to \alpha$ transition.

Further imaging studies using in-situ EBSD may be interesting to explore, since the phase composition can be determined from the collected Kikuchi patterns. Thus, it may be possible to study the movement of the phase boundaries using this technique. However, the sample preparation would be challenging as good quality data generally requires polished samples, while the α-Sn samples are difficult to polish due to their low transition temperature.

4.4 Synchrotron x-ray diffraction studies

While some earlier works use x-ray diffraction (XRD) to study the kinetics of the transformation [17, 118], no studies on the phase transition temperature using this technique exist. Synchrotron x-ray sources are capable of producing very intense x-rays compared to conven-

tional sources of x-rays used in the lab, by accelerating charged particles (usually electrons) in magnetic fields. They are also highly tunable in terms of wavelength, as an appropriate wavelength is optically selected from the continuous spectrum of x-rays generated.

The synchrotron XRD measurements were performed at the angle dispersive XRD beamline of the Indus-2, which is a 2.5 GeV synchrotron radiation source at the national facility RRCAT Indore [8]. The x-ray beam was tuned to 0.83 Å using a Si(311) double crystal monochromator (DCM). The samples were mounted between kapton tapes and loaded in a 2-stage closed cycle refrigerator, which was developed in-house at RRCAT. The temperature was monitored using a PT100 RTD sensor mounted at the heating element and was controlled using the Lakeshore 331 PID controller. The temperature stability was typically around 0.02°C (for a 60 s exposure) in a step of 2°C. The error in the temperature was ~ ± 0.5°C, arising mainly from the accuracy and the position of the sensor. The diffraction data were recorded in the transmission mode using the MAR345 detector. It should be mentioned that spinning of the samples was not possible.
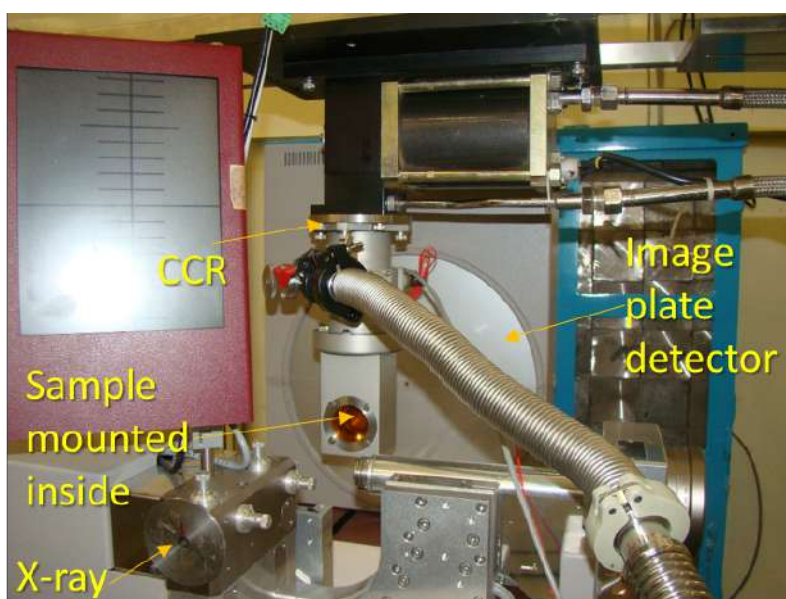
Figure 4.6: The MAR345 desktop beamline station located in ADXRD setup. The samples are cooled by the CCR (Closed Cycle Refrigerator), capable of operating from -243 to +177°C. The direction of the x-ray beam and the 345 mm image plate detector used to record the transmission mode XRD data have been marked.

The sample preparation has already been described earlier for the DSC measurements, and can be referred to in the earlier section. Grinding the samples for the XRD measurements

was infeasible, as this process inevitably caused a large fraction of the sample to reconvert to the β-phase. Instead, the natural disintegration caused by the transformation process from $\beta \rightarrow \alpha$ phase was relied upon for the formation of a granular powder.

For optimizing the use of the available machine time, the heating cycle data (0 to +70°C) were given priority and the cooling cycle data (+20 to -60°C) were recorded with a lower density of points. After recording the data at +70°C (343 K), the sample was cooled down to +20°C (293 K) and a final data was recorded after the heating cycle. This was done to check whether the transition reverses on cooling down from +70 to +20°C. Each run included data of the NIST sample LaB_6 in the same geometry, for calibration purposes. This data was used to refine the energy of the x-ray used as well as the distance of the sample to the detector. The calibration and conversion of the 2-D image plate diffractograms to 1-D 2θ scans were performed using FIT2D [133, 134]. The FIT2D interface is shown in Fig. 4.7. The 2-D image plate data for the Sn sample can be found in the Figs. 4.8 and 4.9. The image plate for the Sn-Cu sample is similar and is, hence, not shown.
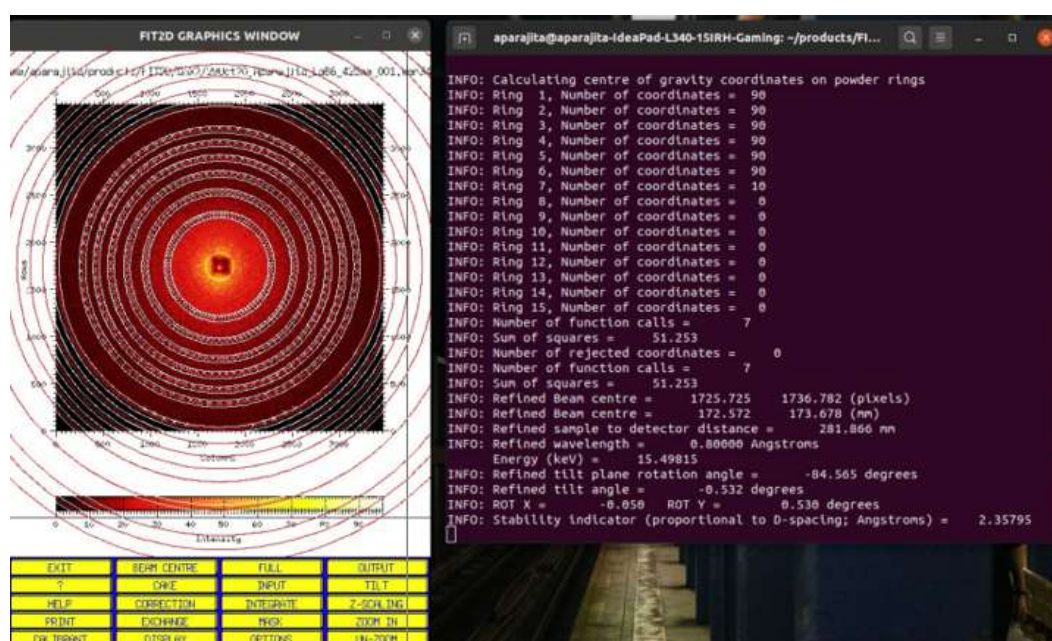
Figure 4.7: The FIT2D interface, showing the calibration using the standard sample LaB_6.

The disappearance (appearance) of the lines from the α-phase (β-phase) could be tracked in the heating cycle data. Conventional XRD measurements were also performed on a Rigaku SmartLab diffractometer with the SHT1500 heating stage. The heating attachment of the Rigaku diffractometer consists of a platinum sample holder which is surrounded by a furnace.
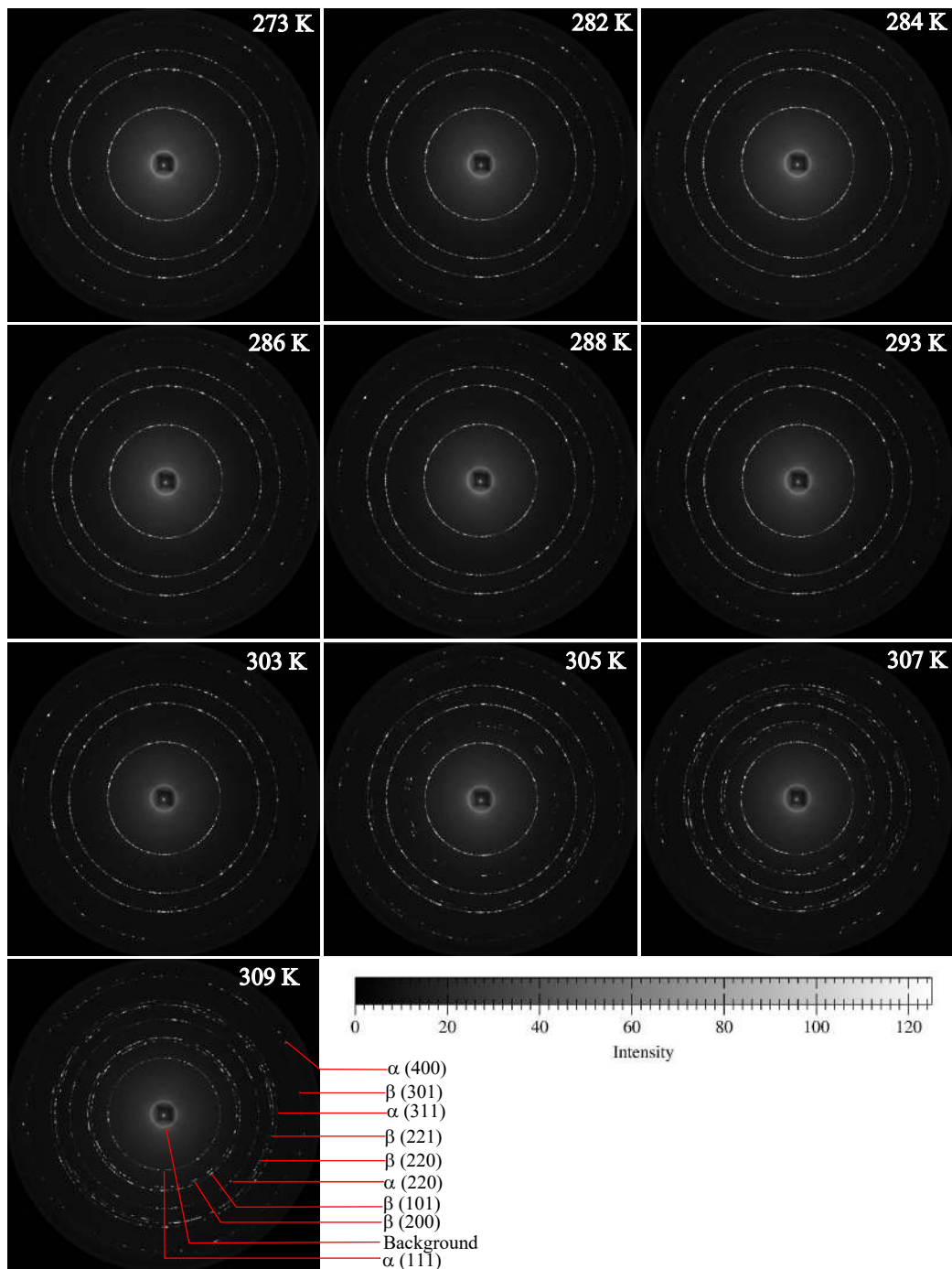
Figure 4.8: Image plate data recorded during the heating of the Sn sample from 0 to +36°C. The Debye-Scherrer rings from the β-phase start appearing $\sim$ +30°C (303 K) and become distinct at $\sim$ +34°C (307 K). The heating cycle data of the Sn sample is continued in the next figure.

This design is expected to provide more uniform heating in comparison to a conventional design in which a heating element is in contact with the sample stage. The thermocouple monitoring the sample temperature was in excellent thermal contact through the platinum sample holder. The temperature was controlled through a PID-temperature controller (PTC-
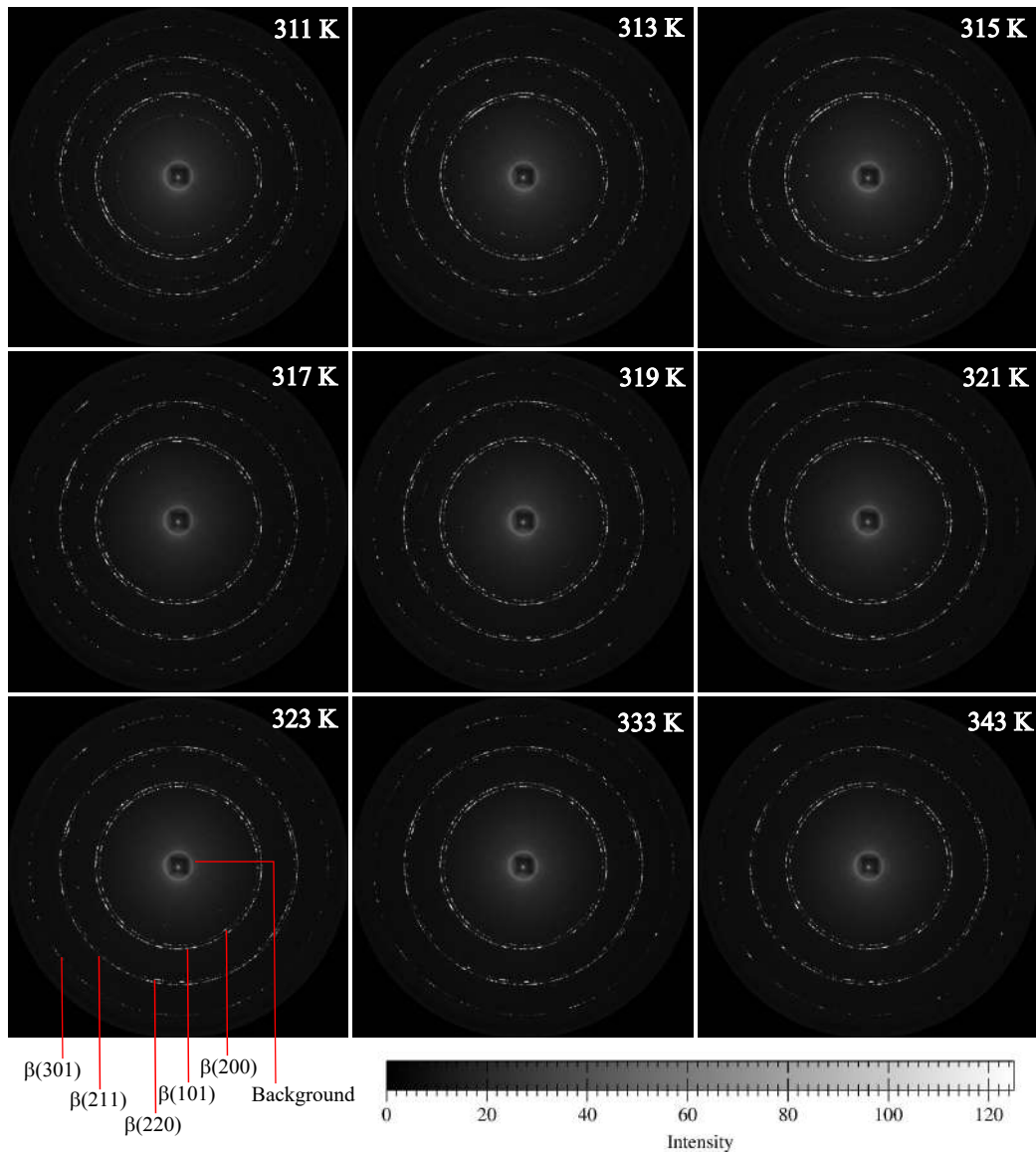
Figure 4.9: Image plate data recorded during the heating of the Sn sample from +36 to +70°C. The Debye-Scherrer rings from the α-phase reduce in intensity, disappearing above ~ +42°C (315 K).

EVO) and the data was taken after temperature stabilization. The temperature error for the reported data is within 0.5°C. Both (synchrotron and conventional) XRD data for the Sn sample are shown in Fig. 4.10. The synchrotron XRD data for the Sn-Cu sample are shown in Fig. 4.11.

Alloying with copper at the level of 0.5 % by weight does not affect the $\alpha \rightarrow \beta$ transition. In case of both the samples, the β-phase grows slowly from +30°C onwards. The peaks from the β-phase become distinct around +34°C. With increasing temperature, the peaks from the β-phase increase in intensity while those from the α-phase reduce in intensity. The samples

90

remain in a mixed $\alpha - \beta$ state upto $\sim +42°C$, above which the α-phase lines disappear.
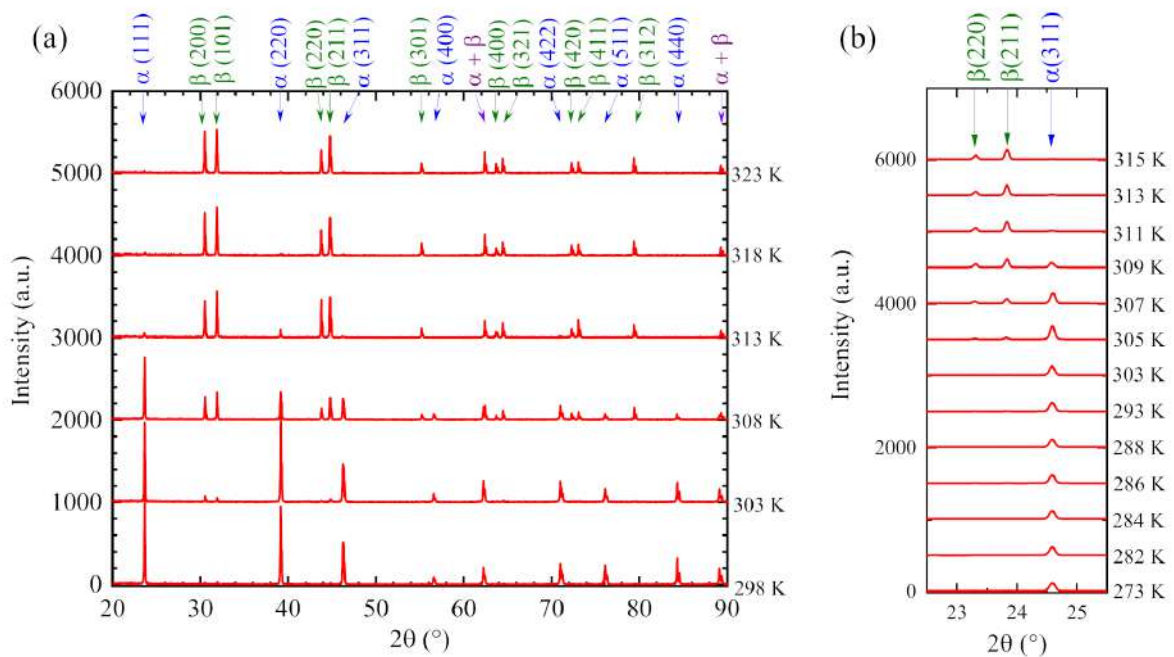
Figure 4.10: XRD data for the Sn sample showing the $\alpha \to \beta$ transition. The baseline of the data at different temperatures is shifted for visibility purposes (a) Conventional XRD acquired on Rigaku diffractometer using Cu-K$_\alpha$ x-ray (b) Synchrotron XRD acquired with $\lambda = 0.83$Å.
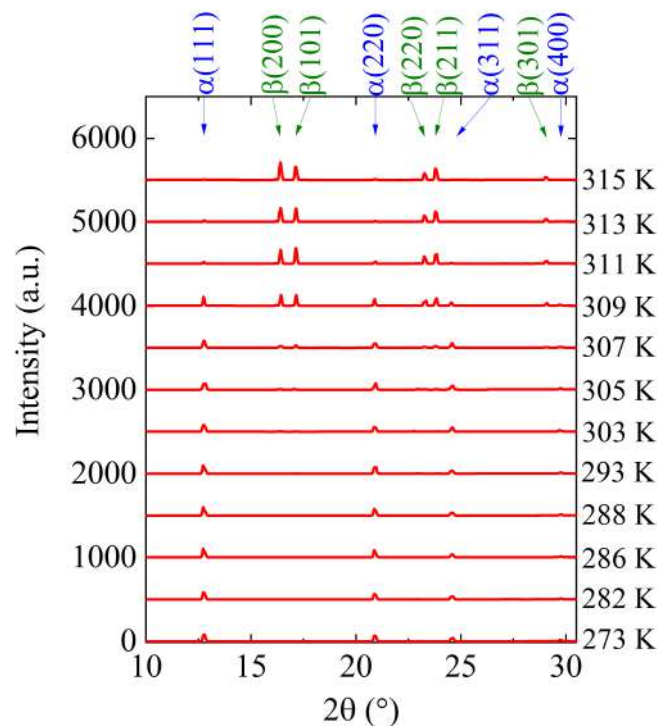
Figure 4.11: Synchrotron XRD data of the Sn-Cu sample showing the $\alpha \to \beta$ transition.

The transformation does not reverse on cooling from +70 to +20°C. The comparison

between the diffractograms of the Sn sample at +20°C before and after the heating cycle is shown in Fig. 4.12. In the DSC measurements, an onset phase transition temperature of +34.4°C for Sn and +36.3°C for 0.5 % Sn-Cu (weight %) was measured. This approximately corresponds to the temperature at which the diffraction peaks from the β-phase start becoming distinct. Thus, the observations from the XRD measurements are consistent with the DSC measurements.

Baking the *TIN.TIN* detector array at a higher temperature like +50°C for a few min (∼ 20 min) should be sufficient to destroy any α-Sn which may have formed during the thermal cycling. However, the risk of a subsequent spontaneous nucleation remains, which is much smaller compared to that of a seeded transformation. If this protocol is used in conjunction with alloying of Sn with Bi, the risk of tin pest should be negligible. This protocol will also be useful for critical circuits that will employ lead-free Sn-Cu solders and operate at low temperatures for long periods. Conversely, α-Sn samples should be stored below +30°C in studies where bulk α-Sn is the phase of interest.
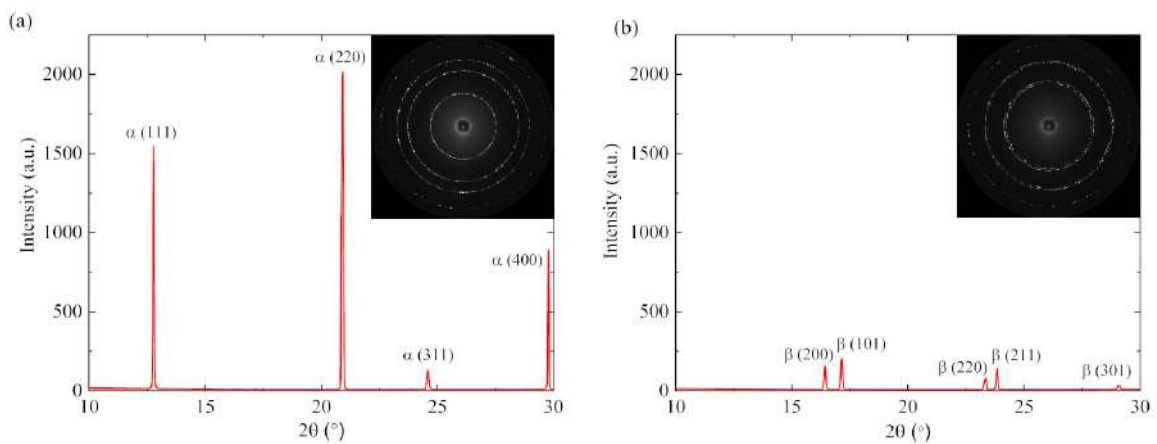
Figure 4.12: Synchrotron XRD data of the Sn sample at +20°C (a) Before heating from +20 to +70°C (b) After heating to +70°C, the sample was cooled down to +20°C. The reverse $\beta \rightarrow \alpha$ transition was not observed and the lines in (b) were identified to belong to the β-phase.

4.5 Summary

The commonly reported thermodynamic transition temperature of the $\alpha \rightleftharpoons \beta$ Sn phase transition is +13.2°C. This value is obtained from dilatometric experiments performed several decades prior. The inconsistency of recent calorimetric measurements and the remarkable

stability of the α-Sn phase at room temperature motivated a reinvestigation of the structural $\alpha \rightarrow \beta$ Sn phase transition temperature. Several modern techniques relying on different experimental signatures were used to measure the transition temperature, namely, differential scanning calorimetry, temperature resolved in-situ scanning electron microscopy and synchrotron x-ray diffraction. Sn-Cu (0.5% Cu by weight) was also studied due to its technological significance as a common lead-free solder.

The $\alpha \rightarrow \beta$ transition temperature in Sn is measured to be +34.4°C (onset). The peak temperature is measured to be 39.2°C which is consistent with the observations by Ojima *et. al.* [14], thereby resolving an observed inconsistency in earlier measurements. The transition temperature for the $\alpha \rightarrow \beta$ process in Sn-Cu (alloyed 0.5% by weight) is measured to be +36.3°C (onset). This is consistent, within errors, with the transition temperature of pure Sn.

The temperature resolved in-situ SEM measurements in Sn provide a unique, visual indication of the phase transition in Sn. The $\alpha \rightarrow \beta$ Sn phase transition temperature extracted from the images indicate an onset temperature around +35°C and a peak temperature around +40°C.

The temperature resolved XRD and synchrotron studies have revealed that the $\alpha \rightarrow \beta$ structural phase transition of Sn and Sn-Cu (0.5% Cu by weight) occurs between $\sim$ +30°C and $\sim$ +34°C. The synchrotron measurements are expected to be more sensitive compared to the other measurements, and the temperature region around $\sim$ +34°C is consistent with the temperature at which the DSC signal indicates an onset.

In summary, observations from conventional XRD, in-situ SEM and DSC measurements were consistent with the synchrotron XRD data. No strong temperature dependence of the transition temperature is observed with the alloying material (Cu). All the measurements indicate a phase transition temperature significantly higher than +13.2°C.

Based on these observations, it is expected that baking the *TIN.TIN* detector at $\sim$ +50°C between thermal cycles will significantly minimize the risk of tin pest. If used in conjunction with the alloying of Sn with Bi, it is unlikely that tin pest would affect the bolometer array. This protocol would also be useful in other critical systems that use lead-free solders and operate in extreme conditions.

Chapter 5

Radiation background studies for Sn-Bi bolometers

5.1 Introduction

The sensitivity of a $0\nu\beta\beta$ decay experiment is strongly limited by the background in the region of interest (ROI). For a background-free experiment, the sensitivity would scale linearly with the detector exposure Mt, as opposed to $\sqrt{Mt}$ in the presence of a finite background. Thus, there is a strong motivation for $0\nu\beta\beta$ experiments to improve the background index of the experiment. In this regard, the identification and modelling of the sources of radiation background is of paramount importance as it often leads to the formulation of new techniques for background suppression.

The major sources of background for $0\nu\beta\beta$ can be broadly summarized as below. A detailed review of the background sources can be found in a review paper by Heusser [135].

1. **Environmental radioactivity:** The radionuclides present in the environment arise from three sources – primordial, cosmogenic and anthropogenic.

- Primordial radionuclides ^{40}K, ^{232}Th and ^{238}U are long-lived, having half-lives in the range of $10^9 - 10^{10}$ y. The γ rays from these sources constitute the dominant source of environmental radioactivity. Neutrons are also generated due to spontaneous fission and (α,n) reactions in the rock.

- Cosmic rays, particularly cosmic muons, can contribute to the background directly or indirectly via the generation of secondary particles through muon induced reactions.

- Anthropogenic (man-made) radionuclides include sources such as ^{137}Cs and ^{90}Sr, which are released as a consequence of nuclear weapons testing or reactor accidents. After the infamous Chernobyl accident of 1986, increased activity due to the radioactive contamination from ^{137}Cs was found on the surfaces exposed to the plume. For such reasons, it is important to screen materials in a low background setup before use in a $0\nu\beta\beta$ experiment.

In order to attenuate the environmental background, various shielding techniques are used. The proposed site for INO will have a rock overburden of 1.2 km, which is expected to reduce the cosmic muon flux by around six orders of magnitude. High Z shielding (usually low activity lead) surrounds the detector, effectively attenuating the γ component of the environmental background. In contrast, it is more challenging to shield against neutrons, and thereby, neutron induced background.

2. **Internal radioactivity of the detector and the shielding material:**

- Internal radioactive contamination leads to an increase in the background. A common source of background arises from the trace impurities of ^{238}U and ^{232}Th.

- The tail events of the $2\nu\beta\beta$ decay continuum is an irreducible background arising internally within the bolometer.

- Depending on the cross sections for neutron induced reactions, the neutron activation of the detector and shielding material is important.

- Muon spallation reactions can lead to the continuous in-situ production of radioisotopes in the detector material. In high Z material such as lead, capture of μ^- can produce neutrons having energies upto $\sim 10\,\text{GeV}$, which can lead to neutron capture backgrounds after thermalization. It should be mentioned that in underground laboratories having an equivalent vertical depth greater than 1000 m.w.e, the flux of muon induced neutrons is suppressed in comparison to that of the neutrons from fission and (α,n).

The background arising from sources which are internal to the detector material constitutes an irreducible background for the experiment. These backgrounds are especially of concern in experiments employing detectors which are incapable of particle identification, such as the superconducting bolometers which will be used in *TIN.TIN*. Therefore, while the introduction of Bi into the Sn matrix stabilizes it against tin pest, it is important to critically assess and estimate the change in the background ROI. Another source of background which was explored was potential trace impurities which may be introduced during the crystal growth.

This chapter will outline the studies performed to identify and estimate internal background in Sn-Bi bolometers. The chapter is arranged as follows: Section 5.2 describes the radiopurity evaluation of the Sn-Bi crystals after synthesis by means of γ spectroscopic measurements in the TIFR low background experimental setup (TiLES), which is located ~ 10 m above sea level. Section 5.3 outlines the neutron activation studies of Sn-Bi performed at the Pelletron Linac Facility (PLF) at TIFR Mumbai. Sections 5.4 and 5.5 detail the GEANT4 simulations performed to evaluate the internal background anticipated from the rare α decay of ^{209}Bi and the α/β decays from the primordial decay chains of the ^{238}U and ^{232}Th present in the Sn-Bi bolometer. Section 5.6 outlines the projected sensitivity of the Sn-Bi bolometers for $0\nu\beta\beta$ signal. The chapter is summarized in Section 5.7.

5.2 The estimation of the radioimpurities in Sn-Bi alloys using TiLES

Although the stock used for the synthesis of the alloy samples has high purity (7N pure Sn and 5N pure Bi), it is important to ensure that the crystal growth process does not introduce any radioactive impurities. The intrinsic radiopurity of the alloy samples grown at TIFR were checked by γ spectroscopic measurements in the TIFR low background experimental setup (TiLES) [20]. TiLES is comprised of a shielded coaxial p-type HPGe detector (ORTEC
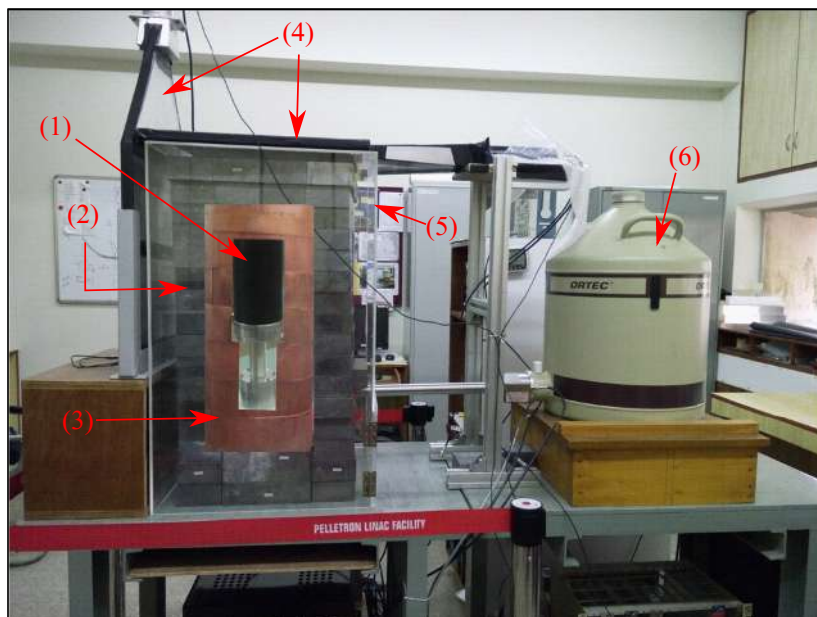
Figure 5.1: The TIFR low background experimental setup (TiLES). The annotations correspond to the following: (1) HPGe detector (2) Lead shielding (3) OFHC Cu shielding (4) Muon veto (5) Radon exclusion box and (6) Liquid nitrogen dewar with cold finger.

GEM75-95-LB-C-HJ), which has a carbon fibre outer body and is specially designed for low background measurements. The HPGe detector, operated at 4.0 kV, has a relative efficiency of ~70% and an active volume of ~230 cc. The detector is cooled using a 60 cm cold finger connected to a liquid nitrogen cryostat. The background suppression in TiLES is performed using a combination of several techniques:

1. The detector is passively shielded by a Cu + Pb graded shielding, which consists of an inner 5 cm layer of low activity OFHC Cu and an outer 10 cm layer of low activity Pb (^{210}Pb < 0.3 Bq/kg). The Pb shield attenuates γ-rays from the surroundings. The decay of ^{210}Pb impurity present in the Pb produces ^{210}Bi and ^{210}Po. The Cu shield reduces

the background from the bremsstrahlung radiation of ^{210}Bi and the x-rays produced in Pb.

2. The detector is actively shielded by a cosmic muon veto system. The veto system consists of four plastic scintillators (50 cm x 50 cm x 1 cm) placed at the top and three sides. The plastic scintillators are coupled to a PMT (Photonis XP2262/B) through a light guide. The operating voltage for the plastic scintillators is -1.8 kV.

3. The detector and the passive shielding is placed in a Radon exclusion box fabricated from perspex. This volume is continuously purged with dry N_2 gas, at an over-pressure of ~10 mbar. This suppresses the background from the gaseous radionuclide ^{222}Rn and its progenies.

TiLES is sensitive to radioactive contamination from ^{40}K and ^{232}Th at the level of 2 mBq/g (~60 ppm) and 1 mBq/g (~0.25 ppm), respectively [136, 137].

For the radiopurity measurements, each sample was counted in the TiLES set-up at a distance of ~1 cm from the face of the detector (see Fig 5.2). Energy spectra were acquired using a commercial 14-bit CAEN N6724 digitizer (100 MS/s). Anti-coincidence between the muon veto and the HPGe spectra was performed within a ±2.5 μs window in an offline analysis using a ROOT based code. The spectrum analysis was performed using LAMPS [138]. Dead time correction was performed using a 10 Hz pulser.

Figure 5.2: Pictures showing the typical sample mounting arrangement for samples in TiLES (close geometry).

In the first run, measurements were performed using the Sn-Bi sample which was synthesized with the largest concentration of Bi, i.e., 9.2% Bi by mass. In order to obtain a reference spectrum, data was acquired for Sn as well as the ambient background. Table 5.1 gives the details of the spectroscopic measurements (run 1). The measurement times were optimized as per the availability of the setup, with more time being allocated for samples having lower concentration of Bi (see run 2).

Table 5.1: Details of the measurements on TiLES (run 1).

Sample	Mass (g)	Runtime (days)
background (bkg)	-	4.8
Sn (crystal)	21.3	2.9
Sn-Bi (9.2% Bi by mass)	4.0	4.9
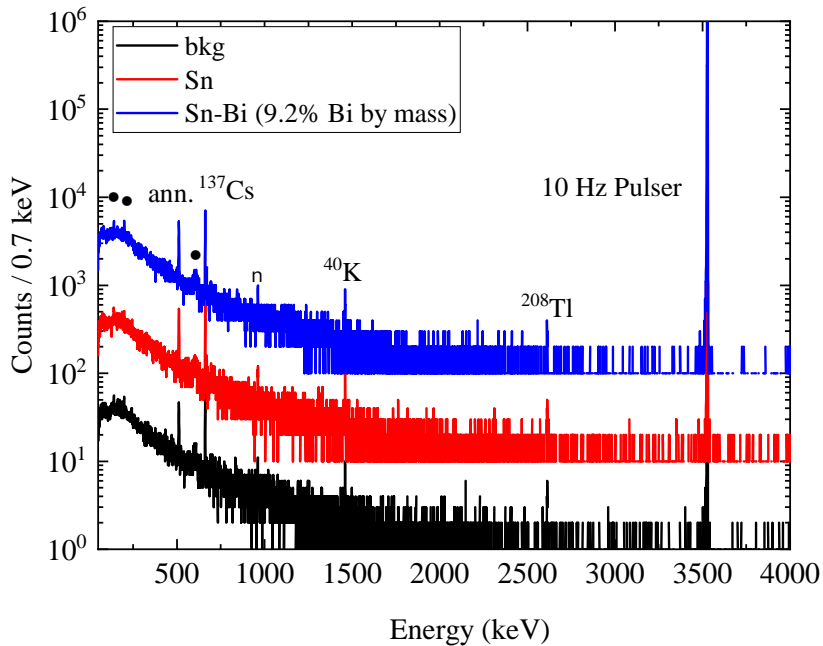
Figure 5.3: The time normalized spectra ($T_{data} = 1$ d) for the Sn-Bi sample (9.2% Bi by mass), Sn and the ambient background. Note that the spectra for Sn and Sn-Bi have been scaled for better visibility by arbitrary factors of 10 and 100, respectively. The peaks corresponding to neutron induced reactions in Ge and Cu have been annotated by • and ■, respectively. The abbreviation "ann." denotes the 511 keV annihilation peak.

The time normalized spectra of Sn-Bi, Sn and the ambient background can be found

in Fig. 5.3. The γ lines observed in the Sn-Bi and Sn spectra were consistent with those in the ambient background. The γ lines from neutron capture in the Ge detector and the inelastic scattering of fast neutrons in the Cu shielding and the Ge were also observed in the spectra. These features in the spectra have been marked in the figure. Table 5.2 lists the time normalized counts of the prominent γ rays observed in the spectra of the background (bkg), tin (Sn) and tin-bismuth (Sn-Bi) samples. The neutron induced lines in Ge have not been included in the table due to their low intensities.

Table 5.2: Intensities of the prominent γ rays observed in the ambient background (bkg), tin (Sn) and tin-bismuth (Sn-Bi) spectra.

Energy	Source	bkg	Sn	Sn-Bi
keV		cts/d	cts/d	cts/d
661.7	^{137}Cs	218 (12)	183 (15)	209 (13)
669.6	$^{63}Cu(n,n'\gamma)^{63}Cu$	18 (5)	28 (9)	24 (7)
962.1	$^{63}Cu(n,n'\gamma)^{63}Cu$	36 (8)	21 (6)	24 (6)
1460.8	^{40}K	31 (6)	30 (7)	36 (6)
2614.4	^{208}Tl	17 (5)	16 (5)	16 (4)

At the sensitivity level of TiLES, no new γ lines apart from the background lines were observed in the spectra. No enhancements were observed in the Sn-Bi sample in comparison to the background or Sn.

Table 5.3: Details of the measurements on TiLES (run 2).

Sample	Mass	Runtime
	(g)	(days)
Sn	22.8	22.1
Sn-Bi (0.92% Bi by mass)	12.3	51.9

The next run consisted of a different Sn-Bi sample having 10x lower concentration (0.92% Bi by mass), which was counted for a time period which was ~10x longer. The spectrum of the stock material (7N pure Sn) was acquired for the purpose of comparison. The Table 5.3 gives the details of the spectroscopic measurements (run 2). The Fig. 5.4 shows the spectra

of the Sn-Bi and Sn samples, both of which have been normalized to 22 d. The counts of the prominent γ rays which were observed in the Sn (stock) and 0.92% Sn-Bi spectra are listed in Table 5.4.
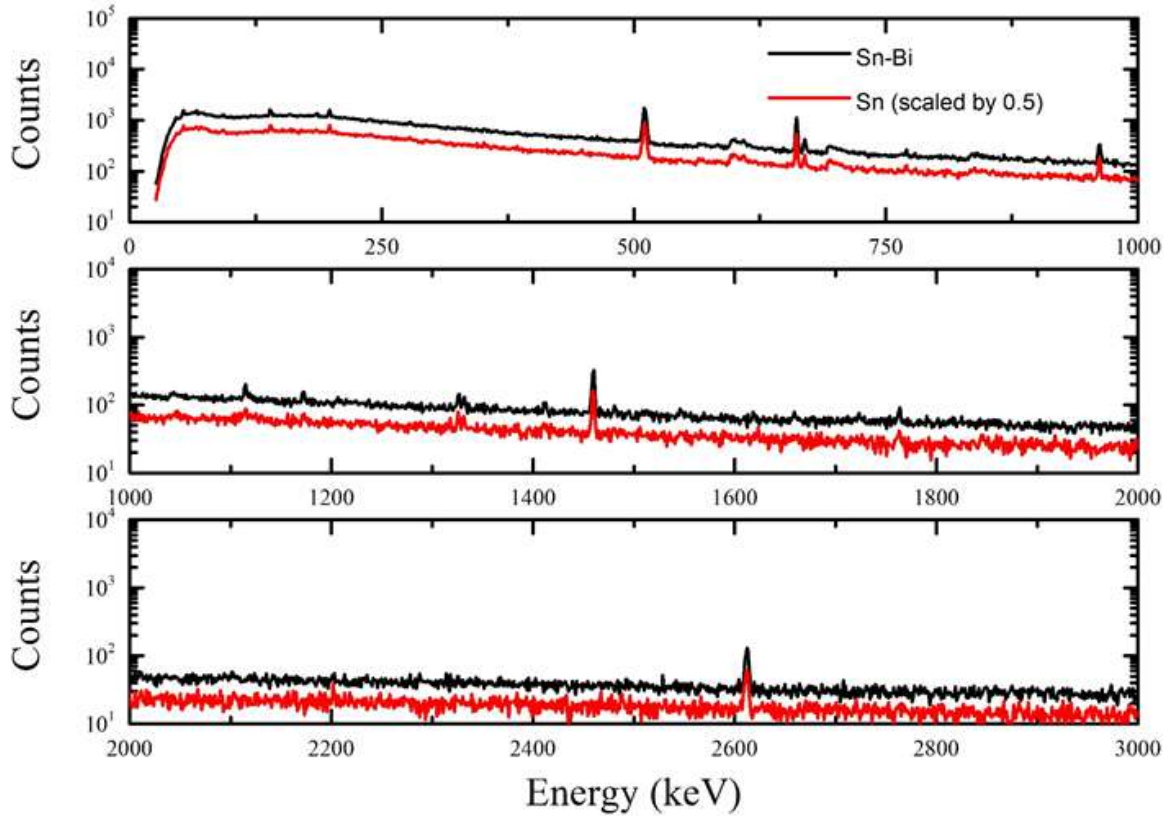
Figure 5.4: The spectra for the Sn-Bi alloy sample (0.92% Bi by mass) and Sn (7N pure stock material). Note that the spectra for Sn has been scaled by 0.5 for better visibility. Both spectra have been time normalized to 22 d.

Table 5.4: Counts of the prominent γ rays which were observed in the Sn (stock) and 0.92% Sn-Bi spectra (T_{data} = 22 d).

Energy	Source	Sn	Sn-Bi
keV		cts	cts
139.4	$^{74}Ge(n,\gamma)^{75m}Ge$	804 (144)	828 (77)
197.9	$^{70}Ge(n,\gamma)^{71m}Ge$	883 (108)	948 (100)
351.9	^{214}Pb	209 (125)	114 (102)
511.0	Ann., ^{40}K, ^{208}Tl	4846 (216)	5017 (129)

Table 5.4 is continued on the next page.

Energy	Source	Sn	Sn-Bi
keV		cts	cts
594.4 - 604.9	$^{74}Ge(n, n'\gamma)^{74}Ge$	1077 (208)	849 (98)
609.3	^{214}Bi	696 (227)	621 (72)
661.7	^{137}Cs	1905 (73)	1866 (70)
669.6	$^{63}Cu(n, n'\gamma)^{63}Cu$	352 (48)	450 (61)
690.1 - 704.2	$^{72}Ge(n, n'\gamma)^{72}Ge$	1083 (33)	1079 (33)
770.6	$^{65}Cu(n, n'\gamma)^{65}Cu$	146 (47)	115 (26)
962.1	$^{63}Cu(n, n'\gamma)^{63}Cu$	553 (64)	559 (43)
1115.5	$^{65}Cu(n, n'\gamma)^{65}Cu$	110 (45)	194 (37)
1172.5	^{60}Co	172 (104)	133 (33)
1327.0	$^{63}Cu(n, n'\gamma)^{63}Cu$	158 (44)	153 (27)
1332.5	^{60}Co	121 (43)	99 (17)
1460.8	^{40}K	752 (52)	738 (40)
1764.5	^{214}Bi	174 (52)	87 (22)
2614.5	^{208}Tl	369 (40)	382 (33)

Consistent with the earlier run, no new γ lines or enhancements were observed in the Sn-Bi sample.

5.3 Neutron activation of Sn-Bi at Pelletron Linac Facility

Although the measurement of the Sn-Bi samples on the TiLES detector setup allows for the investigation of radioactive impurities which may have been introduced into the crystals, it is not possible to detect the presence of trace impurities consisting of stable isotopes using this technique. Neutron activation analysis (NAA) is often used as a sensitive probe to identify the presence of such trace impurities. This technique involves the irradiation of the target nuclei with a large flux of neutrons, which leads to the production of radioactive progenies. The subsequent γ decay is then measured to identify the activated nuclei and the reaction channels by which they are produced. The sensitivity of detection depends on the incident neutron flux as well the nucleus dependent cross section of neutron interaction. This technique is

also useful to study the anticipated neutron-induced activity in the target, which is highly relevant for the radiation background studies. The neutron-induced background in ^{nat}Sn and other materials which are commonly used in low temperature detectors has been previously reported by Dokania *et. al.* in [22]. Using the same methodology, the fast neutron-induced reactions in Sn-Bi were investigated as a part of this thesis, in order to determine its suitability as an absorber for the superconducting bolometer.
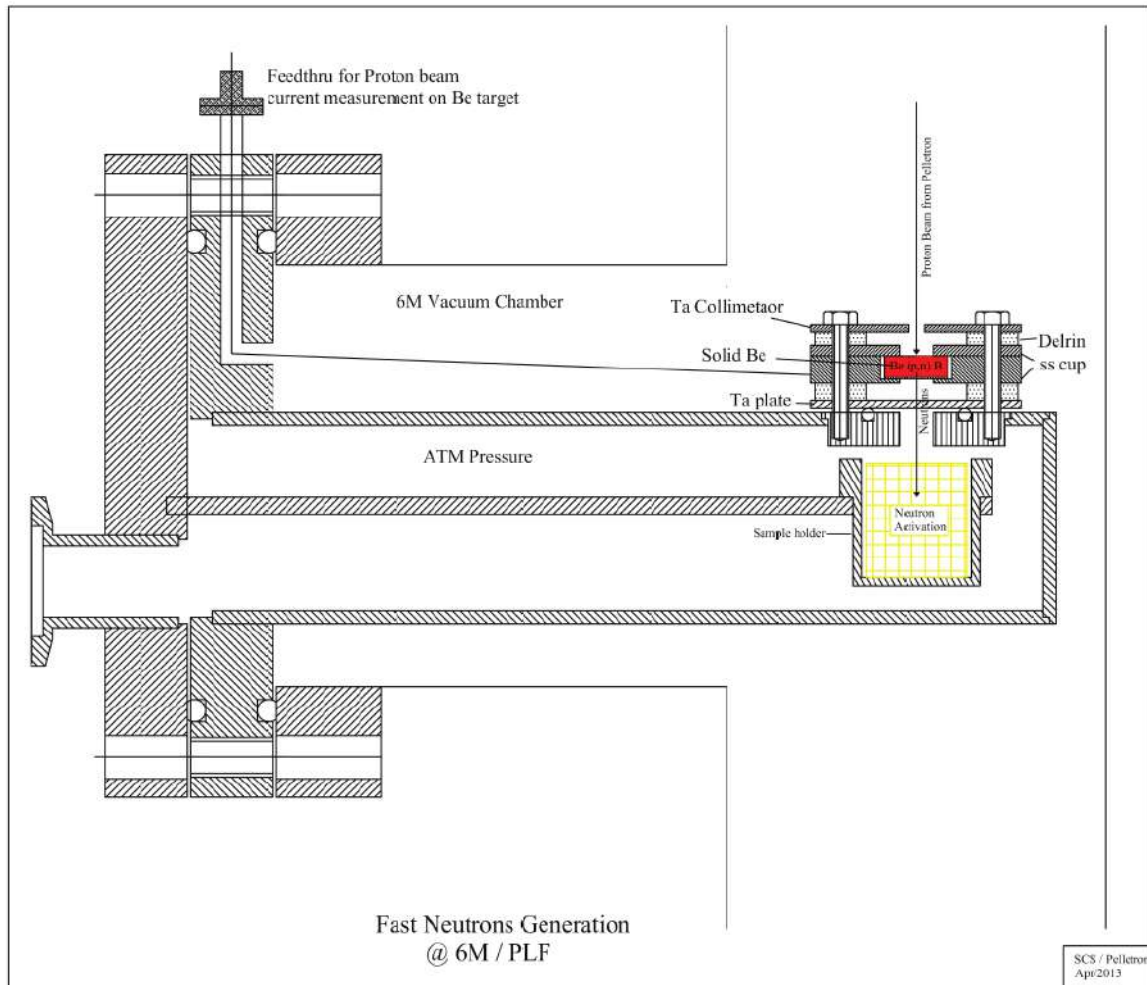
Figure 5.5: A schematic representation showing sample position with respect to the 5 mm ^{9}Be target at the 6 m irradiation facility, PLF. The picture is taken from [137].

The neutron activation experiment was performed at the 6 m irradiation facility, Pelletron Linac Facility, Mumbai [21]. A broad range of neutrons upto $E_{max} = E_p - Q_{th}$, where Q_{th}=2.057 MeV, were generated using an accelerated proton beam on a 5 mm thick ^{9}Be target via the ^{9}Be(p,n)^{9}B channel. Rolled target foils of Sn-Bi alloys, having Bi concentrations of 4.53% (material tag: SB6) and 0.09% by weight (material tag: SB1) were fabricated with

a mass thickness $\sim$ 50 - 60 mg/cm^2. The stock material of Sn and Bi which were used to synthesize the alloys, were included in the irradiation sample sets for comparison with the Sn-Bi sample. In this manner, it would be possible to identify any activity originating from impurities introduced during the crystal growth phase by comparison of the spectra of the Sn-Bi samples with that of the stock materials Bi and Sn. While rolled foils of the Sn sample were easily fabricated due to its malleability, it was not feasible to roll the Bi sample due to its brittle nature. Instead, the Bi shots were melted in vacuum and then resolidified to form large masses. In addition to the samples in which the neutron induced background was to be investigated, a Fe foil was included in each run in order to estimate the neutron flux, integrated over the energy region 0.1 MeV upto E_n. This was done by using the ^{56}Fe(n,p)^{56}Mn reaction channel (for more details, refer [22]). The energy integrated neutron flux (ϕ_n) was estimated to be $\sim$ 10^6 ncm^{-2}s^{-1} for the long irradiation run (Run 5). The samples were stacked in a teflon holder and mounted in the forward direction with respect to the proton beam outside the vacuum chamber in order to allow for a quick sample change, without the need to vent the vacuum chamber. A schematic representation of the irradiation setup can be found in Fig. 5.5.

The beam details, along with the irradiated targets, can be found in Table 5.5. A five letter alphanumeric label convention was followed for the targets: the first three letters were reserved for the material tag, followed by the run number and finally the number denoting the position of the sample in the teflon cup with respect to the top.

Table 5.5: The details of the beamtime runs.

Run No.	E_p (MeV)	Irradiation time	Targets
Run 1	18	$\sim$ 30 min	Fe011, SB112, Bi014
Run 2	18	$\sim$ 1 h	Fe021, SB622, Sn023
Run 3	15	$\sim$ 50 min	Fe031, SB132, Bi034
Run 4	15	$\sim$ 50 min	Fe041, SB642, Sn043
Run 5	21	$\sim$ 11 h	Fe051, Sn052, SB653 + SB153, Bi054

After the end of the neutron irradiation run, the samples were removed from the irradiation

facility only after a suitable cooldown period. The samples were then counted offline. The Fe foils were counted on a CeBr$_3$ detector as there was only one line of interest, while the other samples were counted in HPGe detectors to acquire data with better energy resolution. The TiLES setup was used only if the activity of the samples resulted in an integrated count rate which did not exceed 1 kHz. While the TiLES setup was occupied, the other samples were counted on the Bruker Baltic HPGe detectors D1 and D2 (see Fig. 5.6). These detectors have a relative efficiency of $\sim$ 30%, and a normal lead shielding ($\sim$ 5 cm). All the spectra were acquired using CAEN N6724 digitizers and the acquired spectra were analyzed using LAMPS [138] software. Half-life tracking was used to verify/identify the source of the γ-rays, wherever possible. The Fig. 5.7 shows a few select examples of half-life tracking of observed γ-rays in the Sn-Bi spectrum.

Figure 5.6: Bruker Baltic HPGe detectors D1 and D2.

The short and the long irradiation of Bi samples did not show any activity [1]. Given the low cross-sections of the reaction channels in Bi, it was inferred from this that any activity in the Sn-Bi alloys is expected to originate from the activation of Sn or trace impurities, rather than from Bi. The spectra of the Sn and Sn-Bi samples were compared to understand the additional activity arising in the Sn-Bi samples. The Sn-Bi and Sn samples were counted in TiLES sequentially with cooling times corresponding to 5 h and 29 h, respectively. Fig. 5.8 shows the spectra of the Sn and the Sn-Bi samples from the long irradiation run (Run 5), acquired in TiLES.

---

[1] For reference, the channels of interest which were most likely to have been observed were the ^{209}Bi(n, α)^{206}Tl (T$_{1/2}$ = 4.202 min), ^{209}Bi(n, α)^{206m}Tl (T$_{1/2}$ = 3.74 min) and the ^{209}Bi(n, 3n)^{207}Bi (T$_{1/2}$ = 31.55 y) channels.
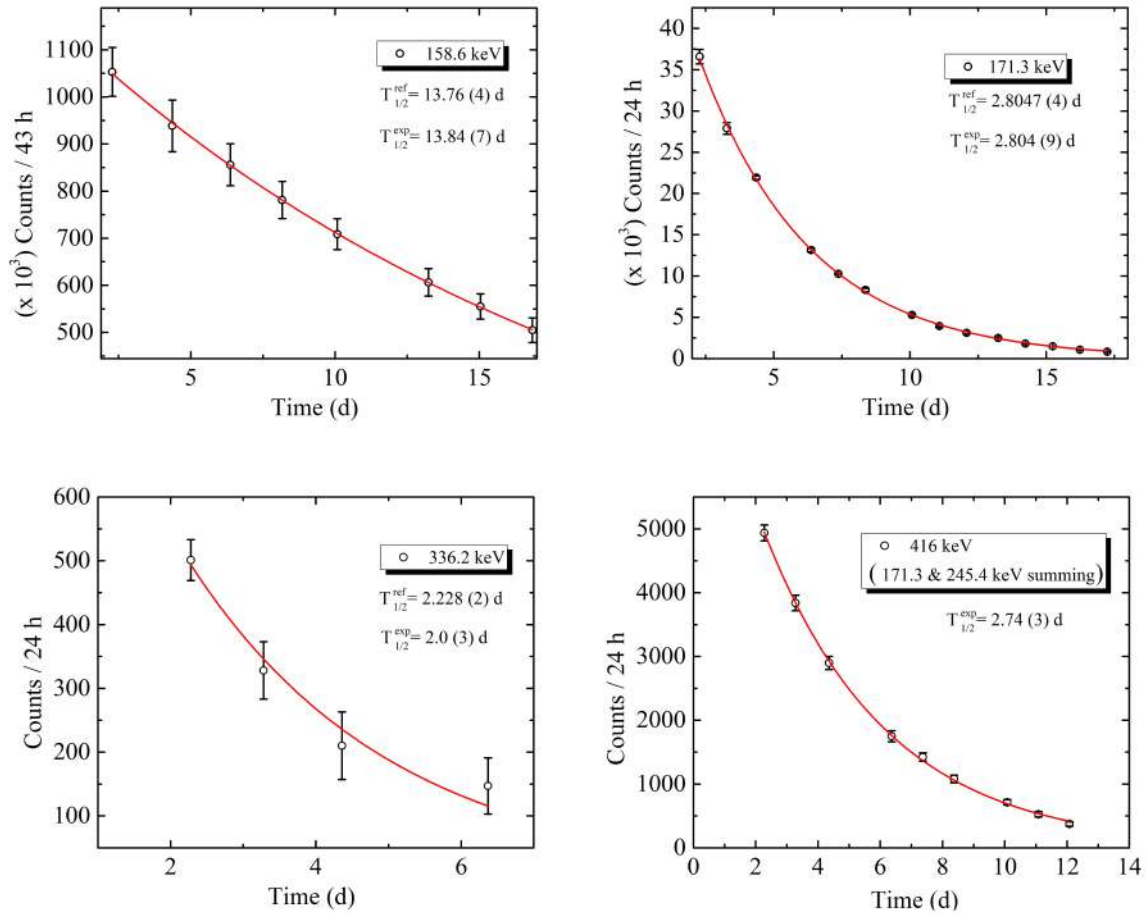
Figure 5.7: A few select examples of the half-life tracking for clear identification of observed γ-rays in the Sn-Bi spectrum.

Table 5.6 lists the prominent reaction channels that were observed in the samples of Run 5. The activity observed in the Sn-Bi spectrum could be attributed solely to the neutron activation of Sn. Due to the longer cooldown for the Sn sample, the γ corresponding to channels with half-lives < 1 h were not observed. Namely, these channels are ^{116}Sn(n,p)^{116m}In and ^{117}Sn(n,p)^{117}In [2].

The 416.9 keV line was visible in the Sn spectrum even after the ~29 h cooldown, which implied a longer half-life than the 54.29 min associated with the channel ^{116}Sn(n,p)^{116m}In. On further investigation, the half-life for the γ line at 416.9 keV was tracked and found to be 2.74 (3) d. Thus, it was surmised that the 416.9 keV has a long-lived contribution from the coincident summing of the 171.3 keV and 245.4 keV γ cascade in the ^{112}Sn(n, np)^{111}In

---

[2]These channels are present in the spectra of both Sn-Bi and Sn acquired on D1 and D2 after a short cooldown of ~20 min, which was performed prior to the data acquisition in TiLES. This further confirms the short-lived nature of these activation channels in Sn.
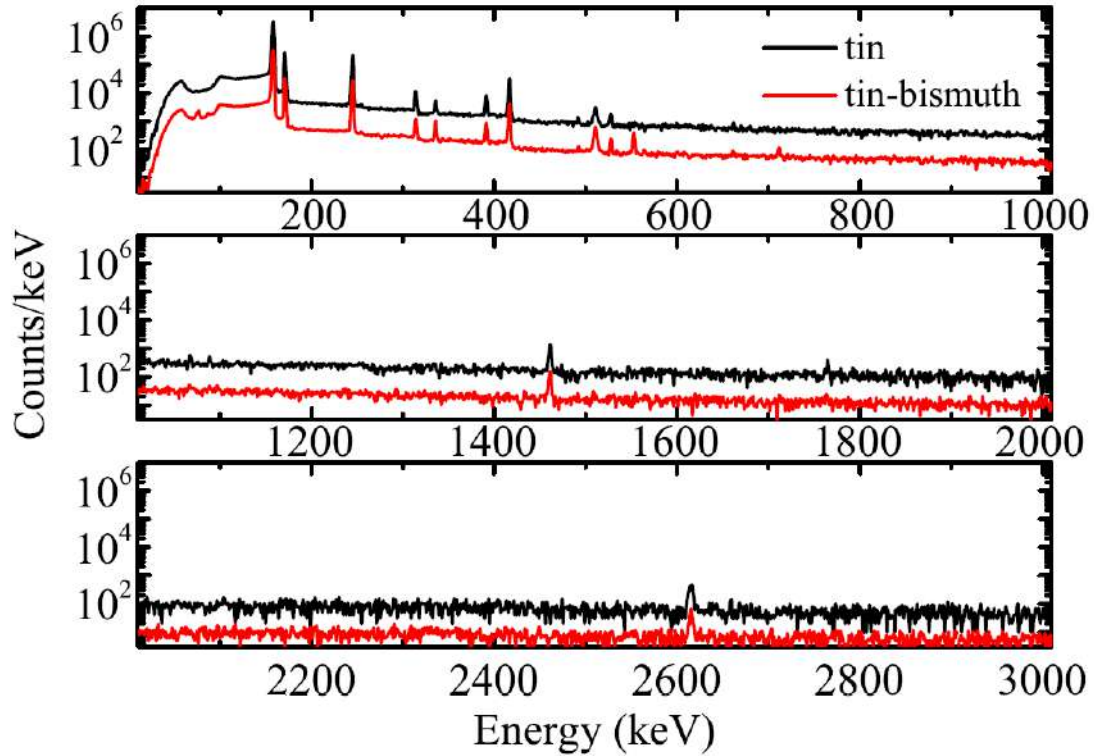
Figure 5.8: Spectra of the tin-bismuth and tin samples acquired in TiLES (T_{data} = 1 d) after a cool-down time of ~ 5 h and ~ 29 h, respectively. The spectrum of tin has been scaled by a factor of 10 for better visibility.

channel.

A γ line at 711.5 keV was observed in the Sn-Bi spectrum but not the Sn spectrum. The source was identified to be the coincident summing of the γ cascade of 158.6 keV and 552.9 keV from the ^{117}Sn(n,p)^{117}In ($T_{1/2}$ = 43.2 min).

The 336.2 keV line was found to arise from a long-lived channel in addition to the expected short-lived reaction channels producing ^{115m}In. The half-life of the short-lived channels could not be verified from tracking due to a corruption of the data from the long-lived channel. Excluding data from the first two days after irradiation, the long-lived component was fitted and the half-life was found to be 2.0 (3) d. This corresponds to the channel ^{118}Sn(n, α)^{115}Cd which has a half-life of 2.228 (2) d. This channel also produces the γ line at 527.9 keV, which was also observed in the spectra.

Although no γ-rays which could be attributed to activation channels of Bi were found, two x-ray peaks consistent with the Bi K_{α} (77.1 keV) and the Bi K_{β} (87.3 keV) were visible in the Sn-Bi sample but not in the Sn sample. These x-rays possibly arise due to the fluorescence

Table 5.6: Reaction channels observed in the Sn and the Sn-Bi samples ($T_{irr} \sim 11$ h). The half-life of the channels marked with * could not be measured due to poor statistics.

Channel	E_γ (keV)	$T^{ref}_{1/2}$	$T^{obs}_{1/2}$
^{112}Sn(n,2n)^{111}Sn [a]	1153.0	35.3 (8) min	*
^{112}Sn(n,np)^{111}In	171.3, 245.4	2.8047 (4) d	2.804 (9) d
^{112}Sn(n,γ)^{113}Sn			
^{114}Sn(n,2n)^{113}Sn	391.7	115.09 (3) d	155 (40) d
^{118}Sn(n,α)^{115}Cd	336.2, 527.9	2.228 (2) d	2.0 (3) d
^{116}Sn(n,np)^{115m}In			
^{115}Sn(n,p)^{115m}In			
^{115}In(n,n')^{115m}In	336.2	4.486 (4) h	*
^{116}Sn(n,p)^{116m}In [c]	416.9[b], 1097.3, 1293.6, 1507.6	54.29 (17) min	*
^{120}Sn(n,α)^{117}Cd [a]	273.3	2.49 (4) h	*
^{120}Sn(n,α)^{117m}Cd	564.4, 1065.98	3.36 (5) h	*
^{117}Sn(n,p)^{117}In [c]	158.6, 552.9	43.2 (3) min	*
^{117}Sn(n,n')^{117m}Sn			
^{116}Sn(n,γ)^{117m}Sn	156.0, 158.6,		
^{118}Sn(n,2n)^{117m}Sn	314.3	13.76 (4) d	13.84 (7) d
^{124}Sn(n,2n)^{123}Sn			
^{122}Sn(n,γ)^{123}Sn	1088.6	129.2 (4) d	*
^{124}Sn(n,γ)^{125}Sn	822.5, 1067.1, 1089.2	9.64 (3) d	9.0 (14) d

[a]Present in the spectra acquired on D1 and D2.
[b]γ-ray present in Sn spectrum: source is coincident summing of 171.3 keV + 245.4 keV.
[c]Absent in Sn spectrum (TiLES) due to ~ 29 h cooldown.

of Bi.

Note that in the case of the short irradiation sets (Run 1 to 4), the Sn-Bi and Sn samples were counted on D1 and D2, respectively. The prominent reaction channels observed in the Sn and Sn-Bi samples have been listed in Table 5.7. In addition to these prominent channels listed, the presence of some weak lines (< 50 counts) arising from a few long-lived channels

in Sn were also observed. However, due to differences in the irradiation times, detector efficiencies and ambient background, these γ lines were not consistent across samples.

Table 5.7: Prominent reaction channels observed in the Sn and the Sn-Bi samples, collated from the short irradiation runs 1 to 4.

Channel	E_γ (keV)	$T_{1/2}^{ref}$	$T_{1/2}^{obs}$
^{122}Sn(n, γ)^{123m}Sn			
^{124}Sn(n, 2n)^{123m}Sn	160.3	40.06 (1) min	42.5 (27) min
^{124}Sn(n, γ)^{125m}Sn	331.9	9.52 (5) min	*

To summarize, neutron activation studies in Sn-Bi were performed at the 6 m irradiation facility, PLF. No measurable neutron induced activity which could be attributed to trace impurities or to the alloying element Bi was observed. All the activity could be attributed to reaction products arising from the neutron activation channels of Sn - ^{111}Sn, ^{111}In, ^{113}Sn, ^{115}Cd, ^{115m}In, ^{116m}In, ^{117m}Cd, ^{117}In, ^{117m}In, ^{117m}Sn, ^{123}Sn, ^{123m}Sn, ^{125}Sn and ^{125m}Sn. These activation channels were compared to the channels observed in an earlier neutron activation experiment in Sn by Dokania *et. al.* [22], and additional channels leading to the production of ^{111}Sn, ^{113}Sn, ^{115}Cd, ^{117}Cd, ^{117m}Cd, ^{117}In and ^{117m}In were observed.

5.4 Estimation of the internal background arising from the α decay of ^{209}Bi

For a long time, ^{209}Bi was considered to be the heaviest stable isotope. However, in 2003, an experiment using a 45.7 g scintillating BGO bolometer detected the rare α decay of ^{209}Bi [23]. The half life of this α decay was found to be $(1.9 \pm 0.2) \times 10^{19}$ y, which is comparable to the half-life of a few $\beta\beta$ emitters.

Table 5.8: Decay data for ^{209}Bi from NNDC NuDAT database.

Isotope	Natural isotopic abundance	Decay mode	Half-life	Q value
^{209}Bi	100%	α	$(1.9 \pm 0.2) \times 10^{19}y$	3137.2 keV

The decay data from the NNDC NuDat database [139] for ^{209}Bi is shown in table 5.8.

The decay scheme of ^{209}Bi has been shown in the figure 5.9.
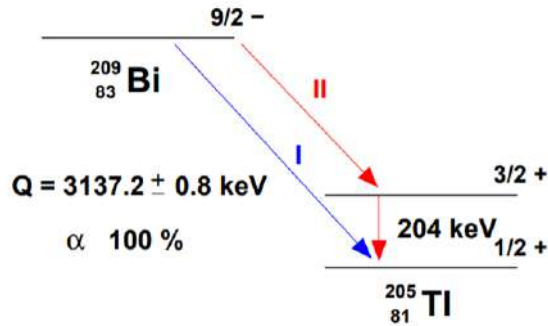
Figure 5.9: Bismuth decay scheme, taken from [140].)

Fig. 5.10 shows examples of bulk and surface events in the bolometer. It is important to note that only partial deposition events will contribute to the region of interest (ROI) since the fully deposited peak (at ~2.9 MeV and ~3.1 MeV) will be well separated from the ROI (around ~2.3 MeV).
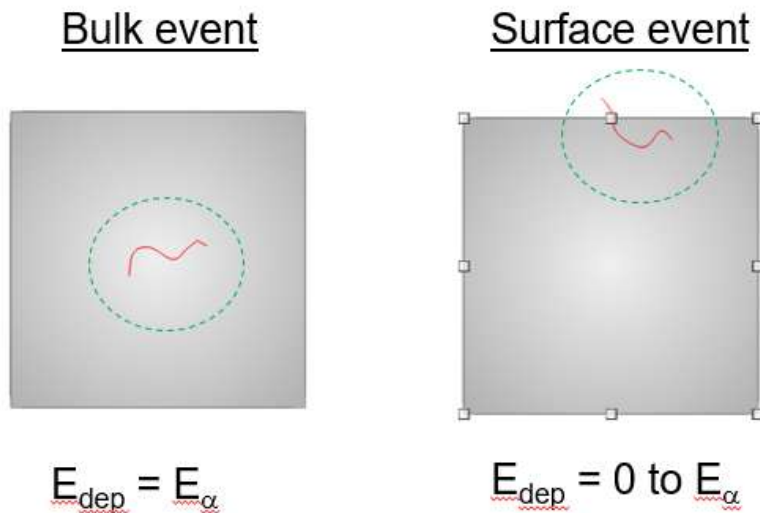
Figure 5.10: Schematic examples of bulk and surface events.

A cube-shaped bolometer was considered for the simulation. The bolometer volume was divided into an inner cube 'D1' and an outer shell 'D2'. The events originating in the region 'D1' would correspond to bulk events while the events originating in 'D2' would correspond to surface events. In order to decide the thickness of the 'D2' shell, the range of the α particle was considered. As per TRIM software [141], the range of a 3.1 MeV α particle in tin is $\sim 8~\mu m$. Accordingly, the width of D2 was set as 10 μm, to allow some tolerance

for straggling. Thus, the sensitive detector volumes 'D1' and 'D2' together comprise the bolometer. Fig 5.11 shows the detector schematic (not to scale). The GEANT4 simulations were performed for different combinations of bolometer volumes (27 cc, 64 cc and 125 cc) and bismuth concentrations (0.25 %, 0.5 %, 0.75 % and 1.00 % by mass).
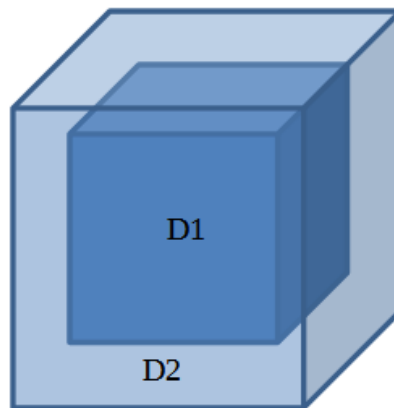
Figure 5.11: Detector scheme employed in simulation to study Bi α background (not to scale).

The standard physics list QGSP_BERT_HP was used. The processes of interest in this physics list are mentioned below, alongside their GEANT4 process names in the parenthesis:

1. α particle : multiple scattering (msc) and ionization (ionIoni).

2. electron : multiple scattering (msc), ionization (eIoni), bremsstrahlung (eBrem) and Coulomb scattering (CoulombScat).

3. positron : multiple scattering (msc), ionization (eIoni),bremsstrahlung (eBrem), annihilation (annihil) and Coulomb scattering (CoulombScat).

4. photon : Photoelectric effect (phot), Compton scattering (compt) and pair production (conv).

5. Generic ion : multiple scattering (msc) and ionization (ionIoni).

The processes relating to other particles such as protons, anti-protons, muons, kaons and pions, have not been listed above since they are not relevant to this study.

Since the bulk events will lead to fully deposited events, it would be computationally inefficient to simulate them. The position coordinates (x,y,z) were generated using independent, uniform random variables within the bolometer size. Acceptance-rejection sampling was used such that the (x,y,z) point was accepted for particle generation if it was within the D2 detector volume and rejected if it fell within the D1 detector volume. In this manner, only surface events were simulated to optimize computation time and memory. The α particles were generated according to the energies and branching ratios listed on NNDC NuDAT [139]. These have been listed in the Table 5.9. The Fig. 5.12 shows the energies with which the α particles are generated in the simulations.

Table 5.9: α decay data for ^{209}Bi from NNDC NuDAT database

α energy E_α keV	Intensity I_α (%)
2876	0.04
3077	99.92
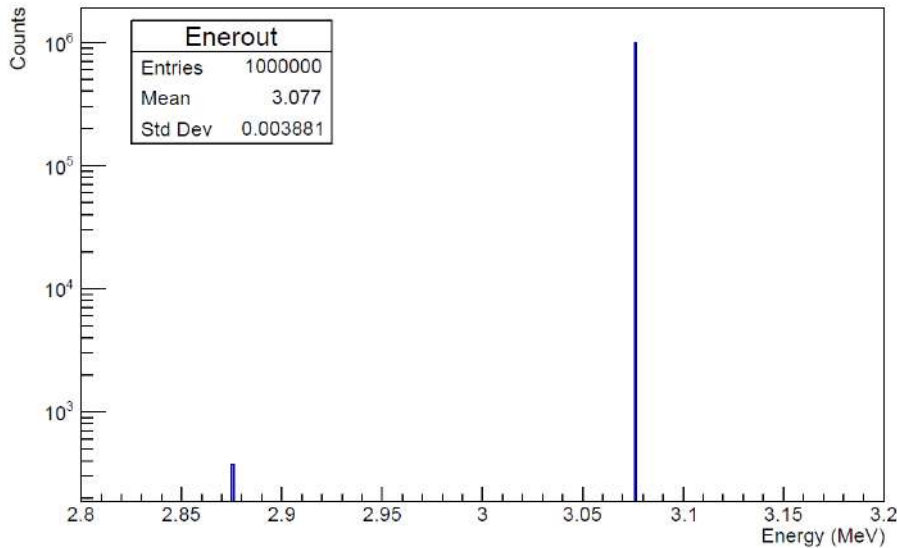
Figure 5.12: Energy spectra of generated α particles.

The momentum of the non-relativistic α particle was calculated and initialized using classical equations. In order to simulate the isotropic emission of the α particles, the unit vector along the direction of the momentum was chosen uniformly at random from the surface

of a unit sphere. The initial kinematical variables with which the α particles were generated were recorded in a ROOT Tree and the spectra were plotted as a diagnostic check. The typical position and angular distributions are shown in the Fig. 5.13. The componentwise momentum distributions are shown in Fig. 5.14.
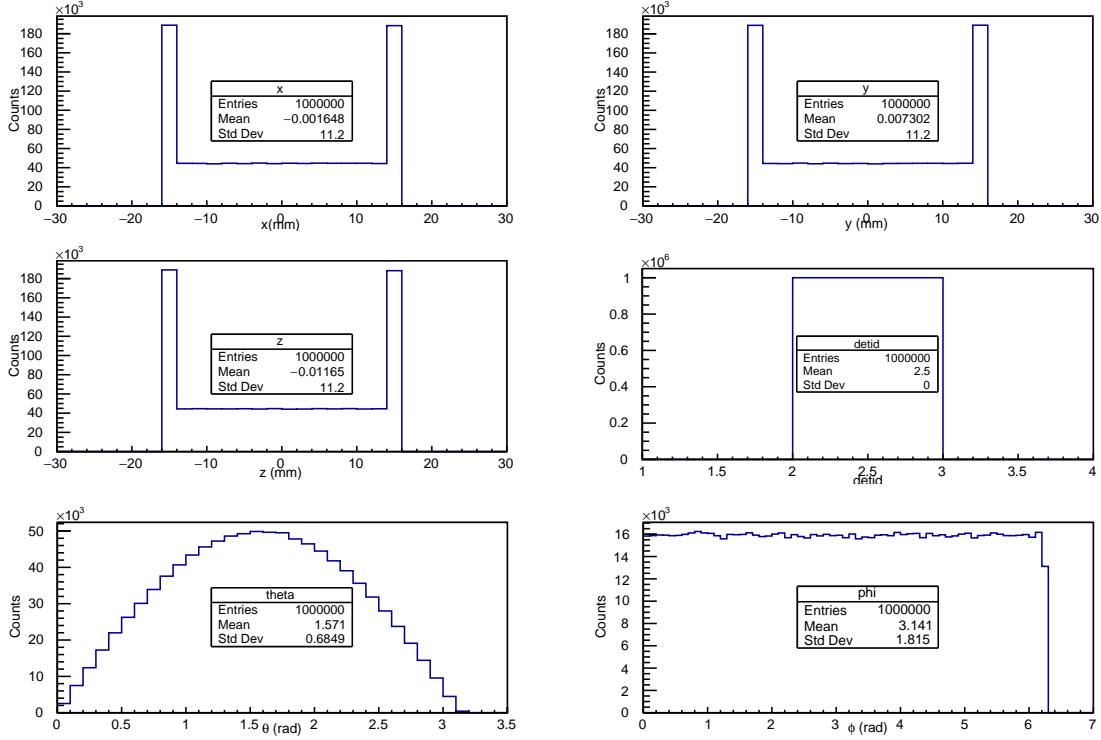
Figure 5.13: Position and angular distribution of the α particles generated within the detector volume.
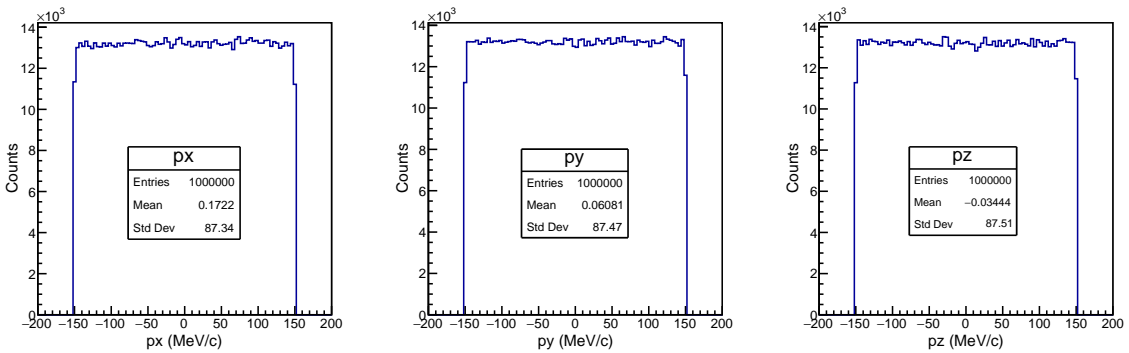
Figure 5.14: The momentum spectra of the generated α particles.

The energy deposited (E_{dep})in the total bolometer volume was recorded. This energy was the sum of the energies deposited in the detector volumes 'D1' and 'D2':

$$E_{dep} = E_{dep,D1} + E_{dep,D2}. \tag{5.1}$$

114

The E_{dep} spectrum is shown in Fig. 5.15 for a 27 cc bolometer, with Bi alloying at 0.5 % by weight.
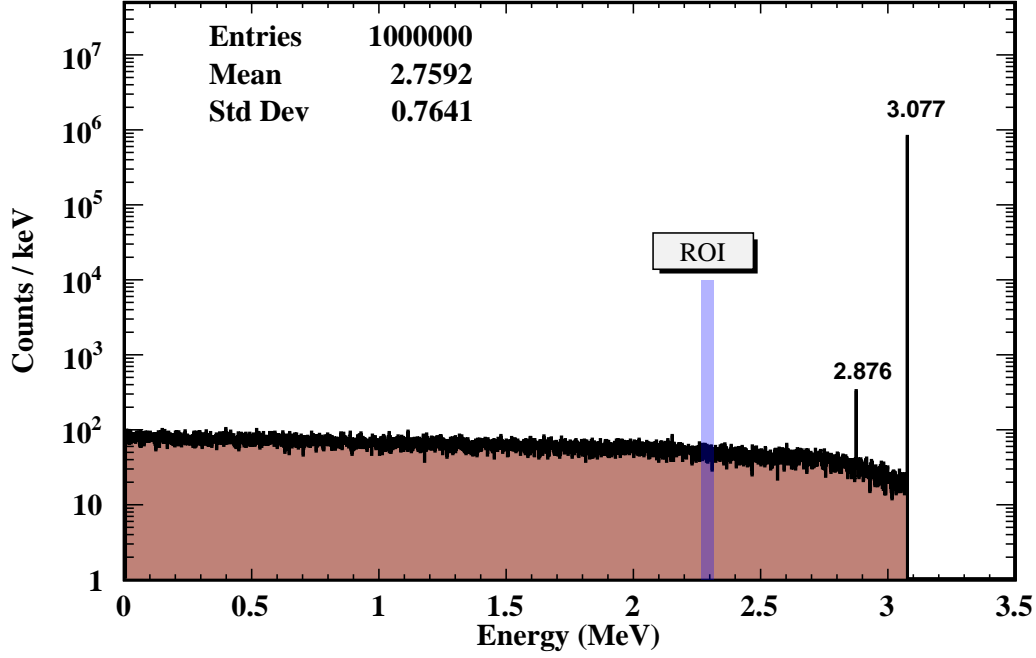
Figure 5.15: The simulated E_{dep} spectrum of the α particles for a 27 cc bolometer, with Bi alloying at 0.5 % by weight. In the figure, the ROI is marked.

From the E_{dep} spectrum, the fraction of events (f_{ROI}) that contribute to the ROI ($Q_{\beta\beta}\pm$ 25 keV) was extracted using a ROOT based code. The background contribution from the α decay of ^{209}Bi ($Bkg_{\alpha,Bi}$) is then calculated as follows:

$$Bkg_{\alpha,Bi} = \frac{0.693}{T_{1/2}} * N_{Bi} * f_{ROI} \qquad (5.2)$$

where $T_{1/2} = 1.9 \times 10^{19}$y and N_{Bi} is the number of ^{209}Bi nuclei in the shell D2. The estimated contributions for Sn-Bi bolometers are listed in Table 5.10.

As expected, the contribution of the background index (in counts/(keV.kg.y)) from the α decay of ^{209}Bi reduces with the increasing volume. This is due to the inverse dependence of the surface to volume ratio on the volume of the bolometer. The order of magnitude of the contribution of the α decay of ^{209}Bi is $\sim 10^{-5}$ counts/(keV.kg.y). This is three orders of magnitude smaller than the typical background budget of a bolometric experiment, which does not have particle identification capabilities to discriminate against α decays. In the

Table 5.10:   Background contribution in the ROI from the α decay of ^{209}Bi ($\text{Bkg}_{\alpha,\text{Bi}}$) estimated from GEANT4 simulations.

Bi alloying	Bolometer volume	Background $counts/(keV.kg.y)$
0.25%	27 cc	2.6×10^{-5}
	64 cc	2.0×10^{-5}
	125 cc	1.6×10^{-5}
0.50%	27 cc	5.3×10^{-5}
	64 cc	4.2×10^{-5}
	125 cc	3.1×10^{-5}
0.75%	27 cc	7.8×10^{-5}
	64 cc	5.9×10^{-5}
	125 cc	4.7×10^{-5}
1.00%	27 cc	1.1×10^{-4}
	64 cc	7.6×10^{-5}
	125 cc	6.1×10^{-5}

next section, the background contribution from the α decay of ^{209}Bi is compared with the contributions from trace impurities of Uranium and Thorium in the detector.

5.5 Estimates on Uranium and Thorium activities

As mentioned earlier, another common source of internal radioactive background arises from the trace impurities of Uranium and Thorium in the detector. While Uranium is composed of 99.27% ^{238}U and 0.72% ^{235}U, the contribution from the ^{235}U is negligible in comparison to that of ^{238}U. Therefore, for the purpose of this estimation, we will not consider the contribution from ^{235}U. Both ^{238}U and ^{232}Th result in a cascade of decays, leading to a series of α, β and γ emission along the respective chains which end in the stable isotopes of lead ^{206}Pb and ^{208}Pb, respectively. The Uranium decay chain is shown in 5.17 and 5.12 while the Thorium decay scheme is shown in 5.16 and 5.11.

Table 5.11: Thorium decay chain, as per NNDC NuDAT [139]. The modes with end point energy $< Q_{\beta\beta} - 25~keV$ have been denoted in blue text.

Parent Nucleus	Daughter Nucleus	Mode	Half-life	Branching ratio (%)	Q_{gs} value keV
^{232}Th	^{228}Ra	α	1.4×10^{10} y	100 %	4081.6
^{228}Ra	^{228}Ac	$\beta-$	5.75 y	100 %	45.8
^{228}Ac	^{228}Th	$\beta-$	6.15 h	100 %	2124
^{228}Th	^{224}Ra	α	1.9 y	100 %	5520.08
^{224}Ra	^{220}Rn	α	3.66 d	100 %	5788.87
^{220}Rn	^{216}Po	α	55.6 s	100 %	6404.67
^{216}Po	^{212}Pb	α	145 ms	100 %	6906.4
^{212}Pb	^{212}Bi	$\beta-$	10.64 h	100 %	569.9
^{212}Bi	^{212}Po	$\beta-$	60.55 m	64.06 %	2252.1
^{212}Bi	^{208}Tl	α	60.55 m	35.94 %	6207.26
^{212}Po	^{208}Pb	α	0.3 μs	100 %	8954.12
^{208}Tl	^{208}Pb	$\beta-$	3.053 m	100 %	4998.5 [a]

[a]The $\beta-$ decay mode is associated with an end point energy of 1801.3 keV, which cannot contribute to the background.

Table 5.12: Uranium decay chain, as per NNDC NuDAT [139]. The modes with low branching ratio or end point energy $< Q_{\beta\beta} - 25\ keV$ have been denoted in blue text.

Parent Nucleus	Daughter Nucleus	Mode	Half-life	Branching ratio (%)	Q_{gs} value keV
^{238}U	^{234}Th	α	4.5×10^9 y	100 %	4269.9
^{234}Th	^{234}Pa	$\beta-$	24.1 d	100 %	274.0
^{234m}Pa	^{234}U	$\beta-$	1.16 m	100 %	2194.0
^{234}U	^{230}Th	α	2.46×10^5 y	100 %	4857.5
^{230}Th	^{226}Ra	α	7.5×10^4 y	100 %	4769.9
^{226}Ra	^{222}Rn	α	1600 y	100 %	4870.7
^{222}Rn	^{218}Po	α	3.82 d	100 %	5590.4
^{218}Po	^{218}At	$\beta-$	3.098 m	0.02 %	259.0
^{218}Po	^{214}Pb	α	3.098 m	99.98 %	6114.75
^{218}At	^{218}Rn	$\beta-$	1.5 s	0.01 %	2881.0
^{218}At	^{214}Bi	α	1.5 s	99.90 %	6874.0
^{218}Rn	^{214}Po	α	35 ms	100 %	7262.5
^{214}Pb	^{214}Bi	$\beta-$	26.8 m	100 %	1018.0
^{214}Bi	^{214}Po	$\beta-$	19.9 m	99.979 %	3269.0
^{214}Bi	^{210}Tl	α	19.9 m	0.021 %	5621.0
^{214}Po	^{210}Pb	α	163.6 μs	100 %	7833.54
^{210}Tl	^{210}Pb	$\beta-$	1.30 m	100 %	5482.0
^{210}Pb	^{206}Hg	α	22.2 y	1.9×10^{-6} %	3792.0
^{210}Pb	^{210}Bi	$\beta-$	22.2 y	~ 100 %	63.5
^{210}Bi	^{210}Po	$\beta-$	5.012 d	~ 100 %	1161.2
^{210}Bi	^{206}Tl	α	5.012 d	1.32×10^{-4} %	5036.5
^{210}Po	^{206}Pb	α	138.37 d	100 %	5407.53
^{206}Hg	^{206}Tl	$\beta-$	8.32 m	100 %	1308.0
^{206}Tl	^{206}Pb	$\beta-$	4.202 m	100 %	1532.2
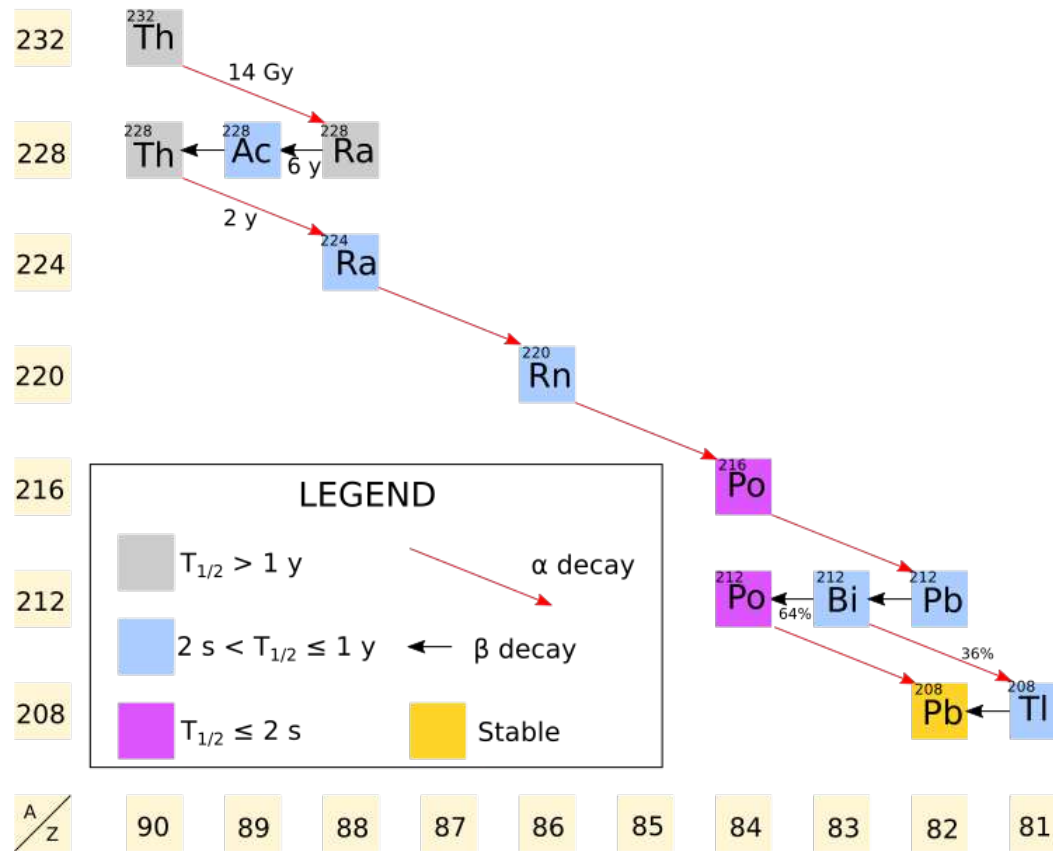
Figure 5.16: Thorium decay chain.
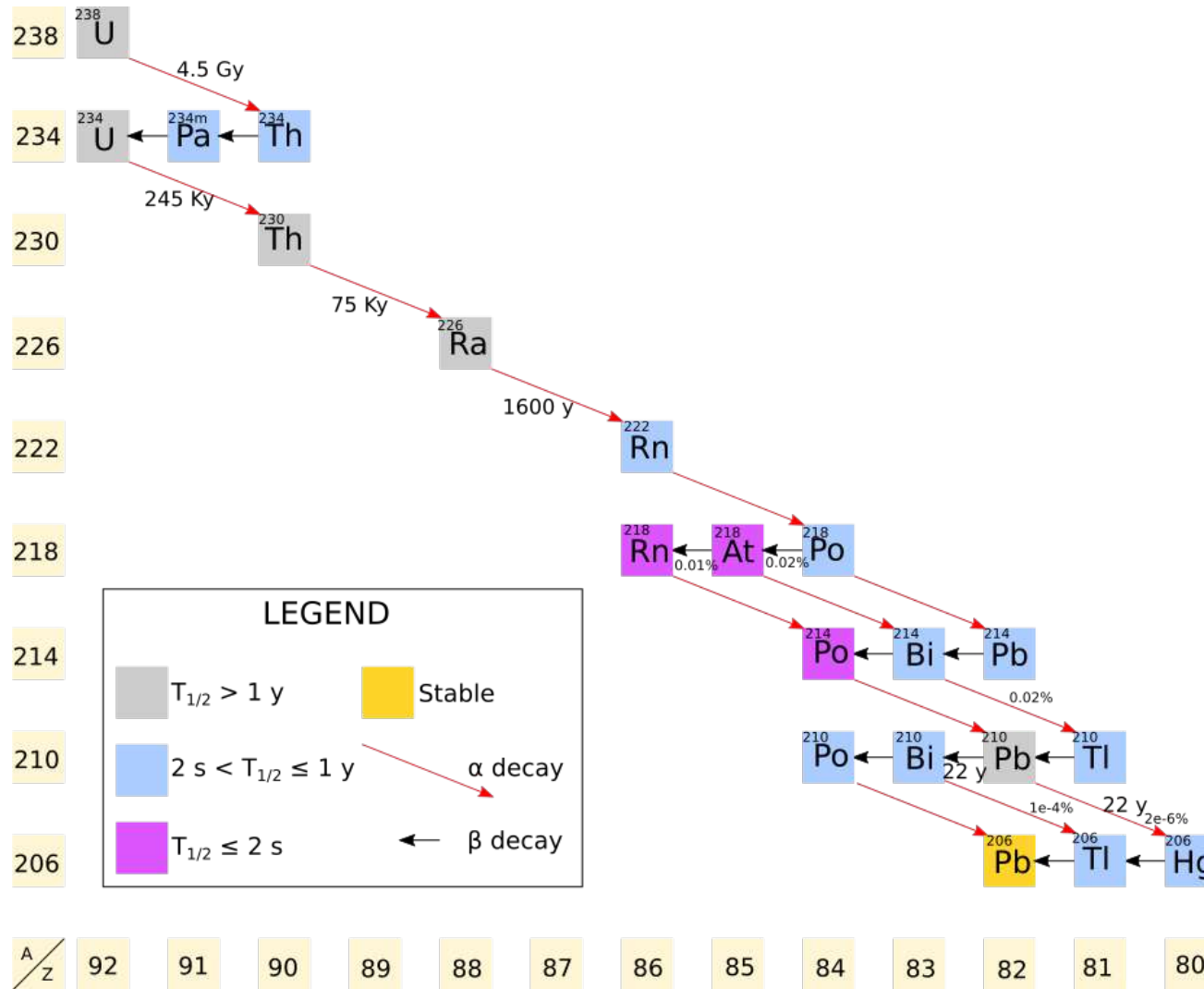
Figure 5.17: Uranium decay chain.

It is appropriate to introduce the concept of a hit multiplicity before proceeding. Hit multiplicity can be defined as the number of bolometers which register an energy deposition event within a coincident time interval. Since the characteristic lengths for α, β and γ particles are very different, the average hit multiplicity for γ versus α and β particles is different. To illustrate this, consider 3 MeV of each type of radiation propagating through Sn – the ranges of the α and β particles are 8 μm and 3 mm, respectively, and the half value layer ($d_{1/2}$) for γ rays is 2.6 cm. Due to the penetrating nature of γ rays, background events arising from the Compton scattering of high energy γ, for e.g. 2614.5 keV γ rays originating from ^{208}Tl decay, have a high probability of having a hit multiplicity greater than 1. In contrast, due to the short range of α and β particles, these events are more likely to have a hit multiplicity equal to 1. Thus, it is possible to discriminate against γ backgrounds on the basis of hit multiplicity [142], but it is difficult to do so for the α and β backgrounds. Due to this reason, the γ background is not considered for the purpose of this estimation as it is believed that it would be insignificant in comparison to the α / β background, after multiplicity cuts. The decay modes and branching ratios were adopted from the NNDC database, neglecting branching ratios / intensities < 1%. Moreover, β emitters having an end point energy $< Q_{\beta\beta} - 25\ keV$ were not simulated, since it would not contribute to the region of interest. In case these modes were to be simulated, the estimation would remain unchanged, and only the spectral shape in the low energy region would be modified.

The simulation of the individual radionuclides was similar to the process followed in the case of ^{209}Bi. However, there were a few distinct differences. In the case of the relevant β emitters, the bulk events would also contribute to the background due to the continuous nature of the β energy spectrum. Thus, in these cases, it was imperative to allow for the particle generation throughout the bolometer volume, i.e, both D1 and D2 regions. In order to avoid additional weight factors arising from surface to volume considerations, the particle generation was performed in an identical manner for the α and the β emitters. For electrons, relativistic kinematics was employed.

In general, the activities of progenies in a radioactive decay chain can be calculated using the Bateman equations, which are computationally complex. However, the estimation is greatly simplified in the case of primordial radioactive chains, where the parent nucleus has

a much longer half-life than its progenies. In these special cases, the system attains secular equilibrium whereby the activity of the parent nucleus is equal to that of the daughter nucleus. Thus, using the property of secular equilibrium, the activity of the total radioactive decay chain can be estimated from the weighted sum of the activities of the individual radionuclides. The respective weights are calculated after taking into consideration the branching ratio of the modes associated with the decay.
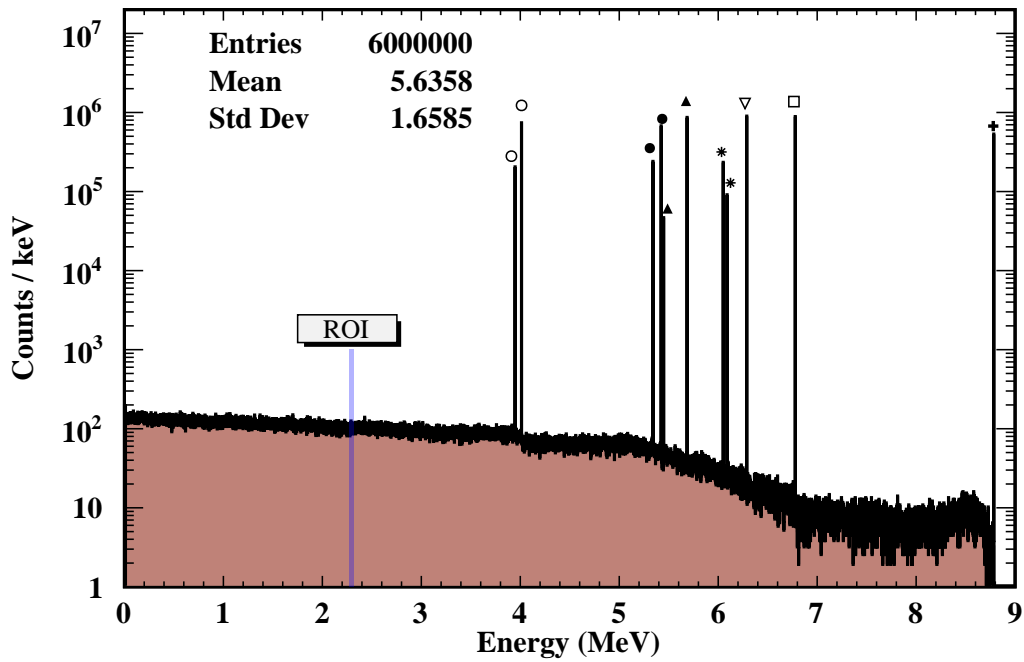
Figure 5.18: The typical simulated energy spectrum from ^{232}Th decay chain arising from Th impurities in a Sn-Bi bolometer (summed contributions of all products). The shaded blue box denotes the region of interest (ROI). The peaks from full energy deposition of the α particles, originating from ^{232}Th($\circ$), ^{228}Th($\bullet$), ^{224}Ra($\blacktriangle$), ^{220}Rn($\triangledown$), ^{216}Po($\square$), ^{212}Bi ($\ast$) and ^{212}Po ($\plus$), have been marked.

The Table 5.13 lists the estimated internal background arising from the Uranium and Thorium decay chains in Sn-Bi bolometers of various sizes. For the estimation, a radiopurity level similar to that of the CUORE bolometer [24] was assumed. These background contributions were compared to the contribution from ^{209}Bi α decay, also listed in the Table 5.13. For this comparison, 0.25 % Bi is considered, which is close to the lowest concentration found to be effective in the cooling tests. While the background contributions from ^{232}Th are α dominated in the ROI, the contribution from ^{238}U is β dominated. The primary contribution to the background from the U decay chain arises from the β decay of ^{214}Bi ($Q_\beta =$
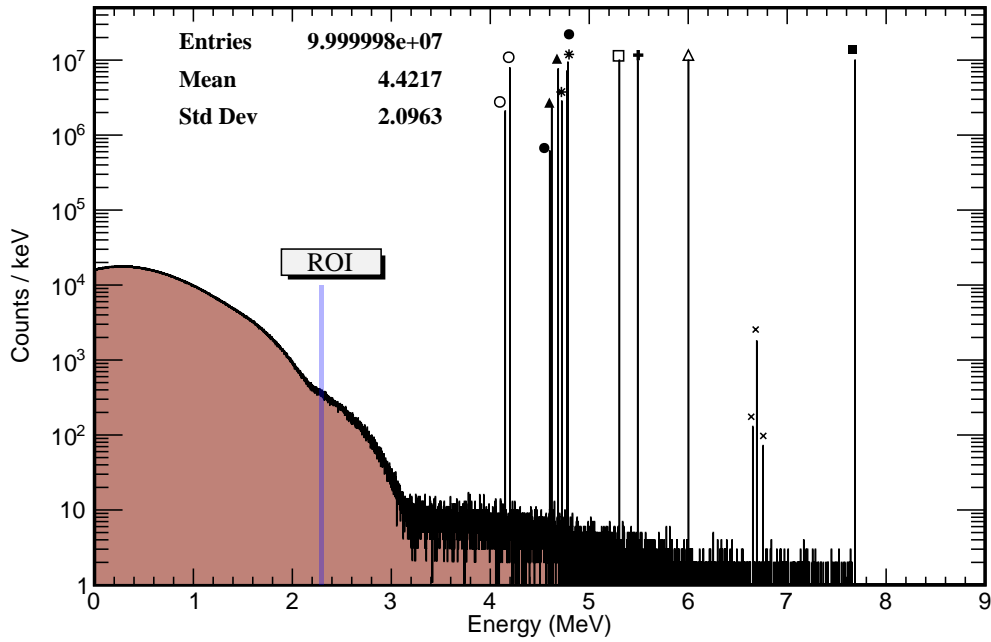
Figure 5.19: The typical simulated energy spectrum from ^{238}U decay chain arising from U impurities in a Sn-Bi bolometer (summed contributions of all products). The shaded blue box denotes the region of interest (ROI). The peaks from full energy deposition of the α particles, originating from ^{238}U($\circ$), ^{234}U ($\ast$), ^{230}Th($\blacktriangle$), ^{226}Ra($\bullet$), ^{222}Rn ($\boldsymbol{+}$), ^{218}Po($\triangle$), ^{218}At($\times$) , ^{214}Po($\blacksquare$) and ^{210}Po($\square$) have been marked.

3270 keV). The Uranium decay chain dominates the total internal background by around 2 orders of magnitude, while the radioactivity of ^{209}Bi has negligible effect on the background ($\sim 10^{-5}$ counts/(keV.kg.y)). Nevertheless, the total internal background is within the background budget of 10^{-2} counts/(keV.kg.y), which is typical for a bolometric experiment without particle discrimination against α decays. It is important to note that presently this estimation does not take into consideration coincident summing energy effects.

Table 5.13: Comparison of the estimated background from the trace impurities of Uranium and Thorium, compared to that from the α decay of ^{209}Bi for Sn-Bi bolometer.

Bolometer volume	Source	Impurity level	Background $counts/(keV.kg.y)$
	0.2 ppt	Th chain	5.7×10^{-5}
27 cc	0.2 ppt	U chain	5.6×10^{-3}
	0.25%	$^{209}Bi\ \alpha$ decay	2.6×10^{-5}
Total			5.7×10^{-3}
	0.2 ppt	Th chain	3.9×10^{-5}
64 cc	0.2 ppt	U chain	5.7×10^{-3}
	0.25%	$^{209}Bi\ \alpha$ decay	2.0×10^{-5}
Total			5.8×10^{-3}
	0.2 ppt	Th chain	3.1×10^{-5}
125 cc	0.2 ppt	U chain	5.8×10^{-3}
	0.25%	$^{209}Bi\ \alpha$ decay	1.6×10^{-5}
Total			5.8×10^{-3}

5.6 Projected sensitivity for the Sn-Bi bolometer

5.6.1 Efficiency of signal detection

As the signal for $0\nu\beta\beta$ is a peak at the $Q_{\beta\beta}$ value, true $0\nu\beta\beta$ events would be remain undetected in cases where the energy of the event is not fully contained:

- **Loss of surface events:** The range of 2.2 MeV electron in Sn-Bi (Bi <1% by mass) is 2.6 mm. Depending on the angle at which the electrons are emitted during the $0\nu\beta\beta$ event, the length travelled by the electron in Sn-Bi will be different. Thus, the following cases are possible:

  1. both electrons fully deposit their energy in the bolometer

  2. one electron escapes the bolometer after partially depositing its energy in the bolometer

3. both electrons escape the bolometer after partially depositing their energies in the bolometer.

Events with topologies that result in partial energy deposition as described in the cases (2) and (3) will not contribute to the region of interest. This results in a loss of efficiency for the bolometer.

- **Bremsstrahlung radiation:** The linear specific energy loss due to bremsstrahlung radiation is given by

$$-\frac{dE}{dx} = \frac{NEZ(Z+1)e^4}{137m_0^2c^4}\left(4\,ln\frac{2E}{m_0c^2} - \frac{4}{3}\right) \tag{5.3}$$

Due to its low rest mass, radiative energy loss due to bremsstrahlung is a significant effect for electrons, especially at relativistic velocities and in absorber materials with a large Z. The bremsstrahlung photons have a continuous energy spectrum, extending till the energy of the electron itself. For reference, the intensity of a 2 MeV γ ray beam would be reduce to half its original intensity after traversing a length of 2.3 cm in Sn. Hence, energy loss due to the escape of a bremsstrahlung photon is possible even in the case of events originating in the bulk region of the bolometer.

The single electron spectrum was generated as per the distribution given in [26]. The total energy of the electrons in the final state is constrained to be equal to $Q_{\beta\beta}$. Relativistic kinematics was used for the electrons. For the purpose of this simulation, the angular correlations between the final state electrons was ignored and they were generated independently. This assumption is justified as the bolometer is insensitive to the angular distributions of the final state electrons.

The simulation was benchmarked by calculating the efficiency of 125 cc TeO$_2$ crystals for the $0\nu\beta\beta$ signal of ^{130}Te. An efficiency of 86.6% was obtained using this code, which is similar to the reported efficiency of 88.4% [27].

The Figs. 5.20 and 5.21 show the full range and the zoomed view of the simulated energy spectrum for the generated $0\nu\beta\beta$ events. In addition to loss from surface and bremsstrahlung events, it was found that the x-ray escape peaks can also lead to the loss of efficiency of the bolometer. The efficiencies for the bolometers are tabulated in Table 5.14.
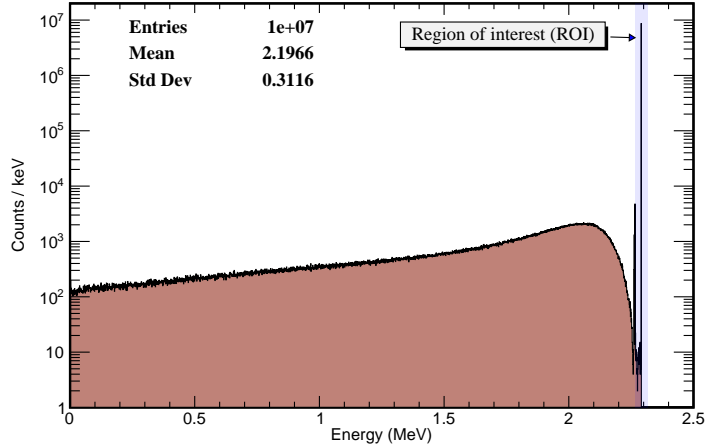
Figure 5.20: Typical simulated energy spectrum showing the energy deposited by $0\nu\beta\beta$ events in the Sn-Bi bolometer.
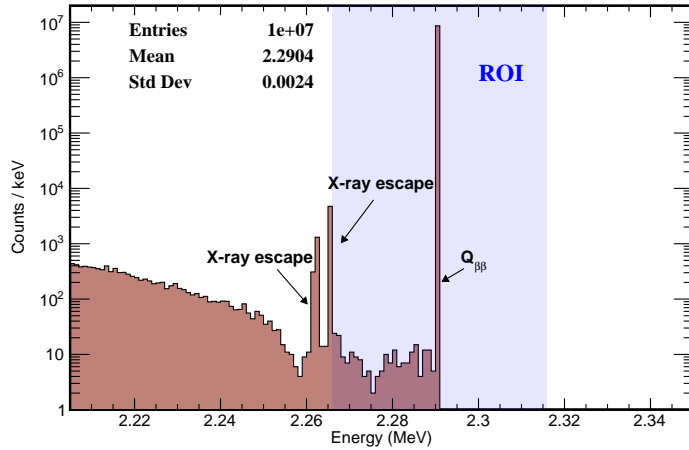
Figure 5.21: Zoomed view of the energy spectrum around the region of interest (ROI).

Table 5.14: Simulated efficiency corresponding to the full energy deposition events for the Sn-Bi bolometers.

Bolometer volume	Efficiency
27 cc	86.6 %
64 cc	89.0 %
125 cc	90.7 %

Using the simulated efficiency for a 27 cc Sn-Bi bolometer and assuming an energy resolution of 5 keV (σ_E), the projected sensitivity for the half-life $T^{0\nu}_{1/2}(1\sigma)$ was estimated for both natural and enriched (90% ^{124}Sn). The projected sensitivity as a function of detector runtime has been shown in Fig. 5.22.
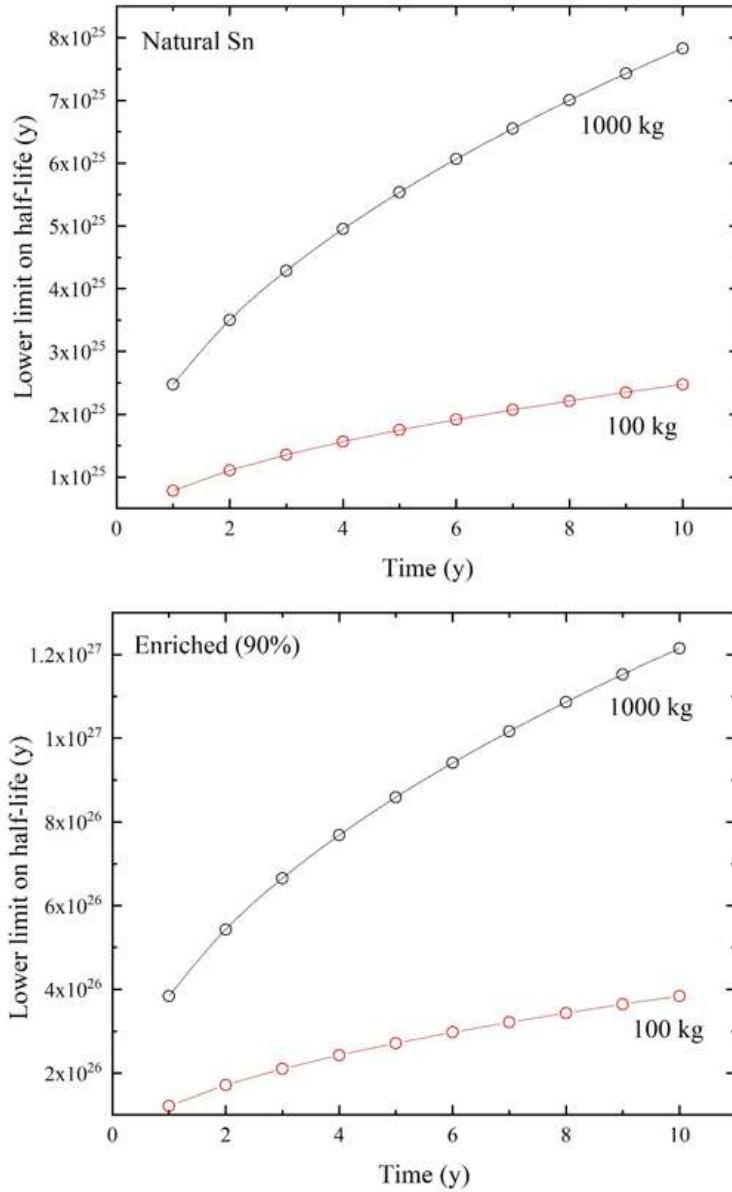
Figure 5.22: The projected sensitivity for *TIN.TIN*, using the efficiency of a 27 cc bolometer and assuming an energy resolution of 5 keV (σ_E).

5.7 Summary

Radiation background studies for Sn-Bi bolometers were performed in order to check its suitability for NDBD. The Sn-Bi crystals were synthesized and subsequently assessed for radiopurity in the TIFR low background experimental setup (TiLES). No additional γ lines or enhancements compared to the ambient background were found at the measured sensitivity level. Neutron activation of Sn-Bi was performed at the Pelletron Linac Facility, TIFR Mumbai. No activation channels from Bi or any possible impurities in the crystal were

measured. All the activity could be attributed to products produced from neutron activation channels in Sn.

^{209}Bi can decay by emitting an α particle of 3.1 MeV. However, the α decay is extremely rare, having a half-life of $\sim 2 \times 10^{19}y$ (comparable to the typical half-life of a $\beta\beta$ candidate). The background from surface activity of ^{209}Bi was estimated using GEANT4 simulations. The anticipated internal background from U/Th impurities was also simulated and compared to the background from ^{209}Bi α decay. The β decay from ^{214}Bi (product of the ^{238}U chain) was found to be the limiting background, while the radioactivity of ^{209}Bi had negligible effect on the background ($\sim 10^{-5}$ counts/(keV.kg.y)).

Chapter 6

Summary and Future Scope

This thesis explores the suitability of potential Sn alloy candidates for the *TIN.TIN* bolometer. The summary and future outlook are presented in this chapter.

6.1 Summary

The observation of the hypothesized $0\nu\beta\beta$ decay would conclusively establish the Majorana nature of the neutrino, and provide insights into physics beyond the standard model. Several experimental programmes across the world are pursuing this goal. In India, R & D has been initiated for the India-based tin detector (*TIN.TIN*), which proposes to use a large superconducting bolometer array to search for $0\nu\beta\beta$ decay in ^{124}Sn.

The goal of developing a cryogenic Sn bolometer array having a large mass and operating for a period of several years can be critically undermined by the phenomenon of tin pest. Tin pest is an allotropic phase transition in Sn which can occur when Sn is cooled down, wherein metallic β-Sn transforms to semiconducting α-Sn. The phase transition is associated with a change in its crystal structure, leading to a sudden increase in the volume of the sample by 27%. This leads to the cracking and disintegration of the Sn sample, and can even result in

129

powdering of the sample. A pure Sn bolometer array is susceptible to the formation of tin pest, during the thermal cycling of the cryostat between mK and room temperatures. The formation of even a small mass of α-Sn could act as a seed, catalyzing the transformation of larger masses of Sn. Therefore, it is of utmost importance to inhibit or strongly suppress the formation of tin pest, for the longevity and performance of the superconducting bolometer array.

Although it is well known that alloying Sn with an appropriate element can hinder the transformation, there are large variations in the observations quoted in the literature with regard to the efficacy of alloying elements and the concentrations in which they are useful. The main thrust of this thesis was to qualify a Sn-rich binary alloy for which:

- tin pest would be inhibited or strongly suppressed.

- the superconducting critical temperature T_c would be close to the value of pure tin, i.e., 3.71 K.

- the introduction of the alloying element into the Sn matrix should not significantly change the radiation background in the region of interest around $Q_{\beta\beta}$.

Several alloy candidates (Sn-Bi, Sn-Cd, Sn-Cu, Sn-In, Sn-Pb and Sn-Sb) were fabricated and tested for resistance against tin pest by means of seeded cooling tests. Note that the starting purity of the materials used was very high - the Sn was 99.99999% and the alloying elements were at least 99.999% pure. In terms of inhibition of tin pest, Sn-Bi, Sn-In and Sn-Sb showed promise in early tests at around 0.5% - 0.6% alloying by mass. However, the anticipated neutron background from Sn-Sb and Sn-In made them unsuitable for fabricating a rare decay bolometer. The reaction channels of concern would lead to the production of β emitters with end point energy $> Q_{\beta\beta}$. Namely, these channels were ^{115}In$(n, \gamma)^{116}$In, ^{123}Sb$(n, \gamma)^{124}$Sb and ^{121}Sb$(n, \alpha)^{118}$Sb. The reaction channel ^{123}Sb$(n, \gamma)^{124}$Sb also has a weak γ peak at 2294 keV ($I_\gamma = 0.032\%$) which is close to the expected peak at $Q_{\beta\beta} = 2291 \ keV$. In addition to the issues of the anticipated neutron induced background in Sn-In, 0.1% Sn-In was found to be susceptible to tin pest.

The Sn-Bi crystals showed the most promise and were extensively explored. Several crystals were fabricated with successively lower concentrations of Bi (down to 0.08% Bi by mass), and tested for resistance to tin pest. The best performance was observed in 0.22% Sn-Bi, which has resisted the formation of tin pest for >1 y at the time of writing this thesis. It should also be mentioned that although the Sn-Bi sample with a lower concentration (0.08% Sn-Bi) alloy developed tin pest eventually, it survived for around 66 days without showing signs of tin pest. Moreover, the growth of the α phase was found to be severely hindered in the 0.08% Sn-Bi sample, resulting in a very slow rate of transformation even under conditions optimal for the growth of the α-phase.

Measurements of the superconducting critical temperature T_c of the Sn-Bi samples (0.08% - 1.69% Bi by mass) revealed that the critical temperature was similar to that of pure tin. Thus, it should be possible to fabricate superconducting Sn-Bi bolometers which are resistant to tin pest.

The allotropic transition $\beta \rightleftharpoons \alpha$ transition in tin, which forms the central challenge to the stability of Sn bolometers, is itself an extremely interesting phenomenon. Recently, it has been pointed out that this phase transition provides a sensitive test for the accuracy of density functionals and computational methods. Therefore, a precision measurement of the phase transition temperature is very important. Although the phenomenon of tin pest has been studied for at least a century, there were several inconsistencies in the literature regarding the $\alpha \leftrightharpoons \beta$ transition temperature. The transition was revisited with the use of modern material characterization techniques as a part of this thesis, with the aim to learn more about the phase transition and adopt an appropriate strategy to mitigate the risk of tin pest formation in *TIN.TIN*. Improved measurements of the $\alpha \rightarrow \beta$ transition were performed to extract the transition temperature using the following techniques:

- differential scanning calorimetry

- temperature resolved scanning electron microscopy

- conventional and synchrotron x-ray diffraction

The transition was found to occur between 30°C and 34°C, instead of 13.2°C, which is often

quoted in the literature. This was also consistent with the observed stability of the sample at room temperature. Based on these measurements, it is suggested that the *TIN.TIN* array should be baked at ~ +50°C between thermal cycles, to reconvert any α-Sn which may have formed. If used in conjunction with the alloying of Sn with Bi, it is unlikely that tin pest would affect the bolometer array. This baking protocol would also be useful in other critical systems that use lead-free solders and operate in extreme conditions.

It is well known that the sensitivity of $0\nu\beta\beta$ experiments depends on the background in the region of interest. Hence, radiation background studies were performed for Sn-Bi bolometers in the region of interest around $Q_{\beta\beta}$ (2291 $\pm$ 25 keV for ^{124}Sn) to assess whether the introduction of Bi into the Sn matrix significantly changes the background. The radiopurity of the Sn-Bi alloys fabricated at TIFR was assessed by γ spectroscopic measurements in the TIFR low background experimental setup. No new γ lines or enhancements were observed in the spectra of the Sn-Bi samples in comparison to the background or Sn, at the measured sensitivity level.

Neutron Activation Analysis was used to investigate the short and long lived neutron-induced activity in Sn-Bi alloys. The samples (Sn, Bi, Sn-Bi and Fe) were irradiated with fast neutrons at the 6 m target setup of the Pelletron Linac Facility, TIFR Mumbai. Fast neutrons were generated through the ^{9}Be(p, n)^{9}B reaction (Q_{th}= 2.057 MeV) by using proton beams with energy E_p = 15 - 21 MeV on a ^{9}Be target, upto a maximum flux of $\phi_n \sim 10^6$ n $\cdot$ cm$^{-2} \cdot$ s^{-1}. The activated samples were counted offline. No activity arising from either Bi or any impurity in the Sn-Bi samples was found. Instead, all the activity could be attributed to reaction products arising from the neutron activation channels of Sn.

^{209}Bi undergoes a very rare α decay with a half-life of 2.0 $\times$ 10^{19} y which is comparable to the half-lives of some $2\nu\beta\beta$ emitters. Nevertheless, the surface events can become a source of internal background for $0\nu\beta\beta$ in ^{124}Sn. The α background from this decay was simulated for Sn-Bi bolometers for various detector sizes (27, 64 and 125 cc) and Bi alloying concentrations (0.25%, 0.5%, 0.75% and 1.0%). For comparison, the internal background contribution anticipated from the primordial ^{238}U/^{232}Th impurities was also simulated. The background arising from the ^{238}U decay chain was found to be the dominant background source. Despite this, the anticipated total background from these sources was within the

background limit of 10^{-2} cts/(keV.kg.y), which is typical for a first generation bolometric experiment without particle discrimination.

The efficiency of $0\nu\beta\beta$ detection was estimated for Sn-Bi bolometers of different sizes. For this purpose, a GEANT4 based $0\nu\beta\beta$ event generator was developed. The efficiencies were found to be 86.6% (27 cc), 89.0% (64 cc) and 90.7% (125 cc). The sensitivity of *TIN.TIN* for $0\nu\beta\beta$ was calculated for a range of enrichment percentages (natural - 99%) and detector sizes using these simulated efficiencies.

In conclusion, this thesis provides important inputs towards the consideration of a suitable Sn-rich alloy for a superconducting bolometer. Based on this work, a 0.22% Sn-Bi alloy (Bi by mass) is suggested to be a good candidate for the fabrication of superconducting bolometers for *TIN.TIN*.

6.2   Future Outlook

The alloy Sn-Bi appears to be a promising candidate for the fabrication of superconducting bolometers. It is important to exhaustively explore experimental aspects which can affect the performance of Sn-Bi bolometers. A few possible directions for future research are listed below:

6.2.1   Thermal neutron induced background in ^{209}Bi

As mentioned earlier, one of the reasons Bi is preferable to Sb and In as an alloying element was due to neutron capture reactions of concern in In and Sb which would lead to the production of internal β backgrounds. As can be seen from Table 6.1, the neutron capture cross-sections for ^{209}Bi are smaller in magnitude compared to ^{115}In, ^{123}Sb and even ^{124}Sn. It is anticipated that the only contributions to the background in the ROI from the thermal neutron capture reactions in Bi should result from α emitters generated due to the activation of the Bi, as opposed to the β emitters which create background in the cases of In and Sb. This is relevant as the α activity is further suppressed greatly by the surface to volume ratio while β activity is not. The fast neutron induced background in Sn-Bi and Bi were investigated in this thesis by neutron activation studies at PLF, TIFR Mumbai, and no reaction channels in Bi

were observed. It would be interesting to perform a neutron activation study by irradiating the samples with thermal neutrons at the Dhruva research reactor, which is capable of providing a high fluence of thermal neutrons ($\sim 10^{18}n/cm^2$). This experiment would be along similar directions of an earlier experiment by Letourneau *et. al.* [143], and would be useful in validating the anticipated reaction channels.

Table 6.1: Neutron capture cross-sections $\sigma(n,\gamma)$ for ^{209}Bi, ^{115}In, ^{123}Sb and ^{124}Sn, taken from NNDC database.

Nucleus	$\sigma(n,\gamma)$ (b)
^{209}Bi	3.381×10^{-2}
^{124}Sn	1.337×10^{-1}
^{123}Sb	3.875
^{115}In	$2.022 \times 10^{+2}$

The following are the radiative neutron capture channels in ^{209}Bi:

$$^{209}Bi(n,\gamma)^{210}Bi \xrightarrow{\beta^-} {}^{210}Po$$

$$^{209}Bi(n,\gamma)^{210m}Bi \xrightarrow{\alpha} {}^{206}Tl$$
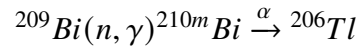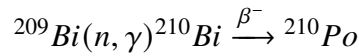
The decay scheme has been shown in Fig. 6.1. ^{210}Bi is a β^- emitter having a half-life
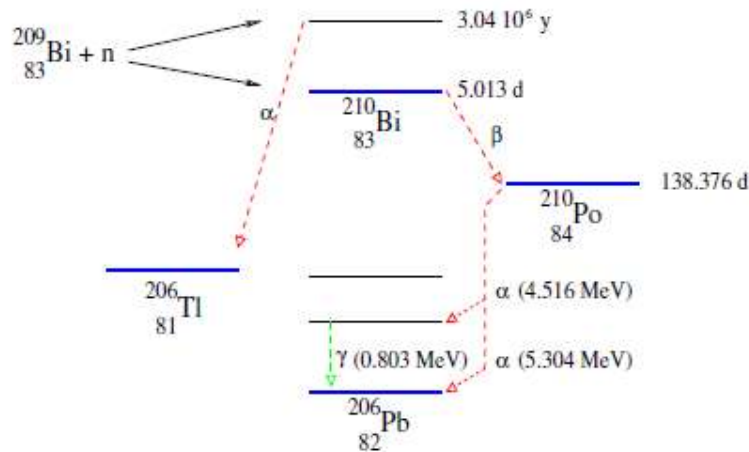
Figure 6.1: The neutron capture on ^{209}Bi, taken from [143].

$T_{1/2} = 5.012$ d, which decays to the ground state of ^{210}Po. The end point of the energy spectrum of ^{210}Bi is 1162.2 keV. ^{210}Po mainly decays via the emission of 5304 keV α particle. ^{210}Po can also decay by emitting a 4516 keV α particle followed by a subsequent

γ having energy 803.06 keV. However, the intensity associated with this branch is extremely small, with the $I_\gamma = 0.001\%$ for 803.06 keV. The final daughter is the stable isotope ^{206}Pb.

^{210m}Bi is a long-lived metastable state, having a half-life 3.04×10^6 y. Due to its longer half-life, it is of secondary concern. Nevertheless, the decay is described for the sake of completeness. ^{210m}Bi decays to ^{206}Tl via the emission of α particles 4568 keV ($I_\alpha = 3.9\%$), 4582 keV ($I_\alpha = 1.4\%$), 4909 keV ($I_\alpha = 39.5\%$) and 4946 keV ($I_\alpha = 55\%$). This decay mode is followed by subsequent γ from the de-excitation of ^{206}Tl, leading to γ having energies 265.6 keV, 304.6 keV and 649.4 keV. ^{206}Tl is a short-lived β emitter with $T_{1/2} = 4.202$ min, having an end point energy of 1532.3 keV. Again, the final daughter is the stable isotope ^{206}Pb. In this series of decays, the rate limiting step is the production of ^{206}Tl via the decay of the long-lived ^{210m}Bi.

It is unlikely that the singles events of the β / γ decays described above would contribute to the background index, since their energies were less than 2 MeV. The activity from the α decays would contribute to the background, but this is expected to be a relatively small contribution due to the following reasons:

- The population of the neutron activated products are expected to be low due to the small doping of Bi in the alloys, combined with the small cross-sections for neutron capture in Bi.

- Only the surface events would contribute to the background.

Since the expected intensities for the γ at 803.06 keV are expected to be low, it would be more interesting if both α and γ spectroscopy could be performed for the activated samples, to acquire complementary data.

6.2.2 Exploring coincident energy summing contributions in the U/Th decay simulations

In the present simulations, the internal activity of the U/Th radioactive decay chains are estimated by accounting for the weighted contributions from individual radionuclides in the chain. The background is dominated by the β background from ^{214}Bi. These estimates

are conservative, and can be further improved by considering potential coincident energy summing effects.

When operated in the equilibrium mode, bolometers are relatively slow detectors having pulses with an anticipated rise time of ~10 ms and fall time of 0.1 - 1 s [10]. Energy deposition events which are coincident within few ms cannot be discriminated, and the total energy deposited ($E_1 + E_2$) is observed as a single event. Coincident energy summing events may arise from short-lived cascades in the radioactive decay chain or from chance coincidence, although the contribution from the latter is expected to be small when U/Th contamination is at the sub-ppt level.

^{214}Bi-^{214}Po is an important cascade in the Uranium decay chain, wherein ^{214}Bi decays to the short lived ^{214}Po ($T_{1/2}$ = 164.3 μs). The end point of the ^{214}Bi β spectrum is 3270 keV and the daughter nucleus ^{214}Po decays by the emission of an α particle having energy 7686.82 keV. When a coincident energy summing Bi-Po event occurs in the bulk region of the bolometer, the total energy deposited by the emitted α and β particles would effectively be recorded as a single event. In these cases, the energy deposited would be $\geq$ 7686.82 keV, thereby greatly reducing the contribution of ^{214}Bi events to the background in the region of interest around $Q_{\beta\beta}$.

Since α particles generally have energies > 3 MeV, the coincident summing of α-β events will shift events to higher energies, leading to an overall decrease in the background ROI. On the other hand, the coincident summing of β-β events may lead to an increase in the background ROI. Potential candidates for these events can be identified and studied.

6.2.3 Heat capacity measurements of the Sn-Bi alloys below 400 mK

As described previously, the superconducting T_c of the Sn-Bi samples were measured and found to be consistent with that of pure Sn. This would imply that the exponential suppression of the electronic heat capacity for the Sn-Bi alloys should be similar to that of pure Sn. In the absence of any anomalous contributions to the heat capacity, Sn-Bi would behave like a Debye solid $C \propto T^3$ and the bolometer performance would not be expected to be affected by the alloying of Bi in Sn. However, it would be advantageous to assess the presence of

anomalous contributions to the heat capacity by measuring the heat capacity of the Sn-Bi absorber at temperatures below 400 mK.

The anomalous contributions to the heat capacity may arise from Schottky-type magnetic terms ($\propto T^{-2}$) or due to the interactions of the nuclear electric quadrupole moment with the electric field gradient. In particular, the heat capacity contribution from electric quadrupole moment interactions may be of concern in crystal systems without cubic symmetry and for nuclear spin $I \neq 1/2$ [103]. These contributions were ruled out in the case of pure Sn [144], but should be investigated in the case of Sn-Bi.

Since Bi has 83 protons (odd) and 126 neutrons (even), it has a ground state nuclear spin $I = 9/2^-$ which would generate a non-zero quadrupole moment Q. Due to the tetragonal symmetry of the crystal, the quadrupole moment would interact with the electric field gradient V_{zz} resulting in an interaction energy of

$$E_m = \frac{e^2 V_{zz} Q}{4I(2I-1)}[3m^2 - I(I+1)] \tag{6.1}$$

In the high temperature approximation, the heat capacity due to the spin degree of freedom is given by [103]

$$C_Q = \alpha \left(\frac{e^2 V_{zz} Q}{k_B T}\right)^2 - \beta \left(\frac{e^2 V_{zz} Q}{k_B T}\right)^3 + ... \tag{6.2}$$

where the constants α and β are given by

$$\alpha = \frac{R}{80} \frac{(2I+2)(2I+3)}{(2I-1)2I} \tag{6.3}$$

and

$$\beta = \frac{R}{1120} \frac{(2I-3)(2I+2)(2I+3)(2I+5)}{(2I-1)^2(2I)^2} \tag{6.4}$$

These relations would be further modified if Zeeman splitting effects are significant.

If anomalous contributions to the heat capacity are present, these terms would become increasingly important at low temperatures and may even limit the working temperature of the bolometer.

Therefore, it is important to assess the contributions to the heat capacity of Sn-Bi at low temperatures. The low temperature heat capacity measurements would also be useful in the thermal modelling [10] of the Sn-Bi bolometer signal, in order to predict its behaviour and optimize the heat links.

6.2.4   Synergy with other rare event studies

If a large scale bolometer array is fabricated from Sn-Bi, there is scope to pursue other avenues of research in addition to neutrinoless double beta decay, due to the synergy between the technological requirements of rare decay experiments. A few examples are as follows:

- Due to their low energy thresholds, bolometric detectors are often used in dark matter searches.

- The $2\nu\beta\beta$ decay spectrum of ^{124}Sn has not yet been measured.

- The rare α decay of ^{209}Bi to the ground state of ^{205}Tl was first measured using a 45.7 g scintillating bolometer fabricated from BGO, which acquired data for ~5 d [140]. The statistics were combined with another BGO bolometer having mass 91.2 g. The decay of ^{209}Bi to the first excited state of ^{205}Tl was later measured by a different group using an 889 g BGO bolometer, using 15.6 d of data [140]. These seminal experiments truly illustrate the sensitivity of bolometers for rare decays. The *TIN.TIN* detector array will acquire data for much longer periods of time (~ years), and it would therefore be possible to acquire even better statistics for the rare α decay of ^{209}Bi if a 0.22% Sn-Bi bolometer array is used.

- ^{209}Bi is a candidate for the rare simultaneous double alpha decay, with a theoretical half-life of 3.4×10^{116} y. Clearly, this is unlikely to cause concern as a background for *TIN.TIN* and there is no discovery potential in the current experimental scenario. However, the best experimental limit has been set at $> 2.9 \times 10^{20}$ y (90% C.L.) [145] using the data from [23]. This can be improved by at least two orders of magnitude, if a 0.22% Sn-Bi bolometer array having mass 1000 kg and runtime 10 y is considered.

6.2.5 Topological phase transitions in novel semiconducting phases of tin alloys

In recent years, α-Sn has generated a lot of interest due to its tunable topological properties (see Fig. 6.2). It also holds the distinction of being the only known elemental member of a class of 3-D topological materials known as Topological Dirac Semimetals.
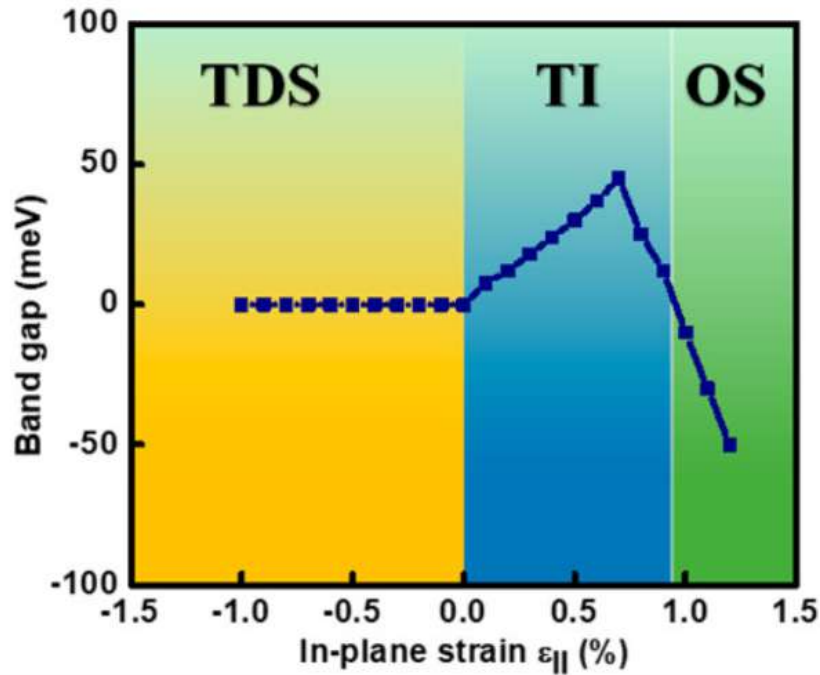
Figure 6.2: The topological phases of α-Sn, depending on the strain in the lattice. In the presence of an in-plane compressive strain, it becomes a Topological Dirac Semimetal (TDS). On the other hand, if an in-plane tensile strain is applied, it could transition to a Topological Insulator (TI) or an Ordinary Semimetal (OS). This image has been taken from [111].

There is a hope that its novel topological properties may be exploited to form the basic unit of a quantum computer in the future. The research on the topological phases of α-Sn has largely been performed on epitaxially grown samples. There were two main justifications behind the preference of epitaxial films as opposed to bulk α-Sn samples:

- It was believed that bulk α-Sn was not stable above 13.2°C.

- The strain in the epitaxial films could be tuned, in order to explore different topological phase transitions.

Investigations of the $\alpha \rightarrow \beta$ phase transition in Sn described in this thesis suggest that α-Sn is more stable at room temperature than was previously believed. It would be interesting

139

to explore the topological properties of unstrained bulk α-Sn. Additionally, the process of alloying can be exploited to induce a compressive or tensile strain in the crystal. This could open avenues to search for the existence of novel topological phases in the alloys which were found to be susceptible to tin pest.

Appendix A

Appendix

A.1 Initial cooling tests in the CFDR-1200

The initial cooling tests were performed in the CFDR-1200, utilizing the thermal cycles during the cooldown from room temperature to mK and warmup from mK to room temperature. The tests are summarized in the Table A.1. The following inferences were drawn from the initial tests performed in the CFDR-1200:

- Seeding is necessary to accelerate the transformation process, and reliably test for inhibition against tin pest.

- Under the experimental conditions of the cooling and warming cycles in the CFDR-1200, no effect from the cryogenic glues on the formation of tin pest could be observed.

- While Ge has a diamond cubic structure, it is unlikely that the NTD Ge thermistor stuck to the tin absorber using a cryogenic glue can act as a seed.

- 0.1% Sn-In (In by mass %) can suppress tin pest but cannot inhibit it. After surviving 4 thermal cycles, it shows signs of tin pest after 6 thermal cycles (3 warming + 3

cooling). Fig. A.2 shows a picture of the sample.

Cooling tests performed in the CFDR-1200 are inefficient since they only a few hours of exposure time is gained in typically two - three weeks operation time. For example, the mixing chamber remains in the temperature window -50°C to 13°C for 24 h, when no external heater is used during the warmup process. The subsequent cooling tests were performed in a deep freezer to gain larger exposure time.

Table A.1: Details of the initial cooling tests performed in the CFDR-1200. The motivation of each run is also listed.

Sample	Thermal cycles[a]	Tin pest
To check if grain boundaries and defects of a polycrystalline sample trigger the transformation		
5N Polycrystalline Sn	2 + 2	No
To compare performance of the Sn single crystal		
Sn single crystal	2 + 2	No
To check if the cryogenic glues trigger the transformation		
GE varnish + Sn	2 + 2	No
N-Grease + Sn	2 + 2	No
Araldite + Sn	2 + 2	No
To check if Ge glued to Sn can trigger the transformation		
virgin Ge + Araldite + Sn	2 + 2	No
virgin Ge + GE varnish + Sn	1 + 1	No
To confirm if seeding trigger the transformation		
seed + GE varnish + Sn	1 + 1	Yes
seed + N-Grease + Sn	1 + 1	Yes
seed + Araldite + Sn	1 + 1	Yes
seed + virgin Ge + Araldite + Sn	2 + 2	Yes
To check if tin-rich Sn-In crystal can inhibit tin pest		
seed + 0.1% Sn-In (In by mass %)	3 + 3	Yes

[a]cooling cycles + warming cycles

142
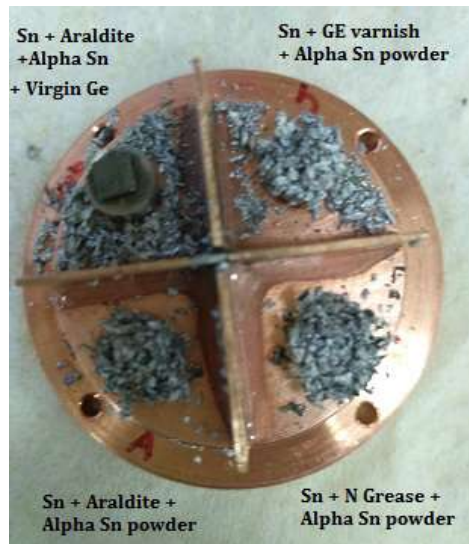
Figure A.1: Seeded cooling test of 5N tin + addenda after 1 cooling and 1 warming cycle. The virgin Ge + araldite + Sn sample showed signs of tin pest after an additional seeded cooling test.

Figure A.2: 0.1% Sn-In (In by mass %) shows signs of tin pest after 3 warming and cooling thermal cycles in the CFDR-1200.

A.2 Anticipated neutron induced background from Sn-In and Sn-Sb

Both In and Sb have large thermal neutron capture cross sections, and are used as activation materials for estimating the thermal neutron fluence. For example, In has been used to monitor the reactor intensities in the reactor core of the Tsing Hua Open-pool reactor [146], while the activation of trace impurities of Sb in device grade Ge is used to estimate the thermal neutron fluence incident for Neutron Transmutation Doped Ge sensors [147].

Natural In consists of 95.7% ^{115}In (σ_{th} = 202.2 b) and 4.3% ^{113}In (σ_{th} = 12.1 b) and natural Sb consists of 57.2% ^{121}Sb (σ_{th} = 5.773 b) and 42.8% ^{123}Sb (σ_{th} = 3.875 b). Activation of In and Sb are known to lead to the production of several radioactive products. The (n,γ) reactions in In and Sb lead to radionuclides with half-lives ranging from 14.1 s to 49.5 d and 1.6 min to 60.2 d, respectively. The cross sections of interaction for other neutron induced reactions such as (n,n'), (n,2n), (n,3n) and (n,α) are also non-negligible. Neutron induced reactions in In and Sb which lead to the production of β emitters with Q_β > 2.3 MeV contribute to the background ROI. The reaction channels of concern are listed in Table A.2.

Table A.2: Neutron activation channels in In and Sb, which will contribute to the background in the region of interest.

Activation channel	Decay mode	Half-life	End Point(keV)
$^{115}In(n,\gamma)^{116}In$	β^- (99.98%)	14.10 s	3278
$^{123}Sb(n,\gamma)^{124}Sb$	β^- (100%)	60.2 d	2301.6 [a].
$^{121}Sb(n,\alpha)^{118}In$	β^- (100%)	5.0 s	4423

[a]This channel is also associated with a weak γ line having energy of 2294.0 keV (I_γ = 0.032%), which is very close to $Q_{\beta\beta}$

A.3 Supporting data for the superconductivity of the Sn-Bi alloys

The DC magnetization measurements performed on the SQUID MPMS to measure the superconducting critical temperature T_c have been described in Chapter 3. Additional heat capacity and vibrating sample magnetometry measurements were performed to verify the superconductivity measurements of the Sn-Bi alloys. The superconductivity of the Sn-Bi samples was found to be robust, and the supporting data is presented in brief in the following subsections.

A.3.1 Heat capacity measurements for Sn-Bi alloys

As the transition from the superconducting state to the normal state is a second order phase transition, the heat capacity of the sample is discontinuous at the critical temperature T_c. The low temperature heat capacity data of the pure tin (7N, Alfa Aesar) and Sn-Bi samples were acquired on the Physical Property Measurement System (Quantum Design, USA). The sample mounting on the heat capacity puck (PK578) can be seen in Fig. A.3.
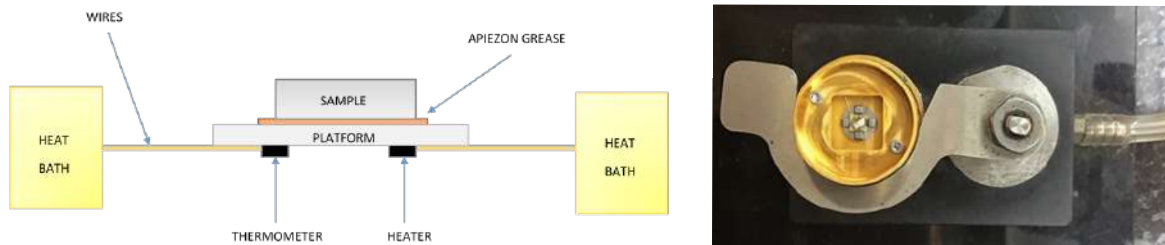
Figure A.3: The sample mounting on the heat capacity puck (PK578).

In the interest of time, the addendum data was used for the correction, in order to extract the heat capacity of the alloy. Therefore, the absolute magnitude of the heat capacity of the samples cannot be compared in this run. However, the extracted superconducting transition temperature T_c was not affected. The heat capacity data for the Sn-Bi samples are shown in Figs. A.4a- A.4c.

(a) Sn

(b) 0.08% Sn-Bi

(c) 1.69% Sn-Bi
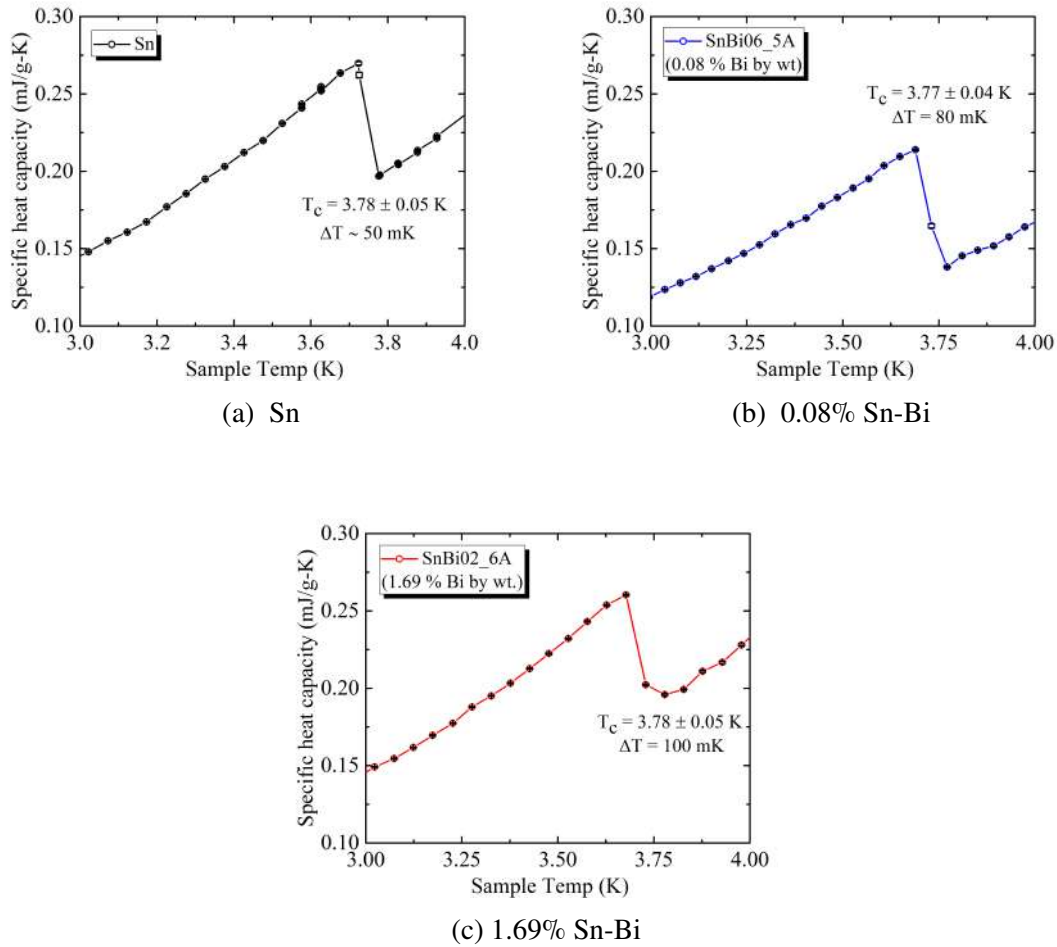
Figure A.4: Low temperature heat capacity measurements for the Sn-Bi samples.

A.3.2 Vibrating Sample Magnetometry

Magnetization data for the Sn-Bi samples was acquired in the vibrating sample magnetometry (VSM) mode on a MPMS3 (Quantum Design, USA). The samples were mounted in brass holders with GE varnish, which were then coupled to the sample rod. An external magnetic field of 10 gauss was used for the measurements. Data was also acquired for pure tin (7N, Alfa Aesar) in order to use it as a reference. The VSM data for the Sn-Bi samples and the Sn reference are shown in Fig. A.5. Table A.3 lists the extracted superconducting critical temperature (T_c) for the samples.
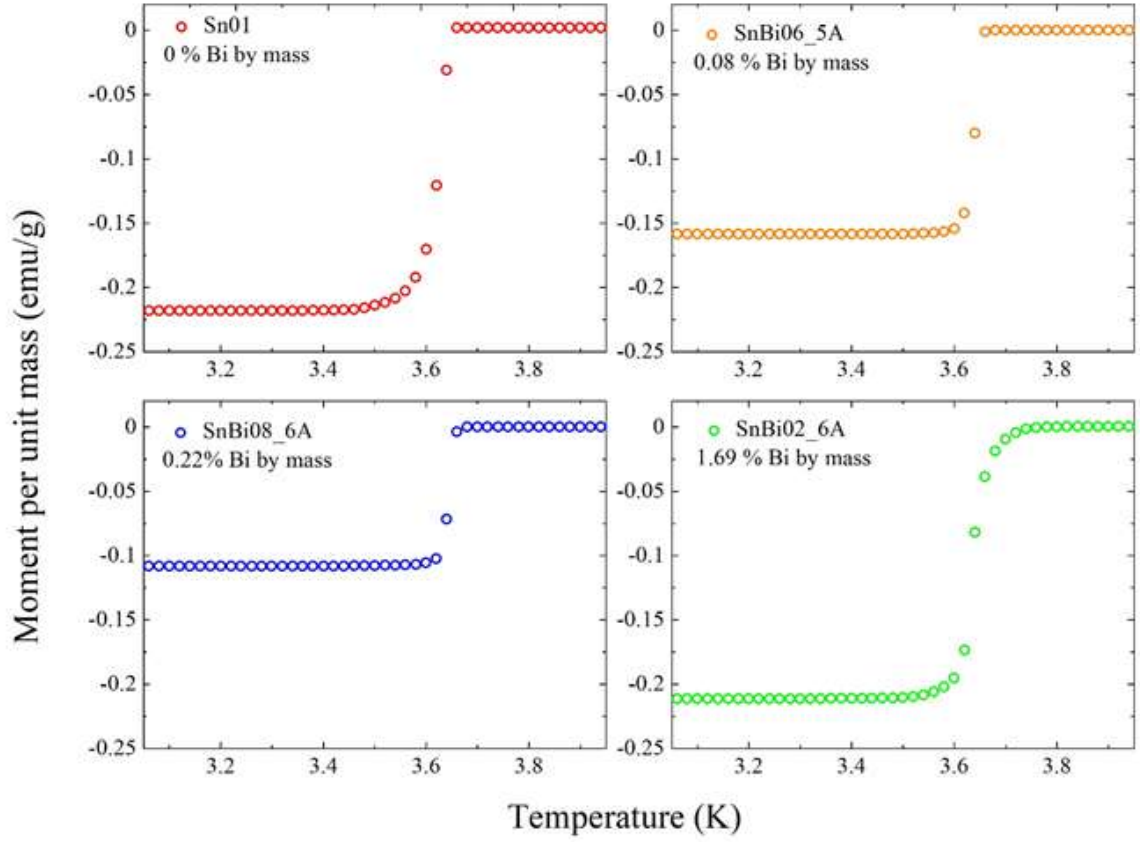
Figure A.5: Vibrating sample magnetometry data for the Sn-Bi samples acquired on the Quantum Design MPMS3.

Table A.3: The extracted superconducting critical temperatures T_c for the Sn-Bi samples (SQUID VSM data).

Bi % (mass %)	T_c (K)
0	3.66 ± 0.02
0.08	3.68 ± 0.02
0.22	3.70 ± 0.02
1.69	3.76 ± 0.02

Bibliography

[1] R. Wendell et al. "Atmospheric neutrino oscillation analysis with subleading effects in Super-Kamiokande I, II, and III". In: *Phys. Rev. D* 81 (2010), p. 092004. DOI: `10.1103/PhysRevD.81.092004`.

[2] B. Aharmim et al. "Combined analysis of all three phases of solar neutrino data from the Sudbury Neutrino Observatory". In: *Phys. Rev. C* 88 (2013), p. 025501. DOI: `10.1103/PhysRevC.88.025501`.

[3] Michelle J. Dolinski, Alan W. P. Poon, and Werner Rodejohann. "Neutrinoless Double-Beta Decay: Status and Prospects". In: *Annu. Rev. Nucl. Part. Sci.* 69 (2019), pp. 219–251. DOI: `10.1146/annurev-nucl-101918-023407`.

[4] Vandana Nanal. "Search for neutrinoless double beta decay in ^{124}Sn". In: *EPJ Web Conf.* 66 (2014), p. 08005. DOI: `10.1051/epjconf/20146608005`.

[5] S. Pirro and P. Mauskopf. "Advances in Bolometer Technology for Fundamental Physics". In: *Annu. Rev. Nucl. Part. Sci.* 67 (2017), pp. 161–181. DOI: `10.1146/annurev-nucl-101916-123130`.

[6] A. Mazumdar et al. "Studies on $\beta \rightleftharpoons \alpha$ transition in Sn and Sn-rich alloys for a cryogenic tin bolometer". In: *Mater. Res. Express* 6 (2019), p. 076521. DOI: `10.1088/2053-1591/ab13c1`.

[7] Neil Douglas Burns. "A Tin Pest Failure". In: *J. Fail. Anal. Prev.* 9 (2009), pp. 461–465. DOI: 10.1007/s11668-009-9280-8.

[8] A. K. Sinha et al. "Angle Dispersive X-ray Diffraction Beamline on Indus-2 Synchrotron Radiation Source: Commissioning and First Results". In: *J. Phys.: Conf. Ser* 425 (2013), p. 072017. DOI: 10.1088/1742-6596/425/7/072017.

[9] V. Singh et al. "Cryogen-free dilution refrigerator for bolometric search of neutrinoless double beta decay ($0\nu\beta\beta$) in ^{124}Sn". In: *Pramana* 81 (2013), pp. 719–725. DOI: 10.1007/s12043-013-0601-9.

[10] Abhijit Garai. "R&D aspects of cryogenic bolometer development for neutrinoless double beta decay search in ^{124}Sn". PhD thesis. 2019.

[11] W. J. Plumbridge. "Tin pest issues in lead-free electronic solders". In: *J. Mater. Sci. Mater. Electron.* 18 (2007), pp. 307–318. DOI: 10.1007/s10854-006-9025-3.

[12] Ben Cornelius et al. "The phenomenon of tin pest: A review". In: *Microelectronics Reliability* 79 (2017), pp. 175–192. DOI: 10.1016/j.microrel.2017.10.030.

[13] Agata Skwarek et al. "Inoculator dependent induced growth of α-Sn". In: *Materials Chemistry and Physics* 166 (2015), pp. 16–19. DOI: 10.1016/j.matchemphys.2015.09.017.

[14] K. Ojima, H. Matsumoto, and Y. Taneda. "Differential scanning calorimetry study of the $\alpha \rightarrow \beta$ transition in tin". In: *Journal of the Less Common Metals* 157.1 (1990), pp. L15–L18. DOI: 10.1016/0022-5088(90)90422-G.

[15] S. Gialanella et al. "Kinetics and microstructural aspects of the allotropic transition in tin". In: *Journal of Alloys and Compounds* 474.1–2 (2009), pp. 134–139. DOI: 10.1016/j.jallcom.2008.06.103.

[16] Xiao-long Zuo and Ai-Ping Xian. "The influence of presetting α-Sn on the transformation of Sn at low temperature". In: *2013 14th International Conference on Electronic Packaging Technology*. 2013, pp. 152–155. DOI: 10.1109/ICEPT.2013.6756444.

[17] G. Zeng et al. "Effects of element addition on the $\beta \rightarrow \alpha$ transformation in tin". In: *Philos. Mag. Lett.* 94.2 (2014), pp. 53–62. DOI: 10.1080/09500839.2013.860247.

[18] G. V. Raynor and R. W. Smith. "The transition temperature of the transition between grey and white tin". In: *Proc. R. Soc. Lond. A* 244 (1958), pp. 101–109. DOI: `10.1098/rspa.1958.0028`.

[19] Ivan Madarevic et al. "Structural and electronic properties of the pure and stable elemental 3D topological Dirac semimetal α-Sn". In: *APL Materials* 8 (2020), p. 031114. DOI: `10.1063/1.5142841`.

[20] N. Dokania et al. "Characterization and modeling of a low background HPGe detector". In: *Nucl. Instruments Methods Phys. Res. Sect. A Accel. Spectrometers, Detect. Assoc. Equip.* 745 (2014), pp. 119–127. DOI: `10.1016/j.nima.2014.01.064`.

[21] Sabyasachi Paul et al. "Measurement of neutron spectra generated from bombardment of 4 to 24 MeV protons on a thick ^9Be target and estimation of neutron yields". In: *Rev. Sci. Instrum.* 85 (2014), p. 063501. DOI: `10.1063/1.4880202`.

[22] N. Dokania et al. "Study of neutron-induced background and its effect on the search of $0\nu\beta\beta$ decay in ^{124}Sn". In: *J. Instrum.* 9 (2014), P11002. DOI: `10.1088/1748-0221/9/11/P11002`.

[23] Pierre de Marcillac et al. "Experimental detection of α-particles from the radioactive decay of natural bismuth". In: *Nature* 422 (2003), pp. 876–878. DOI: `10.1038/nature01541`.

[24] F. Alessandria et al. "CUORE crystal validation runs: Results on radioactive contamination and extrapolation to CUORE background". In: *Astropart. Phys.* 35.12 (2012), pp. 839–849. DOI: `10.1016/j.astropartphys.2012.02.008`.

[25] S. Agostinelli et al. "GEANT4 - A simulation toolkit". In: *Nucl. Instruments Methods Phys. Res. Sect. A Accel. Spectrometers, Detect. Assoc. Equip.* 506.3 (2003), pp. 250–303. DOI: `10.1016/S0168-9002(03)01368-8`.

[26] V. I. Tretyak and Yu. G. Zdesenko. "Tables of double beta decay". In: *Atomic Data and Nuclear Data Tables* 61.1 (1995), pp. 43–90.

[27] D. Q. Adams et al. "Improved Limit on Neutrinoless Double-Beta Decay in ^{130}Te with CUORE". In: *Phys. Rev. Lett.* 124 (2020), p. 122501. DOI: 10.1103/PhysRevLett.124.122501.

[28] Carsten Jensen et al. *From Anomaly to Explanation: The Continuous Beta Spectrum, 1929–1934*. Ed. by Finn Aaserud et al. Birkhäuser, 2000, pp. 145–184. ISBN: 978-3-0348-8444-0. DOI: 10.1007/978-3-0348-8444-0_6.

[29] W. Pauli. "Letter to L. Meitner and her colleagues dated 4 December 1930". In: *Phys. Today 31N9* 27 (1978).

[30] E. Fermi. "Towards the Theory of β-Rays". In: *Z. Phys* 88 (1934), pp. 161–177. DOI: 10.1007/BF01351864.

[31] H. Bethe and R. Peierls. "The Neutrino". In: *Nature* 133 (1934), pp. 689–690. DOI: 10.1038/133689b0.

[32] C. L. Cowan et al. "Detection of the Free Neutrino: A Confirmation". In: *Science* 124.3212 (1956), pp. 103–104. DOI: 10.1126/science.124.3212.103.

[33] C. S. Wu et al. "Experimental Test of Parity Conservation in Beta Decay". In: *Phys. Rev.* 105 (1957), pp. 1413–1415. DOI: 10.1103/PhysRev.105.1413.

[34] Richard L. Garwin, Leon M. Lederman, and Marcel Weinrich. "Observations of the Failure of Conservation of Parity and Charge Conjugation in Meson Decays: the Magnetic Moment of the Free Muon". In: *Phys. Rev.* 105 (1957), pp. 1415–1417. DOI: 10.1103/PhysRev.105.1415.

[35] M. Goldhaber, L. Grodzins, and A. W. Sunyar. "Helicity of Neutrinos". In: *Phys. Rev.* 109 (1958), pp. 1015–1017. DOI: 10.1103/PhysRev.109.1015.

[36] A. Aguilar et al. "Evidence for neutrino oscillations from the observation of $\overline{\nu}_e$ appearance in a $\overline{\nu}_\mu$ beam". In: *Phys. Rev. D* 64 (2001), p. 112007. DOI: 10.1103/PhysRevD.64.112007.

[37] A. A. Aguilar-Arevalo et al. "Significant Excess of Electronlike Events in the MiniBooNE Short-Baseline Neutrino Experiment". In: *Phys. Rev. Lett.* 121 (2018), p. 221801. DOI: 10.1103/PhysRevLett.121.221801.

[38] Esra Bulbul et al. "Detection of an unidentified emission line in the stacked x-ray spectrum of galaxy clusters". In: *ApJ* 789.1 (2014), p. 13. DOI: 10.1088/0004-637X/789/1/13.

[39] Raymond Davis, Don S. Harmer, and Kenneth C. Hoffman. "Search for Neutrinos from the Sun". In: *Phys. Rev. Lett.* 20 (1968), pp. 1205–1209. DOI: 10.1103/PhysRevLett.20.1205.

[40] T. A. Kirsten. "GALLEX solar neutrino results". In: *Prog. Part. Nucl. Phys.* 40 (1998), pp. 85–99. DOI: 10.1016/s0146-6410(98)00013-1.

[41] Y. Fukuda et al. "Evidence for Oscillation of Atmospheric Neutrinos". In: *Phys. Rev. Lett.* 81 (1998), pp. 1562–1567. DOI: 10.1103/PhysRevLett.81.1562.

[42] J. N. Bahcall et al. "Solar Neutrino Flux." In: *ApJ* 137 (1963), pp. 344–346.

[43] B. Pontecorvo. "Mesonium and antimesonium". In: *J. Exptl. Theoret. Phys. (U.S.S.R.)* 33 (1957), pp. 549–551.

[44] Ziro Maki, Masami Nakagawa, and Shoichi Sakata. "Remarks on the Unified Model of Elementary Particles". In: *Prog. Theor. Phys.* 28.5 (1962), pp. 870–880. DOI: 10.1143/PTP.28.870.

[45] Q. R. Ahmad et al. "Direct Evidence for Neutrino Flavor Transformation from Neutral-Current Interactions in the Sudbury Neutrino Observatory". In: *Phys. Rev. Lett.* 89 (2002), p. 011301. DOI: 10.1103/PhysRevLett.89.011301.

[46] G. Alimonti et al. "Science and technology of Borexino: A real-time detector for low energy solar neutrinos". In: *Astropart. Phys.* 16.3 (2002), pp. 205–234. DOI: 10.1016/S0927-6505(01)00110-4.

[47] K. Eguchi et al. "First Results from KamLAND: Evidence for Reactor Antineutrino Disappearance". In: *Phys. Rev. Lett.* 90 (2003), p. 021802. DOI: 10.1103/PhysRevLett.90.021802.

[48] An F. P. et al. "Improved measurement of electron antineutrino disappearance at Daya Bay". In: *Chinese Phys. C* 37 (2013), p. 011001. DOI: 10.1088/1674-1137/37/1/011001.

[49] Y. Abe et al. "Reactor $\overline{\nu}_e$ disappearance in the Double Chooz experiment". In: *Phys. Rev. D* 86 (2012), p. 052008. DOI: `10.1103/PhysRevD.86.052008`.

[50] J. K. Ahn et al. "Observation of reactor electron antineutrinos disappearance in the RENO experiment". In: *Phys. Rev. Lett.* 108 (2012), p. 191802. DOI: `10.1103/PhysRevLett.108.191802`.

[51] P. Adamson et al. "Measurement of the neutrino mass splitting and flavor mixing by MINOS". In: *Phys. Rev. Lett.* 106 (2011), p. 181801. DOI: `10.1103/PhysRevLett.106.181801`.

[52] P. Adamson et al. "First Measurement of Electron Neutrino Appearance in NOvA". In: *Phys. Rev. Lett.* 116 (2016), p. 151806. DOI: `10.1103/PhysRevLett.116.151806`.

[53] K. Abe et al. "Constraint on the matter–antimatter symmetry-violating phase in neutrino oscillations". In: *Nature* 580 (2020), pp. 339–344. DOI: `10.1038/s41586-020-2177-0`.

[54] P. F. de Salas et al. "2020 global reassessment of the neutrino oscillation picture". In: *J. High Energy Phys.* 2021 (2021), p. 71. DOI: `10.1007/JHEP02(2021)071`.

[55] Stephen F. King and Christoph Luhn. "Neutrino mass and mixing with discrete symmetry". In: *Rep. Prog. Phys.* 76 (2013), p. 056201. DOI: `10.1088/0034-4885/76/5/056201`.

[56] N. Aghanim et al. "Planck 2018 results: VI. Cosmological parameters". In: *Astronomy & Astrophysics* 641 (2020), A6. DOI: `10.1051/0004-6361/201833910`.

[57] F. M. Fraenkle and for the KATRIN collaboration. "The neutrino mass experiment KATRIN". In: *J. Phys.: Conf. Ser.* 1342 (2020), p. 012024. DOI: `10.1088/1742-6596/1342/1/012024`.

[58] D. M. Asner et al. "Single-Electron Detection and Spectroscopy via Relativistic Cyclotron Radiation". In: *Phys. Rev. Lett.* 114 (2015), p. 162501. DOI: `10.1103/PhysRevLett.114.162501`.

[59] L. Gastaldo et al. "The electron capture in ^{163}Ho experiment – ECHo". In: *Eur. Phys. J. Spec. Top.* 226 (2017), pp. 1623–1694. DOI: `10.1140/epjst/e2017-70071-y`.

[60] A. Puiu et al. "HOLMES, an experiment for a direct measurement of neutrino mass". In: *Il Nuovo Cimento C* 42 (2019), p. 178. DOI: `10.1393/ncc/i2019-19178-6`.

[61] M. Goeppert-Mayer. "Double Beta-Disintegration". In: *Phys. Rev.* 48 (1935), pp. 512–516. DOI: `10.1103/PhysRev.48.512`.

[62] Ettore Majorana. "Teoria simmetrica dell'elettrone e del positrone". In: *Nuovo Cim.* 14 (1937), pp. 171–184. DOI: `10.1007/BF02961314`.

[63] W. H. Furry. "On Transition Probabilities in Double Beta-Disintegration". In: *Phys. Rev.* 56 (1939), pp. 1184–1193. DOI: `10.1103/PhysRev.56.1184`.

[64] Steven R. Elliott and Petr Vogel. "Double Beta Decay". In: *Annu. Rev. Nucl. Part. Sci.* 52 (2002), pp. 115–151. DOI: `10.1146/annurev.nucl.52.050102.090641`.

[65] Stefano Dell'Oro et al. "Neutrinoless Double Beta Decay: 2015 Review". In: *Adv. High Energy Phys.* 2016 (2016), p. 2162659. DOI: `10.1155/2016/2162659`.

[66] Vandana Nanal. "Is neutrino its own antiparticle?" In: *Current Science* 112.7 (2017), pp. 1375–1380.

[67] Ruben Saakyan. "Two-Neutrino Double-Beta Decay". In: *Annu. Rev. Nucl. Part. Sci.* 63.1 (2013), pp. 503–529. DOI: `10.1146/annurev-nucl-102711-094904`.

[68] Meng Wang et al. "The AME2016 atomic mass evaluation (II). Tables, graphs and references". In: *Chinese Physics C* 41.3 (2017), p. 030003. DOI: `10.1088/1674-1137/41/3/030003`.

[69] Jason Detwiler. "Future Neutrinoless Double Beta Decay Experiments". In: Presented at the Neutrino 2020 (neutrino2020), Zenodo (2020). DOI: `10.5281/zenodo.4154380`.

[70] M. Agostini et al. "Final Results of GERDA on the Search for Neutrinoless Double-β Decay". In: *Phys. Rev. Lett.* 125 (2020), p. 252502. DOI: `10.1103/PhysRevLett.125.252502`.

[71] N. Abgrall et al. "The MAJORANA DEMONSTRATOR Neutrinoless Double-Beta Decay Experiment". In: *Adv. High Energy Phys.* 2014 (2014), p. 365432. DOI: `10.1155/2014/365432`.

[72] N. Abgrall et al. "The large enriched germanium experiment for neutrinoless double beta decay (LEGEND)". In: *AIP Conf. Proc.* 1894 (2017), p. 020027. DOI: `10.1063/1.5007652`.

[73] A. E. Chavarria et al. "A high-resolution CMOS imaging detector for the search of neutrinoless double β decay in ^{82}Se". In: *JINST* 12 (2017), P03022. DOI: `10.1088/1748-0221/12/03/P03022`.

[74] I. Nutini et al. "The CUORE Detector and Results". In: *J. Low Temp. Phys.* 199 (2020), pp. 519–528. DOI: `10.1007/s10909-020-02402-9`.

[75] M. H. Lee. "AMoRE: A search for neutrinoless double-beta decay of 100Mo using low-temperature molybdenum-containing crystal detectors". In: *JINST*. Vol. 15. Institute of Physics Publishing, 2020, p. C08010. DOI: `10.1088/1748-0221/15/08/C08010`.

[76] D. R. Artusa et al. "Enriched TeO_2 bolometers with active particle discrimination: Towards the CUPID experiment". In: *Phys. Lett. Sect. B* 767 (2017), pp. 321–329. DOI: `10.1016/j.physletb.2017.02.011`.

[77] The NEXT collaboration. "Sensitivity of NEXT-100 to neutrinoless double beta decay". In: *J. High Energy Phys.* 2016 (2016), p. 159. DOI: `10.1007/JHEP05(2016)159`.

[78] Kaixiang Ni et al. "Searching for neutrino-less double beta decay of ^{136}Xe with PandaX-II liquid xenon detector". In: *Chinese Phys. C* 43 (2019), p. 113001. DOI: `10.1088/1674-1137/43/11/113001`.

[79] J. B. Albert et al. "Search for Neutrinoless Double-Beta Decay with the Upgraded EXO-200 Detector". In: *Phys. Rev. Lett.* 120 (2018), p. 072701. DOI: `10.1103/PhysRevLett.120.072701`.

[80] D. S. Akerib et al. "Projected sensitivity of the LUX-ZEPLIN experiment to the $0\nu\beta\beta$ decay of ^{136}Xe". In: *Phys. Rev. C* 102 (2020), p. 014602. DOI: `10.1103/PhysRevC.102.014602`.

[81] F. Agostini et al. "Sensitivity of the DARWIN observatory to the neutrinoless double beta decay of ^{136}Xe". In: *Eur. Phys. J. C* 80 (2020), p. 808. DOI: `10.1140/epjc/s10052-020-8196-z`.

[82] A. Gando et al. "Search for Majorana Neutrinos Near the Inverted Mass Hierarchy Region with KamLAND-Zen". In: *Phys. Rev. Lett.* 117 (2016), p. 082503. DOI: `10.1103/PhysRevLett.117.082503`.

[83] S. Andringa et al. "Current Status and Future Prospects of the SNO+ Experiment". In: *Adv. High Energy Phys.* 2016 (2016), p. 6194250. DOI: `10.1155/2016/6194250`.

[84] H. Gómez (NEMO-3 & SuperNEMO collaborations). "Latest results of NEMO-3 experiment and present status of SuperNEMO". In: *Nucl. Part. Phys. Proc.* 273-275 (2016), pp. 1765–1770. DOI: `10.1016/j.nuclphysbps.2015.09.284`.

[85] S. Pascoli and S. T. Petcov. "Majorana neutrinos, neutrino mass spectrum, and the $|<m>| \sim 10^{-3}$ eV frontier in neutrinoless double beta decay". In: *Phys. Rev. D* 77 (2008), p. 113003. DOI: `10.1103/PhysRevD.77.113003`.

[86] Sergey Petcov. "Neutrinoless double beta decay searches: theory and motivation". In: Presented at the Neutrino 2020 (neutrino2020), Zenodo (2020). DOI: `10.5281/zenodo.4134015`.

[87] A. Kumar et al. "Invited review: Physics potential of the ICAL detector at the India-based Neutrino Observatory (INO)". In: *Pramana* 88 (2017), p. 79. DOI: `10.1007/s12043-017-1373-4`.

[88] Isotope Rosatom. *Tin-124*. `http://www.isotop.ru/en/view/1804/` (Last accessed: 02-07-2021).

[89] A. Garai et al. "Development of NTD Ge Sensors for Superconducting Bolometer". In: *J. Low Temp. Phys.* 184 (2016), pp. 609–614. DOI: `10.1007/s10909-015-1379-6`.

[90] S. Mathimalar et al. "Characterization of Neutron Transmutation Doped (NTD) Ge for low temperature sensor development". In: *Nucl. Instruments Methods Phys. Res. Sect. B Beam Interact. with Mater. Atoms* 345 (2015), pp. 33–36. DOI: `10.1016/j.nimb.2014.12.020`.

[91] M. J. Hwang et al. "A search for $0\nu\beta\beta$ decay of ^{124}Sn with tin-loaded liquid scintillator". In: *Astropart. Phys.* 31.6 (2009), pp. 412–416. DOI: 10.1016/j.astropartphys.2009.05.001.

[92] YangYang Underground Laboraborty (Y2L). https://cupweb.ibs.re.kr/en/facilities-and-equipment/underground-labs/y2l/ (Last accessed: 02-07-21).

[93] Andrei Neacsu and Mihai Horoi. "Shell Model Studies of Competing Mechanisms to the Neutrinoless Double-Beta Decay in ^{124}Sn, ^{130}Te, and ^{136}Xe". In: *Adv. High Energy Phys.* 2016 (2016), p. 1903767. DOI: 10.1155/2016/1903767.

[94] O. Chkvorets et al. "A tin-loaded liquid scintillator approach for the 2 neutrino double-beta decay measurement of Sn-124". In: *arXiv* (2017). arXiv: 1707.08001.

[95] O. Chkvorets et al. "Liquid scintillator for search of double beta decay with Tin". In: *J. Phys.: Conf. Ser.* 1342 (2020), p. 12112. DOI: 10.1088/1742-6596/1342/1/012112.

[96] S. P. Langley. "The Bolometer and Radiant Energy". In: *Proceedings of the American Academy of Arts and Sciences* 16 (1880), pp. 342–358. DOI: 10.2307/25138616.

[97] Klaus Pretzl. "Cryogenic Detectors". In: *Particle Physics Reference Library: Volume 2: Detectors for Particles and Radiation*. Ed. by Christian W. Fabjan and Herwig Schopper. Cham: Springer International Publishing, 2020, pp. 871–912. ISBN: 978-3-030-35318-6. DOI: 10.1007/978-3-030-35318-6_19.

[98] G. Angloher et al. "Results on light dark matter particles with a low-threshold CRESST-II detector". In: *Eur. Phys. J. C* 76 (2016), p. 25. DOI: 10.1140/epjc/s10052-016-3877-3.

[99] E. Armengaud et al. "Constraints on low-mass WIMPs from the EDELWEISS-III dark matter search". In: *Journal of Cosmology and Astroparticle Physics* 2016 (2016), p. 019. DOI: 10.1088/1475-7516/2016/05/019.

[100] R. Agnese et al. "Search for Low-Mass Weakly Interacting Massive Particles with SuperCDMS". In: *Phys. Rev. Lett.* 112 (2014), p. 241302. DOI: `10.1103/PhysRevLett.112.241302`.

[101] S. Pirro et al. "Scintillating double-beta-decay bolometers". In: *Physics of Atomic Nuclei* 69 (2006), pp. 2109–2116. DOI: `10.1134/S1063778806120155`.

[102] N. Casali et al. "Discovery of the ^{151}Eu α decay". In: *J. Phys. G: Nucl. Part. Phys.* 41 (2014), p. 075101. DOI: `10.1088/0954-3899/41/7/075101`.

[103] Frank Pobell. *Matter and Methods at Low Temperatures*. Berlin, Heidelberg: Springer, 2007.

[104] H. London. In: *Proc. Int. Conf. on Low Temp. Phys* (1951), p. 157.

[105] P. Das, R. de Bruyn Ouboter, and K. W. Taconis. "A Realization of a London-Clarke-Mendoza Type Refrigerator". In: *Proc. of Low Temperature Physics LT9* (1965), pp. 1253–1255. DOI: `10.1007/978-1-4899-6443-4_133`.

[106] G. Frossati. "Experimental techniques: Methods for cooling below 300 mK". In: *J. Low Temp. Phys.* 87 (1992), pp. 595–633. DOI: `10.1007/BF00114918`.

[107] Rachpon Kalra et al. "Vibration-induced electrical noise in a cryogen-free dilution refrigerator: Characterization, mitigation, and impact on qubit coherence". In: *Review of Scientific Instruments* 87 (2016), p. 073905. DOI: `10.1063/1.4959153`.

[108] C. Lee et al. "Vibration isolation system for cryogenic phonon-scintillation calorimeters". In: *JINST* 12 (2017), p. C02057. DOI: `10.1088/1748-0221/12/02/C02057`.

[109] JPE. *CVIP*. `https://www.jpe-innovations.com/cryo-nano-products/cryo-vibration-isolation-platform-cvip/` (Last accessed: 02-07-2021).

[110] Cai-Zhi Xu et al. "Elemental Topological Dirac Semimetal: α-Sn on InSb(111)". In: *Phys. Rev. Lett.* 118 (2017), p. 146402. DOI: `10.1103/PhysRevLett.118.146402`.

[111] Nan Si et al. "Recent Advances in Tin: From Two-Dimensional Quantum Spin Hall Insulator to Bulk Dirac Semimetal". In: *J. Phys. Chem. Lett.* 11.4 (2020), pp. 1317–1329. DOI: `10.1021/acs.jpclett.9b03538`.

[112] O. L. Erdmann. In: *J. Prakt. Chem.* 52 (1951), p. 428.

[113] Mark Gilberg. "History of tin pest: the museum disease". In: *AICCM Bulletin* 17.1-2 (1991), pp. 3–20. DOI: `10.1179/bac.1991.17.1-2.001`.

[114] W. J. Plumbridge. "Recent observations on tin pest formation in solder alloys". In: *J. Electron. Mater.* 37.2 (2008), pp. 218–223. DOI: `10.1007/s11664-007-0165-x`.

[115] Weiqun Peng. "An investigation of Sn pest in pure Sn and Sn-based solders". In: *Microelectron. Reliab.* 49.1 (2009), pp. 86–91. ISSN: 00262714. DOI: `10.1016/j.microrel.2008.11.001`.

[116] Y. Kariya et al. "Tin pest in Sn-0.5 wt.% Cu lead-free solder". In: *JOM* 53.6 (2001), pp. 39–41. DOI: `10.1007/s11837-001-0101-0`.

[117] W. G. Burgers and L. J. Groen. "Mechanism and kinetics of the allotropic transformation of tin". In: *Discussions of the Faraday Society* 23 (1957), pp. 183–195. DOI: `10.1039/DF9572300183`.

[118] K. Nogita et al. "XRD study of the kinetics of $\beta \leftrightarrow \alpha$ transformations in tin". In: *Philosophical Magazine* 93.27 (2013), pp. 3627–3647. DOI: `10.1080/14786435.2013.820381`.

[119] D. Di Maio and C. P. Hunt. "Monitoring the growth of the α phase in tin alloys by electrical resistance measurements". In: *J. Electron. Mater.* 38 (2009), pp. 1874–1880. DOI: `10.1007/s11664-009-0822-3`.

[120] Agata Skwarek et al. "Early stage detection of $\beta{\rightarrow}\alpha$ transition in Sn by Mössbauer spectroscopy". In: *Mater. Chem. Phys.* 182 (2016), pp. 10–14. DOI: `10.1016/j.matchemphys.2016.07.061`.

[121] A. Skwarek et al. "Identification and characterization of $\alpha \rightarrow \beta$-Sn transition in SnCu1 bulk alloy inoculated with InSb". In: *J. Mater. Sci. Mater. Electron.* 28 (2017), pp. 16329–16335. DOI: `10.1007/s10854-017-7539-5`.

[122] A. D. Styrkas. "Mechanisms of the allotropic transition of Sn". In: *Inorg. Mater.* 39.8 (2003), pp. 806–810. DOI: `10.1023/A:1025065027495`.

[123]   Michael J. Mehl et al. "The Tin Pest Problem as a Test of Density Functionals Using High-Throughput Calculations". In: (2020). arXiv: `2010.07168`.

[124]   Fleur Legrain and Sergei Manzhos. "Understanding the difference in cohesive energies between alpha and beta tin in DFT calculations". In: *AIP Adv.* 6 (2016), p. 045116. DOI: `10.1063/1.4948434`.

[125]   Pasquale Pavone and Stefano Baroni. "$\alpha \leftrightarrow \beta$ phase transition in tin: A theoretical study based on density-functional perturbation theory". In: *Phys. Rev. B* 57 (1998), pp. 10421–10423. DOI: `10.1103/PhysRevB.57.10421`.

[126]   Fleur Legrain et al. "Comparison of alpha and beta tin for lithium, sodium, and magnesium storage: An ab initio study including phonon contributions". In: *J. Chem. Phys.* 143 (2015), p. 204701. DOI: `10.1063/1.4936284`.

[127]   G. W. H. Höhne, W. Hemminger, and H. J. Flammersheim. *Theoretical Fundamentals of Differential Scanning Calorimeters*. Berlin, Heidelberg: Springer, 1996, pp. 21 – 40. DOI: `10.1007/978-3-662-03302-9_3`.

[128]   Heiko K. Cammenga et al. "The temperature calibration of scanning calorimeters. Part 2. Calibration substances". In: *Thermochim. Acta* 219 (1993), pp. 333–342. DOI: `10.1016/0040-6031(93)80510-H`.

[129]   Hussein Farahani et al. "In Situ High-Temperature EBSD and 3D Phase Field Studies of the Austenite-Ferrite Transformation in a Medium Mn Steel". In: *Microsc. Microanal.* 25.3 (2019), pp. 639–655. DOI: `10.1017/S143192761900031X`.

[130]   Tatsuya Fukino and Sadahiro Tsurekawa. "In-Situ SEM/EBSD Observation of = Phase Transformation in Fe-Ni Alloy". In: *Materials Transactions* 49 (2008), p. 12. DOI: `10.2320/matertrans.MAW200824`.

[131]   A.-F. Gourgues-Lorenzon. "Application of electron backscatter diffraction to the study of phase transformations: present and possible future". In: *J. Microsc.* 233.3 (2009), pp. 460–473. DOI: `10.1111/j.1365-2818.2009.03130.x`.

[132] G. G. E. Seward et al. "In situ SEM-EBSD observations of the hcp to bcc phase transformation in commercially pure titanium". In: *Acta Mater.* 52.4 (2004), pp. 821–832. DOI: `10.1016/j.actamat.2003.10.049`.

[133] A. P. Hammersley et al. "FIT2D: an introduction and overview". In: *Eur. Synchrotron Radiat. Facil. Intern. Rep. ESRF97HA02T* 68 (1997), p. 58.

[134] A. P. Hammersley et al. "Two-dimensional detector software: From real detector to idealised image or two-theta scan". In: *High Press. Res.* 14.4-6 (1996), pp. 235–248. DOI: `10.1080/08957959608201408`.

[135] Gerd Heusser. "Low-radioactivity background techniques". In: *Annual review of Nuclear and Particle science* 45.1 (1995), pp. 543–590.

[136] Harisree Krishnamoorthy. "Radiation background studies for rare decay experiments". PhD thesis. 2020.

[137] Neha Dokania. "Radiation background studies for Neutrinoless Double Beta Decay in ^{124}Sn". PhD thesis. 2015.

[138] Linux Advanced Multi Parameter System (LAMPS). Available at `https://www.tifr.res.in/~pell/lamps.html` (Last accessed: 11/04/21).

[139] National Nuclear Data Center. Available at `https://www.nndc.bnl.gov/nudat2/` (Last accessed: 25/06/21).

[140] J. W. Beeman et al. "First Measurement of the Partial Widths of ^{209}Bi Decay to the Ground and to the First Excited States". In: *Phys. Rev. Lett.* 108 (2012), p. 062501. DOI: `10.1103/PhysRevLett.108.062501`.

[141] The Stopping and Range of Ions in Matter. Available at `http://www.srim.org/` (Last accessed: 21/06/21).

[142] Vivek Singh. "Development of Cryogenic Bolometer for Neutrinoless Double Beta Decay in ^{124}Sn". PhD thesis. 2014.

[143] A. Letourneau et al. "Measurement of the ^{210}Po production induced by thermal neutron capture on ^{209}Bi". In: *Annals of Nuclear Energy* 33.4 (2006), pp. 377–384. DOI: `10.1016/j.anucene.2005.11.005`.

[144] V. Singh et al. "Heat Capacity Setup for Superconducting Bolometer Absorbers below 400 mK". In: *Journal of Low Temperature Physics* 175 (2014), pp. 604–613. DOI: `10.1007/s10909-013-1081-5`.

[145] V. I. Tretyak. "Spontaneous double alpha decay: First experimental limit and prospects of investigation". In: *arXiv preprint arXiv:2102.12005* (2021).

[146] J. H. Chao and A. C. Chiang. "Activation detection using indium foils for simultaneous monitoring neutron and photon intensities in a reactor core". In: *Radiation Measurements* 45.9 (2010), pp. 1024–1033. DOI: `https://doi.org/10.1016/j.radmeas.2010.08.012`.

[147] S. Mathimalar et al. "Study of radioactive impurities in neutron transmutation doped germanium". In: *Nucl. Instruments Methods Phys. Res. Sect. A Accel. Spectrometers, Detect. Assoc. Equip.* 774 (2015), pp. 68–73. DOI: `https://doi.org/10.1016/j.nima.2014.11.056`.